

ADVISORY COMMITTEE

Chairman – JAN KMITA¹

Subchairman – WOJCIECH GLABISZ²
JAN BILISZCZUK (Poland)
CZESŁAW CEMPEL (Poland)
ANTONI GRONOWICZ (Poland)
M.S.J. HASHMI (Ireland)
HENRYK HAWRYLAK (Poland)
RYSZARD IZBICKI (Poland)
WACLAW KASPRZAK (Poland)
MICHAEL KETTING (Germany)
MICHAŁ KLEIBER (Poland)
VADIM L. KOŁMOGOROV (Russia)

ADOLF MACIEJNY (Poland)
ZDZISŁAW MARCINIĄK (Poland)
KAZIMIERZ RYKALUK (Poland)
ANDRZEJ RYŻYŃSKI (Poland)
ZDZISŁAW SAMSONOWICZ (Poland)
WOJCIECH SZCZEPIŃSKI (Poland)
PAWEŁ ŚNIADY (Poland)
RYSZARD TADEUSIEWICZ (Poland)
TARRAS WANHEIM (Denmark)
WŁADYSŁAW WŁOSIŃSKI (Poland)
JERZY ZIÓŁKO (Poland)
JÓZEF ZASADZIŃSKI (Poland)

EDITORIAL BOARD

Editor-in-chief – ZBIGNIEW GRONOSTAJSKI³
ROBERT ARRIEUX (France)
AUGUSTO BARATA DA ROCHA (Portugal)
GHEORGHE BRABIE (Romania)
LESŁAW BRUNARSKI (Poland)
EDWARD CHLEBUS (Poland)
LESZEK F. DEMKOWICZ (USA)
KAZIMIERZ FLAGA (Poland)
YOSHINOBI FUJITANI (Japan)
FRANCISZEK GROSZMAN (Poland)
MIECZYSŁAW KAMIŃSKI (Poland)
Scientific secretary – SYLWESTER KOBIELAK
ANDRZEJ KOCAŃDA (Poland)

WACŁAW KOLLEK (Poland)
PIOTR KONDERLA (Poland)
ZBIGNIEW KOWAL (Poland)
TED KRAUTHAMMER (USA)
ERNEST KUBICA (Poland)
CEZARY MADRYAS (Poland)
TADEUSZ B. MASSALSKI (USA)
TADEUSZ MIKULCZYŃSKI (Poland)
HARTMUT PASTERNAK (Germany)
MACIEJ PIETRZYK (Poland)
EUGENIUSZ RUSIŃSKI (Poland)
HANNA SUCHNICKA (Poland)
EDMUNDAS K. ZAVADSKAS (Lithuania)

¹ The Faculty of Civil Engineering, Wrocław University of Technology
Wybrzeże Wyspiańskiego 27, 50-370 Wrocław, Poland
Tel. +48 71 320 41 35, Fax. +48 71 320 41 05, E-mail: jan.kmita@pwr.wroc.pl

² The Faculty of Civil Engineering, Wrocław University of Technology
Wybrzeże Wyspiańskiego 27, 50-370 Wrocław, Poland
Tel. +48 71 320 34 04, E-mail: wojciech.glabisz@pwr.wroc.pl

³ The Faculty of Mechanical Engineering, Wrocław University of Technology
ul. Łukasiewicza 5, 50-371 Wrocław, Poland
Tel. +48 71 320 21 73, Fax. +48 71 320 34 22, E-mail: metalplast@pwr.wroc.pl

Archives of Civil and Mechanical Engineering is indexed and abstracted in the following:

- Science Citation Index Expanded (also known as SciSearch®),
- Journal Citation Reports/Science Edition.

POLISH ACADEMY OF SCIENCES – WROCŁAW BRANCH
WROCŁAW UNIVERSITY OF TECHNOLOGY

**ARCHIVES
OF CIVIL AND MECHANICAL
ENGINEERING**

**Quarterly
Vol. XI, No. 3**

WROCŁAW 2011

EDITOR IN CHIEF

ZBIGNIEW GRONOSTAJSKI

EDITORIAL LAYOUT AND PROOF-READING

WIOLETTA GÓRALCZYK

TYPESETTING

SEBASTIAN ŁAWRUSEWICZ

SECRETARY

WIOLETTA GÓRALCZYK

**Publisher: Committee of Civil and Mechanical Engineering
of Polish Academy of Sciences – Wrocław Branch,
Faculty of Civil Engineering and Faculty of Mechanical Engineering
of Wrocław University of Technology**

© Copyright by Oficyna Wydawnicza Politechniki Wrocławskiej, Wrocław 2011

OFICYNA WYDAWNICZA POLITECHNIKI WROCŁAWSKIEJ

Wybrzeże Wyspiańskiego 27, 50-370 Wrocław

<http://www.oficyna.pwr.wroc.pl>

e-mail: oficwyd@pwr.wroc.pl

ISSN 1644-9665

Drukarnia Oficyny Wydawniczej Politechniki Wrocławskiej. Zam. nr 898/2011.

Contents

A. BAKIĆ, D. SEMENSKI, S. JECIĆ, Contact caustics measurements expanded to anisotropic materials	497
A. BIEGUS, D. WOJCZYSZYN, Studies on buckling lengths of chords for out-of-plane instability	507
J. BIEŃ, Modelling of structure geometry in Bridge Management Systems	519
E. BŁAZIK-BOROWA, J. BĘC, T. NOWICKI, T. LIPECKI, J. SZULEJ, P. MATYS, Measurements of flow parameters for 2-D flow around rectangular prisms of square and rectangle cross-sections located on the ground	533
CZ. BYWALSKI, M. KAMIŃSKI, Estimation of the bending stiffness of rectangular reinforced concrete beams made of steel fibre reinforced concrete	553
P. CZUBAK, Equalization of the transport velocity in a new two-way vibratory conveyer	573
M. M. FAYYADH, H. A. RAZAK, Z. ISMAIL, Combined modal parameters-based index for damage identification in a beamlike structure: theoretical development and verification	587
T. GORZELAŃCZYK, J. HOŁA, Pore structure of self-compacting concretes made using different superplasticizers	611
P. KMIECIK, M. KAMIŃSKI, Modelling of reinforced concrete structures and composite structures with concrete strength degradation taken into consideration	623
L. KORUSIEWICZ, B. KUNECKI, Behaviour of the steel box-type culvert during backfilling	637
M. LEITNER, T. FÖSSL, M. STOSCHKA, W. EICHLSEDER, Evaluation of fillet weld properties and fatigue behaviour in dependence of welding parameters	651
L. MADEJ, L. RAUCH, K. PERZYNSKI, P. CYBULKA, Digital Material Representation as an efficient tool for strain inhomogeneities analysis at the micro scale level	661
M. MEDINECKIENE, E. K. ZAVADSKAS, Z. TURSKIS, Dwelling selection by applying fuzzy game theory	681
T. NOWAKOWSKI, Analysis of modern trends of logistics technology development	699
M. PIETRZYK, R. KUZIAK, Computer aided interpretation of results of the Jominy test	707
U. RADÓŃ, Reliability analysis of Misses truss	723
J. ROŃDA, A. SIWEK, Modelling of laser welding process in the phase of keyhole formation	739
K. ŚCIGALA, R. BĘDZIŃSKI, J. FILPIAK, E. CHLEBUS, B. DYBALA, Application of generative technologies in the design of reduced stiffness stems of hip joint endoprosthesis	753
L. TOMSKI, S. UZNY, A hydraulic cylinder subjected to Euler's load in aspect of the stability and free vibrations taking into account discrete elastic elements	769
T. T. YU, P. LIU, Improved implementation of the extended finite element method for stress analysis around cracks	787

Spis treści

A. BAKIĆ, D. SEMENSKI, S. JECIĆ, Rozszerzenie metody Caustic do pomiaru kontaktu dla materiałów anizotropowych	497
--	-----

A. BIEGUS, D. WOJCZYSZYN, Analiza długości wyboczeniowej pasów kratownic z płaszczyną ustroju	507
J. BIEŃ, Modelowanie geometrii obiektów w Systemach Zarządzania Mostami	519
E. BŁAZIK-BOROWA, J. BĘC, T. NOWICKI, T. LIPECKI, J. SZULEJ, P. MATYS, Pomiary parametrów opływu dwuwymiarowego wokół kwadratu i prostokąta ustawionych na podłożu	533
Cz. BYWALSKI, M. KAMIŃSKI, Szacowanie sztywności giętnej prostokątnych, żelbetowych belek wykonanych z betonu modyfikowanego włóknami stalowymi	553
P. CZUBAK, Wyrównanie prędkości transportowania w nowym dwukierunkowym prześnówku vibracyjnym	573
M. M. FAYYADH, H. A. RAZAK, Z. ISMAIL, Łączny parametr modalny jako indeks identyfikacji zniszczenia konstrukcji belkowych: podstawy teoretyczne i weryfikacja numeryczna	587
T. GORZELAŃCZYK, J. HOŁA, Struktura porów w betonach samozeszczonych wykonanych z użyciem różnych superplastyfikatorów	611
P. KMIECIK, M. KAMIŃSKI, Modelowanie konstrukcji żelbetowych oraz zespolonych z uwzględnieniem degradacji wytrzymałościowej betonu	623
L. KORUSIEWICZ, B. KUNECKI, Zachowanie się skrzynkowego przepustu stalowego w procesie zasypywania gruntem	637
M. LEITNER, T. FÖSSL, M. STOSCHKA, W. EICHLSEDER, Ocena właściwości oraz zachowania zmęczeniowego spoiny pachwinowej w zależności od parametrów spawania	651
L. MADEJ, L. RAUCH, K. PERZYNSKI, P. CYBULKA, Analiza niejednorodności odkształcenia w skali mikro z wykorzystaniem Cyfrowej Reprezentacji Materiału	661
M. MEDINECKIENE, E. K. ZAVADSKAS, Z. TURSKIS, Wybór mieszkania przez zastosowanie teorii gier	681
T. NOWAKOWSKI, Analiza aktualnych trendów rozwoju technologii logistycznych	699
M. PIETRZYK, R. KUZIAK, Wspierana komputerowo interpretacja wyników próby Jominy	707
U. RADOŃ, Probabilistyczna nieliniowa analiza konstrukcji kratowej	723
J. ROŃDA, A. SIWEK, Modelowanie procesu spawania laserowego stali w fazie tworzenia kanału parowego	739
K. ŚCIGAŁA, R. BĘDZIŃSKI, J. FILIPIAK, E. CHLEBUS, B. DYBAŁA, Zastosowanie technologii generatywnych w konstrukcji trzpieni endoprotezy stawu biodrowego o obniżonej sztywności	753
L. TOMSKI, S. UZNY, Siłownik hydrauliczny poddany obciążeniu Eulera w aspekcie staćczności i drgań własnych z uwzględnieniem dyskretnych elementów sprężystych	769
T. T. YU, P. LIU, Udoskonalone zastosowanie rozszerzonej metody elementów skończonych do analizy naprężeń wokół pęknięcia	787

Contact caustics measurements expanded to anisotropic materials

A. BAKIĆ, D. SEMENSKI, S. JECIĆ

University of Zagreb, Faculty of Mechanical Engineering and Naval Architecture, Ivana Lučića 5, 10000 Zagreb, Croatia

Regions with high stress gradients represent critical zones of engineering structures, such as crack tip or vicinity of the contact zone. The optical method of caustics is one of the few experimental methods which provide applicable results in these locations. This method was originally developed for crack-tip measurements of stress intensity factors and J-integral for isotropic and then for anisotropic materials. Subsequently, it was extended to the contact problems, where the size and the shape of caustics are related to the amount and the inclination of loading force. Here, the application of the method of caustics is extended to the analysis of contact problems for mechanically anisotropic materials. This makes the caustics method widely applicable to the analysis of any high stress gradient locations in a structure.

Keywords: caustics, composites, contact

1. Introduction

During the application of the contact force, surfaces of the model are deformed to a convex shape and the reflected light is not homogenous any more; instead, a dark spot surrounded by the concentrated light on its edge (caustics) can be observed on the screen. When non-transparent materials are concerned, it is possible to record caustics only by utilizing the light reflected from the model surface. On the other hand, when transparent materials are concerned, caustics can be formed by the reflecting light from both the front and the rear surface of a model. Since the screen is in front of the model, only a virtual image is obtained. It can be converted into a real image by transferring the light through the focus of a convex lens.

Simulations of the optical effect for the anisotropic materials indicated that the size and the shape of caustic curve depend not only on the loading condition but also on the mechanical material properties. In isotropic materials the shape of the caustics curve is of unique shape for all materials and can be expressed by the epicycloids equation [1], [2].

A plate loaded by cylindrical punch is considered as material model. The illustrative examples for two materials will be shown. A referent isotropic material is Araldit B ($E=3,48$ GPa, $\nu=0.38$) and as anisotropic material uniaxial carbon fibre-reinforced (CFRP131) is used ($E_L=131$ GPa, $E_T=E_B=12$ GPa, $G_{LT}=18$ GPa, $\nu_{LT}=0.29$, $\nu_{TL}=0.29$,

$v_{TB} = 0.34$). Uniaxial carbon fibre-reinforced materials are extremely anisotropic materials which is suitable for analyzing how anisotropy effect on the shape of caustics. Another benefit of such material is a small diameter of fibres (up to 10 μm), which makes it applicable for macro-mechanical analysis. Dimensions of the plate specimen are 50x50x3 mm and they are the same for both materials.

2. Theory of contact caustics

For an analytical approach of the optical effect it is necessary to connect model deformations with the load condition. Lekhnitskii [3], among others, provided an explicit solution to this problem for anisotropic materials by using a complex variable under the following assumptions: the material is of linear elastic characteristics, from a macro-mechanical point of view the material is a homogeneous continuum and the model is in a state of plane stress.

These conditions are satisfied for a thin plate of material with general rectilinear anisotropy and one plane of elastic symmetry (x - y plane). Therefore, the compliance material matrix, S_{ij} , consist 13 nonzero elastic constants.

The contact problem is described as the action of a force F inclined by the angle α on the anisotropic semi-infinite plane (Figure 1). The complex variable is $z_k = x + \mu_k y$, where μ_k are the roots of the characteristic equation

$$S_{11}\mu_k^4 - 2S_{16}\mu_k^3 + (2S_{12} + S_{66})\mu_k^2 - 2S_{26}\mu_k + S_{22} = 0 \quad (1)$$

$$\begin{aligned} \mu_1 &= \alpha_1 + i\beta_1 \quad (\beta_1 > 0), & \mu_3 &= \bar{\mu}_1, \\ \mu_2 &= \alpha_2 + i\beta_2 \quad (\beta_2 > 0), & \mu_4 &= \bar{\mu}_2. \end{aligned} \quad (2)$$

The equation contain information about the mechanical characteristics of the material in the x and y direction. If the principal axes of orthotropy are arbitrarily rotated regarding to x - y coordinates corresponding coefficients S_{mn} should be recalculated before applying to the characteristic equation

$$S_{ij} = a_{im} a_{jn} S_{mn} \quad (i, j, m, n = 1, 2, 3, 6) \quad (3)$$

The stress state can be derived in the following form

$$\sigma_r = -\frac{FS_{11}}{r\pi L(\varphi)} [(a \sin \varphi + b \cos \varphi) \sin \alpha + ((\beta + \delta) \sin \varphi + a \cos \varphi) \cos \alpha], \quad (4)$$

$$\sigma_\varphi = \sigma_{r\varphi} = 0$$

where,

$$L(\varphi) = S_{11} \cos^4 \varphi + 2S_{16} \sin \varphi \cos^3 \varphi + (2S_{12} + S_{66}) \sin^2 \varphi \cos^2 \varphi + \\ + 2S_{26} \sin^3 \varphi \cos \varphi + S_{22} \sin^4 \varphi, \quad (5)$$

$$a = \alpha_1 \beta_2 + \alpha_2 \beta_1, \quad b = (\alpha_1^2 + \beta_1^2) \beta_2 + (\alpha_2^2 + \beta_2^2) \beta_1 \quad (6)$$

Transversal deformation for the stress state is derived from Hooks law

$$\varepsilon_z = S_{31} \sigma_x + S_{32} \sigma_y + S_{36} \tau_{xy}. \quad (7)$$

Although all these equation are valuable for general rectilinear anisotropy analytical solution of the caustic curve will be carried out for orthotropic materials. Materials at our disposal are mainly of orthotropic structure and it is possible to find the principal axes of orthotropy: L-longitudinal, T-transversal and B-bitransversal, which is directed across the plate thickness.

2.1 The formation of caustics on the screen

The explanation of the reflection method of caustics to the non-transparent materials starts from the basic principle of the optical law of reflection. The specimens is loaded and illuminated by the concentrated field of light in the zone of high deformation gradients. The light beams were reflected and transferred from the specimen surface to the virtual plane at distance z_0 . The result on the screen is a dark spot, surrounded by the concentrated light on its edge. The position of single light at the point $P'(x',y')$ on the screen is defined by the vector \vec{r}' , and its corresponding point $P(x,y)$ on the model is defined by the vector \vec{r} (Figure 2).

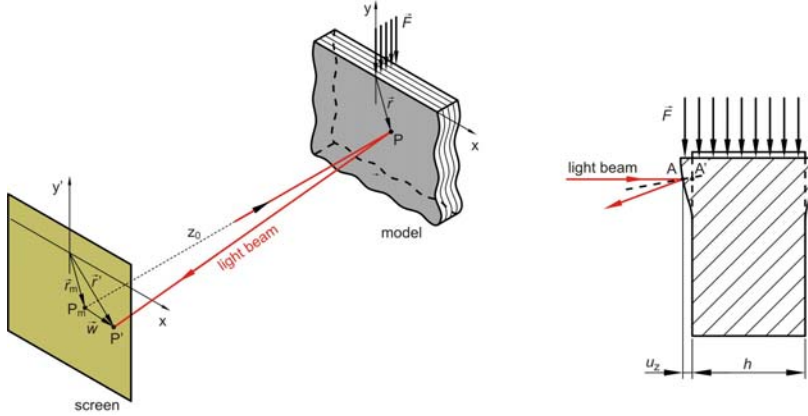


Figure 1. Geometric principle of the beam deflection in the reflecting optical setup

The vectors are related by equations

$$\vec{r}' = \vec{r}_m + \vec{w} = m\vec{r} + z_0 \text{grad} \Delta s, \quad (8)$$

where m is a magnification factor and Δs is the light beam retardation. Magnification factor depends on modulated light: parallel light $m=1$, convergent light $m<1$ and divergent light $m>1$.

Retardation of the reflected light beam for non-transparent materials is given by a simple equation (Figure 2)

$$\Delta s = s - s' = 2|AA'| = 2u_z(x, y) = h\varepsilon_z. \quad (9)$$

where s is the optical path of the light beam for unloaded and s' is optical path for loaded specimen. So, formula (5) transformed to:

$$\vec{r}' = \vec{r}_m + \vec{w} = m\vec{r} + z_0 h \text{grad} \varepsilon_z, \quad (10)$$

where

$$\text{grad} \varepsilon_z = \varepsilon_{z,r} \vec{e}_r + \frac{1}{r} \varepsilon_{z,\phi} \vec{e}_\phi. \quad (11)$$

Finally, the position of the light beam on the screen is

$$x' = mr \sin \phi - z_0 h \left(\varepsilon_{z,r} \sin \phi + \frac{1}{r} \varepsilon_{z,\phi} \cos \phi \right), \quad (12)$$

$$y' = -mr \sin \phi - z_0 h \left(-\varepsilon_{z,r} \cos \phi + \frac{1}{r} \varepsilon_{z,\phi} \sin \phi \right). \quad (13)$$

2.2 Singular caustics curve and initial curve

The singular caustic curve is a highly illuminated edge surrounding the dark spot. The condition of singularity is the Jacobian determinant equals to zero

$$J = \frac{\partial(x', y')}{\partial(r, \phi)} = x'_{,r} y'_{,\phi} - x'_{,\phi} y'_{,r} = 0. \quad (14)$$

This function represents the position of the initial curve on the specimen, where the light beams are reflected and projected onto the singular caustic curve. In order to show the solution equation the following function are introduced.

The solution r_0 of the equation (14) leads to six roots: two of them are the pairs of complex conjugate roots, one root is out of the material and has no physical meaning. Only one root is the real and represents the initial curve on the specimen surface [4]

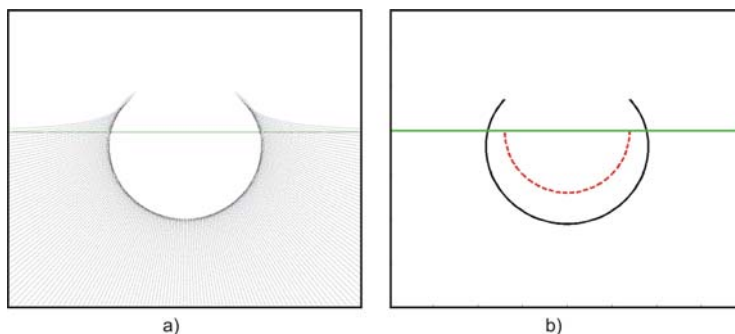


Figure 2. Position of the light beams on the screen a), single caustics curve (solid line) and initial curve (dash line) b)

Figure 2a shows simulated position of the light beams on the screen while Figure 2b shows singular caustic curve (solid line) and initial curve (dash line).

3. Experiments and results

The optical setup consists of a white light source, lenses, a semi-mirror and a digital camera used as a screen. The thickness of models is 3 mm, which is sufficient for the purpose of avoiding the buckling effect. The surface of Araldit is optically flat and needs no preparation, but the surface of carbon fibre-reinforced composite is textured and should be treated. Here, chemical vapour deposition of an aluminium layer is performed; [5]. The applied aluminium layer has the thickness of approximately 20 microns; therefore, it has no influence on the material strength.

Cause of non-transparent properties of composite material only recording in a reflecting light is considered (Figure 3). Semi-mirror is used to make possible perpendicular path of the light rays onto model surface. Light beam comes from the light source (LS) and passes through the convergent lens (L_1) and semi-mirror (M) prior to illuminates the specimen. Semi-mirror reflects the light on a digital camera (RP) which is used as a screen. Lens (L_2) is optional and it can be convergent ($m < 1$), divergent ($m > 1$) or it can be left out ($m = 1$).

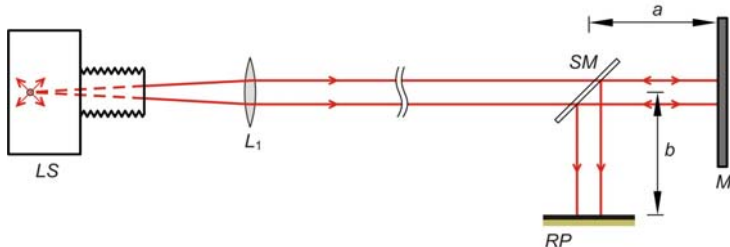


Figure 3. Schematic illustration of the optical setup for recording caustics in the reflecting light.
Light source (LS), lenses (L), semi-mirror (SM), model (M) and reference plane (RP)

Table 1. Parameters of the optical setup

f_{L1}	f_{L2} (divergent lens)	f_{L2} (convergent lens)	x_{L2}	a	b
1000 mm	-600 mm	2000 mm	100 mm	160 mm	100-1200 mm

The optimized values and distances for recording clear image are given in Table 1. Figure 4 shows elements of the optical setup in the laboratory. All elements can be accurately set in optical axis by screws and can be moved along the axis in order to

optimize setup. Large distances between lenses are used to clear the light of unwanted reflections and filter (F) is added to control light intensity on the screen.

Digital camera is set up on the slider which allows continuously changing of z_0 which affect directly on position of initial curve on the specimen.

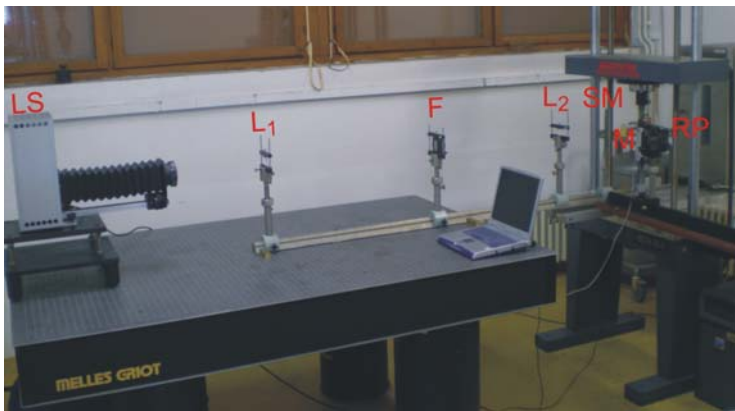


Figure 4. Experimental optical setup

By described optical layout virtual image is obtained on the screen. For obtaining real image it is necessary to add another convergent lens between mirror and digital camera which will invert light through the focus before the screen. Experimental recordings shown that real image is much smaller than virtual one and has no characteristic value to measure.

The bigger one of two caustics shown in Figure 5a is formed on the screen as a reflection from the front surface of the specimen, while the smaller caustics is formed as a reflection from its rear surface. The double effect appears due to birefraction properties of Araldit B because in the case of rear surface reflection light ray should pass through the specimen. Mathematical description of this effect includes not only the surface deformation but also the stress state of a model. Characteristic size of caustics is chosen as y_c which corresponds to radial component of singular caustics curve for $\varphi=0$.

Figure 5b shows the experimentally recorded caustics on the composite material CFRP131 for the case when the fibers are oriented at an angle 45° relative to the direction of the load. The asymmetric optical effect confirms a strong influence of the material orientation on the shape of caustics.

Position of the initial curve on a model depends upon parameter $r_0(\varphi)=r_0(F,m,z_0,S_{ij})$. For the same loading conditions and same specimen, the value of r_0 can still be changed by modifying m (lens L₂) or z_0 (sliding the camera).

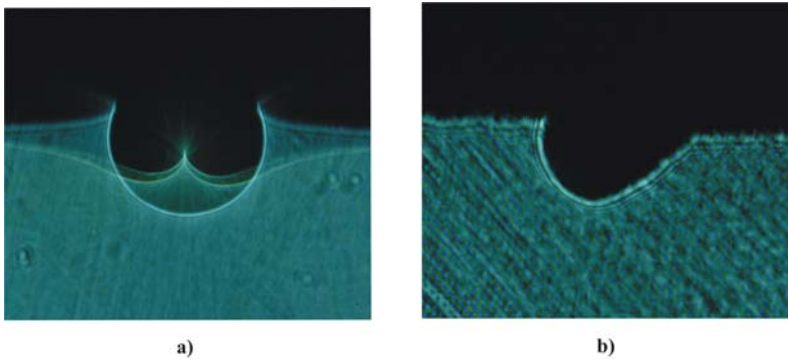


Figure 5. Visual optical effect of the caustics recorded on Araldit B a) and on CFRP131 with fibers orientation at an angle of 45° to the direction of the load b)

Diagram shown on the Figure 6 shows the comparison of analytical and experimental value of characteristic size of caustics. Intensity of contact force was 100 N for Araldit B and 600 N for composite CFRP131. Maximal range of r_0 with presented optical setup was between 1mm and 5 mm. The highest value of r_0 is achieved in convergent light with the large distance z_0 .

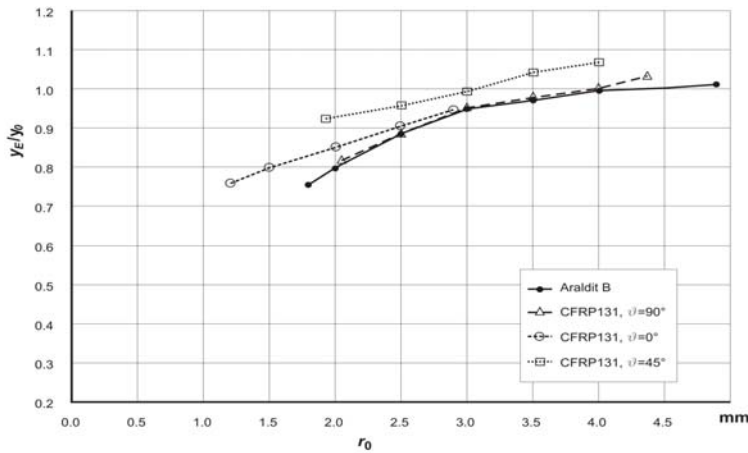


Figure 6. Comparison between experimental and analytical size of caustics for different position of initial curve and different material properties

3. Conclusion

The simulations of the optical effect and the experiments confirm that for the anisotropic materials size and shape of caustic curve depend not only on the loading condition but also on the mechanical material properties. In isotropic materials the shape of the caustics curve is unique for all materials and can be expressed by the epicycloide.

The obtained results show that significant differences between analytical and experimental approach for small r_0 because analytical model has assumption of elastic material which is not valid for plasticity region near the contact point. Outside this nonlinear zone the results have good agreement but for value of r_0 grater then 5mm size of caustics going down and measuring uncertainty rise up.

The asymmetric optical effect appeared when coordinate axes are not parallel to the principal axes of orthotropy which confirms a strong influence of the material orientation on the shape of caustics.

By varying the input parameters, it is revealed that virtual image is sensitive to the intensity of contact force, while the real image is sensitive to the contact force inclination. Also it is noticed that for anisotropic specimen the real image is small and has no characteristic value to measure, while virtual image is characteristically distinguished for the same load condition.

References

- [1] Kalthoff J. F.: *Stress Intensity Factor Determination by Caustics*, Proc. of Int. Conf. on Experimental Stress Analysis, Honolulu-Maui-Hawaii, 1982.
- [2] Papadopoulos G. A.: *Fracture Mechanics: The Experimental Method of Caustics and the Det.-Criterion of Fracture*, Springer-Verlag publisher, Berlin 1992.
- [3] Lehnitskii S. G.: *Theory of Elasticity of an Anisotropic Body*, Mir Publishers, Moscow 1950.
- [4] Bakić A.: *The method of caustics in contact problems of composite materials (in Croatian)*, PhD thesis, FSB Zagreb, 2009.
- [5] Semenski D.: *The application of caustics in fracture mechanics of anisotropic materials (in Croatian)*, PhD thesis, FSB Zagreb, 1995.



Studies on buckling lengths of chords for out-of-plane instability

A. BIEGUS, D. WOJCZYSZYN

Wrocław University of Technology, Wybrzeże Wyspiańskiego 25, 50-370 Wrocław, Poland.

In the article a more precise models of assessing the out-of-plane loss of stability of chords of one-way trusses have been proposed. The more exact values of the out-of-plane buckling length coefficients of chords have been determined. On this basic the more estimation assesses of chord's resistance is possible by using the indirect method of analysis and designing of steel bar structures. The model of compression chord as a straight member isolated from the one-way truss associated with the space model of lateral buckling of the truss have been analysed. The problem has been studied parametrically by changing the number of web panels. For the tested models, the comparative analyses of the out-of-plane buckling length coefficients have been carried out referring to the guidelines of chosen design codes. It has been confirmed that the chord's out-of-plane buckling length might be smaller or larger than the distance between the points of truss' bracing.

Keywords: *out-of-plane buckling, trusses, buckling length coefficient*

1. Introduction

Analysing the phenomenon of bars' instability in one-way trusses according to principles of the indirect method of designing, the buckling lengths of both the in-plane (xz – buckling about the axis y of the cross-section) as well as the out-of-plane (yz – buckling about the axis z of the cross-section) have to be considered, respectively

$$l_{ey} = \mu_y l_y, \quad (1)$$

$$l_{ez} = \mu_z l_z, \quad (2)$$

where:

l_y, l_z – theoretical lengths between bracing points in-plane (y) and out-of-plane (z) of the truss, respectively,

μ_y, μ_z – appropriate coefficients of buckling lengths.

In the in-plane buckling analysis of the compression chords $l_y = l_t$, where l_t is the distance between joints. For the out-of-plane buckling, the length l_z is equal to the

distance between the bracings situated perpendicularly to the truss plane, and generally $l_z \neq l_t$.

In the roof structures, in which purlins are not used, the upper chords are protected against out-of-plane buckling under the condition of a sufficient resistance of the both roof plates and the roof plates to the truss connections. At the stage of assembly, preceding the roof plate installation, the immovable support for the upper chord is usually provided by bracings of T_1 type (see Figure 1a). For the roof shown in Figure 1b, the supporting points are created by those purlins, which are attached to the immovable joints of transverse roof bracing T_2 . For the situation depicted in Figure 1, the upper chord may buckle out-of-plane along few panels of the truss' web. It should be noticed that the similar considerable lengths may occur for bottom chords in open buildings under the wind uplift.

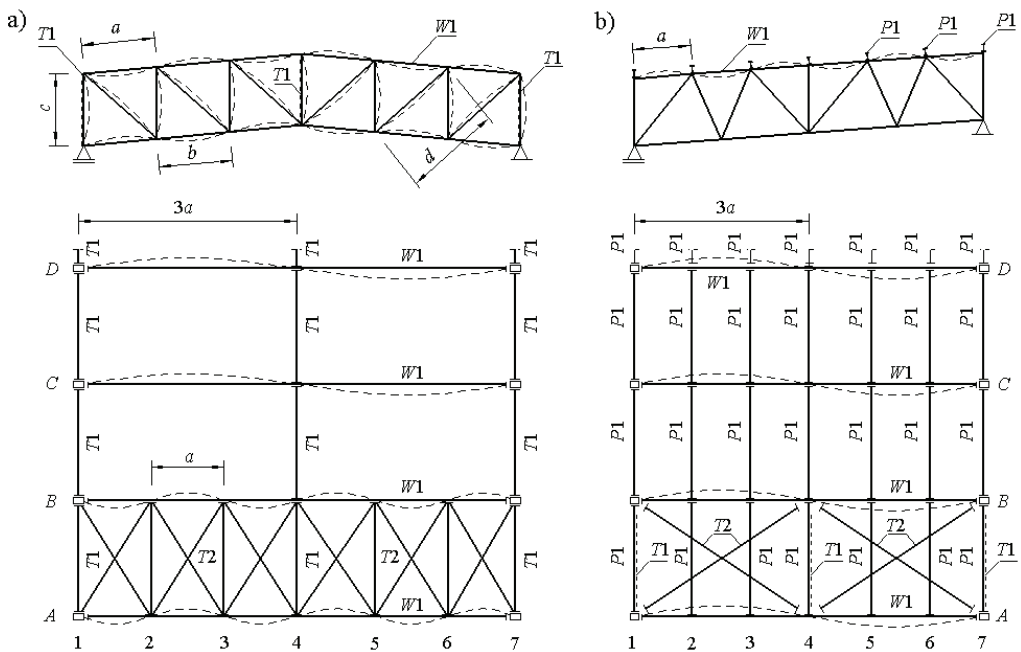


Fig. 1. Examples of determining the theoretical lengths in trusses for roofs without (a) or with purlins (b): W_1 – truss, T_1 – longitudinal vertical bracing, T_2 – transverse roof bracing, P_1 – purlin

If the accurate out-of-plane stability analysis of chords is not conducted, then according to [1] and [2]

$$l_{ez} = l_z. \quad (3)$$

Nevertheless, the standardisation 0 also defines the specified chord's out-of-plane buckling lengths in chosen design cases. In the situation of trusses with tubular rectangle chords (RHS profiles) 0 recommends

$$l_{ez} = 0.9l_z. \quad (1)$$

This model is represented by a hinged ($\mu_z = 1$) or *quasi-hinged* ($\mu_z = 0.9$) member that is compressed by a constant force and not connected with web members. This conservative assumption is acceptable for $l_z = l_y$. In the real situation, where distance between bracings covers the length of few panels of the truss' web, the above simplification is not sufficiently accurate.

The assumed model due to [1] and [2] ignores the real distribution of the chord's axial force that changes between individual panels and may proceed from compression to tension. The significant simplification results from omitting the out-of-plane rigidity of the chord to web members (verticals and diagonals) intermediate connections. The chords are usually made of continuous profiles to which web members are welded directly or by means of gusset plates. The truss' joints constructed in this way are able to resist certain bending moments and may be considered as rigid or semi-rigid. Thus, the web members' length, the rigidity and the state of stressing of diagonals, verticals and tension chord have an effect on the chord's out-of plane buckling. The assumption of the model in which the compression force along the entire chord is constant and the effect of the rest of truss' bars is omitted can lead to a conservative estimation of the critical load associated with the chord's out-of-plane buckling. This form of chord's buckling might initiate the global instability of the truss similar to the lateral buckling observed in compact beams.

A low number of publications are relatively devoted to the lateral buckling of one way-trusses.

In [5] the out-of-plane stability of freely supported one-bay trusses with "V" type web has been investigated. The lattice girders of parallel chords have been transversally braced at both ends i.e. in the upper and bottom nodes. The influence of the place of nodal load applying on the chords spatial stability has been examined. The specified buckling length coefficients μ_z have been determined using the theoretical lengths of chords equal to the span of examined trusses. It has been shown that the chord's out-of-plane buckling length coefficients μ_z might be both lower as well as higher than unity.

A similar design situation has been analysed in [4]. Differently from [5] the tested truss models have been transversally braced at different regions such as: supports, at the midspan, only at support nodes or at supports and every node of the tension chord. On the basis of numerical and experimental analyses of steel trusses having rigid joints it has been shown that the buckling lengths for out-of-plane instability of chords are considerably smaller than the distance between bracings.

In [3] the buckling phenomenon of tubular trusses with unsupported span has been described. The practical algorithm for designing of trusses that allows considering the contribution of torsional stiffness against the out-of-plane buckling has been presented. The methodology has been experimentally verified with full-scale test of one-bay truss. It has been shown that taking into consideration torsional stiffness of the both chords can considerably decrease the out-of-plane chord's buckling length.

In the paper, the results of the parametric analyses are introduced for out-of-plane buckling of the truss' chords considering: the irregular distribution of the axial force along the chord, the way of the chord to support as well as chord to web members connections considered in- and out-of-plane of the structure, and the place of load application (to the upper or bottom nodes).

2. The description of the analysed problem

The subject of the paper is an attempt of specifying the computational model of the out-of-plane buckling of the compression chords in trusses. A model of a straight bar isolated from the original truss and a model of one-way truss considered as a spatial system (model of lateral buckling of the truss) have been studied. The purpose of the isolated bar's analysis of buckling has been the consideration of the real gradually varying axial load. Whereas, the model of lateral buckling of the truss additionally allowed taking into account the both effect of the other members of the truss and the influence of the rigidity of the intermediate as well as supporting joints on the out-of-plane stability of the analysed chord.

The single-span trusses freely supported at the ends, loaded uniformly by forces P alternatively applied to the upper or bottom nodes have been examined (see Figure 2). The depth h of the truss has been equal to the panel's length a . The trusses have been made of steel rectangular hollow sections. The stability of the compression chords has been analysed parametrically, varying the number of the trusses' panels n .

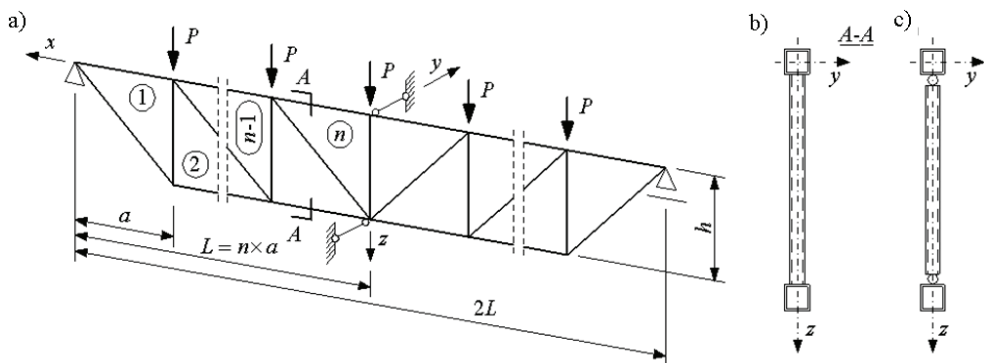


Fig. 2. Static scheme of the analysed trusses

The critical force $N_{cr,z}$ of the upper chords for the out-of-plane buckling has been obtained analytically for the isolated bar model and numerically (using FEM [6]) – for the model of truss' lateral buckling. On the basis of the received results $N_{cr,z}$, the coefficients of buckling lengths have been determined using equation

$$\mu_z = \frac{\pi}{L} \sqrt{\frac{EJ_z}{N_{cr,z}}}, \quad (5)$$

where:

EJ_z – the flexural stiffness of the chord in the plane of buckling,

$N_{cr,z}$ – the critical load for the out-of-plane buckling of the chord.

3. The stability analysis of chord based on the bar's model isolated from the truss

The computational model of the bar isolated from the truss (Figure 2) is shown in Figure 3. This model is represented by a simply supported at the ends straight strut with a constant flexural stiffness EJ_z . The length of the bar is equal to the distance between out-of-plane immovable supports of the truss. The examined bar has been divided into n elements having panels' length a . Load N_i changes irregularly along the upper chord (between panels of the web). The distribution of the axial force is analogous to the stressing state of the chord and has been determined for unit loads P (see Figure 2). The employed method enables the examination of bars' stability with arbitrary changes of the axial load, even gradually varying from compression to tension e.g. in the case of trusses rigidly connected with columns.

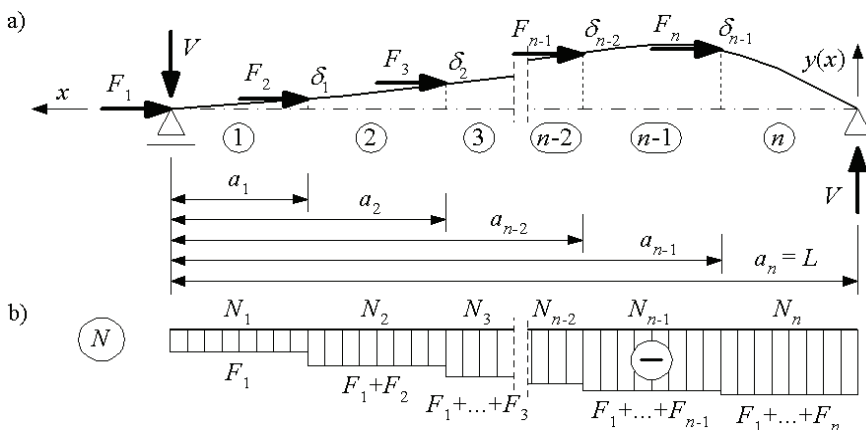


Fig. 3. Scheme of the computational model for the out-of-plane buckling of the compression chord based on the isolated bar

The critical force of the bar has been determined on the basis of the static criterion of stability [7]. For pure nonuniform compression, the critical multiplier $\lambda_{cr,z}$ has been obtained and in sequence the critical load $N_{cr,z}$ has been calculated. At the first stage of calculations the function of displacements of the strut's axis $y_1(x) - y_n(x)$ has been determined between the forces F_i taking the corresponding coordinates $\delta_1 - \delta_{n-1}$ in the y direction for points where the load F_i have been applied (see Figure 3a). The function of bar's axis deflection has been expressed integrating the second order differential equation

$$M_i(x) = -EJ_{z,i} \frac{d^2 y_i(x)}{dx^2}, \quad (6)$$

in which:

$M_i(x)$ – bending moment over the i -segment,

$y_i(x)$ – the function of displacement of the bar's axis at the i -segment,

$EJ_{z,i}$ – flexural stiffness of the i -segment.

The Equation (6) for the i -segment becomes

$$EJ_{z,i} \frac{d^2 y_i(x)}{dx^2} = -V(L-x) - \sum_{k=2}^i F_k [y_i(x) - \delta_{k-1}], \quad (7)$$

where V denotes the shear force associated with bar's buckling and is determined by the formula

$$V = \frac{1}{L} \sum_{k=2}^n F_k \delta_{k-1}. \quad (8)$$

The constants of integration $C_{1,i}$, $C_{2,i}$ of the displacement function over the i -segment have been determined from the boundary conditions

$$\left\{ \begin{array}{l} y_1(L) = 0 \\ y_i(x=L-a_{i-1}) = \delta_{i-1} \end{array} \right. \Rightarrow C_{1,i}, C_{2,i}. \quad (9a)$$

$$\left\{ \begin{array}{l} y_i(x=L-a_i) = \delta_i \\ y_n(0) = 0 \end{array} \right. \quad (9b)$$

$$\left\{ \begin{array}{l} y_n(0) = 0 \end{array} \right. \quad (9c)$$

$$\left\{ \begin{array}{l} y_n(0) = 0 \end{array} \right. \quad (9d)$$

The criterion for determining the next values of the critical load results from the continuity of a derivative for the function of deflection of adjacent segments $i - i+1$ introduced as

$$\left. \frac{dy_i(x)}{dx} \right|_{x=L-a_i} = \left. \frac{dy_{i+1}(x)}{dx} \right|_{x=L-a_i}, \quad \text{for } i = 1 - (n-1). \quad (10)$$

From conditions (10) the system of equations has been obtained as

$$[\mathbf{K}] \boldsymbol{\delta} = \mathbf{0}, \quad (11)$$

where:

$\boldsymbol{\delta} = \{\delta_1, \dots, \delta_{n-1}\}^T$ – vector of global coordinates,

\mathbf{K} – stiffness matrix of the strut, taking into account compression force in the bar.

The problem has been solved by equating the determinant of matrix \mathbf{K} to zero and using the symbolic-numerical analysis system *Mathematica*® [8]. The obtained general solution has been employed for the analysis of the out-of-plane instability of the upper chords that have been considered as bars isolated from the symmetrically loaded one-way trusses (see Figure 2). Knowing the critical loads $N_{cr,z}$, analytically determined for the compression chords with $n = 2-9$, which denotes the changes of axial forces, the corresponding coefficients of the buckling lengths $\mu_z(n)$ have been calculated from the formula (5) and listed in Table 1.

Table 1. Coefficients of buckling lengths for out-of-plane instability

Model	Nodal load	Attaching to		Buckling length coefficient μ_z							
		support	web members	number of panel n							
				2	3	4	5	6	7	8	9
1	2	3	4	5	6	7	8	9	10	11	12
isolated bar		hinged		0.94	0.89	0.87	0.85	0.84	0.84	0.83	0.83
lateral truss buckling	upper	hinged	rigid	0.91	0.79	0.71	0.65	0.60	0.56	0.53	0.50
				0.79	0.70	0.64	0.60	0.56	0.52	0.50	0.47
	bottom		torsion-ally fixed	0.80	0.68	0.60	0.54	0.49	0.46	0.43	0.41
				1.09	1.01	0.94	0.88	0.83	0.79	0.75	0.72
	upper		rigid	0.71	0.63	0.56	0.51	0.48	0.44	0.42	0.40
				0.90	0.84	0.80	0.76	0.73	0.70	0.67	0.65
	bottom		hinged								

4. The analysis of chord's buckling due to the spatial instability of a truss

One-way trusses (Figure 2) have been subjected to a numerical analysis that is usually employed for spatial systems. The global instability of trusses (lateral buckling) has been analysed for a varying number of panels $n = 2-9$ and different position of joints in which load P has been applied (for the upper or bottom chords). It has been assumed that continuous RHS chords have been connected with web members at both planes xz and yz (see Figure) alternatively – hinged or fully fixed. Additionally, the effect of support conditions on the critical load has been analysed. In this matter, the case of a truss without torsional support (freedom of rotation about

x axis at the both support joints) and the case with rotation arrested at the upper chord's ends (torsional support) have been considered. The FEM calculation of the general stability of studied trusses has been executed using SOFiSTiK system [6] for the spatial frame models.

Under the growing load P , the trusses may buckle in a global mode similar to the lateral buckling of beams. The spatial mode of the truss global buckling for $n = 4$ is shown in Figure 4. This shape of loss of stability is initiated by out-of-plane buckling of the compression chord.

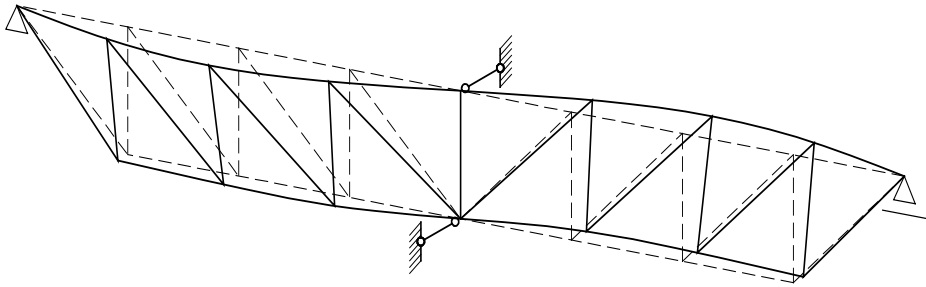


Fig. 4. Spatial mode of global truss buckling for the number of panels $n = 4$

Therefore, the relationship between the critical load of the chord $N_{cr,z}$ and the critical load of the global truss buckling P_{cr} , has been written as

$$N_{cr,z} = \lambda_{cr,z} N_N, \quad (12)$$

where $\lambda_{cr,z}$ is factor of the load P causing the global buckling of the truss, and N_N is maximal axial force in the compression chord (see Figure 3b) resulting from the load $P = 1$ and determined as

$$N_N = \sum_{i=1}^n N_i, \quad (13)$$

in which axial force in i -segment has been calculated from the following formula

$$N_i = \left(\frac{1}{2} (2n - i)(2n - 1) - \sum_{k=1}^{2n-i-1} k \right) P \frac{a}{h}. \quad (14)$$

The coefficients of buckling length $\mu_z(n)$ have been determined from (5) (see Figures 5–7) and listed in Table 1.

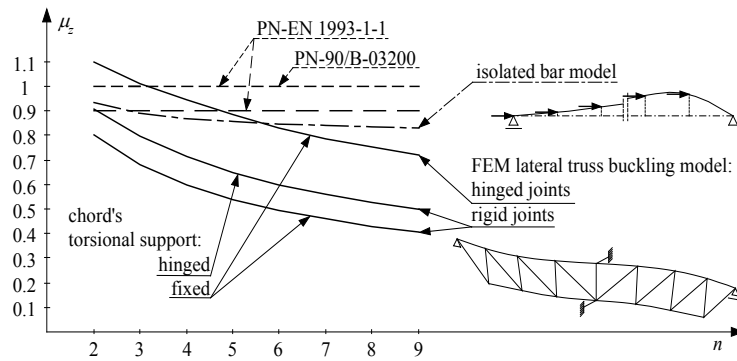


Fig. 5. Buckling length coefficients $\mu_z(n)$ of chords of trusses. Nodal load applied to upper chords

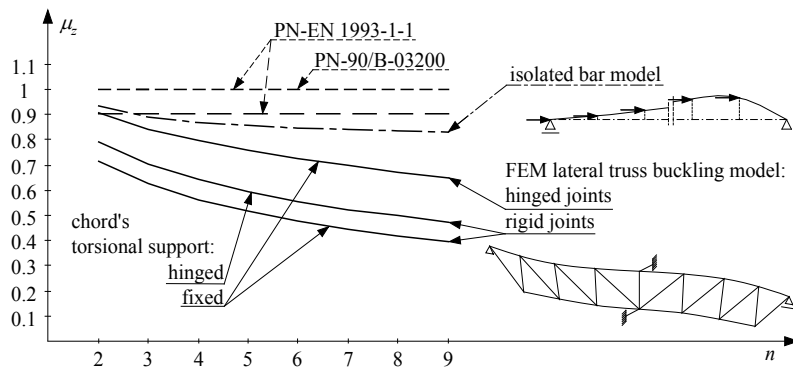


Fig. 6. Buckling length coefficients $\mu_z(n)$ of chords of trusses. Nodal load applied to bottom chords

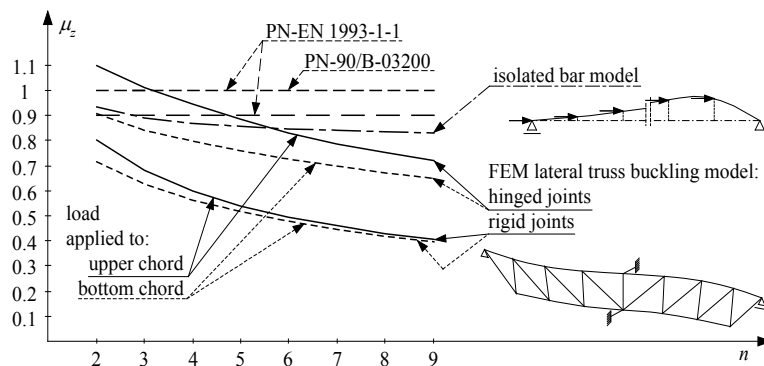


Fig. 7. Buckling length coefficients $\mu_z(n)$ of chords of trusses torsionally fixed in supports

5. Discussion of results and conclusions

The buckling lengths assumed according to [1] and [2] for the out-of-plane instability of the truss may be overestimated for the cases when the buckled segment covers several panels of the system. This effect leads to the underestimation of the critical load and in sequence to uneconomical consumption of material.

The examination of the isolated bars has shown the significant effect of the irregular changing of the axial compression force on the assessment of the critical load $N_{cr,z}$. This model constitutes a more accurate basis of computation and material savings in comparison with [1] and [2]. The buckling length coefficients of the studied cases have given $\mu_z = 0.94\text{--}0.83$, which increases the critical load $N_{cr,z}$ about 13% (for $n = 2$) – 45% (for $n = 9$) and about 2% (for $n = 3$) – 17% (for $n = 9$) referred to $\mu_z = 1$ and $\mu_z = 0.9$ respectively.

The analysis of stability of one-way trusses as spatial models constitutive the next step of the accurate defining of the critical load in comparison with both [1], [2], and the idea of the isolated bar model. Thus, the analysis can take into consideration many additional factors affecting the critical load of the compression chord i.e. the interaction between the chord and the web members (the rigidity of chords to web members connections), the stabilizing effect of the tension chord, the point of load applying (the upper or bottom joints), the geometry of trusses and the construction of chord to support connection (torsionally fixed or free).

The truss joints may have a different stiffness in-plane and out-of-plane due to bending and torsion e.g. rigid, hinged or semi-rigid (see Table 1). The accurate defining of this stiffness is considerable for the trusses' stability analysis.

The numerical analyses have examined truss schemes in which the continuous chords are rigidly or hinge attached to web members. It has been shown that the effect of the in-plane connections' joint rigidity on the out-of-plane chord's stability is not significant, contrary to connections being perpendicular to the truss' plane. The corresponding values of the coefficients of the buckling length μ_z are introduced in Table 1.

For the case depicted in Figure 2b (rigid connections) the effect of interaction between the chord and the web members on the coefficients of buckling length μ_z is very significant. The coefficients for chords in the trusses loaded at upper nodes are lower of about

- 9% (for $n = 2$) to 50% (for $n = 9$) referred to $\mu_z = 1$ and
- 12% (for $n = 3$) to 44% (for $n = 9$) referred to $\mu_z = 0.9$

from that suggested in [1] and [2]. In sequence the chord's critical load $N_{cr,z}$ calculated for the revealed values of μ_z are of 21% (for $n = 2$) to 300% (for $n = 9$) referred to $\mu_z = 1$ and 30% (for $n = 3$) to 224% (for $n = 9$) referred to $\mu_z = 0.9$ higher from that approximated according to [1] and [2]. For the trusses with hinged joints (see Figure 2c) the values of μ_z are higher from that obtained for the rigid joints, but they

can still be lower from the values given in [1] and [2]. By limiting the rotation of the chord at support nodes the decrease of μ_z is observed. For the trusses loaded at upper chords the coefficients μ_z are lower of about 20% (for $n = 2$) to 59% (for $n = 9$) referred to $\mu_z = 1$ and 11% (for $n = 2$) to 54% (for $n = 9$) referred to $\mu_z = 0.9$ from the values given in [1] and [2] (see Table 1). The diagrams of the coefficients of buckling length $\mu_z(n)$ of the compression chords due to the global instability of trusses for load applied to upper and bottom chords are shown in Figures 5–6 respectively.

The global instability of the trusses initiated by the out-of-plane buckling of the compression chord is analogous to the phenomenon of the lateral buckling of beams. Therefore, the place of the load application is considerable. The analyses have shown that coefficients μ_z for trusses loaded at the upper joints are significantly larger than these obtained for trusses loaded at the bottom chords (see Figure 7 and Table 1).

The coefficients of buckling lengths of chords μ_z obtained in the paper represent the truss lateral buckling model having an exemplary characteristic of the joints' rigidity. Therefore, presented results cannot be generalized. For design purposes it is recommended to carry out an individual study of the truss' stability employing available computer programs.

References

- [1] EN1993-1-1: *Design of steel structures – Part 1-1: General rules and rules for buildings*.
- [2] PN-90/B-03200. *Polish standard. Steel structures. Static calculations and designing* (in Polish).
- [3] Chan S.L., Koon C.M., Albermani F.G.: *Theoretical and experimental studies of unbraced tubular trusses allowing for torsional stiffness*, Steel and Composite Structures, Vol. 2, 2002, pp. 209–222.
- [4] Kołodziej J.: *Numerical-experimental analysis of lateral buckling of steel trusses* (in Polish), Ph.D. Dissertation, Koszalin University of Technology, 2005.
- [5] Petersen C., Worch G.: *Kippen freier Fachwerkträger unter Berücksichtigung biege- und torsionssteifer Füllstäbe; Lösung der gekoppelten Differentialgleichungen mittels des Galerkin-Verfahrens*, Die Bautechnik, Vol. 9, 1975, pp. 289–296.
- [6] SOFiSTiK. Analysis Programms. Vol. 12, Manual, SOFiSTiK AG, Oberschleissheim, 2002.
- [7] Timoshenko S.P., Gere J.M.: *Theory of elastic stability*, McGraw-Hill, 1961.
- [8] Wolfram S.: *The Mathematica® Book. 5th Edition*, Wolfram Media, 2003.

Analiza długości wyboczeniowej pasów kratownic z płaszczyzny ustroju

Badano modele obliczeniowe utraty stateczności pasów kratownic płaskich z płaszczyzny ustroju. Analizowano model pasa ścisłanego jako pręta prostego „wyizolowanego” z płaskiej kratownicy, który jest obciążony zmieniającą się skokowo siłą osiową oraz model przestrzennego ustroju prętowego (model „zwierzenia kratownicy”). Problem analizowany w ujęciu parametrycznym zmieniając liczbę przedziałów kratownicy oraz sposób połączenia prętów w węzłach i z podporą.



Modelling of structure geometry in Bridge Management Systems

J. BIĘŃ

Wrocław University of Technology, Wybrzeże Wyspiańskiego 27, 50-370 Wrocław, Poland.

In bridge engineering the following forms of structure geometry representation are typically applied: non-dimensional models preferred in the Bridge Management Systems and one-dimensional (1D), two-dimensional (2D) or three-dimensional (3D) models used in structural analysis. Classification proposed in this paper is more precise and takes into account both the type of model elements and the size of space used for model creation. Proposed taxonomy of the geometrical models and presented notation of the distinguished classes enable consistent and uniform classification as well as objective comparison of all models which can be applied in bridge engineering, both in the Bridge Management Systems and in structural analysis of bridges.

Keywords: bridge, numerical modelling, Bridge Management Systems, structural analysis

1. Introduction

Modelling of bridge structures in the computer-based Bridge Management Systems (BMS) is of great importance to efficiency of the management process. Precision of numerical representation of the structure geometry influences the accuracy of the description of bridge technical parameters in the inventory model and is also fundamental to a correct and efficient assessment of the bridge condition, serviceability, etc. In almost all contemporary Bridge Management Systems only non-dimensional models of bridge structures are applied, e.g. [2, 8, 11–12, 15, 23–25]. It means that the structure is geometrically represented by a set of non-dimensional points modelling the bridge components: abutments, piers, girders, decks, etc. Characteristics of each component (dimensions, material data, inspection data, etc.) are not located in the space but are only assigned to the “name tag” of the structure, usually in the form of tabular data. Such a model of geometry does not enable precise spatial placing of the collected information.

Current development of the computer technology offers more advanced models to BMS users. Models created of one-, two- and three-dimensional elements situated in n-dimensional space can be implemented in the computer systems supporting management of the bridge infrastructure. This means practical integration of the models of geometry applied in the Bridge Management Systems and models used in the Computer Aided Design (CAD) systems based on the Finite Element Method (FEM).

Human neural systems are best trained against relatively simple visual signals. It is important to notice that we perceive about 75% of the information from the real world through the sense of vision. The visual perception is then a crucial element of human cognition, providing us with the information required for attaining awareness, reasoning and learning [9]. Although the physical realism is not yet achievable with the current rendering and display hardware, we can already use computer graphics to build human-machine interfaces that are perceptually effective, which means that their users perceive displayed object evocations as real-looking ones [18], [22].

The above observations are taken into consideration when designing human-computer interactions for modern computer software, including Bridge Management Systems. For this purpose, a whole discipline has been established and called the interaction design [20]. A model-centric user interface is superior to the traditional ones not only because of the properties of human perception, but also thanks to much bigger amount of information that a visual representation can carry when compared to a textual or numerical representation occupying the same physical area. The graphical model has an ability to show multiple aspects of the bridge structure, updated and rendered in real-time, with relevant information visually emphasized. Various characteristics of the structure, such as geometrical, physical or chemical properties, can be shown in-place on the model instead – or as a complement to – the tabular data.

Presented results of scientific research are a part of the Project „Innovative resources and effective methods of safety improvement and durability of buildings and transport infrastructure in the sustainable development” financed by the European Union from the European Fund of Regional Development based on the Operational Program of the Innovative Economy.

2. Taxonomy of bridge geometry models

Classification of the models of bridge geometry useful in BMS can be based on two parameters, as proposed in [2–3] taking into account conception presented in [13]:

- elements used for construction of a model – with possible application of non-dimensional (e^0), one- (e^1), two- (e^2) or three-dimensional elements (e^3);
- dimension of the space needed for model creation – from non-dimensional space (s^0) to real three-dimensional space (s^3).

Proposed taxonomy of the geometric models suitable for the Bridge Management Systems is presented in Figure 1 on the example of the box girder bridge span. The columns in Figure 1 correspond to the dimensionality of space used for model creation, from a non-dimensional point to the full three dimensional space, accordingly. The rows indicate the dimensionality of elements representing the bridge structure in the model. The dimensionality of applied elements must be lower or equal to the dimensionality of space in which model is situated. Combinations of the parameters (e^i) and (s^j) give ten basic classes of the considered models of bridge geometry denoted as (e^i, s^j), where i is the dimensionality of elements, and j is the dimensionality of space.

The distinguished classes of the models can be divided into four main groups (types) with respect to the applied elements:

- type E^0 – containing four model classes: (e^0, s^0) , (e^0, s^1) , (e^0, s^2) , (e^0, s^3) formed of non-dimensional elements (e^0);
- type E^1 – including models built of one-dimensional elements (e^1) and forming classes: (e^1, s^1) , (e^1, s^2) , (e^1, s^3) ;
- type E^2 – encompassing classes (e^2, s^2) , (e^2, s^3) associated with the models using two-dimensional elements (e^2);
- type E^3 – including only (e^3, s^3) models created by means of three-dimensional elements (e^3).

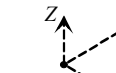
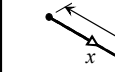
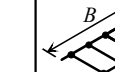
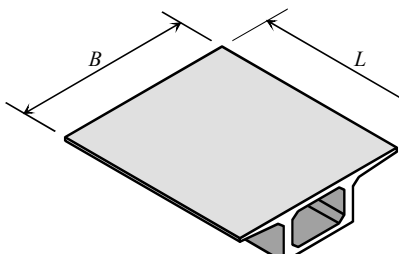
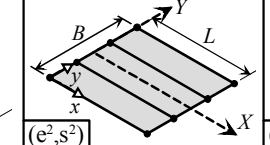
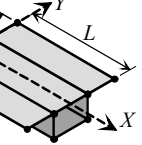
		SPACE DIMENSION			
e	s	$s^0(-)$	$s^1(X)$	$s^2(X, Y)$	$s^3(X, Y, Z)$
ELEMENT DIMENSION	$e^0(-)$	•			
	$e^1(x)$				
	$e^2(x, y)$				
	$e^3(x, y, z)$				

Fig. 1. Basic classes of bridge geometry models – examples of various models of bridge box girder

Selected class of geometrical representation decides on the accuracy of the inventory model of the bridge and – as a consequence – on the correctness and effectiveness of the management decisions undertaken on the basis of information stored in BMS.

Applied model of bridge geometry is crucial to basic management activities because it defines the method of numerical representation of structure defects detected during inspections and tests. Taking into account the basic parameters describing each type of damage [2–3]: intensity I , extent D and location L , the relationships between

type of structure geometry model and form of the geometrical representation of the defect are presented in Table 1.

In case of E^0 type geometry models, the defect parameters I , D and L are described by numbers or linguistic values. Advanced models of geometry (E^1 , E^2 , E^3) enable representation of the defect characteristic by means of functions described in 1-, 2- or 3-dimensional space, respectively.

Table 1. Representation of defect parameters by various types of geometry model [3]

Defect parameter	Type of geometry model			
	E^0	E^1	E^2	E^3
Damage intensity	I	$I(x)$	$I(x, y)$	$I(x, y, z)$
Damage extent	D	$D(x)$	$D(x, y)$	$D(x, y, z)$
Damage location	L	$L(x)$	$L(x, y)$	$L(x, y, z)$

The advanced models of geometry allow also editing of damage information directly on the model of the structure by means of graphical editor to provide the BMS with as much information as possible, keeping the user interaction natural. The defect no longer needs to be described through editing of a table of values; it can simply be brushed onto the model of the structure.

In case of advanced geometry models, as an added value, the system is able to perform multiple supplementary tasks during the real-time damage edition. These tasks include a dynamic calculation of damage extent and performing the technical condition evaluation using the sensitivity function known for the given component of the structure.

3. Non-dimensional models

In the majority of the existing BMS, the bridge components are modelled as non-dimensional (e^0) elements and all the models can be classified as the type E^0 [2, 8, 11–12, 15, 23–25]. The inventory data (length, width, material characteristics, construction type, etc.) as well as the inspection data (defects, maintenance works, etc.) in the models based on the non-dimensional elements are collected in the data base as a set of parameters (numbers or linguistic values) corresponding to the considered bridge components.

In the models class (e^0, s^0), each bridge structure or structure component is identified in the BMS only by the specific number or other label (inventory number). Example of such a model applied in the Railway Bridge Management System SMOK [4], [6] is presented in Figure 2a. The culvert is identified on the map and in the data base by means of the Railway Identification Number only.

Class (e^0, s^1) includes models which are positioned by means of one-dimensional space parameter, usually by the kilometre of the road or the railway track (Figure 2b).

Bridge structure location based on the classic geographical co-ordinates (longitude and latitude) can be classified as (e^0, s^2) model. Class (e^0, s^3) contains models utilizing

three-dimensional Geographical Information Systems (GIS) for location of the structure (Figure 2c).

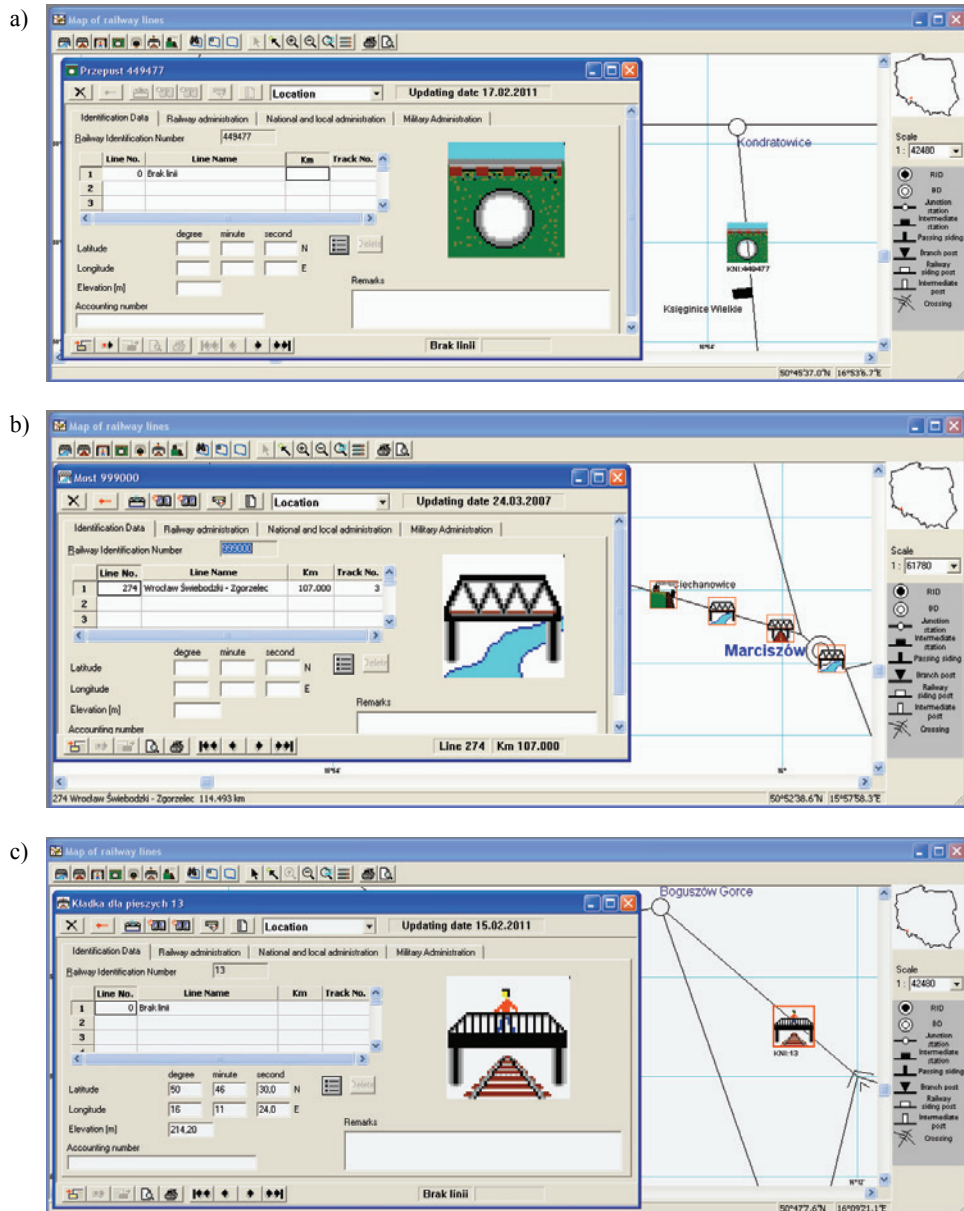


Fig. 2. Geometrical representation of bridge structures in the Railway Bridge Management System SMOK [4] by means of non-dimensional elements: a) class (e^0, s^0) model – inventory number only, b) class (e^0, s^1) model – kilometre of the railway line, c) class (e^0, s^3) model – geographic coordinates

4. Advanced models of geometry

4.1. Models formed of 1-dimensional elements

Representation of the bridge structure by means of the one-dimensional elements (e^1) enables the location of the collected information in relation to the length of the structure components. In the models of the class (e^1, s^1), the bridge component (e.g. span) can be represented by 1-dimensional elements (e^1) as shown in Figure 3.

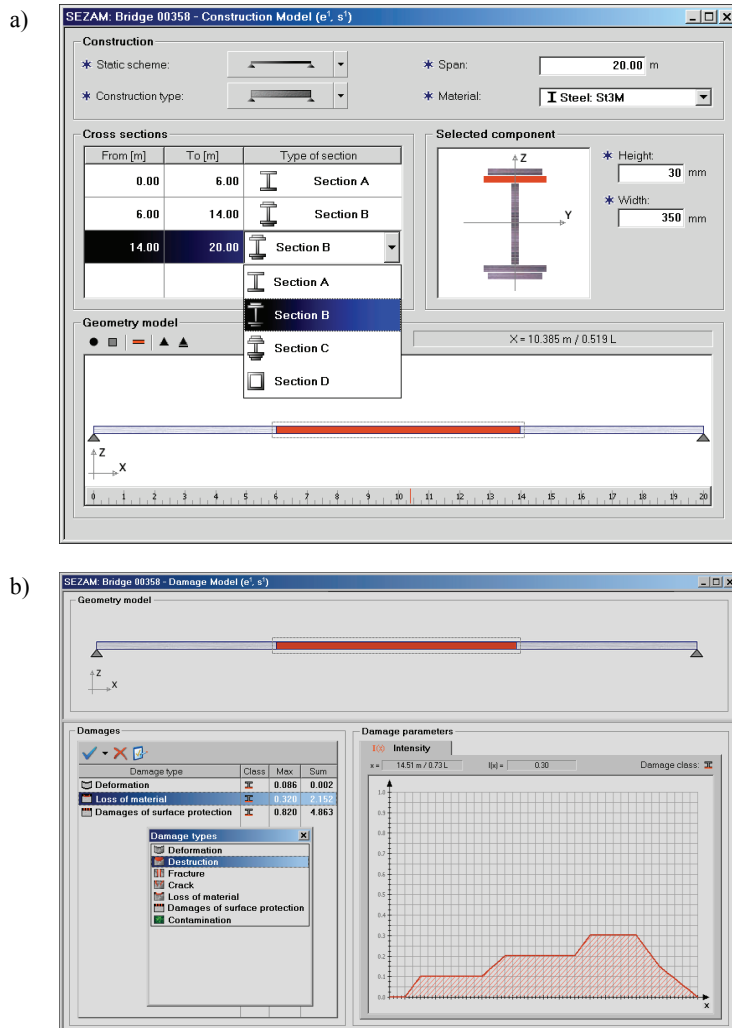


Fig. 3. Class (e^1, s^1) model of bridge geometry [2]: a) modelling of structure technical parameters, b) defect modelling by means of the damage intensity function $I(x)$

More advanced models like: grillage, two-dimensional truss, two-dimensional frame, etc. belong to the class (e^1, s^2) . The most complex models created of (e^1) elements in three-dimensional space (s^3) are included in the (e^1, s^3) class.

Applications of the advanced models of structure geometry in the Bridge Management Systems need specialized tools supporting the creation and utilization of the models belonging to the type E^1 , E^2 or E^3 . Example of a simple model (e^1, s^1) representing the plate girder of a bridge is presented in Figure 3a. The main steps of the inventory model creation by means of the dedicated graphical editor are as follows:

- selection of the static scheme and specification of the span length,
- selection of the construction and material type,
- selection of the cross-section type,
- specification of dimensions of cross-section elements.

In the similar way, the numerical model of structure defects can be created in two steps:

- identification of the types of all existing defects,
- description of the damage intensity function $I(x)$ for each defect by means of the interactive graphical editor (Figure 3b).

Other parameters of defect can be automatically defined on the basis of the damage intensity function $I(x)$:

- damage extent function

$$D(x) = \begin{cases} 1 & \text{for } I(x) \neq 0, \\ 0 & \text{for } I(x) = 0. \end{cases} \quad (1)$$

- damage location function

$$L(x) = \begin{cases} 1 & \text{for } I(x) \neq 0, \\ 0 & \text{for } I(x) = 0. \end{cases} \quad (2)$$

4.2. Models formed of 2-dimensional elements

Application of two-dimensional elements (e^2) in the models of geometry enables improvement of structure representation as well as upgrading of information collected and processed in the Bridge Management Systems. All information can be defined in relation to the length and width (or height) of the structure component.

Example of the application of the (e^2, s^3) model of geometry in the Bridge Monitoring & Management System (BM&MS) is presented in Figure 4. The BM&MS was designed and implemented as a tool supporting management of the Vistula River Bridge along the Motorway A1 near Toruń [2–3]. Model of each component of the structure (span, support) is created of two-dimensional elements (e^2) situated in three-dimensional space (s^3) . Required view of considered bridge component can be

selected by the user and the currently edited part is shown in the top-right corner of the screen (Figure 4). Identified defects of the structure can be directly placed on the bridge geometry model by means of the graphical editor. A user of the system can draw defect representations in the form of simple shapes such as lines, rectangles or freeform polygons creating damage location functions $L(x, y)$. Extent of each defect is automatically calculated on the basis of the $L(x, y)$ function. The damage intensity is assumed to be constant in the whole area of the defect and should be entered manually by the system user.

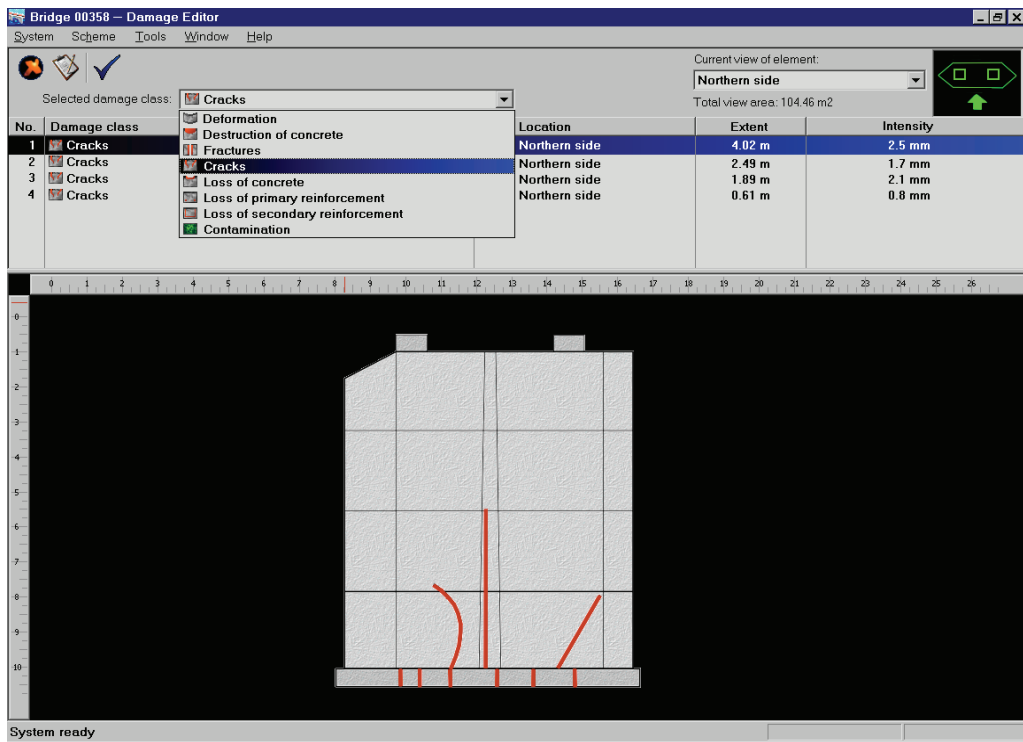


Fig. 4. Modelling of defects using class (e^2, s^3) model of bridge geometry – side view of the damaged pier created by means of graphical editor

In the presented application location and extent of each defect are directly defined in the graphical form for each type of the damage. The intensity function $I(x, y)$ is represented by the mean value I calculated for each individual defect

$$I(x, y) = \begin{cases} I & \text{for } L(x, y) \neq 0, \\ 0 & \text{for } L(x, y) = 0. \end{cases} \quad (3)$$

and the damage extent function is defined for each defect as

$$D(x, y) = \begin{cases} 1 & \text{for } L(x, y) \neq 0, \\ 0 & \text{for } L(x, y) = 0. \end{cases} \quad (4)$$

Defects of diverse intensity can be modelled by dividing the damaged zone into parts (areas) with various but constant intensity within each distinguished area.

4.3. Models formed of 3-dimensional elements

The highest accuracy of the geometry modelling is offered by models of the class (e^3, s^3) . In these models, all dimensions of each bridge component can be directly represented in the computer-based Bridge Management Systems. A prototype of the advanced, fully three-dimensional model of geometry (e^3, s^3) is presented in Figure 5.

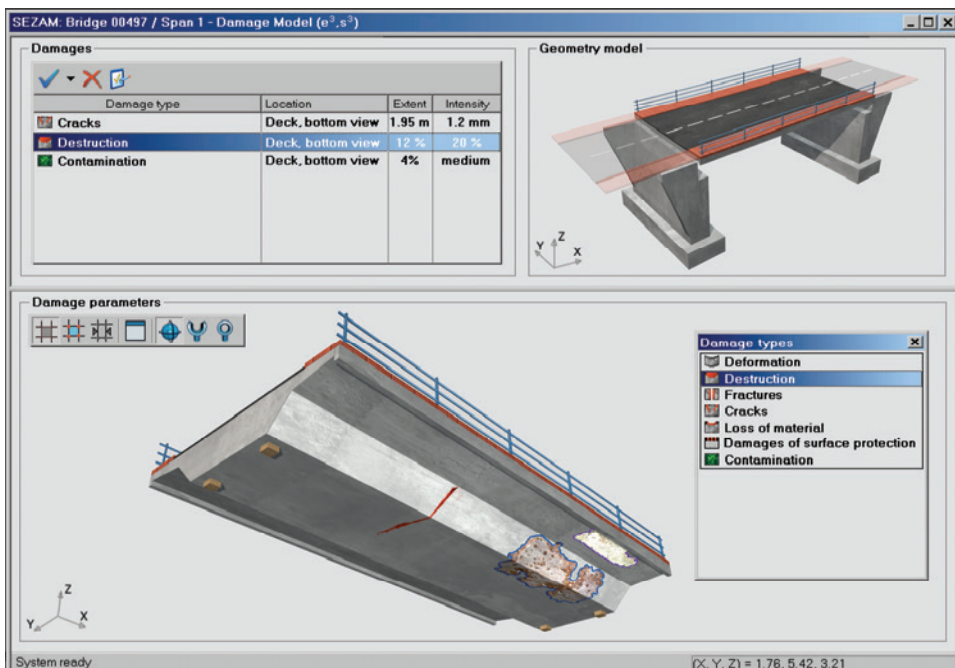


Fig. 5. Class (e^3, s^3) model – example of the numerical representation of bridge structure geometry and defects [3]

The whole bridge structure is modelled in three-dimensional space (s^3) by means of three-dimensional elements (e^3) . The axonometric view of the model is shown in the top-right part of the screen. For each selected component, the defects can be modelled by means of the graphical editor as presented in the bottom part

of Figure 5. This prototype allows full 3-dimensional transformations of the model and the visual information on bridge defects can be positioned on the surface of a model.

In the presented solution, the damage location functions $L(x, y, z)$ are directly edited in the visual form and other damage characteristics can be calculated as follows:

$$I(x, y, z) = \begin{cases} I & \text{for } L(x, y, z) \neq 0, \\ 0 & \text{for } L(x, y, z) = 0, \end{cases} \quad (5)$$

$$D(x, y, z) = \begin{cases} 1 & \text{for } L(x, y, z) \neq 0, \\ 0 & \text{for } L(x, y, z) = 0. \end{cases} \quad (6)$$

Using a full three-dimensional (e^3, s^3) model of the structure promotes but does not imply modelling of defects at the same dimensional level of details. A bridge inspector may just mark them on the model as an icon (e^0, s^3), simply to indicate their existence at a given location. Likewise, they can be modelled as a line (e^1, s^3) or as a delineation of an area on the model's surface (e^2, s^3).

Only in certain cases a very detailed (e^3, s^3) model of defects is required, e.g. in the form presented in Figure 6. Figure 6a is a photo of the loss of material in the reinforced concrete structure and fracture of the stirrup. A very precise three-dimensional (e^3, s^3) model of these defects is presented in Figure 6b.

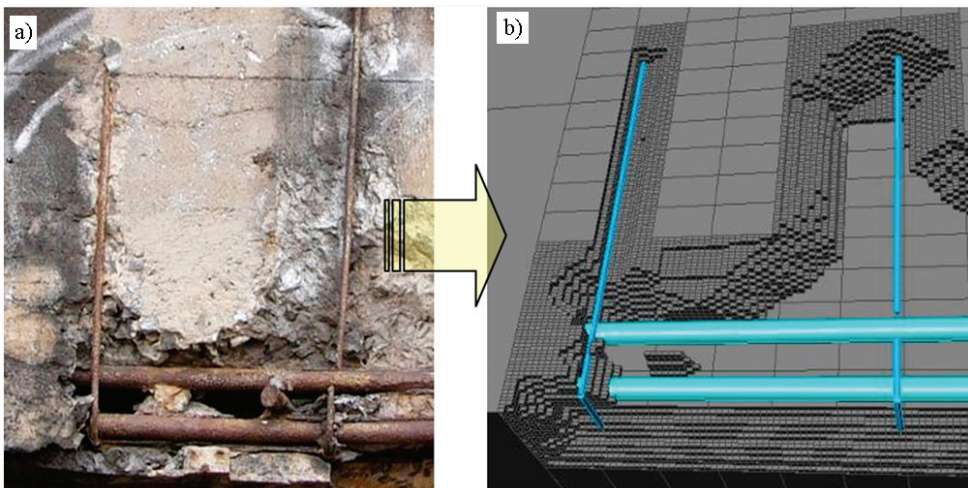


Fig. 6. Detailed modelling of bridge defects: a) defects of RC bridge element,
b) class (e^3, s^3) geometry model of the damaged bridge component [19]

4.4. Hybrid models of geometry

Aside from the homogeneous models of geometry – created of one type of elements as presented in Figure 1 – also non-homogeneous models can be applied. Proposed taxonomy of the geometry models can be easily extended and the proposed notation can also be used to the non-homogeneous models.

The most popular hybrid models of bridge geometry are formed by combination of 1- and 2-dimensional elements located in 3-dimensional space. Class of such a model can be denoted as $(e^1 + e^2, s^3)$. This class is illustrated by the model of beam girder bridge span presented in Figure 7 [5] and by model of cable-stayed bridge (Figure 8) [14].

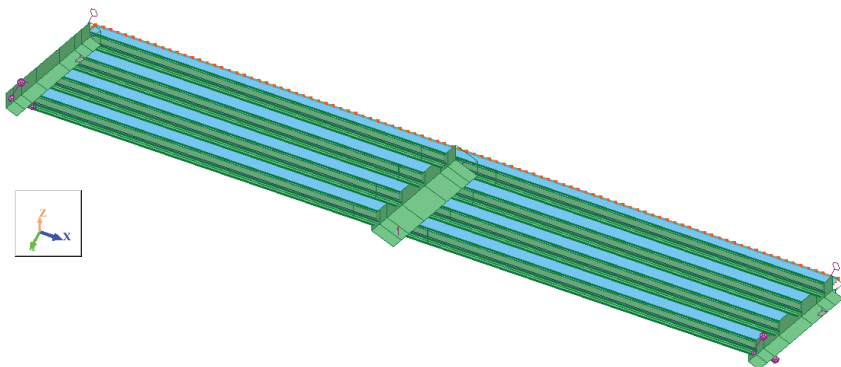


Fig. 7. Hybrid model of geometry of two-span slab-beam superstructure – class $(e^1 + e^2, s^3)$ [5]

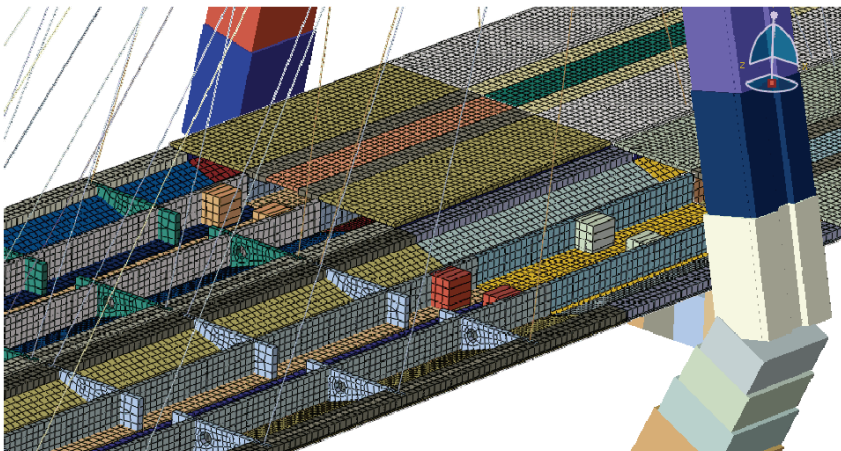


Fig. 8. Hybrid model class $(e^1 + e^2, s^3)$ of cable-stayed bridge geometry – details of the deck modelling [14]

In the model, the span beams are represented by (e^1) elements and deck slab is modelled by means of (e^2) elements taking into account the distance between beam axis and middle surface of the slab. All components of the model are located in the three-dimensional space.

Modelling of a more complicated long-span cable-stayed bridge over the Odra River in Wrocław by means of 1- and 2-dimensional elements placed in the three-dimensional space is presented in Figure 8 [14]. Bridge pylon and cable stays are represented by (e^1) elements and the bridge deck constructed as multi-cell box girder is modelled by means of (e^2) elements.

Aside from the most popular class $(e^1 + e^2, s^3)$ the following hybrid geometry models can be used in the Bridge Management Systems as well as in the structural analysis of bridges: $(e^1 + e^2, s^2)$, $(e^1 + e^2 + e^3, s^3)$, $(e^2 + e^3, s^3)$ and $(e^1 + e^3, s^3)$.

5. Conclusions

In bridge engineering the following forms of structure geometry representation are typically applied: non-dimensional models preferred in the Bridge Management Systems (e.g. [2–4, 6, 8, 11–12, 15, 23–25]) and one-, two- and three-dimensional models used in static (e.g. [1, 5, 10, 13–14, 17, 19, 21]) as well as dynamic (e.g. [7, 16]) structural analysis. Classification proposed in this paper is more precise and takes into account both the type of model elements and the size of space used for model formation. Presented taxonomy of the geometrical models and notation of the distinguished classes of geometry representation enable consistent and uniform classification of all models useful in the Bridge Management Systems as well as in the structural analysis of bridges. The classification system can be used to the homogeneous (created of one type of elements) and non-homogeneous models formed of various types of elements.

Presented survey of the geometry models and experience from the pilot implementations of the selected advanced models form the basis for the following general conclusions:

- proposed classification of bridge geometry representation, based on two parameters, enables objective comparison of all models which can be applied in bridge engineering, both in the Bridge Management Systems and in structural analysis of bridges,
- all considered models of bridge structure geometry can be implemented in the BMS using the currently available computer technologies,
- existing BMS, typically based on non-dimensional E^0 models, can be supplemented by the advanced models applied when higher precision is required,
- variety of the available advanced models of geometry requires selection of the most rational solutions for specific applications, taking into account the increasing accuracy as well as the increasing complexity of representation of the bridge structures in the computer systems,

- integration of the models of geometry applied in the Computer-Aided Design systems and in the Bridge Management Systems can be expected in the near future.

On the basis of the presented analysis we can suppose that a new generation of the Bridge Management Systems will enable free selection of the geometry models applied to each bridge and even to each component of the structure. The future of structure modelling in the Bridge Management Systems is even brighter as the current possibilities. The hardware development will continue, bringing us closer to the physical realism of computer graphics scenes. The Internet will grow, evolve and increase speeds, which will bring capabilities of inline real-time rendering and interaction, where multiple users will cooperate in creation and usage of 3-dimensional scenes – even when using portable, handheld devices.

References

- [1] Bęben D.: *Numerical analysis of a soil-steel bridge structure*, The Baltic Journal of Road and Bridge Engineering, Vilnius: Technika, Vol. IV, No. 1, 2009, pp. 13–21.
- [2] Bień J.: *Modelling of bridge structures in operation* (in Polish), Publishing House of the Wrocław University of Technology, Wrocław, 2002.
- [3] Bień J.: *Defects and diagnostics of bridge structures* (in Polish), Wydawnictwa Komunikacji i Łączności, Warszawa, 2010.
- [4] Bień J., Król D., Rawa P., Rewiński S.: *Computer inventory of engineering structures* (in Polish), Railway Bridge Management System SMOK, Polish State Railways, Warszawa, 1997.
- [5] Bień J., Kużawa M., Zwolski J.: *Load tests of bridge WD 67 over motorway A2 in km 98+593*, Wrocław University of Technology, Institute of Civil Engineering, Report U-125/10, Wrocław, 2010.
- [6] Bień J., Rewiński S.: *SMOK – Integrated railway bridge management system* (in Polish), Inżynieria i Budownictwo, Vol. 53, No. 3, 1996, pp. 180–184.
- [7] Bryja D.: *Stochastic response analysis of suspension bridge under gusty wind with time-dependent mean velocity*, Archives of Civil and Mechanical Engineering, Vol. IX, No. 2, 2009, pp. 15–38.
- [8] Das P.C.: *Development of a comprehensive structures management methodology for the highways agency*, In: P.C. Das (ed.), Management of highway structures, 1999, Thomas Telford, London, pp. 49–60.
- [9] Diehl S.: *Software visualization*, Springer, 2007.
- [10] Grigorjeva T., Juozapaitis A., Kamaitis Z.: *Static analysis and simplified design of suspension bridges having various rigidity of cables*, Journal of Civil Engineering and Management, Vol. 16, No. 3, 2010, pp. 363–371.
- [11] Hawk H., Small E.P.: *The BRIDGIT bridge management system*, Structural Engineering International, Vol. 8, No. 4, 1998, pp. 309–314.
- [12] Hearn G.: *Condition data and bridge management systems*, Structural Engineering International, Vol. 8, No. 3, 1998, pp. 221–225.
- [13] Kmita J., Bień J., Machelski Cz.: *Computer-aided design of bridges* (in Polish), Wydawnictwa Komunikacji i Łączności, Warszawa, 1989.

- [14] Kużawa M., Bień J., Rawa P., Zwolski J.: *Load test of bridge over Odra River along Wrocław Motorway Bypass*, Wrocław University of Technology, Institute of Civil Engineering, Report U-03/11, Wrocław, 2011.
- [15] Lauridsen J., Lassen B.: *The Danish bridge management system DANBRO*, In P.C. Das (ed.), Management of highway structures, Thomas Telford, London, 1999, pp. 61–70.
- [16] Lee Y.-S., Kim S.-H., Skibniewski M.J.: *Analytical and experimental approach for assessing vibration serviceability of highway bridges due to heavy vehicle traffic*, The Baltic Journal of Road and Bridge Engineering, Vilnius: Technika, Vol. IV, No. 3, 2009, pp. 123–133.
- [17] Liu Ch., Xu D.: *Space frame lattice model for stress analysis of bridge*, The Baltic Journal of Road and Bridge Engineering, Vilnius: Technika, Vol. V, No. 2, 2010, pp. 98–103.
- [18] Luebke D. et al.: *Level of detail for 3D graphics*, Elsevier Science, 2003.
- [19] Maksymowicz M.: *Evaluation of load capacity of concrete railway slab spans with defects* (PhD Thesis), University of Minho, Portugal, 2008.
- [20] McCullough M.: *Digital ground: architecture, pervasive computing, and environmental knowing*, MIT Press, 2004.
- [21] Noorzaeia J., Abdulrazega A.A., Jaafara M.S., Kohnehpooshi O.: *Non-linear analysis of an integral bridge*, Journal of Civil Engineering and Management, Vol. 16, No. 3, 2010, pp. 387–394.
- [22] Shirley P. et al.: *Fundamentals of computer graphics*, A.K. Peters, 2005.
- [23] Small E.P., Fraher M., Philbin T., Romack G.P.: *The current status of Bridge Management Systems implementation in United States*, In: Transportation Research Circular, No. 498, 2000, pp. 1–16.
- [24] Soderqvist M.K., Veijola M.: *The finish bridge management system*, Structural Engineering International, Vol. 8, No. 4, 1998, pp. 315–319.
- [25] Thompson P.D., Chetham A., Merlo T., Kerr B.: *The new Ontario bridge management system*, Transportation Research Circular, No. 498, 2000, pp. 1–16.

Modelowanie geometrii obiektów w Systemach Zarządzania Mostami

W systemach wspomagających zarządzanie mostami z reguły obiekty są reprezentowane za pomocą elementów bezwymiarowych, natomiast wśród modeli geometrii stosowanych w analizie konstrukcji mostowych wyróżnia się zazwyczaj modele jedno-, dwu- oraz trójwymiarowe. W pracy zaproponowano bardziej precyzyjną klasyfikację modeli geometrii, w której uwzględniono zarówno typy elementów (bezwymiarowe, 1-, 2- lub 3-wymiarowe) wykorzystywanych do tworzenia geometrycznej reprezentacji obiektów mostowych, jak i wymiar przestrzeni, w której model jest tworzony – z wyróżnieniem modeli definiowanych w przestrzeni bezwymiarowej, a także w przestrzeni 1-, 2- lub 3-wymiarowej. Przedstawiona systematyka modeli geometrii oraz sposób oznaczania poszczególnych klas modeli zapewniają jednolitą klasyfikację oraz stwarzają możliwość obiektywnego porównywania wszystkich sposobów odwzorowywania geometrii obiektów mostowych, zarówno w systemach zarządzania, jak i w statycznych oraz dynamicznych analizach konstrukcji.



Measurements of flow parameters for 2-D flow around rectangular prisms of square and rectangle cross-sections located on the ground

E. BŁAZIK-BOROWA, J. BĘC, T. NOWICKI, T. LIPECKI, J. SZULEJ, P. MATYS
Lublin University of Technology, ul. Nadbystrzycka 40, 20-618 Lublin, Poland.

The results of measurements of 2-D flow around rectangular prisms of square and rectangle cross-sections in wind tunnel are presented in this paper. The results include pressure and standard deviation distributions over the model walls, components of velocity vectors and statistical moments for fluctuations of the velocity in the wind tunnel measuring space. The arrangements of models and the range of measurements have been matched in order to the results could be used to the calibration of the numerical turbulence model and to the verification of computer calculations for the civil engineering problems. The values of parameters have been presented in graphs and subsequently used in a comparative analysis of the flows around both models.

Keywords: *wind tunnel, measurement of pressure distribution, measurements of velocity field, 2D flow, statistical moments of flow properties, rectangular and square cylinders*

1. Introduction

The paper presents results of measurements in a wind tunnel. The arrangements of models and the range of measurements have been matched in order to the results could be used to the calibration of the numerical turbulence model and to the verification of computer calculations for the civil engineering problems. For thirty years the computational fluid dynamics (CFD) has been applied in the wind engineering. Unfortunately, the turbulence models still do not properly described all aerodynamic phenomena. The calculations results are not properly for all cases. Sometimes errors occur in a small part of calculation domain only, but sometimes the calculation results are completely incorrect. Therefore the computer calculation should be checked by comparison with measurements results which should include the components of velocity and their fluctuations apart from averaged pressure distribution. The agreement of calculations and measurements for one flow parameter does not mean that other parameters are correct and it is only chance that obtained results of analysed parameter are the same as the measurement results. Moreover the wind velocity is a very important parameter for wind comfort problems. Simultaneously, it comes from the literature studies that the research of fundamental problems with measurements of

velocities and their fluctuations lacks. Hence the main aim of this paper is shown the measurements results which contain average pressure and its standard deviation distributions, average components of velocity and its statistical moments, which are called Reynolds stress after multiplying by the air density.

The results of measurements of 3-D flow around square or rectangular cylinders of similar dimensions and located at the ground can be found in many publications, e.g.: [2, 6, 11, 13]. There are several other publications which deal with the 2-D flow around a free square e.g. [5, 7, 15]. These studies include measurements of pressure distributions over the surfaces, components of velocity vectors and Reynolds stresses. However, there are a few studies concerning the measurements of the flow around a square cylinder located at the ground, for which the assumption of the 2-D flow, is applicable. Such research have been described by e.g.: [8–10], but during these measurements only pressure distributions had been measured. On the opposite, here in this paper not only analysis of pressure distributions are presented, but additionally the velocity fields and especially the results of measurements of two velocity vector components and their fluctuations are analysed. As a part of this research, flow parameters around two rectangular cylinders have been measured: with square cross-section and with cross-section dimensions ratio set to 1:2. The measurements have been carried in the wind tunnel of the Wind Engineering Laboratory in Cracow University of Technology directed by Prof. Andrzej Flaga. The research range has been set to allow verification of computational results of 2-D flows with use of the results presented here.

2. The description of the experiment

The models have been set at the ground of the wind tunnel. Since they have been perpendicularly located to the average direction of wind the flow in the mid-plane has been treated as two-dimensional one. The measurements have been provided for the smaller cylinder of the square cross-section with dimensions $a \times a \times b$ and for the larger one with dimensions $2a \times a \times b$; where: $a = 200$ mm and $b = 2050$ mm. The models layout is presented in Figure 1. All measurements have been taken at the velocity above the boundary layer with approximate value of 10 m/s. The vertical profiles of averaged components of the inflow velocity, the second order statistical moments for $x_1/a = -4.0$ are shown in Figure 2 and the reduced power spectral density for the inflow on the height 0.5 m is shown in Figure 3.

As the result of the measurements the variations in time of pressure distributions on model walls, mean values of the pressures on the ground in front of and behind models and time series of velocities in eight cross-sections of the wind tunnel measuring space have been obtained. The measurements of pressures on models have been obtained with use of pressure scanner based on piezoresistive two-directional pressure sensors Motorola MPX 2010 and battery of manometers. The measurements carried with use of pressure scanner have been made in 30 points distributed over the model surface and with the sample frequency 500 Hz. Battery of manometers has been connected with 30

points located on models and 16 points in the ground. Additional measurements have been provided with use of hot-wire anemometers with the sampling frequency 500 Hz, as well. Hot-wire anemometer probes, measuring system ATU2001 and the software used in data acquisition have been made in Strata Mechanics Research Institute of the Polish Academy of Sciences. The measurements have been made with use of two single-wire probes and four X wire ones. The measurements from both single-wire probes have been used to obtain the mean velocity value, so these devices have been set in the front of the model. In the nearby of the hot-wire anemometers there has been set a small tube connected with the pressure scanner.

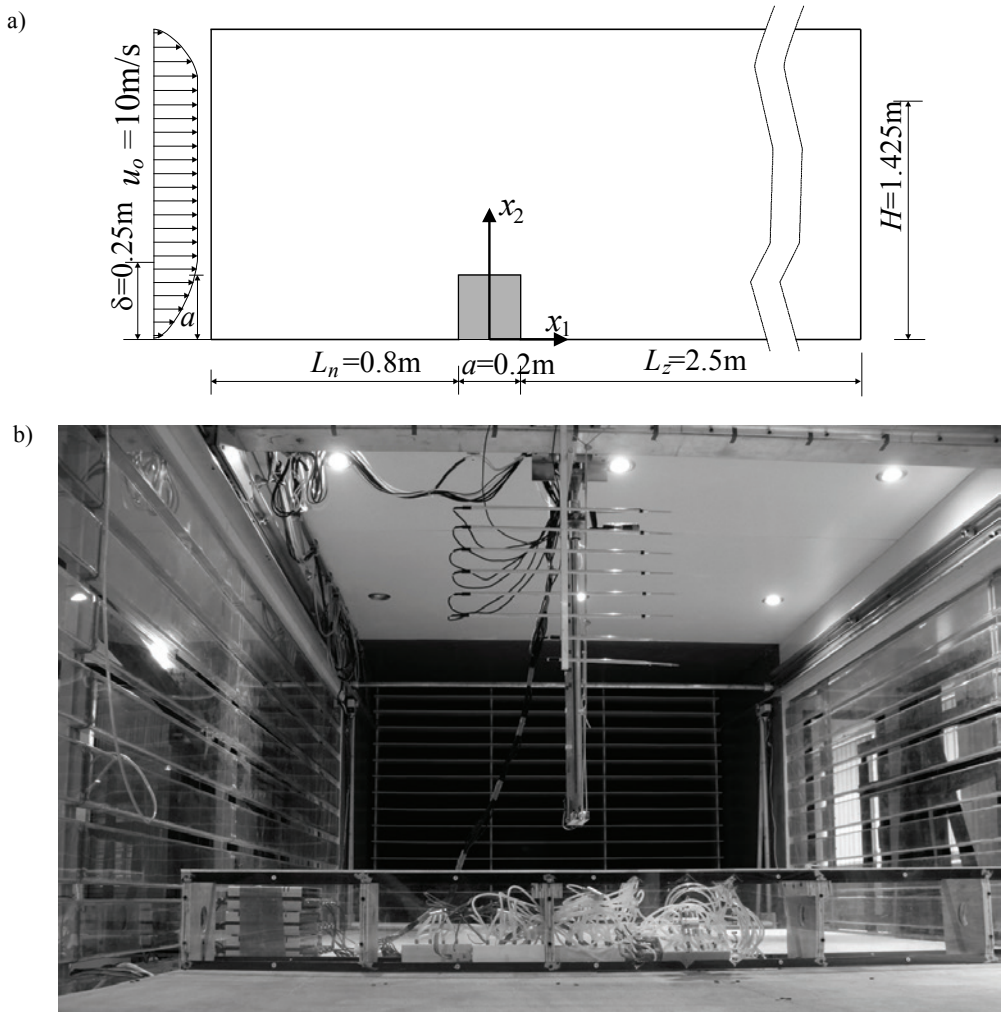


Fig. 1. Exemplary location of the model in the wind tunnel for the specimen with dimensions $a \times a$:
a) geometrical scheme; b) model in the wind tunnel

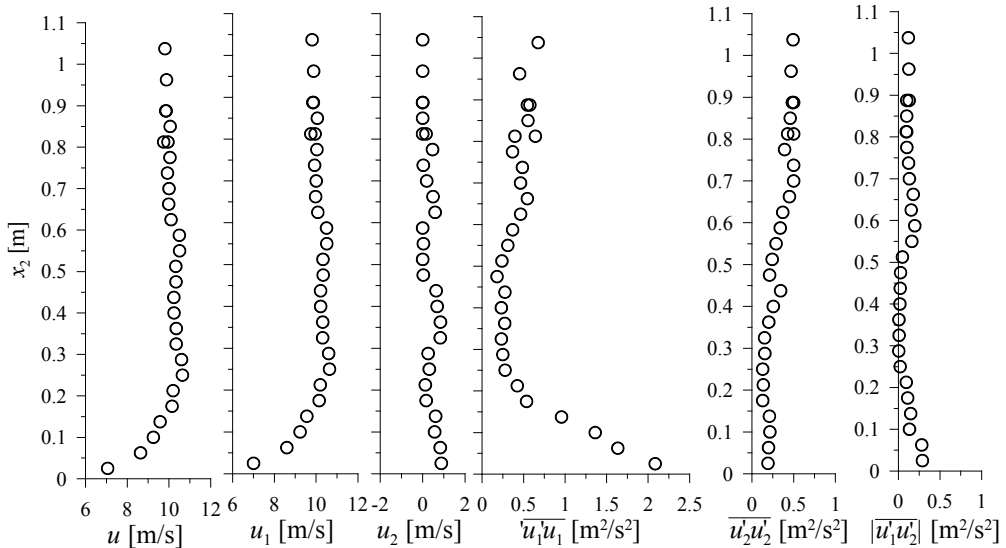


Fig. 2. The vertical profiles of the averaged inlet velocity and their statistical properties for both models at $x_1/a = -4.0$, where axes x_1 and x_2 are introduced in Figure 1

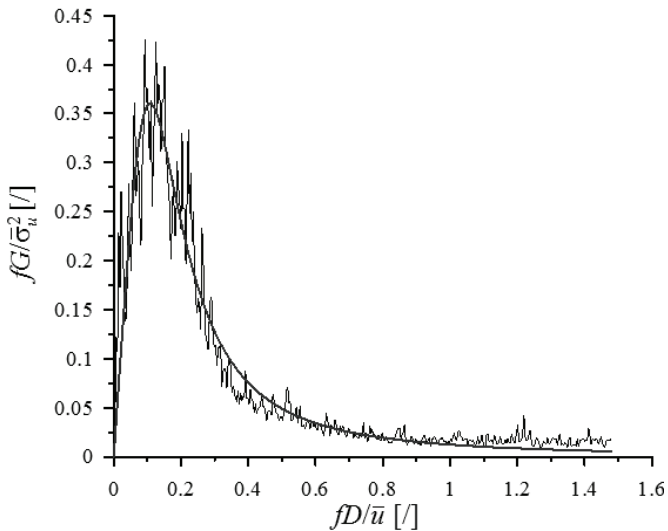


Fig. 3. The reduced power spectral density for the inflow on the height 0.5 m, where $D = a = 0.2$ m and $\bar{u} = 10$ m/s

The results from this measuring point have been used to calculate the pressure coefficient and verification of the hotwire anemometric velocity measurements. The probes have been applied to a mobile carriage and could be set at any given

point in the measuring space of the wind tunnel. The wires of the probes have been set up to obtain the angle of about $\pi/4$ between the wires and the direction of the mean flow.

On the basis of measurements there have been calculated time series of velocity components along directions perpendicular to the wires. The ultimate components of velocity vector along mean flow and in the perpendicular direction have been calculated according to the recommendations which can be found in the papers such as [1, 3, 12]. Such procedure allows removal of the influence of the turbulence in the direction perpendicular to the measurement plane and the influence of wire cooling due to flow along the wire direction.

3. The measurements results

3.1. The description of flow parameters

The pressure has been measured with use of two types of devices: manometers and the pressure scanner. It has been assumed that due to fluid inertia mean values of pressures p and p_o can be obtained with use of the first device, while the pressure scanner allows acquisition of data varying in time. The results of measurements obtained with the scanner are described with the quantities calculated on the basis of the following formulae:

- mean dynamic pressure (first order statistical moment) in the measurement point on the model

$$p = \frac{1}{N} \sum_{i=1}^N \hat{p}_i, \quad (1)$$

- mean dynamic pressure (first order statistical moment) in the flow in front of the models at the height of the top edge of the model

$$p_o = \frac{1}{N} \sum_{i=1}^N \hat{p}_{oi}, \quad (2)$$

- standard deviation of dynamic pressure (central statistical moment of the second order) in the measurement point on the model

$$\sigma_p = \sqrt{\frac{1}{N} \sum_{i=1}^N (\hat{p}_i - p)^2}, \quad (3)$$

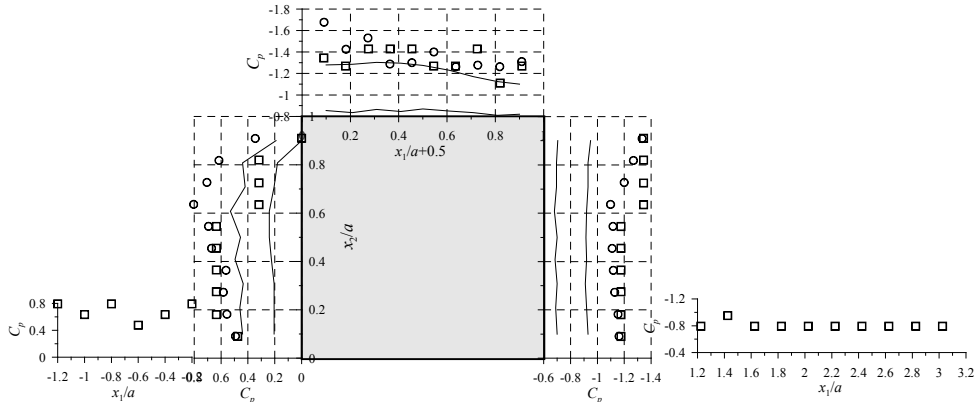
where:

\hat{p} – measured value of pressure in the point on the model and averaged over the time $dt = 1/500$ s,

\hat{p}_o – measured value of pressure in the free flow in the front of the model and averaged over the time $dt = 1/500$ s,

$N = 10\,000$ – number of samples.

a)



b)

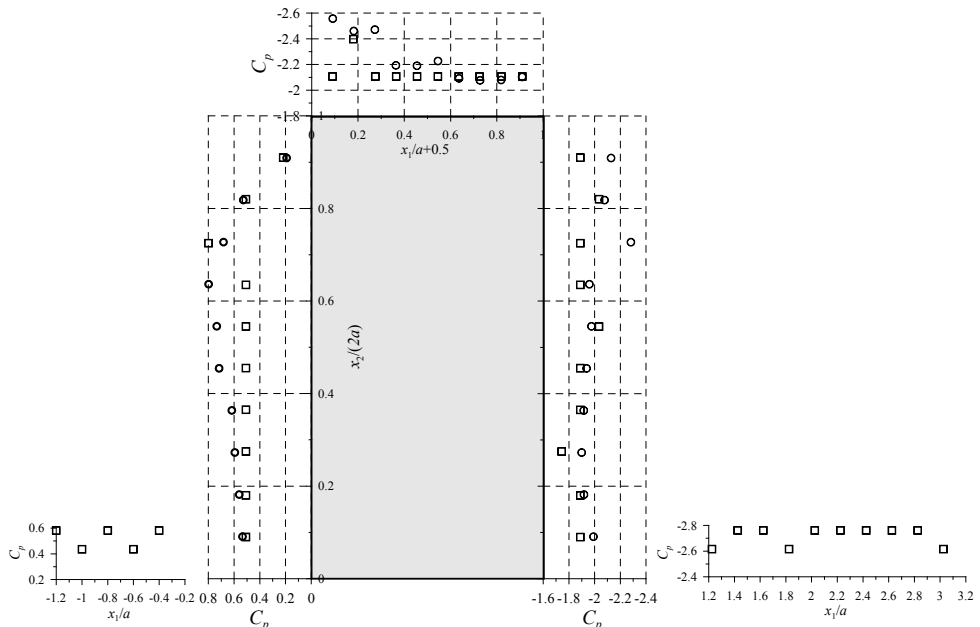


Fig. 4. Mean pressure coefficient distribution: a) on the model with dimensions $a \times a$; b) on the model with dimensions $2a \times a$; \bullet – the results obtained with the pressure scanner; \square – the results obtained with battery of manometers; — the results from [9, 10] with relation of the coefficient to the velocity at the height of the model edge

Finally the results shown in Figures 4 and 5 are calculated with the following formulae:

- coefficient of pressure distribution

$$C_p = \frac{p}{p_o}, \quad (4)$$

- coefficient of pressure standard deviation distribution

$$\sigma_{C_p} = \frac{\sigma_p}{p_o}, \quad (5)$$

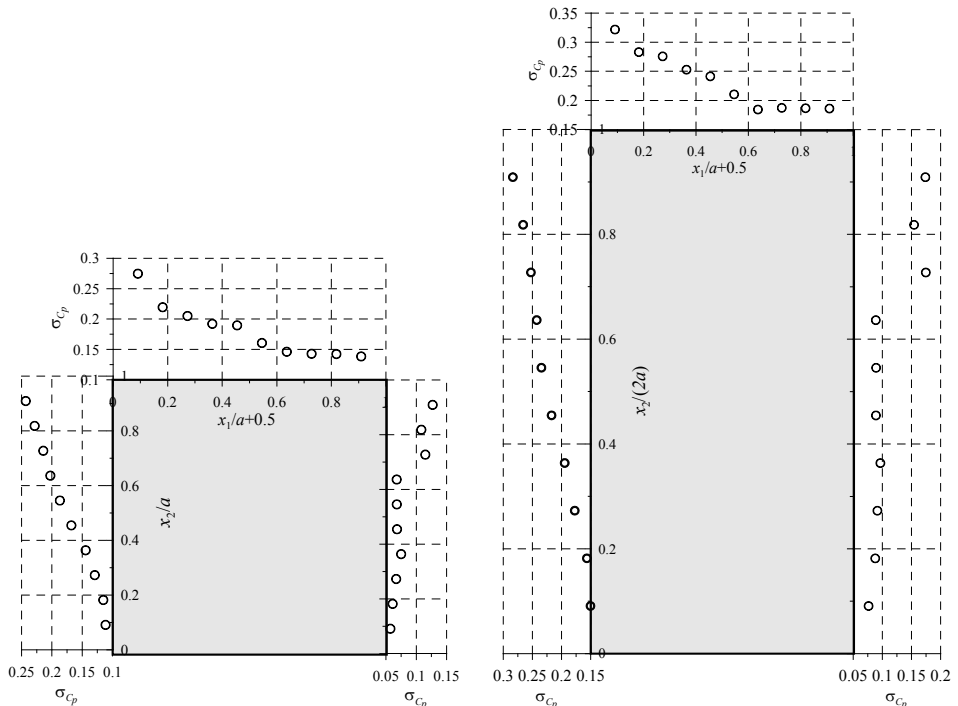


Fig. 5. Distribution of the coefficient of pressure standard deviation: a) on the model with dimensions $a \times a$; b) on the model with dimensions $2a \times a$

Time series of velocity have been measured with use of hot-wire anemometers. The graphs presenting velocity components and their fluctuations in eight sections in the measuring space are shown in Figures 6–15. Each value are obtained with use of the following formulae:

- mean value of velocity component u_1

$$u_1 = \frac{1}{N} \sum_{i=1}^N \hat{u}_{1i}, \quad (6)$$

- mean value of velocity component u_2

$$u_2 = \frac{1}{N} \sum_{i=1}^N \hat{u}_{2i}, \quad (7)$$

- second order statistical moment $\overline{u'_1 u'_1} = \sigma_{u_1}$

$$\overline{u'_1 u'_1} = \frac{1}{N} \sum_{i=1}^N (\hat{u}_{1i} - u_1)^2, \quad (8)$$

- second order statistical moment $\overline{u'_2 u'_2}$

$$\overline{u'_2 u'_2} = \frac{1}{N} \sum_{i=1}^N (\hat{u}_{2i} - u_2)^2, \quad (9)$$

- modulus of second order statistical moment $|\overline{u'_1 u'_2}|$

$$|\overline{u'_1 u'_2}| = \left| \frac{1}{N} \sum_{i=1}^N (\hat{u}_{1i} - u_1)(\hat{u}_{2i} - u_2) \right|, \quad (10)$$

where:

\hat{u}_1 and \hat{u}_2 are values of velocity components along the wind tunnel and in vertical direction in the analytical point and averaged over the time $dt = 1/500$ s,

$N = 6000$ – number of samples.

3.2. The description of the results

Measurements verification of 2-D flows around models set at the ground is a difficult problem. First of all there are not much of such examples presented in literature and as for velocity fields they practically do not exist. The second difficulty is variations of the results for different velocity and their turbulence intensity profiles. In Figure 4a, next to our own results, there has been shown the envelope of

measurement results presented in the papers [9–10], for the profiles with different thickness of boundary layer (from $\delta/a = 1.7$ to $\delta/a = 5.0$), different exponents in power profile formula (from $\alpha = 0.11$ to $\alpha = 0.30$) and different values of turbulence intensity (from $I_u = 7\%$ to $I_u = 15\%$). The flow parameters for the results presented here from our measurements are $\delta/a = 1.25$, $\alpha = 0.15$ and $I_u = 5\%$, so they unfortunately vary from the ones from the paper [9]. The results of both measurements differ with coefficients of pressure, but despite quite large difference they have same signs and shapes of coefficient distribution, while the higher value of negative pressure in our own research is caused by lower level of turbulence. In case of both models the reattachment point is taking place outside the space where the measurements have been made, i.e. in the distance larger than five heights ($x_1/a > 5.0$) which speaks in favour of results accuracy. In the same manner as for measurements of the 2-D flow velocity field, the location of reattachment point cannot be found in literature in case of such problems. However the measurement results behind rectangle may be compared to the ones obtained in the backward facing step problem. Of course it is only some similarity, but it seems that the character of the flow behind a step is closer to the flow on the leeward side of the rectangle than the 3-D flow around cube. According to the papers [4, 14] the reattachment point obtained in case of flows around a step is taking place between 6 and 7.5 heights, i.e. further than five heights.

Comparison of measurements in both models shows that pressure on the ground in front of models and on windward faces of models is the same, while the negative pressure on other faces and behind the model for the larger model is almost twice as much as for the smaller one. The higher values of pressure is produced, among others, by diminishing space between the ceil and the model. On the basis of mass balance for incompressible flows we may state that the product of the cross-section area and the velocity value is constant. This is the reason for the 20% difference in growth of velocity values in the space between larger model and ceil in comparison to the growth of velocity values observed when smaller model is analysed. This generates over 40% growth of suction. The other 60% growth of suction is produced by the height of the model, or actually by its height being larger than the boundary layer. This generates the variation of the flow character in front of models.

The importance of the relation of model height and boundary layer thickness for the flow may be observed in Figures 6–15 for $x_1/D = -1.0$ in the cross-section in front of the model. The graphs of velocity properties are different for both problems, e.g. in case of smaller model the velocity u_1 values are close to 0, but still positive, while in case of the larger model negative values occur. This is the sign of a vortex occurrence. Both components of velocity in case of larger model on its windward side are higher than for the smaller model, and the difference is bigger when the velocity u_2 is taken into account. Above models the difference in values of the velocity u_1 is bigger, but as it has been mentioned before this is mainly caused by the difference in the area of the flow cross-section. The higher model generates significantly wider and longer aerodynamic wake which may be seen in values of velocity components and their fluctuations.

For both models the shapes of graphs of statistical moments are similar. The extreme values of fluctuations visibly determine the area of intermittent flow. The comparison of graphs leads to the conclusion that the width of area of disturbance is bigger for larger model and this applies to all statistical moments.

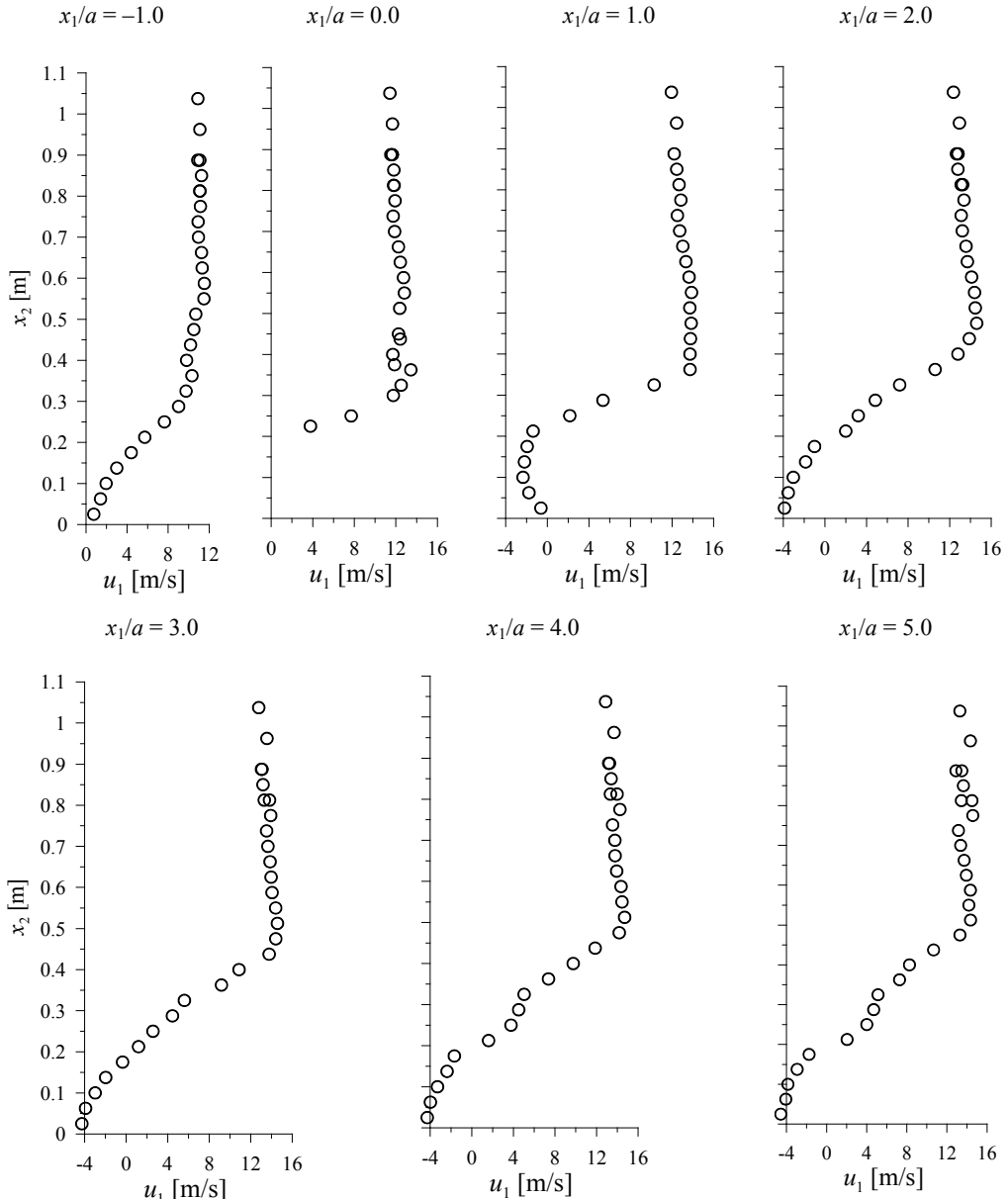


Fig. 6. Velocity component u_1 in vertical cross-sections for the flow around the $a \times a$ model

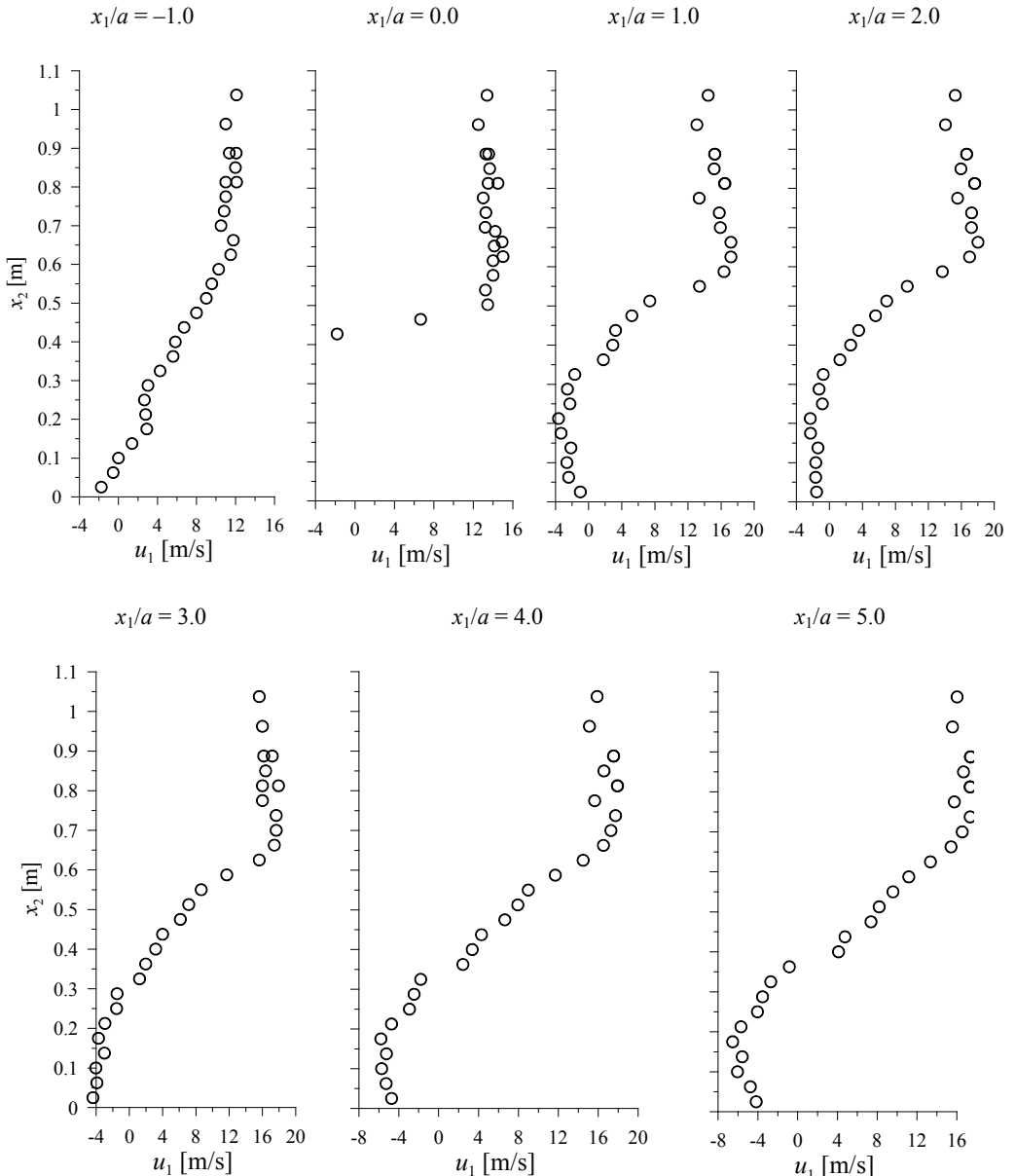


Fig. 7. Velocity component u_1 in vertical cross-sections for the flow around the $2a \times a$ model

4. Conclusion

The directly conclusion comes from measurement results is that the bigger wind load and problems with pedestrian wind comfort can be expected for higher buildings.

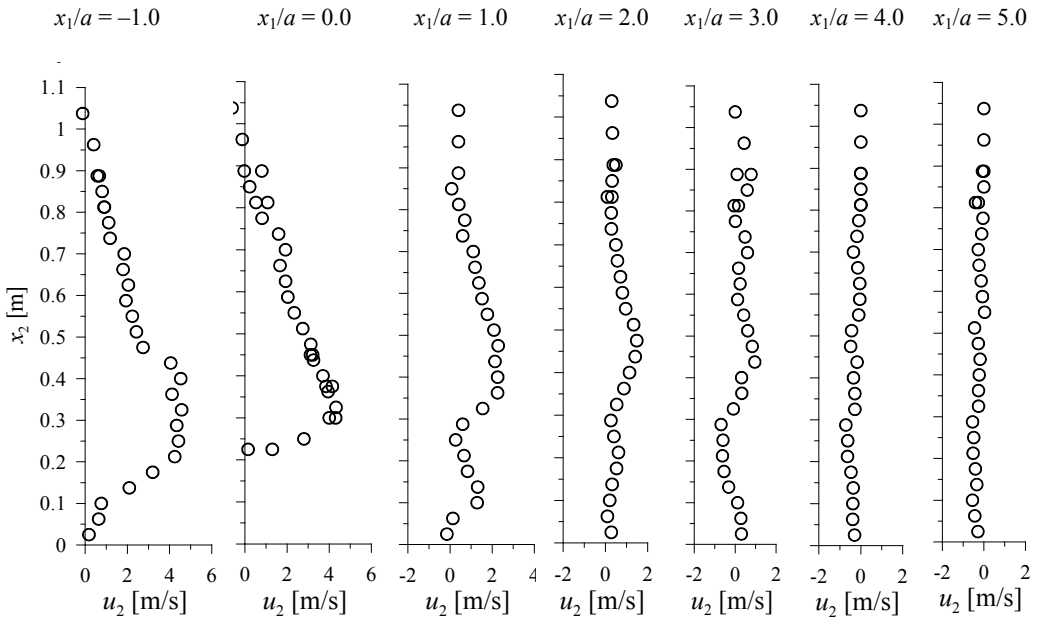


Fig. 8. Velocity component u_2 in vertical cross-sections for the flow around the $a \times a$ model

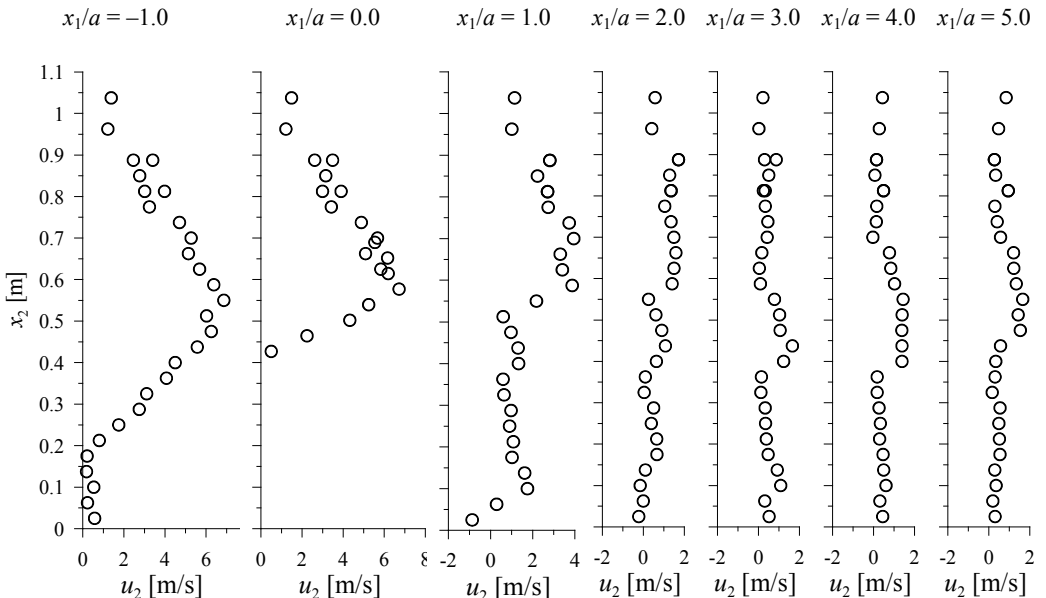


Fig. 9. Velocity component u_2 in vertical cross-sections for the flow around the $2a \times a$ model

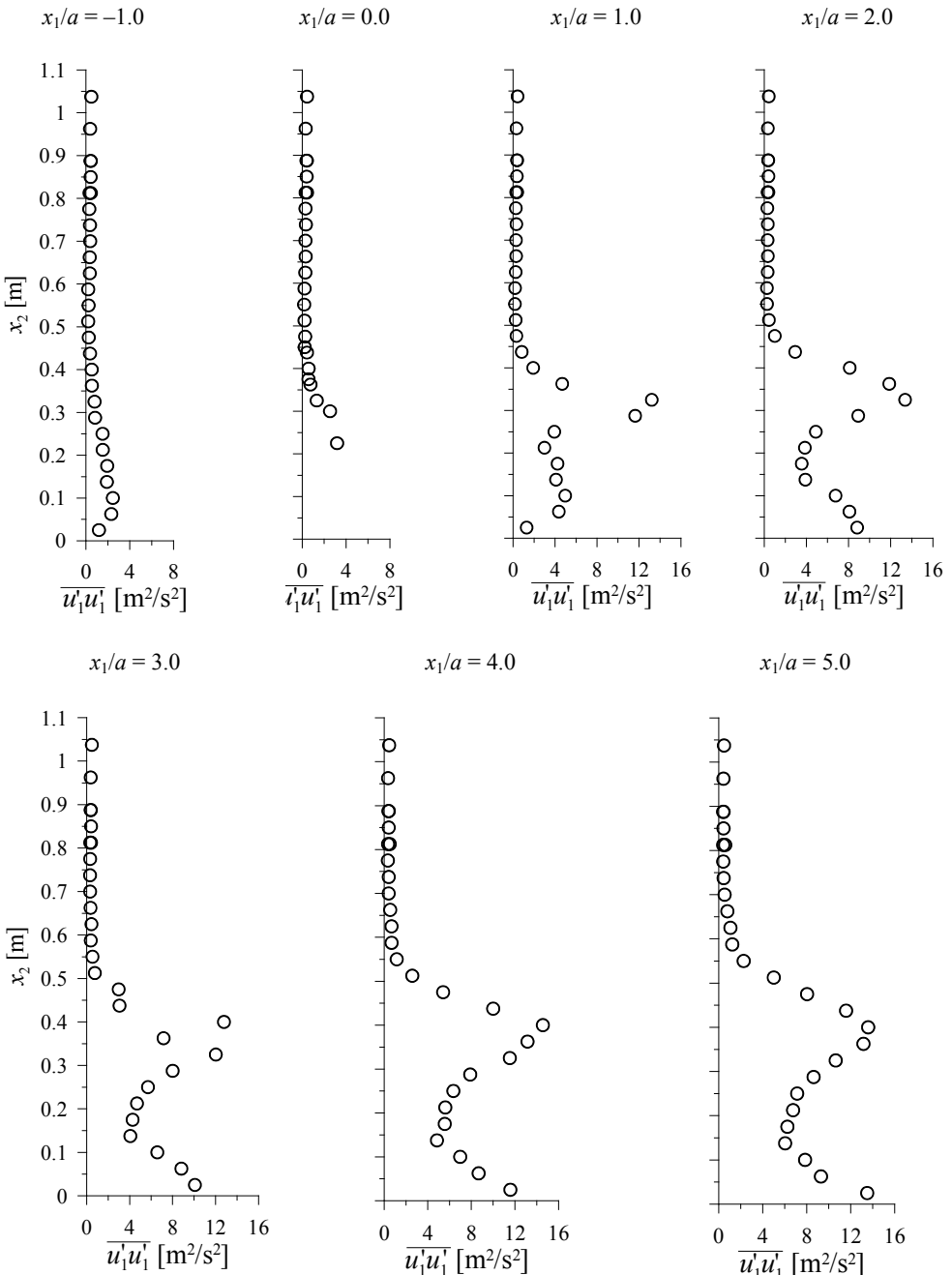


Fig. 10. Statistical moment $\overline{u'_1 u'_1}$ in vertical cross-sections for the flow around the $a \times a$ model

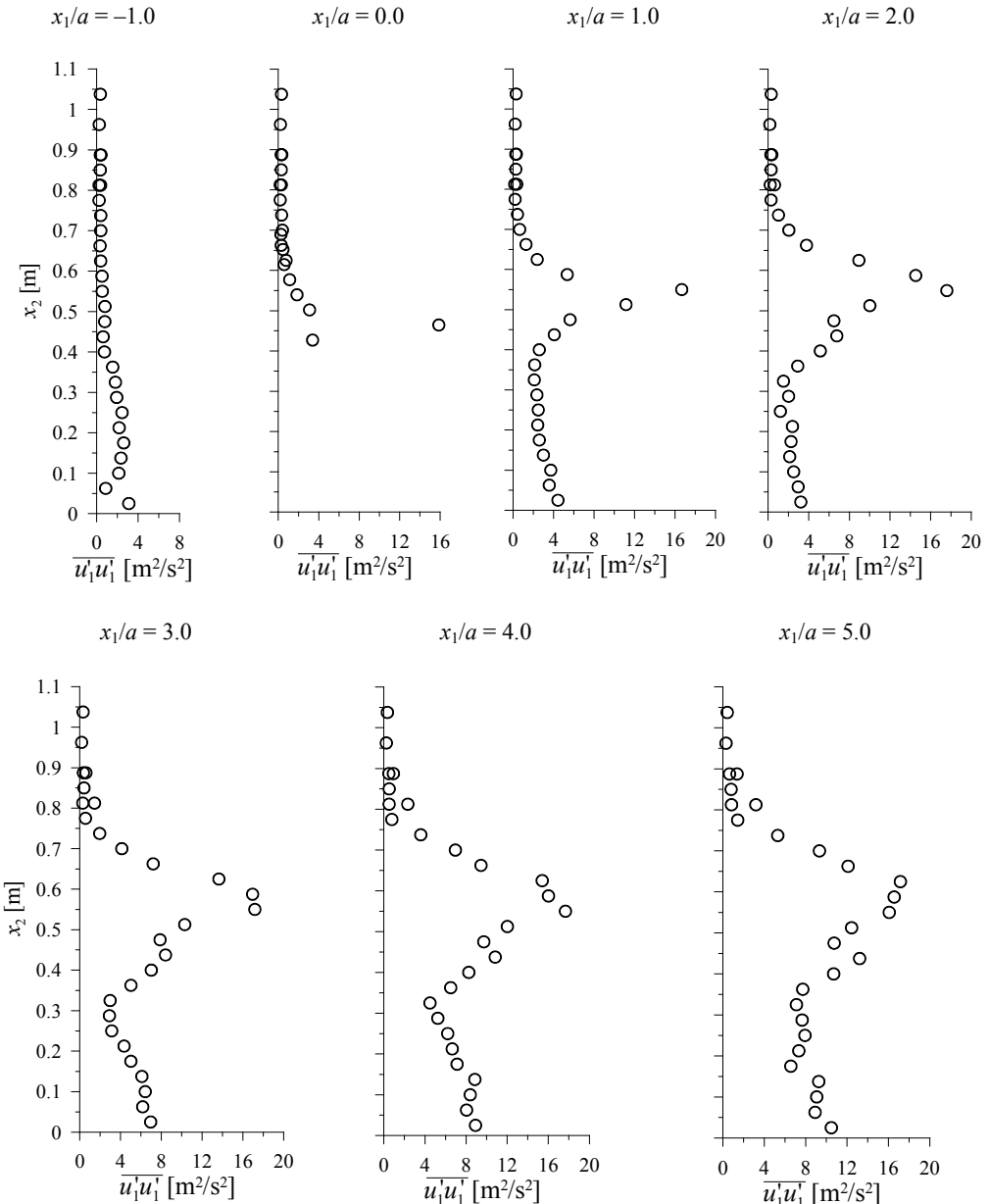


Fig. 11. Statistical moment $\overline{u'_1 u'_1}$ in vertical cross-sections for the flow around the $2a \times a$ model

Moreover the presented results can be used to verify the computer calculation of the flow around buildings. The results can be used both to calibrate turbulence models and to check the shapes of graphs of pressure, velocity and their fluctuations.

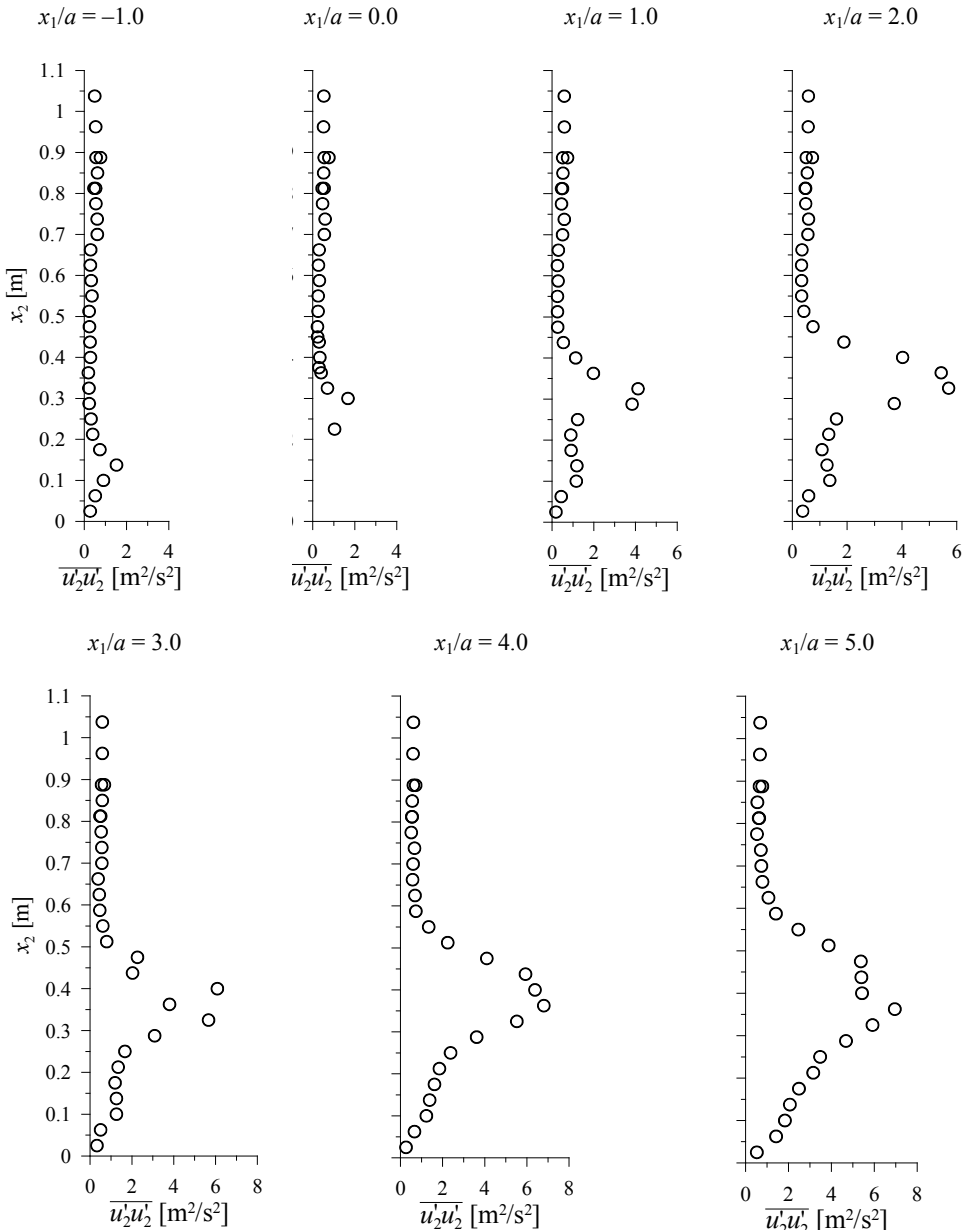


Fig. 12. Statistical moment $\overline{u'_2 u'_2}$ in vertical cross-sections for the flow around the $a \times a$ model

The presented research is one of the stages of the project concerning the possibility of obtaining methods of verification for numerical calculations. The simplest method of such verification is wind tunnel test. In the project mentioned above the comparison

of calculations and tests are the basic for verification of possibility for results quality estimation with use of sensitivity analysis.

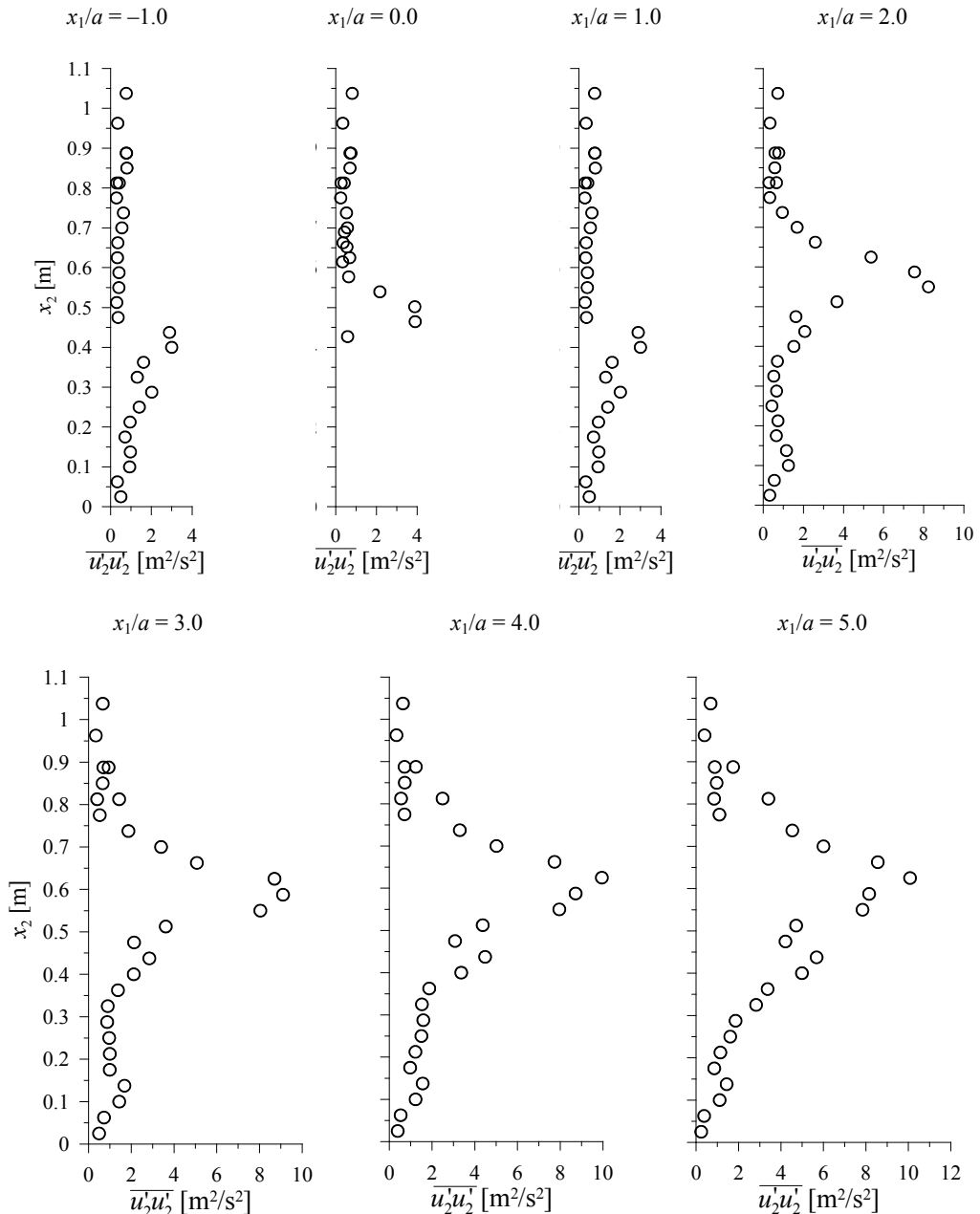


Fig. 13. Statistical moment $\overline{u'_2 u'_2}$ in vertical cross-sections for the flow around the $2a \times a$ model

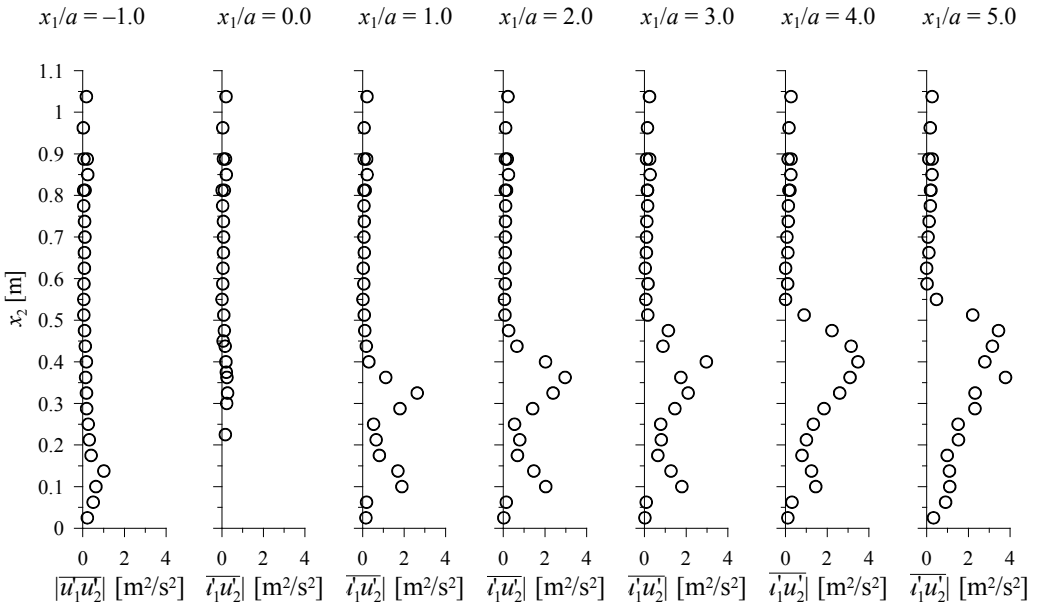


Fig. 14. Modulus of statistical moment $\overline{|u'_1 u'_2|}$ in vertical cross-sections
for the flow around the $a \times a$ model

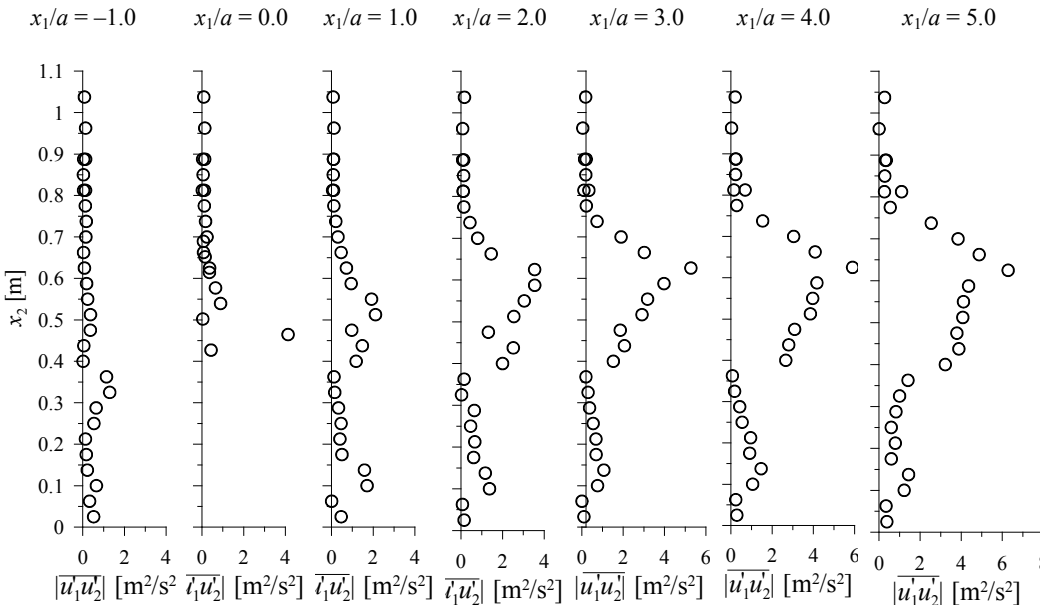


Fig. 15. Modulus of statistical moment $\overline{|u'_1 u'_2|}$ in vertical cross-sections
for the flow around the $2a \times a$ model

In the future the presented results of measurements for single models will be used to estimate the influence of the neighbouring buildings on the parameters of the flow around models of the same dimensions and conditions.

In this paper there has been presented the basic research of flow around single models, but thanks to restriction of the research area to the wind tunnel tests only, the detailed description of the measurements conditions and the wider range of results could be presented than usually in other papers. It seems that the presented results will be used not only by authors in their future work, but thanks to publication here in this paper, by other researchers in verification of 2-D flows numerical calculations, as well.

References

- [1] Evans R.L.: *Free stream turbulence effects on the turbulent boundary layer*, Report No. 1282, Procurement Executive, Ministry of Defence USA, 1974.
- [2] Haan F.L., Kareem A., Szewczyk A.A.: *The effects of turbulence on the pressure distribution around a rectangular prism*, Journal of Wind Engineering and Industrial Aerodynamics, No. 77–78, 1998, pp. 381–392.
- [3] Hinze J.O.: *Turbulence. An introduction to its mechanism and theory*, McGraw-Hill, Nowy York, 1975.
- [4] Kim J.J.: *Investigation of separation and reattachment of a turbulent shear layer: Flow over a backward facing step*, Ph.D. Thesis, Stanford University, 1978.
- [5] Luo S.C., Li L.L., Shah D.A.: *Aerodynamic stability of the downstream of two tandem square-section cylinders*, Journal of Wind Engineering and Industrial Aerodynamics, Vol. 79, 1999, pp. 79–103.
- [6] Martinuzzi R., Tropea C.: *The flow around surface-mounted prismatic obstacle placed in a fully developed channel flow*, Journal Fluids Engineering, Vol. 115, 1993, pp. 85–92.
- [7] Nakagawa S., Nitta K., Senda M.: *An experimental study on unsteady turbulent near wake of rectangular cylinder in channel flow*, Experiments in Fluids, Vol. 27, 1999, pp. 284–294.
- [8] Noda M., Nakayama A.: *Reproducibility of flow past two-dimensional rectangular cylinders in a homogeneous turbulent flow by LES*, Journal of Wind Engineering and Industrial Aerodynamics, Vol. 91, 2003, pp. 265–278.
- [9] Noda M., Utsunomiya H., Nagao F., Takenaka K.: *Effects of the wind velocity profile on the aerostatic forces*, Proc. of the 9ICWE, Vol. 1, 1995, pp. 249–260.
- [10] Noda M., Utsunomiya H., Nagao F.: *Basic study on blockage effects in turbulent boundary layer flows*, Journal of Wind Engineering and Industrial Aerodynamics, No. 54–55, 1995, pp. 645–656.
- [11] Sitheeq M.M., Iyengar A.K.S., Farell C.: *Effect of turbulence and its scales on the pressure field on the surface of a three-dimensional square prism*, Journal of Wind Engineering and Industrial Aerodynamics, No. 69–71, 1997, pp. 461–471.
- [12] Shabbir A., Beuther P.D., George W.K.: *X-wire response in turbulent flows of high-intensity turbulence and low mean velocity*, Experimental Thermal and Fluid Science, Vol. 12, 1996, pp. 52–56.
- [13] Tamura T., Miyagi T.: *The effect of turbulence on aerodynamic forces on a square cylinder with various corner shapes*, Journal of Wind Engineering and Industrial Aerodynamics, Vol. 83, 1999, pp. 135–145.

- [14] Tsan-Hsing Shih, Liou W.W., Shabbir A., Zhigang and Jiang Zhu: *A new k- ε eddy viscosity model for high Reynolds number turbulent flows*, Computers Fluids, Vol. 24, No. 3, 1995, pp. 227–238.
- [15] Wong P.T.Y., Ko N.W.M., Chiu A.Y.W.: *Flow characteristics around two parallel adjacent square cylinders of different sizes*, Journal of Wind Engineering and Industrial Aerodynamics, Vol. 54–55, 1995, pp. 263–275.

Pomiary parametrów oplotu dwuwymiarowego wokół kwadratu i prostokąta ustawionych na podłożu

W pracy przedstawiono wyniki pomiarów parametrów płaskiego przepływu w odniesieniu do dwóch kształtów przekrójów poprzecznych modeli prostopadłościennych: kwadratu i prostokąta. Obiektami badań są prostopadłościany o wymienionych przekrojach, ułożone na podłożu i ustawione najbliższym (trzecim) bokiem prostopadle do średniego kierunku wiatru. Wynikami pomiarów są średnie ciśnienia na powierzchni modeli i odchylenie standardowe pomiaru ciśnienia w poszczególnych punktach oraz składowe prędkości przepływu i momenty statystyczne pierwszego rzędu fluktuacji prędkości w punktach przestrzeni pomiarowej tunelu. Ustawienie modeli oraz zakres pomiarów zostały dobrane w taki sposób, aby wyniki pomiarów mogły zostać użyte do kalibracji numerycznych modeli turbulencji i weryfikacji obliczeń komputerowych w odniesieniu do problemów przepływów wokół budynków. Wyniki zostały zaprezentowane w formie rysunków natomiast w tekście zamieszczono dyskusję wyników, zawierającą między innymi porównanie z innymi badaniami w tunelach aerodynamicznych podobnych zagadnień.



Estimation of the bending stiffness of rectangular reinforced concrete beams made of steel fibre reinforced concrete

CZ. BYWALSKI, M. KAMIŃSKI

Wrocław University of Technology, Wybrzeże Wyspiańskiego 25, 50-370 Wrocław, Poland.

A method of calculating the location of the neutral axis of a rectangular steel fibre reinforced concrete cross section before and after cracking, and its moments of inertia relative to this axis is proposed. Moreover, the method of calculating the cross section's geometrical characteristics for both the cracked stage and the uncracked stage is based on a model of fibres distribution along the length of the beam. Consequently, two algorithms for estimating the immediate and long-term deflections of steel fibre reinforced concrete beams are proposed. One of the algorithms is for uncracked beams and the other for cracked beams. The algorithms have been positively experimentally verified.

Keywords: *steel fibre reinforced concrete, steel fibres, stiffness, moment of inertia, deflections of beams*

1. Introduction

Already the first attempts at designing, making and using reinforced concrete elements showed that a major factor which determines their practical usefulness is their deformation capacity. In the case of beams, it means the capacity to undergo immediate and long-term deflection. An immediate deflection arises immediately after the element is loaded while a long-term deflection occurs after some time. Respectively immediate stiffness and long-term stiffness correspond to the above types of deflection. The increase in the deflection of reinforced concrete beams and steel fibre reinforced concrete beams over time is due to the fact that concrete is a rheological material, mainly because of its creep (i.e. an increase in strain over time under a constant load). However, the problem of the deflection of reinforced concrete beams or fibre reinforced concrete beams is much more complex and the size of the immediate and long-term deflections depends not only on the creep strain, but on many other factors as well.

The problem of immediate and long-term deflections has been solved for reinforced concrete elements, although research aimed at improving the existing theories, based on different models (taking cracking into account) of stiffness distribution along the length of the element, is still continued [1–2]. According to one of the most popular concepts, stiffness is constant along the element's length [3–5].

In the case of steel fibre reinforced concrete beams Ezeldin and Shiah [6] proposed to estimate immediate and long-term deflections by means of an algorithm based on

the moment-curvature relation or the load-displacement relation. The algorithm requires that the characteristics of the fibre reinforced concrete be known. Idealized (e.g. stress-strain) relations for fibre reinforced concrete under compression can be assumed on the basis of [7].

The calculation of long-term deflections of reinforced concrete beams and fibre reinforced concrete beams becomes even more complicated since concrete creep and shrinkage need to be considered. The amount of experimental data on creep for fibre reinforced concretes is rather small [6]. When developing their algorithm Ezeldin and Shah took into account the experimental results concerning the shrinkage and creep of concrete, presented in respectively [8–9] and [8]. Consequently, it was proposed to calculate shrinkage strain and creep strain according to the guidelines of [10].

Cross sectional moment of inertia J should be calculated in accordance with the theory of reduced cross section, taking into account the area of the compressed fibre reinforced concrete and substituting this area for the area of the steel. Unfortunately, this way of calculating the stiffness (and particularly the moment of inertia) of the cross section does not take into account the distribution of fibres in the cross section or along the length of the beam. The problem of describing the distribution of steel fibres in the cross section and along the length of the beam was analyzed by Kamiński and Bywalski [11] who built a simulation model of fibres distribution [12]. The model can be used to estimate the moment of inertia of the beam cross section.

2. Proposed modification of EC2 method

2.1. Assumptions

On the basis of their own experimental results the authors have modified the Eurocode 2 [13] method of estimating deflections, by taking into account the contribution of the fibres to the increase in the moment of inertia of any cross section. For this purpose the above mentioned model of fibres distribution in the cross section and along the length of the element was used. The proposed approach distinguishes between uncracked and cracked beams. In the latter case, the authors propose to neglect the fibres located in the zone of tensile strains greater than 2.5%. The proposed modifications are described in detail later in this paper.

The authors have also proved that the influence of steel fibres on creep strains is negligibly small [14], which means that the magnitude of creep strains is determined by the concrete matrix. Consequently, the existing methods of calculating creep strains for concretes without fibres can be employed. The authors propose to use the method based on the MC 90 model (Model Code 1990) to calculate the creep coefficient (also for steel fibre reinforced concretes). Model Code 1990 was described in detail in the CEB Bulletin [15].

In many simple cases, if the stress in the concrete changes only slightly, one can take rheological strains into account through an equivalent (effective) modulus of elasticity, expressed by this formula

$$E_{c,\text{eff}} = \frac{E_{cm}}{(1 + \Phi)}. \quad (1)$$

2.2. Bending stiffness under long-term loading

Long-term stiffness is a function of effective elasticity modulus $E_{c,\text{eff}}$ defined by formula (1). Depending on the stage in the element's performance and the suitably defined cross-sectional moment of inertia, the formulas for stiffness are as follows: (i) in the uncracked stage – I (for cross-sectional moment of inertia J_I) – formula (2); (ii) in the cracked stage – II (for cross-sectional moment of inertia J_{II}) – formula (3).

$$B_I = E_{c,\text{eff}} J_I, \quad (2)$$

$$B_{II} = \frac{E_{c,\text{eff}} J_{II}}{1 - \beta_1 \beta_2 \left(\frac{\sigma_{sr}}{\sigma_s} \right)^2 \left(1 - \frac{J_{II}}{J_I} \right)}, \quad (3)$$

where:

β_1 – a coefficient representing the influence of the reinforcement's adhesion properties: (i) 1.0 for rebars characterized by high adhesion; (ii) 0.5 for smooth rebars,

β_2 – a coefficient representing the influence of load type and duration: (i) 1.0 for a single short-term load; (ii) 0.5 for long-term loads or loads repeated many times,

σ_s – tensioned reinforcement stress calculated for the cross section through a crack,

σ_{sr} – tensioned reinforcement stress under the cracking load, calculated for the cross section through a crack.

Instead of s_{sr}/s_s one can assume M_{cr}/M .

The authors propose to use the above formulas to estimate the stiffness of the cross sections of steel fibre reinforced concrete beams. But this requires that the moments of inertia be calculated taking into account the presence of the fibres in the cross section.

2.3. Proposed method of calculating location of neutral axis and moment of inertia of cross section for uncracked beams

In order to calculate the location of the neutral axis and the moment of inertia of any cross section of a steel fibre reinforced concrete beam one needs to know exactly the distribution of fibres in the cross section and their orientation relative to the direction of the load. As shown in [12, 14], if a proper process regime is ensured

during the mixing of the concrete mixture, its laying and compaction, then it can be assumed that the arrangement of the steel fibres in the cross section and along the length of the beam can be described by a *beta* distribution with parameters similar to that of a uniform distribution. Then using any method, e.g. the computer simulation method [12], one can determine: the number of fibres, the total area and the moment of inertia of the fibres relative to the prescribed axis, the distance of a fibre from the prescribed axis, etc., as well as the global averages of the above quantities in each cross section of the beam. Adopting the symbols used in Figure 1a, the moment of inertia of the fibres relative to the neutral axis of a fibre reinforced cross section can be written as:

$$I_y^{\text{fib}} = \sum_j A_{sj}^{\text{fib}} (z_j)^2. \quad (4)$$

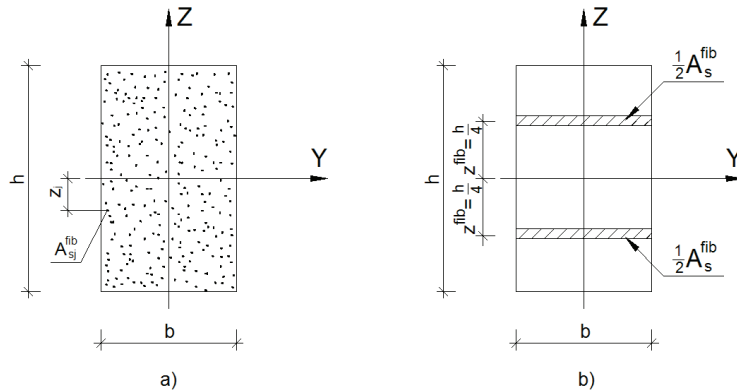


Fig. 1. Distribution of fibres in any cross section of beam:
a) real cross section, b) equivalent cross section

On the basis of a large number of simulations run in [16] it was determined that for the above process conditions the average distance of fibres from the Y-axis is approximately equal to $\frac{1}{4}$ of the beam's height. Therefore it is possible to define equivalent total areas of fibres, lying on both sides of the axis, whose centres of gravity are exactly $\frac{1}{4}$ of the beam's height away from this axis, as shown in Figure 1b. Then equation Equation (4) can be written as:

$$I_y^{\text{fib}} \cong A_s^{\text{fib}} \times (z^{\text{fib}})^2. \quad (5)$$

In formula (5), A_s^{fib} is a total equivalent area of all the fibres in the considered cross section of the beam:

$$A_s^{\text{fib}} \cong \sum_j A_{sj}^{\text{fib}}, \quad (6)$$

and z^{fib} is the distance of the total equivalent fibres area centre of gravity from the principal axis of inertia (Figure 1b).

The equivalent total area of all the fibres in cross section A_s^{fib} and the average distance of the fibres from the prescribed axis can be determined under the following assumptions: (i) the distribution of fibres along the length of the beam is of the *beta* type; (ii) the average number of fibres (n) in each cross section of the beam is known (e.g. from a simulation); (iii) the orientation of the fibres relative to the beam's longitudinal axis (the angle of inclination of each fibre to the considered axis of inertia) is known.

It is apparent from the above assumptions that formula (6) for area A_s^{fib} takes into account the average number of fibres in the cross section whereby the calculated area is larger than the area calculated assuming that the orientation of the fibres is consistent with the longitudinal axis of the beam. The former area must be corrected when the cross section's geometrical characteristics are calculated since the area's ultimate effectiveness as regards bending stiffness depends on: the orientation of the fibres relative to the longitudinal axis, the length of the fibres and their shape and the quality of anchorage. Therefore it is proposed to introduce coefficient b correcting the fibres area assumed for the calculations. For 50 mm long hooked fibres (better anchorage) and their 3D arrangement in concrete it is recommended to assume coefficient $b = 0.8$. In the case of other fibres, the value of this coefficient may be close to unity provided that the fibres are arranged parallel to the beam's longitudinal axis. Whereas when shorter or straight fibres (without hooks at their ends) are used, the value of this coefficient needs to be reduced.

Ultimately formula (3) assumes the form:

$$I_y^{\text{fib}} \equiv \beta \times A_s^{\text{fib}} \times (z^{\text{fib}})^2. \quad (7)$$

The location of the neutral axis and the moment of inertia relative to this axis, taking into account the reinforcement and the fibres, should be calculated using the socalled (previously defined) reduced cross section. The equivalent cross section and the cross section reduced to a double reinforced rectangular beam in performance stage I are shown in Figure 2.

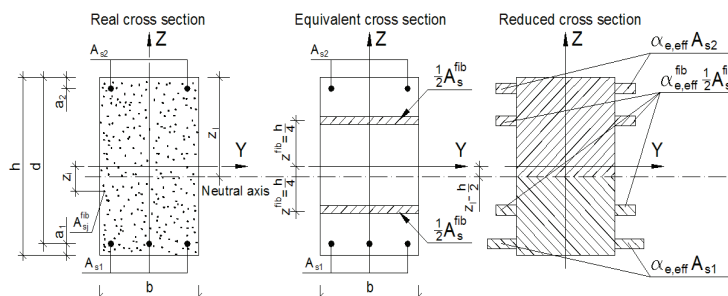


Fig. 2. Equivalent cross section and reduced rectangular cross section in stage II

The location of neutral axis z_I in the cross section can be determined from the equation for the sum of static moments relative to the sought axis:

$$bh\left(z_I - \frac{h}{2}\right) + \alpha_{e,eff} A_{s2}(z_I - a_2) - \alpha_{e,eff} A_{s1}(d - z_I) + \\ + \frac{1}{2}\beta\alpha_{e,eff}^{fib} A_s^{fib}\left(z_I - \frac{h}{4}\right) - \frac{1}{2}\beta\alpha_{e,eff}^{fib} A_s^{fib}\left(\frac{3}{4}h - z_I\right) = 0. \quad (8)$$

The solution of Equation (8) is as follows:

$$z_I = \frac{\frac{bh^2}{2} + \alpha_{e,eff}(A_{s2}a_2 + A_{s1}d) + \frac{1}{2}\beta\alpha_{e,eff}^{fib} A_s^{fib}}{bh + \alpha_{e,eff}(A_{s1} + A_{s2}) + \beta\alpha_{e,eff}^{fib} A_s^{fib}}. \quad (9)$$

On this basis one can determine the cross section's moment of inertia in stage I:

$$J_I = \frac{bh^3}{12} + bh\left(z_I - \frac{h}{2}\right)^2 + \alpha_{e,eff} A_{s2}(z_I - a_2)^2 + \alpha_{e,eff} A_{s1}(d - z_I)^2 + \\ + \frac{1}{2}\beta\alpha_{e,eff}^{fib} A_s^{fib}\left(z_I - \frac{h}{4}\right)^2 + \frac{1}{2}\beta\alpha_{e,eff}^{fib} A_s^{fib}\left(\frac{3}{4}h - z_I\right)^2. \quad (10)$$

In expressions (8), (9) and (10) coefficient $\alpha_{e,eff}$ is given by the formula:

$$\alpha_{e,eff} = \frac{E_s}{E_{c,eff}}, \quad (11)$$

whereas $\alpha_{e,eff}^{fib}$ should be calculated as follows:

$$\alpha_{e,eff}^{fib} = \frac{E_s^{fib}}{E_{c,eff}}. \quad (12)$$

2.4. Stress in concrete and steel in uncracked stage

According to the principles of the theory of linear elasticity, the stress in the outermost fibre in the concrete is

$$\sigma_{c,I} = \frac{M}{J_I} z_I \quad (13)$$

and the stress in the tensioned reinforcement is

$$\sigma_{s,I} = \alpha_{e,eff} \frac{M}{J_I} (d - z_I). \quad (14)$$

2.5. Proposed method of calculating location of neutral axis and moment of inertia of cross section for cracked beams

The calculation of the location of the neutral axis and the moment of inertia for cracked beams is more complicated than for uncracked beams.

In order to calculate the location of the neutral axis and the moment of inertia of any cross section of a steel fibre reinforced concrete beam in cracked stage, it is also necessary (similarly as for uncracked beams) to know the exact distribution of fibres in the cross section and their orientation relative to the direction of the load. On the basis of the uncracked stage assumptions one can define equivalent total fibres areas located on both sides of the axis, whose centres of gravity are at a distance of $\frac{1}{4}$ of the beam's height. However, when a fibres distribution of the *beta* type with its parameters similar to those of a uniform distribution is assumed, then it becomes apparent that the equivalent fibres area above any other axis (Figure 3) is $\frac{z_{II}}{h} A_s^{fib}$ and

the area under this axis is $\frac{(h-z_{II})}{h} A_s^{fib}$, where z_{II} and $(h-z_{II})$ are doubled distances of the centres of gravity of the equivalent fibres areas located respectively above and below the considered axis from this axis.

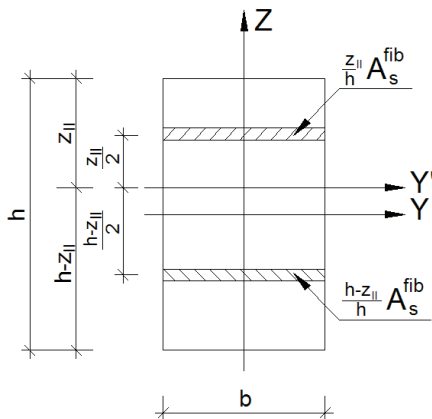


Fig. 3. Location of equivalent fibres areas in any beam cross section relative to any axis

Assuming the symbols used in Figure 3 and coefficient b as in formulas (7) and (10), the moment of inertia of the fibres relative to axis Y' can be written as:

$$I_{y'}^{\text{fib}} \cong \beta \frac{z_{II}}{h} A_s^{\text{fib}} \times \left(\frac{z_{II}}{2} \right)^2 + \beta \frac{h-z_{II}}{h} A_s^{\text{fib}} \times \left(\frac{h-z_{II}}{2} \right)^2. \quad (15)$$

However, it is not always possible to take all the fibres into account when calculating the moment of inertia of a cracked cross section. This depends on the magnitude of the strain in the tensioned zone. Jungwirth and Muttoni [17] showed that in the case of fibre reinforced concrete subjected to unidirectional tension the steel fibres located in a certain area of the tensioned zone still work, increasing the stiffness of the cross section, and the character of their work is similar to that of steel bars. The boundary of the tensioned zone in which steel fibres performance is defined by the maximum strain (experimentally determined to amount to 2.5%). Once the concrete reaches the strain of 2.5%, microcracking ends and a microcrack appears due to the rupture of the fibres or the loss of adhesion between them and the concrete. But the fibres situated in the zone of concrete strains below 2.5% continue to work. In the authors' opinion, this fact should be taken into account in the calculations. However, the problem is how to accurately determine the extent of the zone of tensile strains amounting to 2.5%. It seems that for calculation purposes it is sufficiently accurate to assume that the material is homogenous and so the stresses and strains are linear along the whole height of the beam.

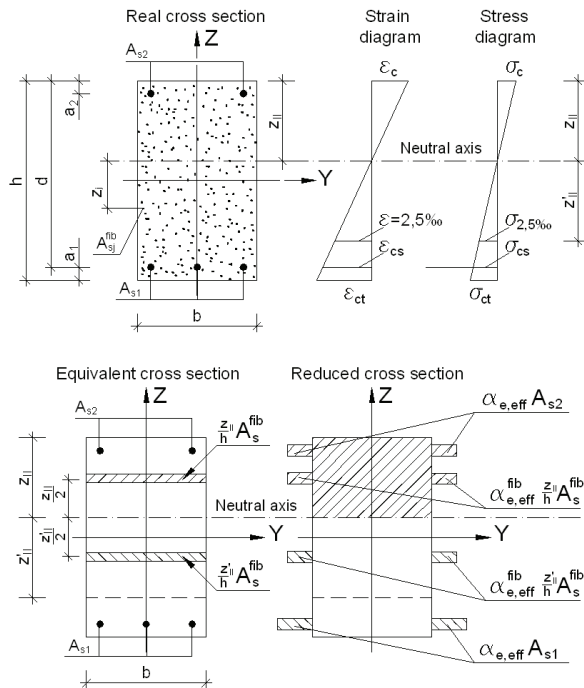


Fig. 4. Equivalent and reduced rectangular cross section in stage II

The location of the neutral axis and the moment of inertia relative to this axis should be calculated using the reduced cross section. It is also necessary to determine distance z'_{II} (Figure 4), i.e. the extent of the zone of tensile stresses lower than or equal to 2.5%. In turn, z'_{II} depends on the strain of the cross section and so it is necessary to introduce a cross-sectional strain parameter. The authors propose to express the strain of the cross section through a real bending moment producing a particular state of stress and strain. The geometrical characteristics of such a reinforced concrete cross section will be determined in accordance with the cracked stage theory while the extent of the uncracked tensioned zone and the area of the fibres in the tensioned zone, affecting the geometrical characteristics of the cross section, will be determined taking into consideration the strain of the cross section, assuming linear changes in stress and strain along the height of the beam.

The equivalent cross section and the reduced cross section for a double reinforced rectangular beam in cracked stage are shown in Figure 4.

In order to determine the geometrical characteristics of the cross section by the proposed method one needs to solve a system of two equations since the sought quantities are mutually implicit (parameter z'_{II} is indirectly expressed through the moment of inertia whose value depends on the sought location of the neutral axis).

First one should determine z'_{II} . Assuming that Hooke's law holds true, the stress in a bar element is expressed as follows:

$$\sigma = E\varepsilon. \quad (16)$$

Substituting stress corresponding to strain 2.5% for s , $e = 2.5\%$ and the effective modulus for E one gets:

$$\sigma_{2.5\%} = E_{c,\text{eff}} 2.5\%. \quad (17)$$

Moreover, it is known that for pure bending the stress in the beam's outermost compressed fibre is expressed by the formula:

$$\sigma_{c,II} = \frac{M}{J_{II}} z_{II}. \quad (18)$$

Hence by substituting the above relations into the equation of a line describing the change in strain one gets:

$$z'_{II} = \frac{\sigma_{2.5\%} J_{II}}{M} = \frac{2.5\% E_{c,\text{eff}} J_{II}}{M}, \quad (19)$$

where $z'_{II} \leq h - z_{II}$.

The location of neutral axis z_{II} in the cross section can be determined from the equation of the sum of static moments relative to the sought axis:

$$\frac{bz_{II}^2}{2} + \alpha_{e,eff} A_{s2}(z_{II} - a_2) - \alpha_{e,eff} A_{s1}(d - z_{II}) + \\ + \frac{\beta\alpha_{e,eff}^{fib} A_s^{fib}}{2h} z_{II}^2 - \frac{\beta\alpha_{e,eff}^{fib} A_s^{fib}}{2h} (z'_{II})^2 = 0. \quad (20)$$

After relation (19) is taken into account and the terms are ordered, Equation (20) assumes the form:

$$\left(\frac{b}{2} + \frac{\beta\alpha_{e,eff}^{fib} A_s^{fib}}{2h} \right) z_{II}^2 + (\alpha_{e,eff} A_{s1} + \alpha_{e,eff} A_{s2}) z_{II} - \\ - \alpha_{e,eff} A_{s1} d - \alpha_{e,eff} A_{s2} a_2 - \frac{\beta\alpha_{e,eff}^{fib} A_s^{fib} (2.5\%)^2 E_{c,eff}^2 J_{II}^2}{2hM^2} = 0. \quad (21)$$

The moment of inertia relative to the sought neutral axis (i.e. taking into account fibres effectiveness coefficient b) can be written as follows:

$$J_{II} = \frac{bz_{II}^3}{12} + bz_{II} \left(\frac{z_{II}}{2} \right)^2 + \alpha_{e,eff} A_{s2} (z_{II} - a_2)^2 + \alpha_{e,eff} A_{s1} (d - z_{II})^2 + \\ + \beta\alpha_{e,eff}^{fib} \frac{z_{II}}{h} A_s^{fib} \left(\frac{z_{II}}{2} \right)^2 + \beta\alpha_{e,eff}^{fib} \frac{z'_{II}}{h} A_s^{fib} \left(\frac{z'_{II}}{2} \right)^2. \quad (22)$$

After relation (19) is taken into account and the terms are ordered relation (22) assumes the form:

$$J_{II} = \frac{bz_{II}^3}{3} + \alpha_{e,eff} A_{s2} (z_{II} - a_2)^2 + \alpha_{e,eff} A_{s1} (d - z_{II})^2 + \\ + \beta\alpha_{e,eff}^{fib} A_s^{fib} \frac{z_{II}^3}{4h} + \beta\alpha_{e,eff}^{fib} A_s^{fib} \frac{(2.5\%)^3 E_{c,eff}^3 J_{II}^3}{4hM^3}. \quad (23)$$

A comparison of expressions (21) and (22) shows that it is necessary to solve the following system of equations:

$$\begin{cases} (21) \\ (23) \end{cases} \quad (24)$$

Equation (21) for the sum of static moments relative to the neutral axis is a quadratic equation and the moment of inertia is expressed by cubic Equation (23). Thus the general solution of system of Equation (24) will be as many as six pairs of numbers, some of which will be expressed in the form of real numbers and some in the form of complex numbers. Therefore one needs to introduce appropriate geometrical conditions (constraints). The conditions can be formulated as follows:

$$\begin{cases} 0 \leq z_{II} \leq h \\ 0 \leq z'_{II} \leq h - z_{II} \\ 0 \leq J_{II} \leq J_I \end{cases} \quad (25)$$

The solution of system of Equations (24) satisfying conditions (25) is this pair of numbers:

$$\begin{cases} (26) \\ (27) \end{cases} \quad (28)$$

Since relations (26) and (27) are complex they were not expanded above. It is optimal to solve such a system in the numerical form.

2.6. Stresses in concrete and steel in cracked stage

According to the principles of the theory of linear elasticity, the stress in the outermost compressed fibre in concrete and the stress in the tensioned reinforcement can be calculated from respectively formula (14) and the following formula:

$$\sigma_{s,II} = \alpha_{e,eff} \frac{M}{J_{II}} (d - z_{II}). \quad (29)$$

2.7. Bending stiffness under short-term load

Immediate stiffness should be calculated taking into consideration average modulus of elasticity E_{cm} of the concrete and the determined moments of inertia J_I and J_{II} . As a result, in all the formulas for long-term stiffness one should substitute α_e , α_e^{fib} and E_{cm} for respectively $\alpha_{e,eff}$, $\alpha_{e,eff}^{\text{fib}}$ and $E_{c,eff}$. Quantities α_e , α_e^{fib} are defined as follows:

$$\alpha_e = \frac{E_s}{E_{cm}}, \quad (30)$$

$$\alpha_e^{\text{fib}} = \frac{E_s^{\text{fib}}}{E_{cm}}. \quad (31)$$

The average modulus of elasticity of the concrete should be determined experimentally or its value should be taken from tables (e.g. from the [13] tables).

Similarly as in the case of long-term loads, immediate stiffness depends on the stage of the element's performance and the suitably defined moment of inertia of the cross section. Hence the formulas for stiffness are as follows: (i) in the uncracked stage (for cross-sectional moment of inertia J_I) – formula (32); (ii) in the cracked stage (for cross-sectional moment of inertia J_{II}) – formula (33).

$$B_I^0 = E_{cm} J_I, \quad (32)$$

$$B_{II}^0 = \frac{E_{cm} J_{II}}{1 - \beta_1 \beta_2 \left(\frac{\sigma_{sr}}{\sigma_s} \right)^2 \left(1 - \frac{J_{II}}{J_I} \right)}, \quad (33)$$

where β_1 , β_2 , σ_s and σ_{sr} as in formula (3). Instead of s_{sr}/s_s one can assume M_{cr}/M .

3. Algorithms for estimating deflections of steel fibre reinforced concrete beams

Below one can find the proposed algorithms for estimating immediate and long-term deflections of steel fibre reinforced concrete beams. The sequence applies to any beam shape but the formulas for geometric characteristics apply to a special case, i.e. the rectangular beam. The other formulas are applicable to any beam shape.

An algorithm for estimating the immediate deflection of steel fibre reinforced concrete beams can be as follows:

- step 1: determine maximum bending moment M ,
- step 2: calculate cracking moment M_{cr} ,
- step 3: check condition $M \leq M_{cr}$; if the condition is fulfilled, the beam is in the uncracked stage (I), if not, it is in the cracked stage (II).

For an **uncracked** beam the further procedure is as follows:

- step 4/I: calculate coefficient α_e from formula (30) and coefficient α_e^{fib} from formula (31),
 - step 5/I: determine location of neutral axis z_I from formula (9) substituting α_e and α_e^{fib} for respectively $\alpha_{e,\text{eff}}$ and $\alpha_{e,\text{eff}}^{\text{fib}}$,
 - step 6/I: calculate reduced cross section moment of inertia J_I from formula (10) substituting α_e and α_e^{fib} for respectively $\alpha_{e,\text{eff}}$ and $\alpha_{e,\text{eff}}^{\text{fib}}$,
 - step 7/I: calculate bending stiffness B_I^0 from formula (32),
 - step 8/I: calculate beam deflection f_I^0 ,
 - end.

For a **cracked** beam ($M > M_{cr}$) the further procedure is as follows:

- step 4/II: calculate coefficient α_e from formula (30) and coefficient α_e^{fib} from formula (31),
- step 5/II: determine the location of neutral axis z_{II} from formula (26), substituting α_e , α_e^{fib} and E_{cm} for respectively $\alpha_{e,\text{eff}}$, $\alpha_{e,\text{eff}}^{\text{fib}}$ and $E_{c,\text{eff}}$,
- step 6/II: calculate reduced cross section moment of inertia J_{II} from formula (27), substituting α_e , α_e^{fib} and E_{cm} for respectively $\alpha_{e,\text{eff}}$, $\alpha_{e,\text{eff}}^{\text{fib}}$ and $E_{c,\text{eff}}$,
- step 7/II: calculate z'_{II} for the determined z_{II} and J_{II} ,
- step 8/II: select z_{II} and J_{II} and z'_{II} satisfying conditions (25); if z'_{II} is greater than $h - z_{II}$, go back to step 5/II and substitute $z'_{II} = h - z_{II}$,
- step 9/II: calculate bending stiffness B_{II}^0 from formula (33),
- step 10/II: calculate beam deflection f_{II}^0 ,
- end.

An algorithm for estimating the long-term deflections of steel fibre reinforced concrete beams can be as follows:

- step 1: determine maximum bending moment M ,
- step 2: calculate cracking moment M_{cr} ,
- step 3: check conditions $M \leq M_{cr}$; if the condition is satisfied, the beam is in uncracked stage (I), if not, is in cracked stage (II).

For an **uncracked** beam the further procedure is as follows:

- step 4/I: calculate the creep coefficient by any method; it is recommended to use Model Code 1990,

- step 5/I: calculate coefficient $\alpha_{e,\text{eff}}$ from formula (11) and $\alpha_{e,\text{eff}}^{\text{fib}}$ from formula (12),
- step 6/I: calculate the location of neutral axis z_I from formula (9),
- step 7/I: calculate reduced cross section moment of inertia J_I from formula (10),
- step 8/I: calculate bending stiffness B_I from formula (2),
- step 9/I: calculate beam deflection f_I ,
- end.

For a **cracked** beam ($M > M_{cr}$) the further procedure is as follows:

- step 4/II: calculate the creep coefficient by any method; it is recommended to use Model Code 1990,

- step 5/II: calculate coefficient $\alpha_{e,\text{eff}}$ from formula (11) and $\alpha_{e,\text{eff}}^{\text{fib}}$ from formula (12),
- step 6/II: determine the location of neutral axis z_{II} from formula (21),
- step 7/II: calculate reduced cross section moment of inertia J_{II} from formula (23),
- step 8/II: calculate z'_{II} for determined z_{II} and J_{II} ,
- step 9/II: select z_{II} and J_{II} and z'_{II} satisfying conditions (25); if z'_{II} is greater than $h - z_{II}$, go back to step 6/II and substitute $z'_{II} = h - z_{II}$,
- step 10/II: calculate bending stiffness B_{II} from formula (3),

- step 11/II: calculate beam deflection f_{II} ,
- end.

When it is necessary to take into account the influence of shrinkage strain on long-term deflection, respectively steps 10/I and 12/II should be added to the algorithm for estimating the long-term deflections in stage I and II. In these steps one should calculate the beam curvature caused by concrete shrinkage from the formula given in [13]. However, as mentioned earlier, the influence of concrete shrinkage strain on long-term beam deflection is generally neglected since the percentage contribution of this strain to the deflection caused by the permanent load and the service load is negligible. This does not apply to composite elements, for which the influence of concrete shrinkage should absolutely be taken into account.

4. Experimental verification of theoretical beam deflections

Theoretical deflections calculated using the above algorithms are presented below against experimental results for fibre reinforced concrete beams A1-A3, B1-B3 and C1-C3. The beams were 3300 mm long and had a 150×250 mm rectangular cross section (Figure 5). The longitudinal reinforcement was in the form of four Ø8 mm bars made of steel 18G2. The lateral reinforcement had the form of Ø6 mm stirrups made of steel St3SX. In the A4, B4 and C4 beams cause the lower longitudinal reinforcement was in the form of four Ø14 mm bars made of steel RB500; other reinforcement was the same as for beams A1-A3, B1-B3 and C1-C3.

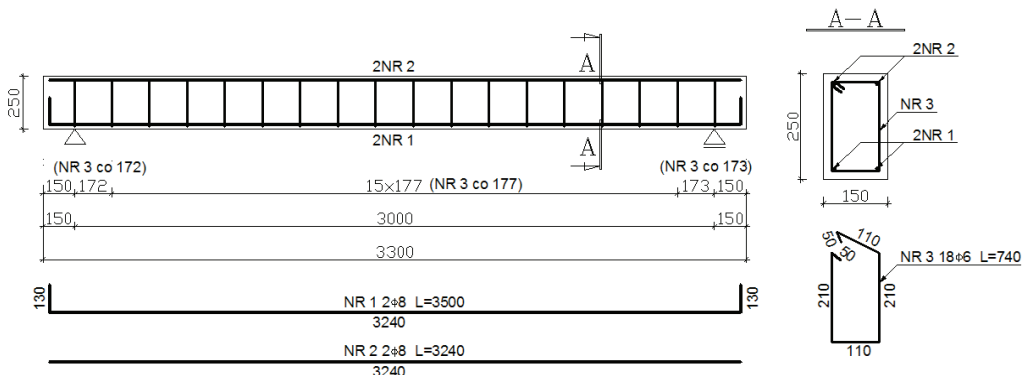


Fig. 5. Reinforcement of the beams

Three series of the beams with a different content of 50 mm long, 0.8 mm in diameter hooked fibres were tested. The content amounted to: 25 kg/m³ for series A, 35 kg/m³ for series B and 50 kg/m³ for series C. Four beams were tested in each series. The average compressive strength of the fibre reinforced concrete was: 47.11 MPa for series A, 40.37 MPa for series B and 42.10 MPa for series C.

Figure 6 shows the static scheme of the beams.

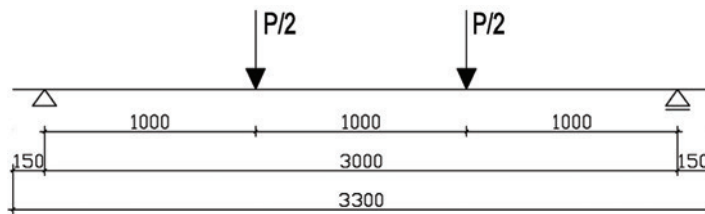


Fig. 6. The static scheme of the beams

The load level of the beams is shown in the Table 1. The beams A1, B1, C1, B4 and C4 worked in uncracked stage whereas the others worked in cracked stage.

Table 1. The load level of the beams

Beam	Load level P , kN
A1, B1, C1	6.22
B4, C4	12.02
A3, B2, C2	14.00
A2, B3, C3	16.98
A4	52.00

The theoretical deflections of the beams were calculated using the experimental averages of the strength and deformation characteristics of the concrete and the steel. The calculation procedure was written in a spreadsheet.

Also experimentally determined creep coefficient values [16] were taken into account in the calculations of the long-term deflections of the beams.

Figure 7 shows the theoretical and experimental total deflections of beams: A1, B1, C1, A4, B4 and C4.

Figure 8 shows the total deflections of beams: A2, A3, B2, B3, C2 and C3.

A comparison of the curves illustrating the increase in deflection over time, calculated by the proposed method, and the experimental curves shows that the proposed calculation method well approximates the real increase in the immediate and long-term deflections of the beams.

5. Conclusion

A method of calculating the location of the neutral axis of a rectangular steel fibre reinforced concrete cross section before and after cracking and the cross section's moments of inertia relative to this axis, taking into account the performance of the steel fibres after the cracking of the cross section in a tensile strain zone bounded by the strain of 2.5%, was proposed.

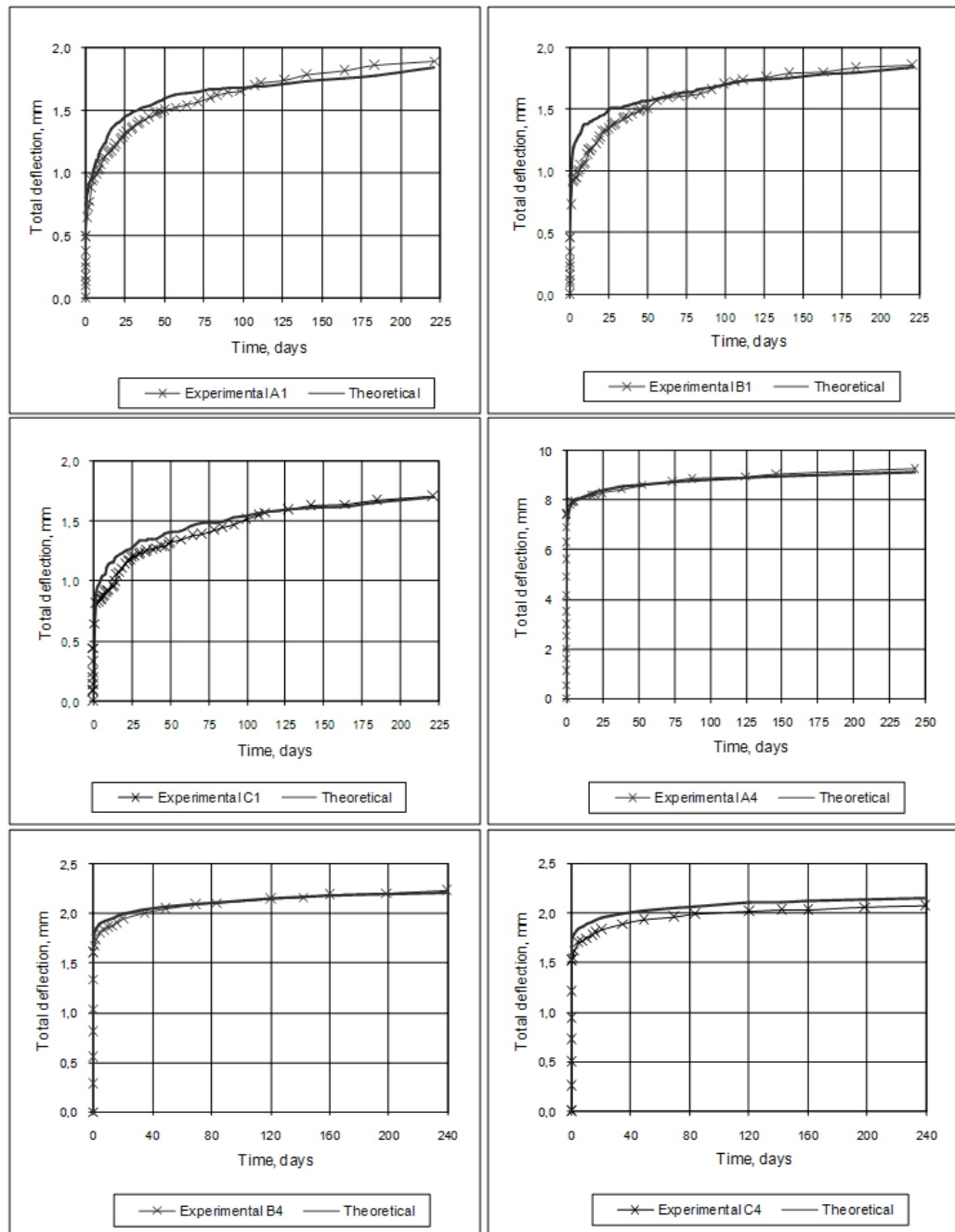


Fig. 7. Increase in total theoretical and experimental deflections for beams A1, B1, C1, A4, B4 and C4

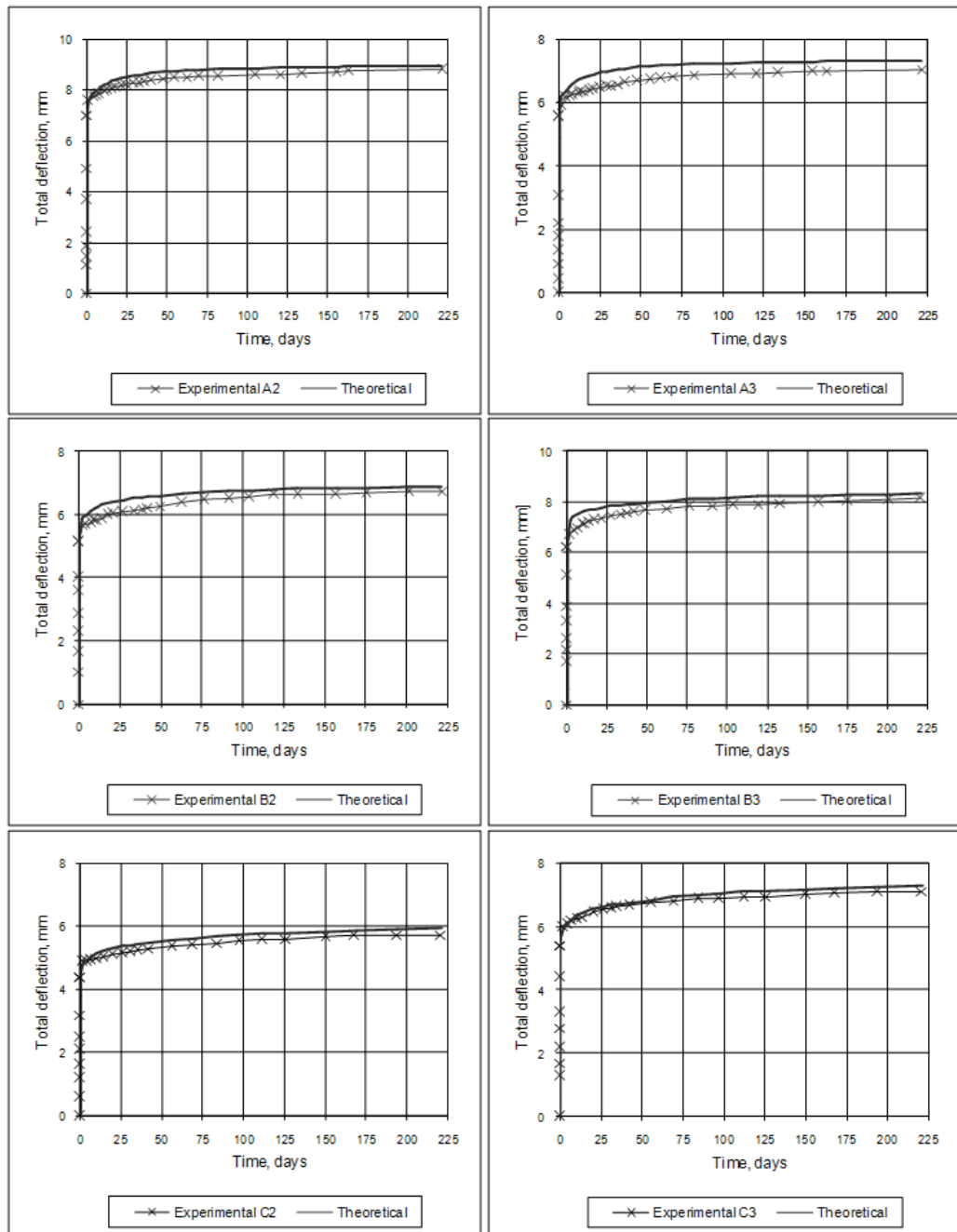


Fig. 8. Increase in total theoretical and experimental deflections for beams: A2, A3, B2, B3, C2 and C3

In the authors' opinion the most significant is the fact that the method of calculating the geometrical characteristics of the cross section for both the cracked and uncracked stage is based on the model of fibres distribution along the length of the beam. Consequently, two algorithms for estimating the immediate and long-term deflections of steel fibre reinforced concrete beams were proposed: one for uncracked beams and the other for cracked beams. The algorithms have been positively experimentally verified which is illustrated in the figures above. The verification has proved the proposed algorithms to be suitable for estimating the immediate and long-term deflections of uncracked and cracked steel fibre reinforce concrete beams.

References

- [1] Szechiński M.: *Long-term deflections of reinforced concrete beams under load* (in Polish), Wrocław University of Technology Publishing House, Wrocław, 2000.
- [2] Szechiński M.: *Deformations of reinforced concrete beams under long-term bending load* (in Polish), Wrocław University of Technology Publishing House, Wrocław, 1996.
- [3] Branson D.E., Shiah A.F.: *Deflections of concrete structures*, ACI SP-86, Detroit, 1986.
- [4] Branson D.E., Kripnarayanan K.M.: *Some experimental studies of time dependent deflections of noncomposite and composite reinforced concrete beams*, ACI SP-4316, Detroit, 1976.
- [5] Branson D.E.: *Deformation of concrete structures*, McGraw Hill Co., New York, 1977.
- [6] Ezeldin A.S., Shiah T.W.: *Analytical immediate and long-term deflections of fibre-reinforced concrete beams*, Journal of Structural Engineering, Vol. 121, No. 4, 1995, pp. 727–738.
- [7] Balaguru P.N., Ezeldin A.S.: *Normal and high strength fibre reinforced concrete. Fibre reinforced concrete under compression*, Journal of Materials in Civil Engineering, ASCE, Vol. 4, No. 4, 1992, pp. 415–429.
- [8] Balaguru P.N., Ramakrishnan V.: *Properties of fibre reinforced concrete: workability behaviour under long term loading and air-void characteristics*, ACI Materials Journal, Vol. 85, No. 3, 1988, pp. 189–196.
- [9] Grzybowski M., Shah S.P.: *Shrinkage cracking in fibre reinforced concrete*, ACI Materials Journal, Vol. 87, No. 2, 1990, pp. 138–148.
- [10] ACI Committee 209: *Prediction of creep, shrinkage and temperature effects in concrete structures*, ACI Publication SP-76, American Concrete Institute, Detroit, 1982.
- [11] Kamiński M., Trapko T., Balbus L., Bywalski C.: *Model of steel fibres distribution along length of steel fibre reinforced concrete beams* (in Polish), Materiały Budowlane, No. 9, 2006, pp. 8–9, 60.
- [12] Kamiński M., Bywalski C.: *Analysis of long steel fibre distribution in fibre reinforced concrete beams*, Modern building materials, structures and techniques: The 10th International Conference: selected paper, Lithuania, Vilnius, Vol. 1, 2010, pp. 117–124.
- [13] ENV 1992-1-1:2008 – Eurocode 2, Design of Concrete Structures, Part 1–1, General Rules and Rules for Buildings, CEN, 2008.
- [14] Kamiński M., Bywalski C.: *Influence of creep deformations on value of long term deflections of steel fibre-reinforced concrete beams*, Proceedings 8th International

- Conference on Creep, Shrinkage and Durability of Concrete and Concrete Structures, Japan, Ise-Shima, Vol. 1, 2008, pp. 729–734.
- [15] Bulletin d'Information, No. 199; *Evaluation of the time dependent behaviour of concrete*, CEB, France, Paris, 1990.
- [16] Bywalski C.: *Long-term deflections of steel fibre reinforced concrete beams*, PhD dissertation, Series PRE 2/2009, Report of the Institute of Building Engineering at Wrocław University of Technology, Poland, Wrocław, 2009.
- [17] Jungwirth J., Muttoni A.: *Structural behaviour of tension members in UHPC*, International Symposium on Ultra High Performance Concrete, Germany, Kassel, 2004, pp. 533–545.

Szacowanie sztywności giętnej prostokątnych, żelbetowych belek wykonanych z betonu modyfikowanego włóknami stalowymi

W pracy zaproponowany został sposób obliczania położenia osi obojętnej prostokątnego przekroju fibrobetonowego przed i po zarysowaniu oraz momentów bezwładności przekroju względem tych osi. Ponadto sposób obliczania cech geometrycznych przekroju dla fazy zarówno zarysowanej, jak i niezarysowanej bazuje na modelu rozkładu włókien na długości elementu belkowego. W konsekwencji zaproponowano dwa algorytmy do szacowania ugięć doraźnych i długotrwałych belek fibrobetonowych, z których jeden dotyczy belek niezarysowanych, a drugi zarysowanych. Algorytmy te zostały pozytywnie zweryfikowane doświadczalnie.

Equalization of the transport velocity in a new two-way vibratory conveyer

P. CZUBAK

AGH University of Science and Technology, al. Mickiewicza 30, 30-059 Cracow, Poland.

Vibratory conveyers that enable material transportation in two opposite directions are often included in a production sequence, however they have various faults and shortages. This situation prompted the author to design the new, two-way vibratory conveyer (Patent Application [4]) characterised by a high efficiency and a fast changing of the transportation direction. The dynamic analysis of the conveyer is presented and the possibility of changing the transportation direction only by changing the vibrator rotational frequency – is indicated in the paper.

Keywords: *two-way vibratory conveyer, feed transport, loose feed model*

1. Introduction

Vibratory conveyers enabling a feed transportation in two directions are often applied in a production sequence [1–2, 12–16]. Transport qualities of the new two-way vibratory conveyer [4] for transporting loose materials or objects of small dimensions were analysed in this study. The problem of uneven transport velocity in the opposing directions was investigated and the method of equalization of these velocities was developed.

2. Different solutions of a two-way vibratory conveyer

Different types of two-way conveyers are currently produced. The solution most often applied is a device with two separate systems of vibrators [2, 12]. The exemplary conveyer of this type constitutes the system produced by the German Company Jost (Figure 1).

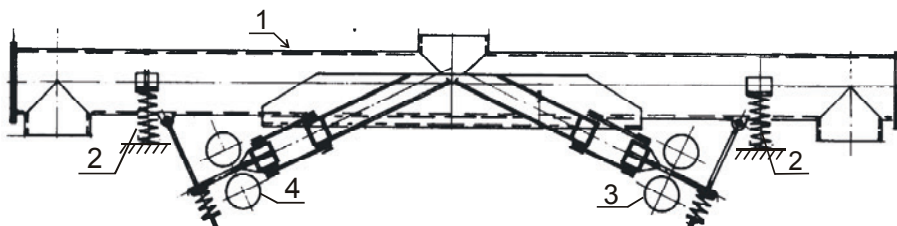


Fig. 1. Two-way conveyer of the Jost Company

Electric motors drive two shafts with the attached to them unbalanced mass, which is forcing vibrations oriented perpendicularly to the line passing via the vibrators axes (3–4) and inclined at a certain angle to the conveyer trough (1) suspended on a system of springs (2). One or the other vibrator system is alternatively switched on depending on the required transportation direction. Conveyers with two systems of vibrators are characterised by a high yield, similar to conveyers which transport material in one direction only, however they are costly both in the production and exploitation processes. The working vibrations of one system of vibrators cause grease squeezing in bearings in the other one, not working at the moment. The false Brinell's imprints occur, which in turn are the reason of a very fast wear of the whole system. The fault of this type of solution is a long time needed for changing the transport direction. This time is related to a rundown time of one system of vibrators and a starting time of the second system [3]. Another fault of this type of structure is transferring significant forces on the foundation. Decreasing of these forces requires the installation of the vibro-insulating frame [5].

Two-way vibratory conveyers having only one vibrator are also known, e.g. from the description of the US5713457 patent [13]. The vibrator (3) of such conveyer is hanging centrally – in the vicinity of the centre of gravity of the conveyer – from the trough (1), which is suspended on the spring system (3) (Figure 2).

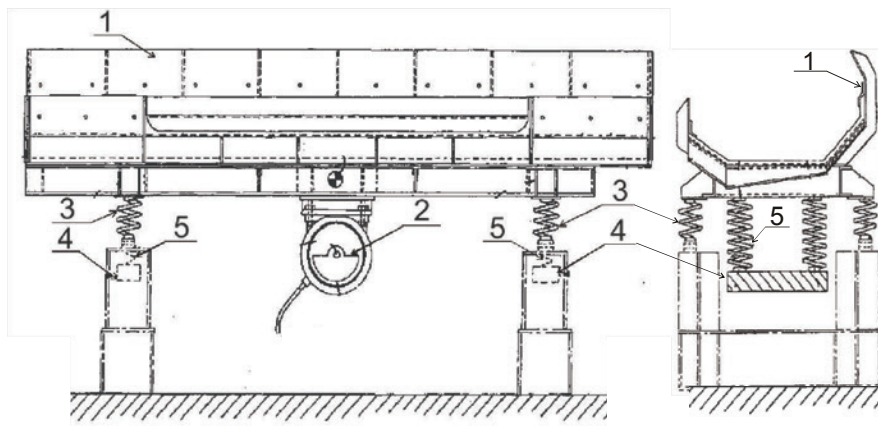


Fig. 2. Two-way vibratory conveyer according to the patent: US5713457

The vibrator (2) is equipped with a motor of variable directions of rotations. Identical vibration eliminators are mounted on both ends of the trough causing a flattening of a vibration ellipse of the main mass (1), at the frequency of exciting vibrations being close to the natural frequencies of eliminators. Each eliminator has a mass (4) suspended perpendicularly from the trough on a spring (5). The negative side of this type of solution is also a long time needed for changing the transport direction, since this is done by changing the direction of the motor rotations, and requires at first the passing

via a rundown and then via a transient resonance. In addition, elliptical trajectories of a vibrating motion of the trough significantly limit the conveyor yield.

Another group constitute conveyers with a mechanical (3) changing of the transport direction done either by a manual or by an automatic change of a suspension angle of the driving vibrators system (4). This causes a change of the vibration direction of the trough (1) suspended on the spring system (2). As an example of such solution, the conveyer produced by the Carrier Vibrating Equipment Company (US 5.064.053 patent) [1] is shown in Figure 3.

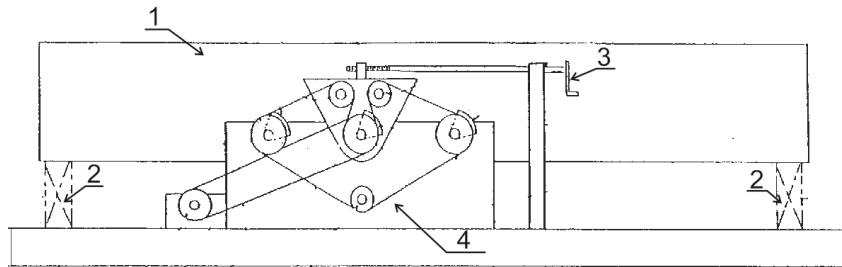


Fig. 3. Two-way vibratory conveyer, according to the US 5064053 patent

3. Principle of operation of the conveyer according to the invention

The newly invented conveyer (Patent Application No P-388654) [4], in a similar fashion as in the described above solutions, has the trough open on both sides and elastically supported on a stiff base, while the rotational vibratory drive is centrally attached to the trough (Figure 4). The main purpose of the invention is the development of the new, improved two-way feeder or conveyer, in which the transport direction can be changed very fast by changing the frequency of vibrator rotations only.

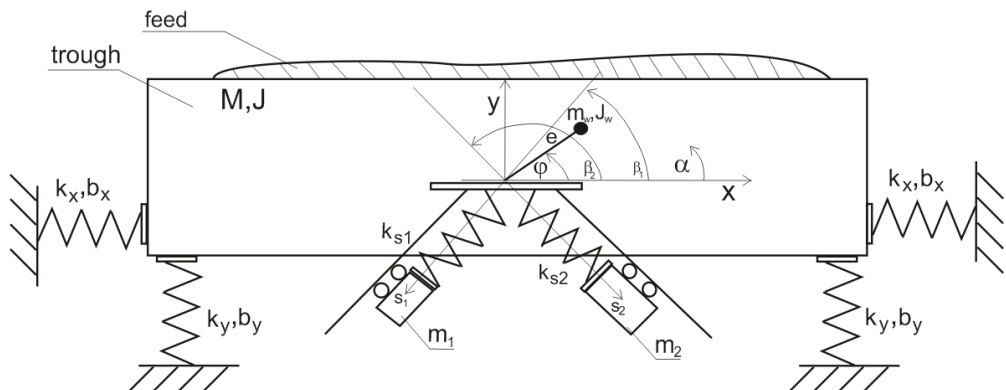


Fig. 4. Two-way vibratory conveyer, according to the invention

The principle of operation of the new conveyer is as follows: when the excitation frequency of the vibrator in a steady state meets a condition: $\omega = \sqrt{\frac{k_1}{m_1}}$, mass m_1 vibrates with the amplitude which triggers – in element k_1 – counter-forces to the vibrator excitation force in the direction s_1 thus causing – at small damping in spring k_1 – an extinction of the trough vibrations in this direction while not changing vibrations in the perpendicular direction s_2 , in accordance with the Frahm's eliminator principle [6–7]. This enables the feed transportation to the right.

When the excitation frequency of the vibrator in a steady state meets a condition: $\omega = \sqrt{\frac{k_2}{m_2}}$, mass m_2 vibrates with the amplitude which triggers – in element k_2 – counter-forces to the vibrator excitation force in the direction s_2 thus causing an extinction of the trough vibrations in this direction, but not changing vibrations in the perpendicular direction s_1 . This enables the feed transportation to the left.

The conveyer can be equipped with two or more eliminators of vibrations mounted to the trough from each side of the shaft.

The proposed solution allows performing fast changes of the transportation direction solely by changing the rotational velocity of the vibrator motor. The achieved vibrations of the trough are of a nearly rectilinear character – which means that the yield of the transportation is similar to the one of the unidirectional conveyer. If the motor with the infinitely variable adjustment of the rotational velocity is applied in the vibrator, there will be the possibility of controlling the material transport velocity in both directions.

An increase of the rotational velocity as well as an increase of the amplitude are increasing the material transport velocity that's why the conveyer transport yield is not the same in both directions, when the vibration directions of masses of additional eliminators are deflected from the horizontal line at an angles: $\beta_1 = 45^\circ$, $\beta_2 = 135^\circ$.

An equal transport velocity in both directions can be obtained due to:

- proper control of the motor angular velocity,
- change of the mounting angle α of the eliminators system,
- inclining of the conveyer trough,
- application of the vibrator of a variable eccentric of an unbalanced mass.

4. Simulation analysis

The possibility of equalising the transport velocity by the application of the vibrator of a variable eccentric of an unbalanced mass – is analysed in the hereby paper. The model of the system assumed for the computer simulation taking into account periodical collisions of the body with a material feed [10–11] is shown in Figure 5.

The model consists of the inertial vibrator of a variable eccentric of an unbalanced mass and the independent inductive drive (described by a static characteristics) of the machine body performing the plane motion and supported on the system of vertical

coil springs, and of five four-layered models of a loose feed [8–9] distributed in various places on the machine working surface.

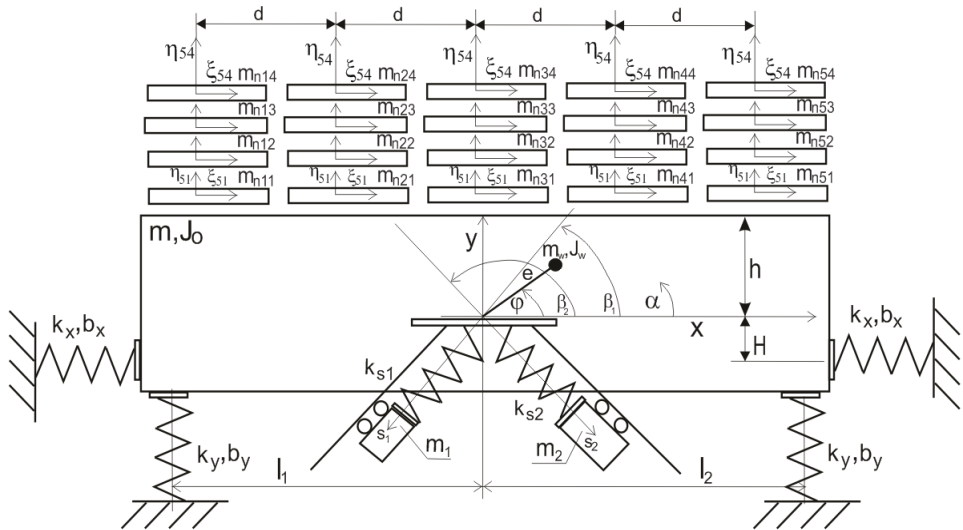


Fig. 5. Model of the feeder with a feed

The mathematical model of such system consists of the matrix Equation (1) describing the machine motion, Equations (8) concerning electromagnetic moments of driving motors, Equations (7) used for the determination of the motion of the successive feed layers as well as of dependencies (5), (6) determining normal and tangent interactions between the feed layers and between the feed and the machine body.

$$M \cdot \ddot{q} = Q, \quad (1)$$

where:

$$M = \begin{bmatrix} m + m_w + m_1 + m_2 & 0 & 0 & m_w e \sin(\varphi) & m_1 \cos(\beta_1) & m_2 \cos(\beta_2) \\ 0 & m + m_w + m_1 + m_2 & 0 & m_w e \cos(\varphi) & m_1 \sin(\beta_1) & m_2 \sin(\beta_2) \\ 0 & 0 & J_0 & 0 & 0 & 0 \\ m_w e \sin(\varphi) & m_w e \cos(\varphi) & 0 & m_w e^2 + J_w & 0 & 0 \\ m_1 \cos(\beta_1) & m_1 \sin(\beta_1) & 0 & 0 & m_1 & 0 \\ m_2 \cos(\beta_2) & m_2 \sin(\beta_2) & 0 & 0 & 0 & m_2 \end{bmatrix} \quad (2)$$

$$\ddot{q} = [\ddot{x} \ \ddot{y} \ \ddot{\alpha} \ \ddot{\varphi} \ \ddot{s}_1 \ \ddot{s}_2]^T \quad (3)$$

$$Q = \begin{bmatrix} -m_w e \dot{\varphi}^2 \cos(\varphi) - 2k_x(x + H\alpha) - 2b_x(\dot{x} + H\dot{\alpha}) - T_{101} - T_{102} - T_{103} - T_{104} - T_{105} \\ m_w e \dot{\varphi}^2 \sin(\varphi) - k_y(y + l_1\alpha) - k_y(y - l_2\alpha) - b_y(\dot{y} + l_1\dot{\alpha}) - b_y(\dot{y} - l_2\dot{\alpha}) - F_{101} - F_{102} - F_{103} - F_{104} - F_{105} \\ -2k_x H^2 \alpha - 2k_x Hx - 2b_x H\dot{x} - 2b_x H^2 \dot{\alpha} - k_y(y + l_1\alpha)l_1 + k_y(y - l_2\alpha)l_2 - b_y(\dot{y} + l_1\dot{\alpha})l_1 + b_y(\dot{y} - l_2\dot{\alpha})l_2 + \\ +(T_{101} + T_{102} + T_{103} + T_{104} + T_{105})h + F_{101}2d + F_{102}d - F_{104}d - F_{105}2d \\ M_{ell} \\ -k_{s1}s_1 - b_{s1}\dot{s}_1 \\ -k_{s2}s_2 - b_{s2}\dot{s}_2 \end{bmatrix} \quad (4)$$

where:

$F_{j,j-1,k}$ – normal component of the j^{th} layer pressure on $j-1$ in the k^{th} column,

$T_{j,j-1,k}$ – tangent component of the j^{th} layer pressure on $j-1$ in the k^{th} column,

j – indicator of the material layer, $j = 0$ concerns the machine body,

k – indicator of the column of the material layer.

If the successive feed layers j and $j-1$ (in the given column) are not in contact with each other, then the contact force in the normal $F_{j,j-1,k}$ and tangent $T_{j,j-1,k}$ direction in between these layers equals zero:

$$F_{j,j-1,k} = 0, \quad T_{j,j-1,k} = 0 \quad \text{for } \eta_{j,k} \geq \eta_{j-1,k}.$$

Otherwise, the contact force occurs in the normal direction between j, k and $j-1, k$ feed layers (or in the case of the first layer and the trough). Model of this force is as follows:

$$F_{j,j-1,k} = (\eta_{j-1,k} - \eta_{j,k})^p \cdot k \cdot \left\{ 1 - \frac{1-R^2}{2} [1 - \text{sgn}(\eta_{j-1,k} - \eta_{j,k}) \cdot \text{sgn}(\dot{\eta}_{j-1,k} - \dot{\eta}_{j,k})] \right\}. \quad (5)$$

Force in the tangent direction, originated from friction:

$$T_{j,j-1,k} = -\mu F_{j,j-1,k} \text{sgn}(\dot{\xi}_{j,k} - \dot{\xi}_{j-1,k}), \quad (6)$$

where:

k and p – Herz–Sztajerman constants,

R – coefficient of restitution of normal impulses at collision,

μ – friction coefficient.

Equations of motion in directions ξ and η of the individual feed layers, with taking into account conveyer interactions with the lower feed layers, are of the form:

$$\begin{aligned} m_{nj,k} \ddot{\xi} &= T_{j,j-1,k} - T_{j+1,j,k}, \\ m_{nj,k} \ddot{\eta} &= -m_{nj,k} g + F_{j,j-1,k} - F_{j+1,j,k}, \end{aligned} \quad (7)$$

M_{eli} – electromagnetic moment developed by the i^{th} motor, assumed in the form corresponding to the static characteristics of the motor:

$$M_{\text{eli}} = \frac{2M_{ut}(\omega_{ss} - \dot{\phi}_{il}) \cdot (\omega_{ss} - \omega_{ut})}{(\omega_{ss} - \omega_{ut})^2 + (\omega_{ss} - \dot{\phi}_i)^2}, \quad i=1, 2 \quad (8)$$

where:

M_{ut} – stalling torque of driving motors,

ω_{ss} – synchronous frequency of driving motors,

ω_{ut} – frequency of stall of driving motors.

The simulation was performed for the following parameters value:

$l_1 = l_2 = 0.5 \text{ m}$,

$h = 0 \text{ m}$,

$H = 0 \text{ m}$,

$b_x = b_y = 50 \text{ Ns/m}$,

$k_x = k_y = 75000 \text{ N/m}$,

$b_{s1} = 60 \text{ Ns/m}$,

$b_{s2} = 50 \text{ Ns/m}$,

$k_{s1} = 444132 \text{ N/m}$,

$k_{s2} = 320885 \text{ N/m}$,

$m_1 = m_2 = 18 \text{ kg}$,

$m = 120 \text{ kg}$,

$m_w = 5 \text{ kg}$,

$J_w = 0 \text{ kgm}^2$,

$J_0 = 25 \text{ kgm}^2$,

$\beta_1 = 45^\circ$,

$\beta_2 = 135^\circ$,

$R = 0.05$,

$\mu = 0.4$,

$p = 1$,

$k = 10^8 \text{ N/m}$,

$e = \text{variable m}$,

$m_{ut} = 50 \text{ Nm}$,

ω_{ss} = variable rad/s,

ω_{ut} = variable rad/s.

The simulation model developed for the verification of the analytical solutions takes into account the influence of the machine body collisions with the feed as well as allows determining the material transport velocity in both directions.

The dependence of the horizontal vibrations on the vertical ones at two different excitation frequencies for which eliminators – m_1 and m_2 (Figure 5) – were tuned, at preserving the same eccentric of the vibrator mass, are presented in Figures 6 and 9. It can be seen, that the vibrations of the conveyor frame are the proper ones (depending on the excitation frequency they are inclined either into the left or into the right direction) but the vibration amplitudes are different, what at various excitation frequencies causes large differences in the material transport velocity in opposite directions (Figures 7 and 10). Such large differences result also from the fact that the coefficient of throw in the case of the lower excitation frequency is less than unity, causing the lack of the material throw (Figure 11).

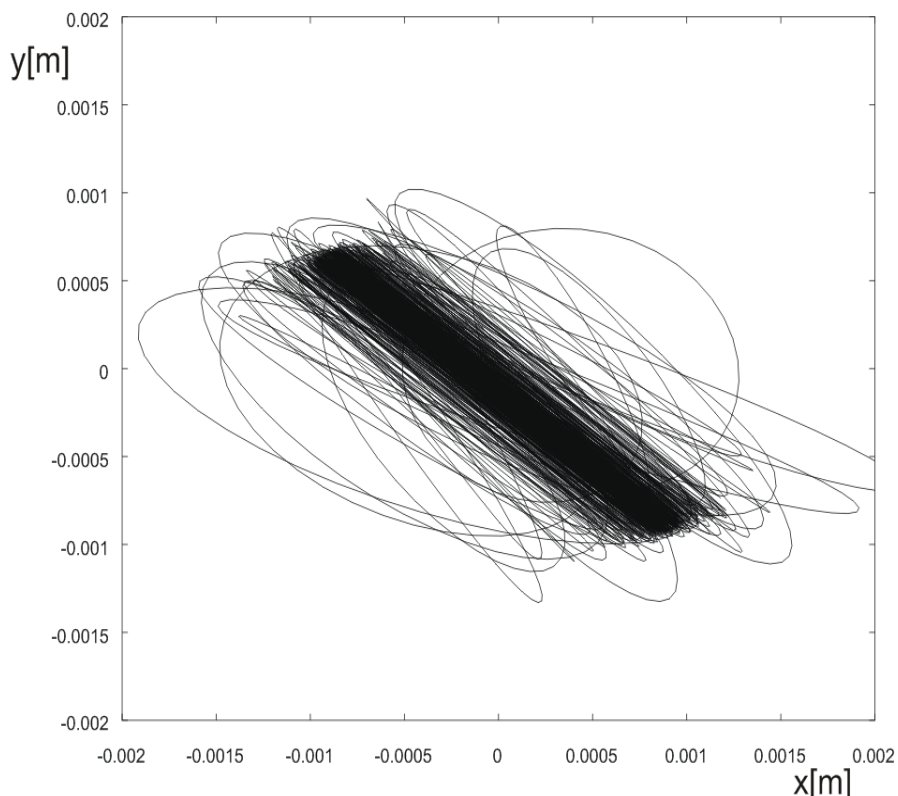


Fig. 6. Dependence of the horizontal vibrations on the vertical ones, at the excitation frequency: $\omega = 157$ rad/s and the vibrator mass eccentric: $e = 0.0215$ m

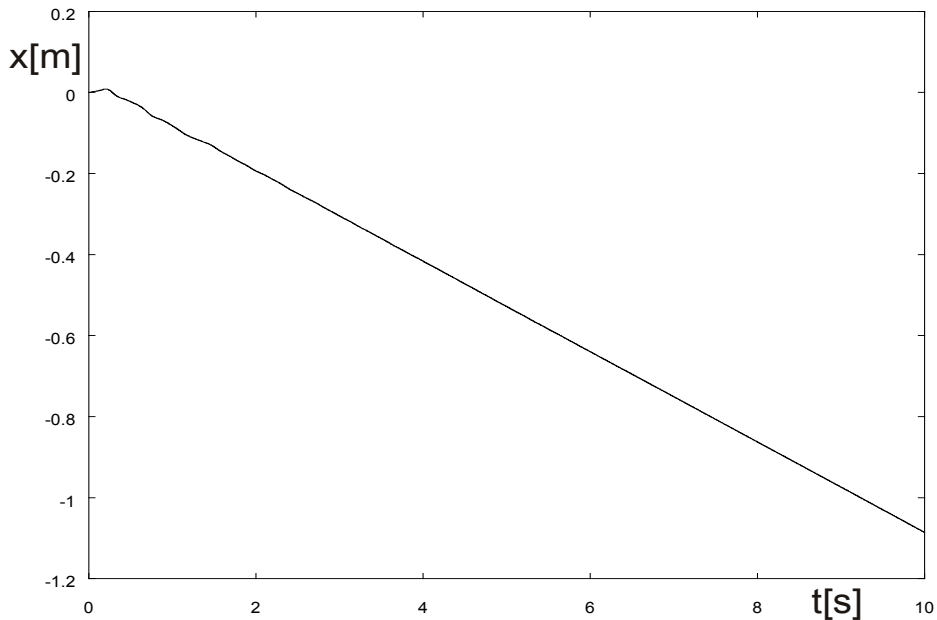


Fig. 7. Feed displacement in the horizontal direction, at the excitation frequency:
 $\omega = 157$ rad/s and the vibrator mass eccentric: $e = 0.0215$ m

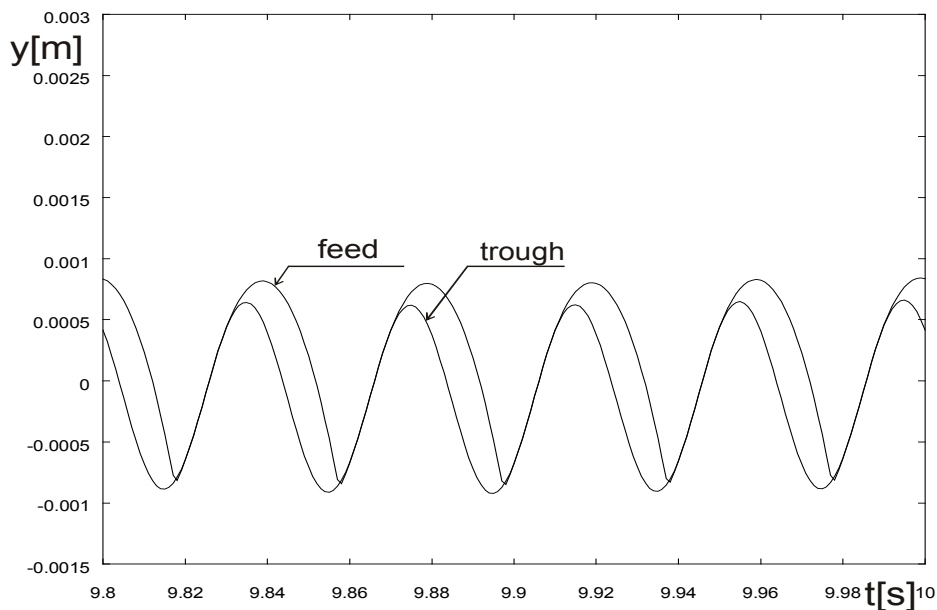


Fig. 8. Displacement of the trough and the feed in the vertical direction, at the excitation frequency:
 $\omega = 157$ rad/s and the vibrator mass eccentric: $e = 0.0215$ m

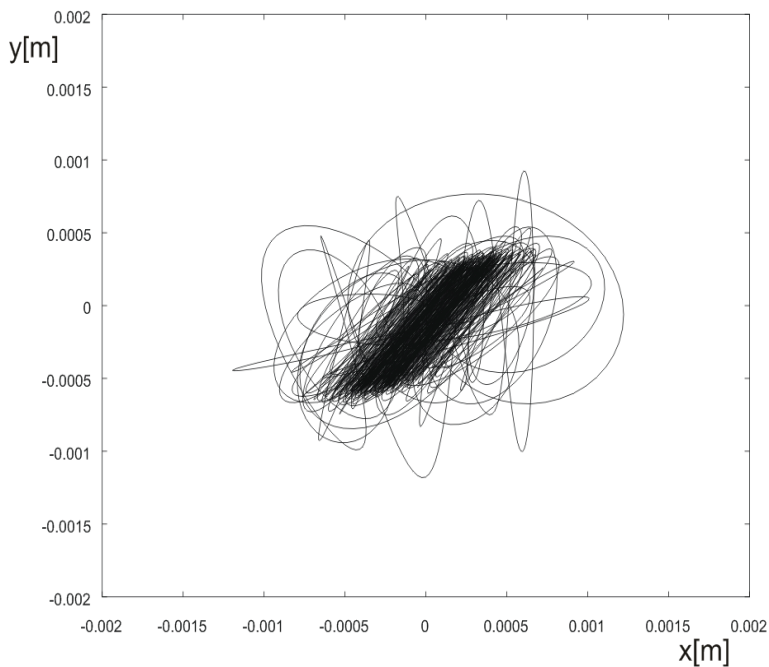


Fig. 9. Dependence of the horizontal vibrations on the vertical ones, at the excitation frequency:
 $\omega = 133.5 \text{ rad/s}$ and the vibrator mass eccentric: $e = 0.0215 \text{ m}$

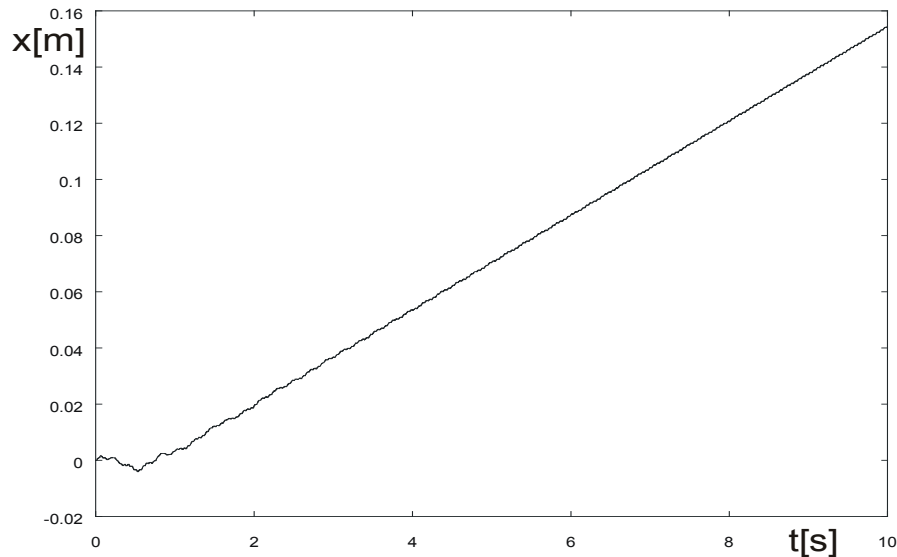


Fig. 10. Feed displacement in the horizontal direction, at the excitation frequency:
 $\omega = 133.5 \text{ rad/s}$ and the vibrator mass eccentric: $e = 0.0215 \text{ m}$

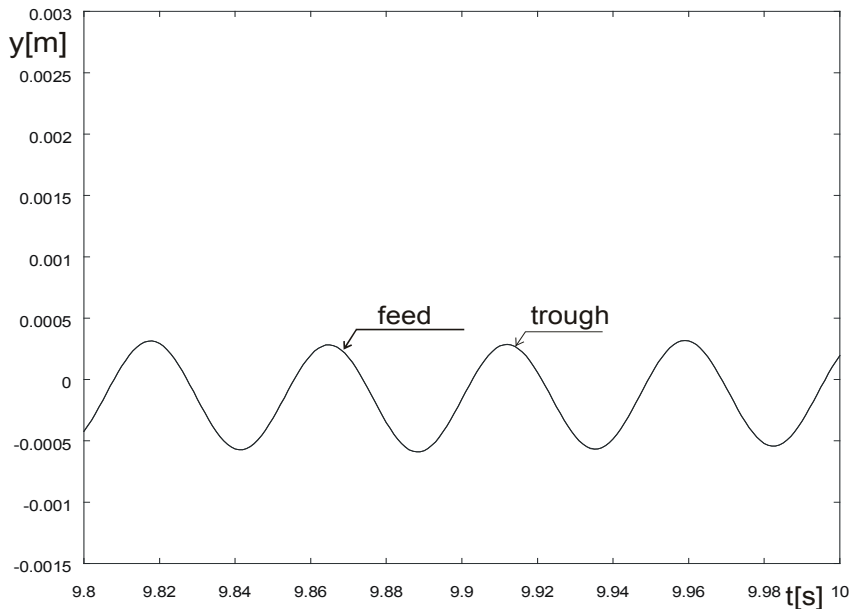


Fig. 11. Displacement of the trough and the feed in the vertical direction, at the excitation frequency: $\omega = 133.5 \text{ rad/s}$ and the vibrator mass eccentric: $e = 0.0215 \text{ m}$

5. Equalization of the transport velocity

An application of the vibrator of the variable excitation force for the two-way conveyer drive is proposed in the presented paper. The vibrator should provide the larger excitation force at the lower frequency and the smaller force at the higher frequency. There are several solutions of these types of vibrators. From a group of externally controlled vibrators to such, in which a part of the mass changes its position and this in turn changes the centrifugal force due to different vibration frequencies.

Such system provides the possibility of equalizing the transport velocity in both directions. The vibrator, which at the higher frequency had the same eccentric as at the previous simulations, was applied in the system (giving identical results as shown in Figures 6–8). At the lower excitation frequency the eccentric was four times larger, which caused the increased amplitude of vibrations of the conveyer trough (Figure 12) and – related to it – the increased transport velocity (Figure 13). The conveyer of the parameters given above at this frequency and the larger eccentric still operates in the single-stroke mode (Figure 14).

Thus it can be seen, that when the vibrator of the variable eccentric of the unbalanced mass is applied, the same transport velocities can be obtained in both directions. However, in the case when there is no need of the transport velocity equalization, the standard vibrator of the constant unbalancing can be used for designing of this type of the conveyer, which would significantly lower the production costs of the device.

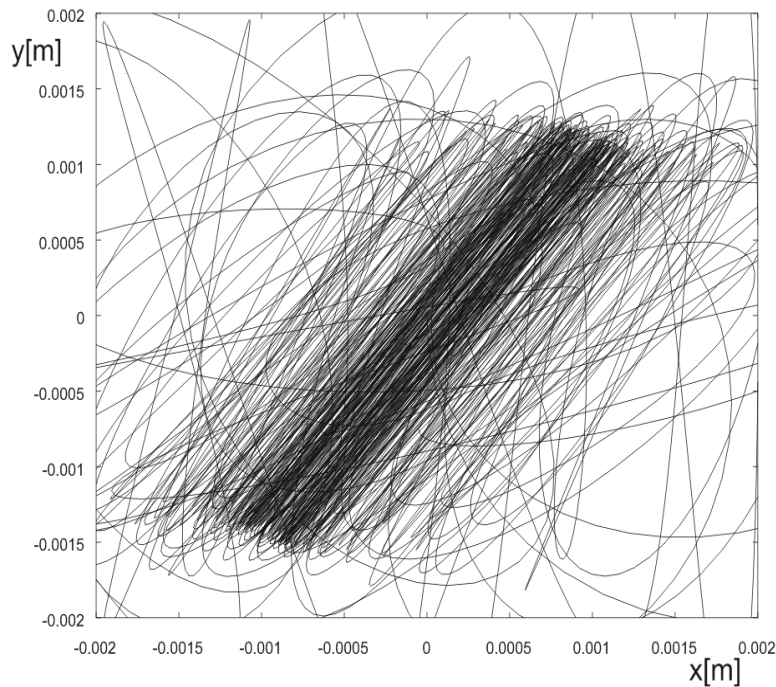


Fig. 12. Dependence of the horizontal vibrations on the vertical ones, at the excitation frequency:
 $\omega = 133.5 \text{ rad/s}$ and the vibrator mass eccentric: $e = 0.086 \text{ m}$

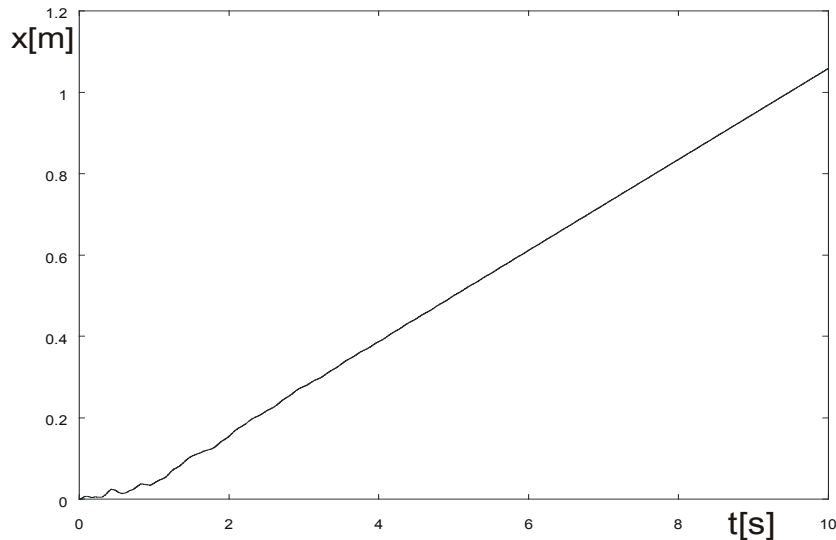


Fig. 13. Feed displacement in the horizontal direction, at the excitation frequency:
 $\omega = 133.5 \text{ rad/s}$ and the vibrator mass eccentric: $e = 0.086 \text{ m}$

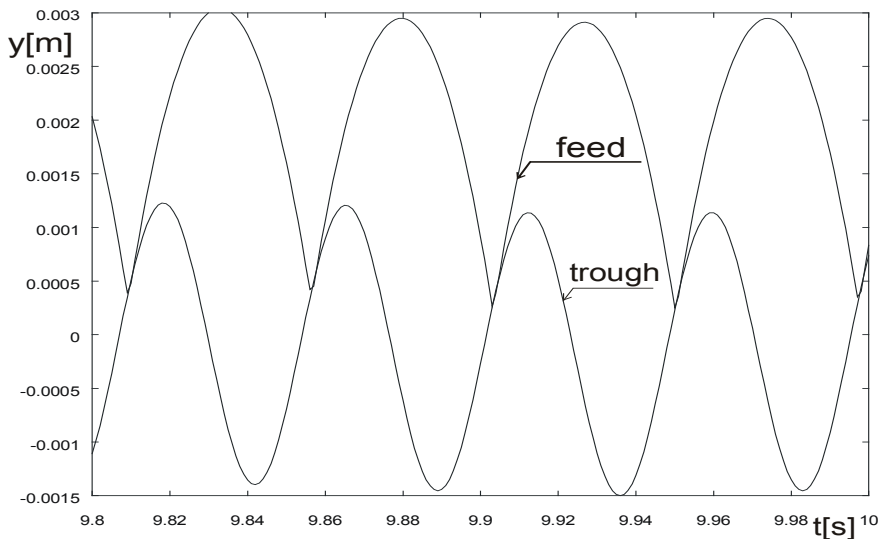


Fig. 14. Displacement of the trough and the feed in the vertical direction, at the excitation frequency: $\omega = 133.5 \text{ rad/s}$ and the vibrator mass eccentric: $e = 0.086 \text{ m}$

6. Conclusions

- 1) Two-way vibratory conveyer presented in the study has a simple and reliable construction.
- 2) There is a possibility of fast changing the direction of the transported material by changing the excitation frequency of the vibrator.
- 3) Applying the vibrator of the variable eccentric of the unbalanced mass it is possible to achieve the same transport velocities in both directions.

References

- [1] Baker S.: *Vibratory drive system for a vibratory conveyor apparatus*, US Patent No. 5064053, 1991.
- [2] Catalogue of the Jost Company.
- [3] Cieplak G.: *Verification of the nomogram for amplitude determination of resonance vibrations in the run-down phase of a vibratory machine*, Journal of the Theoretical and Applied Mechanics, Vol. 47, No. 2, 2009, pp. 295–306.
- [4] Czubak P.: *Two-way vibratory conveyer*, Patent Application No. P-388654, 28.07.2009.
- [5] Czubak P.: *Mass optimisation of the vibroinsulating frame of a short vibratory conveyer*, Mechanics, Vol. 25, No. 1, 2006, pp. 33–40.
- [6] Czubak P., Michalczuk J.: *Mobile properties of vibratory conveyers operating on the basis of the dynamic eliminator*, Modelowanie Inżynierskie, Vol. 2, No. 33, 2007, pp. 55–60.
- [7] Frahm H.: *Device for damping vibrations of bodies*, US Patent No. 989958, 1909.

- [8] Michalczyk J.: *Phenomenon of force impulse restitution in collision modelling*, Journal of Theoretical and Applied Mechanics, Vol. 46, No. 4, 2008, pp. 897–908.
- [9] Michalczyk J., Cieplak G.: *Numerical model of vibrating screen*, Modelowanie Inżynierskie, Vol. 1, No. 32, 2006, pp 381–388.
- [10] Michalczyk J., Czubak P.: *Methods of determination of maximum amplitudes in the transient resonance of vibratory machines*, Archives of Metallurgy and Materials, Vol. 55, No. 3, 2010, pp. 695–706.
- [11] Michalczyk J., Czubak P.: *Influence of collisions with a material feed on cophasal mutual synchronisation of driving vibrators of vibratory machines*, Journal of Theoretical and Applied Mechanics, Vol. 48, No. 1, 2010, pp. 155–172.
- [12] Musschoot A.: *Vibratory conveying apparatus*, US Patent No. 5178259, 1993.
- [13] Musschoot A.: *Two-way vibratory feeder or conveyor*, US Patent No. 5713457, 1998.
- [14] Musschoot A.: *Two-way vibratory conveyor*, US Patent No. 6029796, 2000.
- [15] Rosenstrom R.: *Reversing natural frequency vibratory conveyor system*, US Patent No. 6298978, 2001.
- [16] Thomson T.: *Bi-directional vibratory conveyor*, US Patent No. 5034446, 1999.

Wyrównanie prędkości transportowania w nowym dwukierunkowym przenośniku wibracyjnym

W ciągu produkcyjnym często stosowane są przenośniki wibracyjne umożliwiające transport nadawy w dwóch kierunkach. W pracy analizowano możliwości transportowe nowego autorskiego rozwiązania rewersyjnego przenośnika wibracyjnego (zgłoszenie patentowe [8]) służącego do dwukierunkowego transportu materiałów sypkich lub przedmiotów o niewielkich wymiarach gabarytowych. Przedstawiono analizę dynamiczną przenośnika wykazując możliwości transportowania nadawy w obydwu kierunkach jedynie poprzez zmianę częstotliwości obrotowej wibratora.



Combined modal parameters-based index for damage identification in a beamlike structure: theoretical development and verification

M.M. FAYYADH, H. A. RAZAK, Z. ISMAIL

Dep. of Civil Engineering, Faculty of Engineering, University of Malaya, 50603 Kuala Lumpur, Malaysia.

A new index for detecting the damage severity in structural elements by combining modal parameters is proposed in this study. The index is based on the combined effect of both the natural frequencies and mode shapes when a change in stiffness of the structural element occurs. In order to demonstrate the significance and capability of this new algorithm, the magnitude of damage was calculated from a finite element model of a beam-like structure model and comparisons with previous algorithms were carried out. The new index called Combined Parameter Index (CPI) compares the factor of reduction in stiffness according to reduction in natural frequencies and also the factor of reduction in stiffness according to change in mode shape. Various damage levels starting from reduction in stiffness of 1% were adopted to validate the sensitivity of the new index to detect the damage severity at various deterioration levels. Mid-span and quarter-span damage positions were adopted to verify the capability of the new damage index to detect the damage severity at various locations. Moreover, damage in support condition was investigated in order to ascertain that the new damage index can also identify support damage cases. The results indicate that the new index has better ability and higher sensitivity to determine the severity of the damage due to stiffness changes in the element or support. In addition, the CPI exhibits sensitivity to detect lower level of damage occurring at earlier stage by having the ability to detect a damage of 1% reduction in the structural element stiffness or elastic bearing stiffness.

Keywords: *damage detection, frequency reduction index FRI, mode shape reduction index MSRI, modal assurance criteria MAC, combined parameter index CPI, elastic bearing stiffness*

1. Introduction

Many engineering structures when exposed to various external loads such as earthquakes, traffic, explosion and vibration during their lifetime, suffer damage and deterioration over the years. This seriously affects their performance and may even lead to structural failure. Similar phenomenon is observed in aerospace and mechanical engineering. In addition, inspection of structural components for damage is essential in decision making on the maintenance of such structures. Dynamic testing has become an increasingly popular and important tool in structural health monitoring with the purpose of identifying damage. Classification for damage identification is defined at four levels with increasing difficulty of determination, namely detection of presence of damage, quantification of severity, locating damage position and prediction of the remaining service life of the structure [23]. To date, vibration-based

damage identification methods applied to civil engineering structural elements provide for the first two levels of damage identification with sufficient degree of reliability.

The basic idea behind this approach is that modal parameters i.e. natural frequency, mode shape and modal damping are functions of physical properties of structures namely mass, damping and stiffness. Therefore, any change in the physical properties will cause detectable changes in the modal parameters. Since the measuring of natural frequency is easier than that of change in structural damping, change can be detected from dynamic analysis using natural frequency and mode shapes. However, there is some debate on whether the use of modal parameters is significant enough to be a good indicator of damage or deterioration. From previous studies, it is observed that the effect on natural frequency when damage occurs in a structure is often of relatively low sensitivity. The low sensitivity of frequency shifts to damage requires either very precise measurements or large levels of damage. The alternative to using natural frequency as damage identification is by using mode shape, with the use of Modal Assurance Criteria MAC to determine the level of correlation between modes from the control beam and those from the damaged beam.

There have been many previous studies related to the use of natural frequency or mode shape in damage identification. Non-destructive evaluation procedure for detecting a crack and identifying the location and size of the crack in one dimensional beam type structure using the natural frequency data have been proposed, [16]. The application and accuracy of the proposed procedure was demonstrated by comparison with the results obtained in the literature, [21], on crack detection in a cantilever beam. Experimental investigation to study the effect of corrosion on the modal parameters of RC Beams was carried out, where the trend in the measured natural frequencies was sensitive to the deterioration state of beams, [1]. Different criteria based on frequencies or mode shapes were applied to detect damage in RC beams for which a few natural frequencies and mode shapes were obtained by experimental modal analysis. Similarly, Local Modal Stiffness was proposed as a new damage detection methodology, [20]. Two damage-sensitive features were used to detect the damage by simulating different damage scenarios. The two features are modal flexibility-based deflection and curvature, where both obtained from dynamic parameters. The experimental results showed that both deflection and curvature showed high sensitivity for damage detection and localization, [2]. A new damage detection technique based on the irregularity profile of structural mode shape was proposed, [26]. The results led to the conclusion that the proposed technique required low measurement resolution and that the successful detection of damage on the composite beam proved that the proposed technique was capable of assessing both the location and the size of the crack. The change in wave times was explored as a structural health monitoring method, using strong motion data from the Imperial Valley Earthquake of 1979, [25]. Problems related to damage detection using output only vibration measurement systems under changing environmental conditions were investigated, [5]. Damage localization feature called modal damping factor was proposed where the study explored a methodology to reduce the amount of conventional

sensors with the aim of locating damage for low cost on components that are subject to impact during service, [18]. An innovative health monitoring methodology based on structural strain measurement was proposed; the measurements were then processed by a back-propagation, feed forward, artificial neural network. The proposed methodology, demonstrated on a cracked aircraft lap-joint structure to evaluate its capability and drawbacks in predicting fatigue damaged states, had good capability to predict accurately the crack position and the length of a lap-joint structure, [12].

The effects of input and output noise on the estimation of transfer entropy were evaluated. The study found that input noise lessens the sensitivity of the damage feature by diminishing the ability of the non-parametric density estimation to produce low variance transfer entropy estimation. The study also concluded that output noise had an effect on the feature's sensitivity, [19]. A new proposal for a hybrid health monitoring system was offered, using sequential vibration impedance approaches, to detect damage in pre-stress concrete bridge girders, [13]. Several vibration-based statistical time series were applied as structural health monitoring methods on lightweight aluminium truss structures, [14]. An autoregressive model used the acceleration time histories obtained from two experimental structures in the literature, [15]. The coefficients of the autoregressive model became the damage-sensitive features and acted as input into an artificial neural network. A method for detecting damage in structures without baseline state information was proposed, [22]. The study found that it is possible to identify the location and severity of damage based on singular value decomposition. A wavelet-based method, which not only localized multiple damage sites but also provided information on when the damage occurred was proposed, [27]. Lower modes are found to have higher sensitivity to the change in the support conditions, [7–9]. An analytical model for detecting cracks in a cantilever beam using the modal parameters i.e. natural frequencies and mode shapes, was developed, [11] and found that both modal parameters are affected by the crack regardless of its position or size. A new damage detection index based on combined mode shape vectors and its curvature was developed and it was verified to have higher sensitivity than existing algorithms, [8].

From all the previous studies, it can be concluded that the natural frequency relates well to the global stiffness of structures but is less sensitive to local stiffness change. On the other hand, the use of mode shape and its derivatives, in relation to changes in the local stiffness of structures has been more promising for ascertaining damage location. Thus, the objective of this study is to develop a Health Monitoring Index HMI for detecting damage severity by combining both natural frequency and mode shape through the use of eigenvalue and eigenvectors. In addition, the results obtained by using the proposed HMI will be compared with other indicators.

2. Theoretical development

In this section, a new proposed technique that utilizes both the eigenvalue and eigenvectors as damage identification indicators will be discussed. The indicator,

called Combined Parameters Index (or CPI), is the stiffness percentage ratio of the damaged case to the control case. CPI eliminates all the positive values of this ratio and will average out the negative values for each mode. In addition, this section will summarize and revise two other indicators found in literature that will be used for comparison to CPI. The first indicator is the Frequency Reduction Index (FRI) which is based on the reduction of natural frequency to locate damage; the second is the Mode Shape Reduction Factor (MSRI) which uses the changes in mode shape through Modal Assurance Criteria MAC.

2.1. Developed index: Combined Parameters Index (CPI)

The free vibration dynamic equilibrium equation can be expressed as:

$$\mathbf{M} \ddot{\mathbf{q}}(t) + \mathbf{K}\mathbf{q}(t) = 0, \quad (1)$$

where:

\mathbf{K} – the stiffness matrix,

\mathbf{M} – the analytical mass matrix.

The computation of eigenvalue and eigenvectors for Equation (1) can be found in many references, [6, 10–17]. The solution to Equation (1) will have the form:

$$\mathbf{q}(t) = \Phi_m e^{\lambda t}, \quad (2)$$

where $\lambda = \pm i\omega_m$, taking $\lambda = +i\omega_m$ and $i^2 = -1$ gives:

$$\ddot{\mathbf{q}}(t) = -\omega_m^2 \Phi_m e^{i\omega_m t}. \quad (3)$$

Substituting Equations 2 and 3 into Equation 1, and rearranged will lead to the Eigenvalue problem:

$$(\mathbf{K} - \omega_m^2 \mathbf{M}) \Phi_m = 0. \quad (4)$$

Equation 4 can be re-written as:

$$\mathbf{K} \Phi_m = \omega_m^2 \mathbf{M} \Phi_m. \quad (5)$$

Taking $\lambda = -i\omega_m$ gives the same solution as in Equations 4 and 5.

The Eigenvalue problem has $m = 1, \dots, n$ solutions ($([\omega_m]_m)_m^1$ and Φ_m), and each solution satisfies Equation (5). Taking into account a solutions corresponding to the first a natural modes (Eigenvectors), Equation (5) can be re-written in compact form as:

$$\mathbf{K} \Phi = \mathbf{M} \Phi A \quad (6)$$

or

$$\mathbf{K}[\Phi_1, \dots, \Phi_a] = \mathbf{M}[\Phi_1, \dots, \Phi_a] \operatorname{diag}(\omega_1^2, \dots, \omega_a^2),$$

where:

a – the mode number,

$\mathbf{K} = [\blacksquare]_{axa}$ – the stiffness matrix,

$\mathbf{M} = [\blacksquare]_{axa}$ – the mass matrix,

$\Phi = [\vdots \vdots \vdots]_{nxa}$ – the Eigenvector matrix,

$\mathbf{A} = [\ddot{\cdot} \ddot{\cdot}]_{axa}$ – the Eigenvalue matrix.

For the purpose of this study, the number of solutions and thus of the Eigenvalues must be taken equal to the number of the degrees of freedom and thus of Eigenvectors; one Eigenvalue thus means one Eigenvector and n Eigenvalues implies n Eigenvectors.

The Eigenvector indicator matrix $\Phi^* = [\vdots \vdots \vdots]_{axa}$ is built by using the peak values of the measured modal displacement for the particular mode number a ; for mode numbers less than a , the values that correspond to the peak value location of mode number a are utilized. Figure 1 shows how to fill up the cells of the Φ^* matrix if four modes are adopted, where it shows the selection of the degree of freedoms $D1$ to $D4$ as the peak values on the fourth mode shape ($M4$) and utilizing the same points $D1$ – $D4$ on Modes 1, 2 and 3 ($M1$, $M2$ and $M3$). The first column in the Φ^* matrix will be filled up with the values of $D1$ at cell (1, 1) to $D4$ at cell (4, 1) from first Mode ($M1$), and the same way for the rest of the columns until the fourth column, which would be filled up with values of $D1$ to $D4$ in cells (1, 4) to cell (4, 4) from the fourth mode ($M4$). The Eigenvalue indicator matrix $\mathbf{A}^* = [\ddot{\cdot} \ddot{\cdot}]_{axa}$ contains the measured Eigenvalues for each mode until mode number a in the diagonal.

For the case when four modes are considered as shown in Figure 1, the Eigenvector indicator matrix Φ^* and Eigenvalue indicator matrix \mathbf{A}^* for the fourth mode are as follows:

$$\Phi^* = \begin{bmatrix} D1,M1 & D1,M2 & D1,M3 & D1,M4 \\ D2M1 & D2M2 & D2,M3 & D2,M4 \\ D3M1 & D3M2 & D3M3 & D3,M4 \\ D4,M1 & D4,M2 & D4,M3 & D4,M4 \end{bmatrix}, \quad (7)$$

$$\mathbf{A}^* = \begin{bmatrix} \omega_1^2 & 0 & 0 & 0 \\ 0 & \omega_2^2 & 0 & 0 \\ 0 & 0 & \omega_3^2 & 0 \\ 0 & 0 & 0 & \omega_4^2 \end{bmatrix}. \quad (8)$$

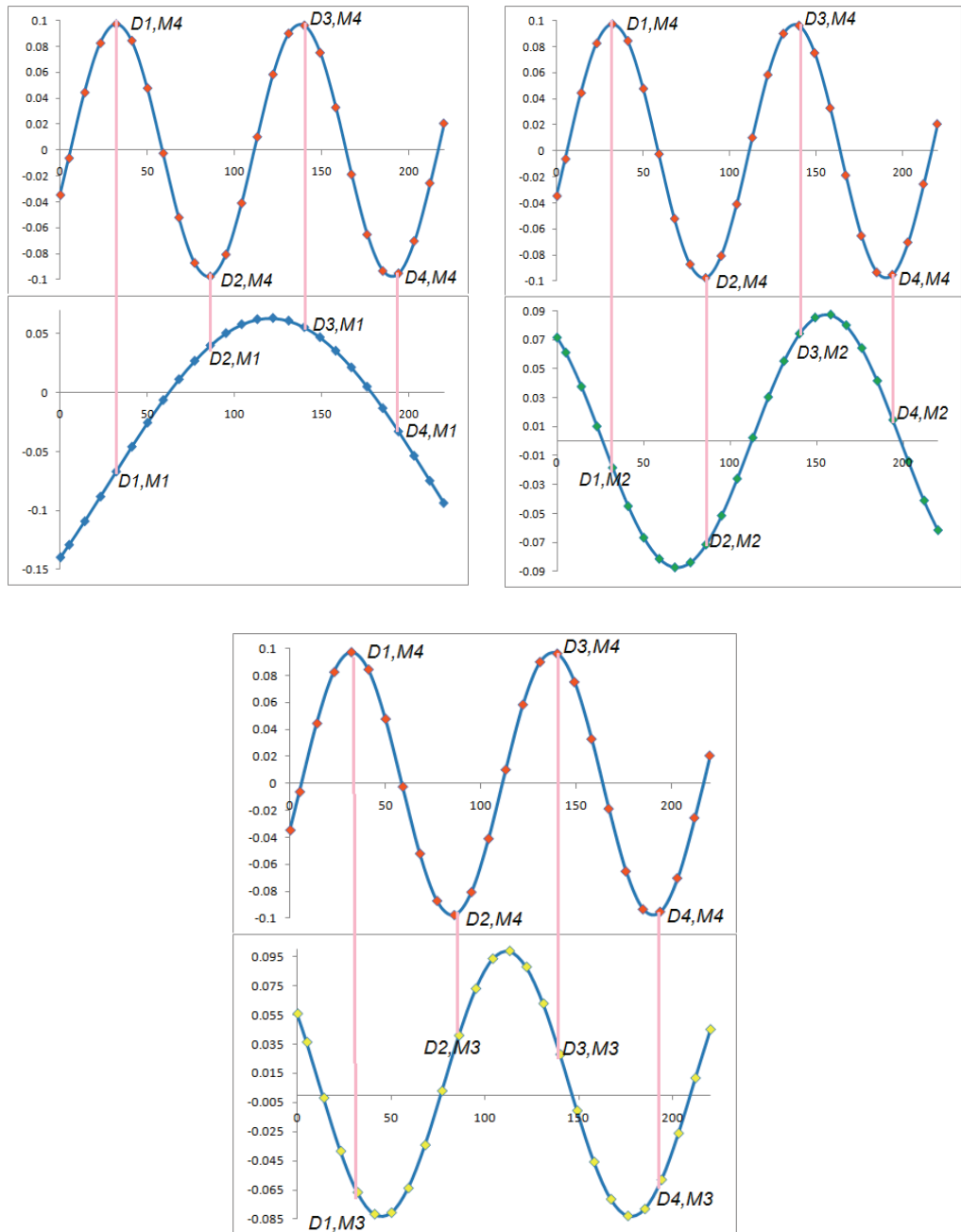


Fig. 1. Selection of peak points on the highest mode and utilization for the remaining modes (Mode 4 is the highest mode)

Based on Eigenvector indicator matrix Φ^* and eigenvalue indicator matrix A^* , Equation 6 can be re-written as

$$\mathbf{K}^* \Phi^* = \mathbf{M}^* \Phi^* A^*, \quad (9)$$

where \mathbf{K}^* and \mathbf{M}^* are stiffness and mass indicator matrices.

Based on the assumption made for the purpose of this study by taking the number of the Eigenvalues equal to the number of the eigenvectors, the indicator matrix Φ^* is a square matrix and thus its inverse can exist. Equation (9) can be further reduced into:

$$\mathbf{K}^* = \mathbf{M}^* \Phi^* A^* (\Phi^*)^{-1} \quad (10)$$

For comparison of stiffness indicator matrices of both the undamaged (control) and damaged cases, considering that there is no reduction in mass for the damaged case, the matrix \mathbf{M}^* remains constant for both control and damaged beams. Equation (10) can be re-written as:

$$\mathbf{K}_c^* = \Phi_c^* A_c^* (\Phi_c^*)^{-1}, \quad (11)$$

$$\mathbf{K}_d^* = \Phi_d^* A_d^* (\Phi_d^*)^{-1}, \quad (12)$$

where indices c and d represent control and damaged cases, respectively.

Subsequently, the Combined Parameters Index matrix, $CPI = [\blacksquare]_{axa}$, at each cell of the matrix is defined by

$$CPI(i, j) = \left(1 - \frac{K_d^*(i, j)}{K_c^*(i, j)} \right), \quad (13)$$

The CPI will be calculated at each cell of the $CPI(i, j)$ matrix, and then the average of the $(a \times a)$ cell values will be found to obtain one single value as shown in Equation (14) below:

$$CPI = \frac{\sum_{i=1, j=a}^{i=a, j=a} CPI(i, j)}{a \times a}, \quad (14)$$

where:

CPI – the single value for the matrix $CPI(i, j)$,

i – the number of the eigenvalue,

j – the number of the eigenvector,

a – the total number of eigenvalues or eigenvectors.

2.2. Index based on Natural Frequency

The natural frequency, f , for transverse free vibration of a simply supported Bernoulli-Euler beam with similar dimensions, [3, 4, 24], is given by:

$$f = \frac{n^2\pi}{2} \sqrt{\frac{El}{mL^4}}, \quad (15)$$

where:

n – mode number,

m – mass per unit length,

L – span length. The natural frequency is proportional to the square root of its flexural rigidity, EI ,

$$f \propto \sqrt{EI}, \quad (16)$$

which implies that a change in flexural rigidity will contribute to the change in natural frequency. The Frequency Reduction Index (FRI) can be defined as:

$$FRI = \left(1 - \frac{f_{i,d}}{f_{i,c}} \right) \cdot 100\%, \quad (17)$$

where $f_{i,c}$ and $f_{i,d}$ are the natural frequency at i -th mode for control and damaged beams, respectively.

2.3. Index based on mode shape

The method used to ascertain configuration errors between experimental mode shapes and eigenvectors predicted from the finite element model is called modal assurance criterion (MAC), [6]. For the purpose of the damage detection and in case of available data at the undamaged case of the structure (control case), the MAC is a correlation between mode shapes of damaged and undamaged cases as given by the following formula:

$$MAC = \frac{\left| \sum_{i=1}^n \varphi_{i,c} \cdot \varphi_{i,d} \right|^2}{(\sum_{i=1}^n \varphi_{i,c} \cdot \varphi_{i,c})(\sum_{i=1}^n \varphi_{i,c} \cdot \varphi_{i,c})}, \quad (18)$$

where $\varphi_{i,c}$ and $\varphi_{i,d}$ are the mode shape vectors at i -th mode for control c and damaged d beam, respectively.

Utilizing the concept in the previous paragraph, Mode Shape Reduction Index (MSRI) which is an indicator that utilizes only the mode shapes, is defined by the following formula:

$$\text{MSRI} = (1 - \text{MAC}) \cdot 100\%. \quad (19)$$

3. Case study

To demonstrate the significance and capability of the proposed index, one finite-element beamlike structure model was built to represent control and damaged cases. The span length of the beam was 3250 mm with a cross-sectional area of 150 mm by 250 mm. The sensitivity level of the new index attempted to detect different damage levels and locations. It also attempted to detect deterioration in elastic-bearing stiffness for cases of bridge girders. Since the dynamic parameters are related to the stiffness of the structural element, the damage is presented by reducing the modules of elasticity E values. The Stiffness Reduction Ratio (SRR) was adopted as denotation for the damage level and can be calculated as:

$$\text{SRR} = (1 - Ed/Ec) \cdot 100\%, \quad (20)$$

where:

Ed – the modulus of elasticity value for the damage cases,

Ec – the modulus of elasticity for the control case.

Four levels of stiffness were adopted as the control where E is 200 GPa, and the SRR was 0%: the first damage level is the smallest level where the SRR was 1% (E is 198 GPa), the second damage level is the medium level where the SRR was 5% (E is 190 GPa) and the third damage level is the higher level where the SRR was 12.5% (E is 175 GPa). The same levels were examined for different damage locations; the first damage was located at the mid-span and the second damage was located at the quarter-span. A total of six cases for different SRR levels and different damage locations were adopted. Table 1 shows the SRR adopted in the present study. Figure 2 shows the beamlike structure model for the control beam, mid-span damage, and quarter-span damage.

Table 1. Damage cases adopted in present study

Stiffness Damage Cases	Stiffness Reduction Ratio SRR	Damage Location
Control C	0%	N/A
SD1	1%	Mid-Span
SD2	5%	Mid-Span
SD3	12.5%	Mid-Span
SD4	1%	Quarter-Span
SD5	5%	Quarter-Span
SD6	12.5%	Quarter-Span

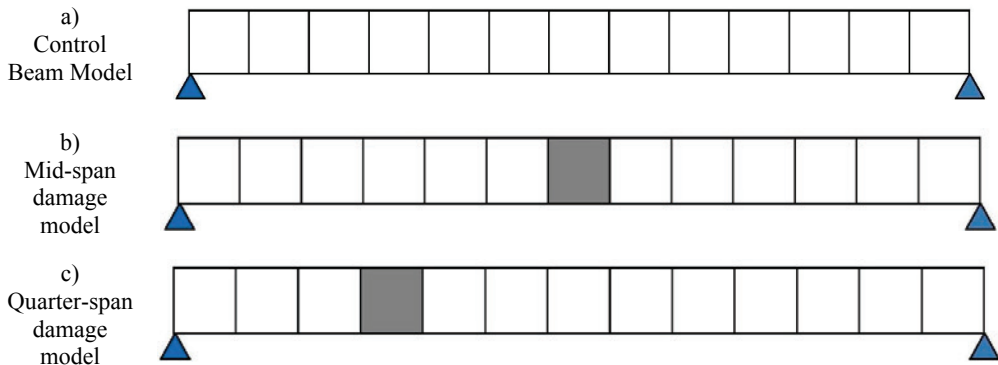


Fig. 2. Beam like structure model used in present study

For support stiffness in cases when elastic bearing was used, four cases were adopted: the control case, when both supports are fixed on elastic bearing with stiffness K of 50000 N/mm; the first damage case where there was 1% deterioration in elastic-bearing stiffness; the second damage case where there was 5% deterioration in elastic bearing stiffness; and the third damage case where there was deterioration of 12.5% in elastic-bearing stiffness. Elastic Bearing Stiffness Reduction Ratio (EBSRR) was adopted to indicate the elastic-bearing stiffness case where:

$$\text{EBSRR} = (1 - K_d/K_c) \cdot 100\%, \quad (21)$$

where:

K_d – the elastic bearing stiffness for the damage cases,

K_c – the elastic bearing stiffness for the control case.

Table 2 shows the EBSRR adopted in the present study. Utilizing a general-purpose finite-element package that is based on the displacement method, one two-dimensional finite-element model was constructed to represent the beamlike structure model. The beam model was built by using a 4-node plane stress element. Figure 3 shows a typical model for the beam constructed using software. The physical and material properties of the beam were Poisson's ratio of 0.2, mass density of 7850 kg/m³ and Young's modulus of 200 GPa for the control case. These vary from one damage case to another. The self-weight was computed by taking gravitational acceleration as 9.81 m/s² in the $-y$ direction.

Initially, Eigen analyses were performed so that modal parameters for the control beam model could be approximated. Next, the damage was created on the beam model by changing the value of the modules of elasticity first at the mid-span surface (Figure 2b) and secondly at the quarter-span surface (Figure 2c). The damage was created by changing the elastic-bearing stiffness on both sides as shown in Table 2. At each damaged case, eigenvalue analysis was again performed to obtain the modal parameters

relevant to the damage case induced. Finally, the indices FRI, MSRI, and CPI were calculated for the first four bending modes.

Table 2. Support Condition cases adopted in present study

Support condition cases	Elastic Bearing Stiffness Reduction Ratio EBSRR	
	Left Support	Right Support
Datum D	0 %	0 %
SC1	1 %	1 %
SC2	5 %	5 %
SC3	12.5 %	12.5 %

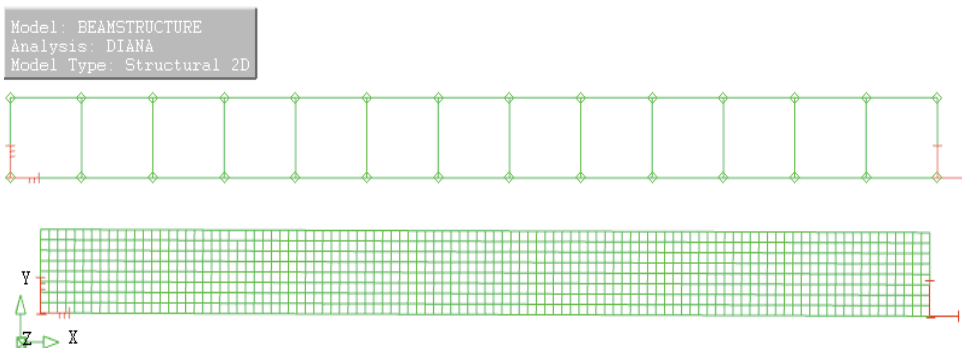


Fig. 3. Finite Element modelling for the beam like structure model

4. Results and discussion

This section will present the results from the analytical modelling of the beamlike structure used in the present study. First, the dynamic parameters as natural frequencies and mode shapes were carried out using Eigen analysis. Then, the damage detection indices FRI, MSRI, and CPI were calculated. Results were divided into two sections: Structural Element Stiffness Reduction Damage, when the value of the modules of elasticity have changed at the mid-span and quarter-span, and elastic-bearing stiffness reduction damage, when the support conditions have been changed from fixed to hinged at one or both of the support sides.

4.1. Structural element stiffness reduction damage

This section will show the results of the calculations of FRI, MSRI, and CPI for the first four modes of the control-beam model and three different damaged levels as 1%, 5%, and 12.5% reduction in E value at the mid-span and quarter-span of the beam model (Figures 1b–1c). Figures 4 and 5 show the comparison of the FRI values at different damage levels for damage located at mid-span and quarter-span, respectively.

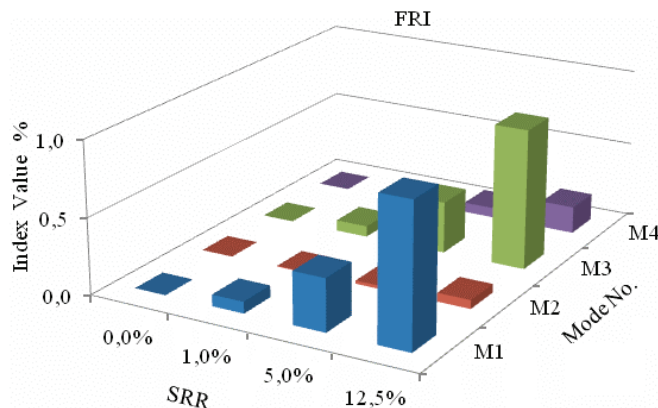


Fig. 4. FRI index values for different damage levels located at mid-span

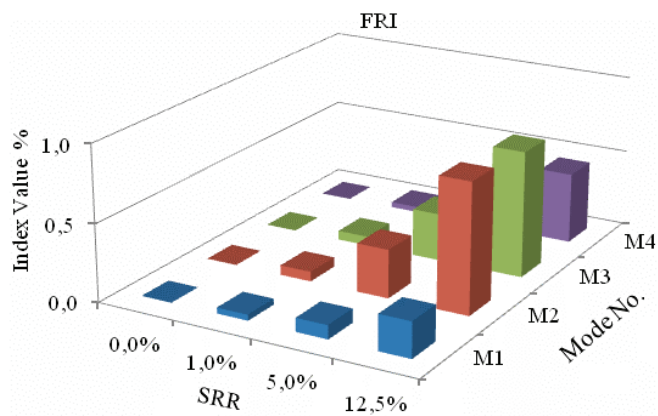


Fig. 5. FRI index values for different damage levels located at quarter-span

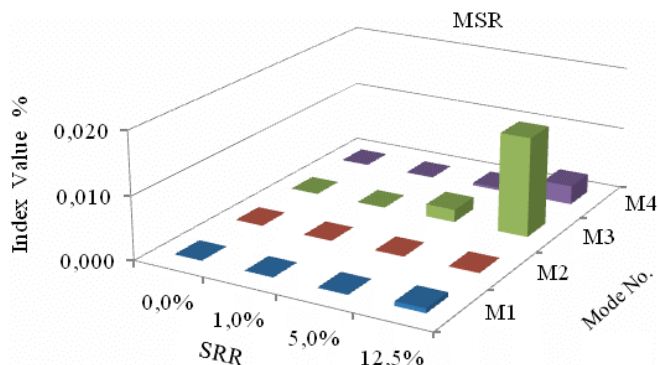


Fig. 6. MSRI index values for different damage levels located at mid-span

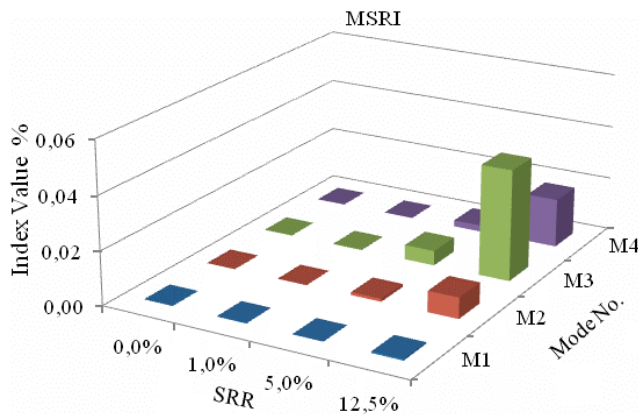


Fig. 7. MSRI index values for different damage levels located at quarter-span

FRI results showed that the first and the third modes are the most sensitive to detect damage severity when the damage was located at mid-span, while modes two and three were the most sensitive when the damage was located at the quarter-span. The higher FRI values for all the modes were at the highest damage level at SRR 12.5% for both damage locations. First mode showed the highest value for damage located at mid-span, while mode two had the highest value when the damage was located at the quarter-span. Figures 6 and 7 show graphically the comparison of MSRI at different damage levels for damage located at mid-span and quarter-span respectively.

MSRI values had lower sensitivity than FRI, where the higher MSRI value was 0.05% at the third mode when the SRR was 12.5% for damage located at quarter-span. However, modes 3 and 4 had higher sensitivity than the first two modes. Figures 8 and 9 show graphically the comparison of CPI at different damage levels for damage located at mid-span and quarter-span, respectively.

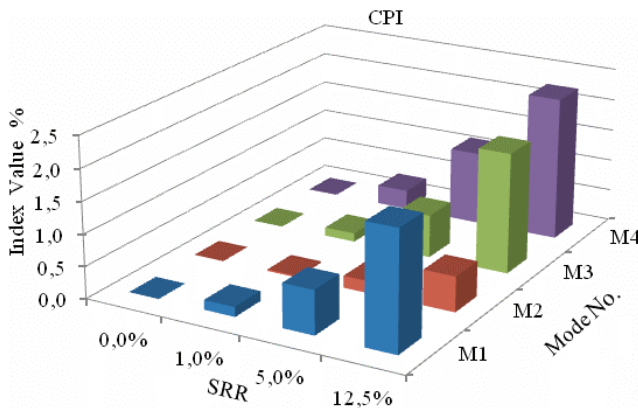


Fig. 8. CPI index values for different damage levels located at mid-span

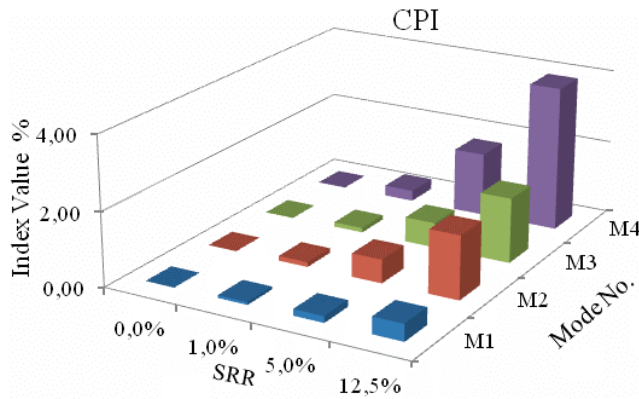


Fig. 9. CPI index values for different damage levels located at quarter-span

The new damage detection index, CPI, had more sensitivity than both indices, where the higher CPI value was 3.9% at the SRR and 12.5% for damage located at quarter-span. In addition, all the four modes show good sensitivity in detecting the damage, with increasing values corresponding to increase in the stiffness-reduction ratio. Moreover, the fourth mode was the most sensitive. The CPI results display unexpected behaviour, with modes two and four (antisymmetric modes) able to detect the damage located at the mid-span, as opposed to FRI and MSRI which show less sensitivity. This is because the values of FRI and MSRI for these antisymmetric modes rely on each mode separately, and due to the antisymmetric shape, less sensitivity was observed. The CPI values at the antisymmetric modes also rely on the odd modes (first and third modes) as discussed in the construction of the Eigenvalue and Eigenvector matrixes in Equations 9 and 10 and Figure 1. For the second mode, the CPI will take into consideration the eigenvector and eigenvalue for the first modes, and for the fourth mode it will take into consideration the eigenvalues and eigenvectors of the first, second and third modes. This helps to improve the sensitivity of the antisymmetric modes to detect the damage located at mid-span.

The results show that the sensitivity of the indices for all the modes increased corresponding to the increase in the damage level. In order to compare the sensitivity for existing and developed damage severity indexes at different damage location each damage level separately, Figures 10 and 11 show the comparison of the indices for the SRR of 1% and damage located at mid-span and quarter-span, respectively.

The results show that the CPI had more sensitivity than the FRI and MSRI, and it increased the sensitivity for both damage locations. The result of the smallest damage level validates the CPI as a sensitive index that can detect damage even with small levels, whether at mid-span or quarter-span. The results show that CPI has higher sensitivity when the damage is located elsewhere than at mid-span.

Figures 12 and 3 show the comparison of the indices for SRR of 5% with damage located at mid-span and quarter-span, respectively.

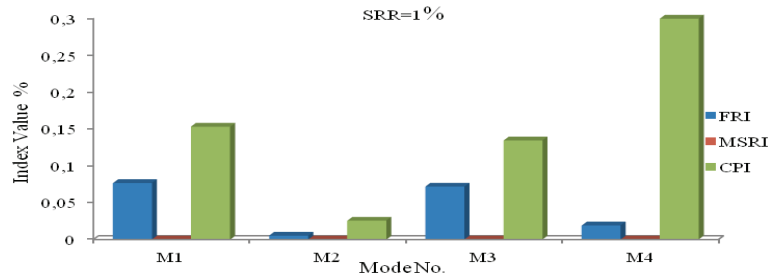


Fig. 10. CPI comparisons with FRI & MSRI for damage located at mid-span

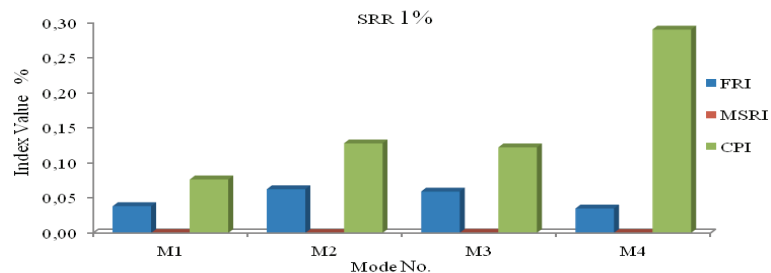


Fig. 11. CPI comparisons with FRI & MSRI for damage located at quarter-span

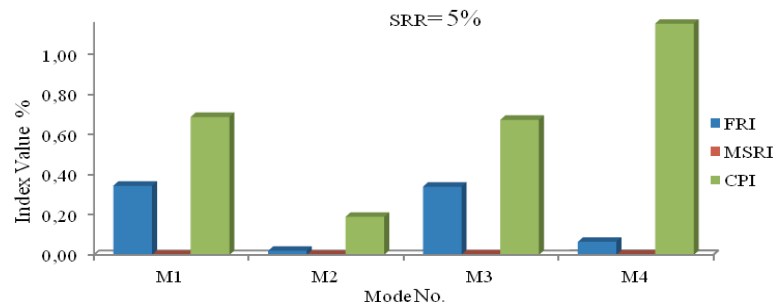


Fig. 12. CPI comparisons with FRI & MSRI for damage at mid-span

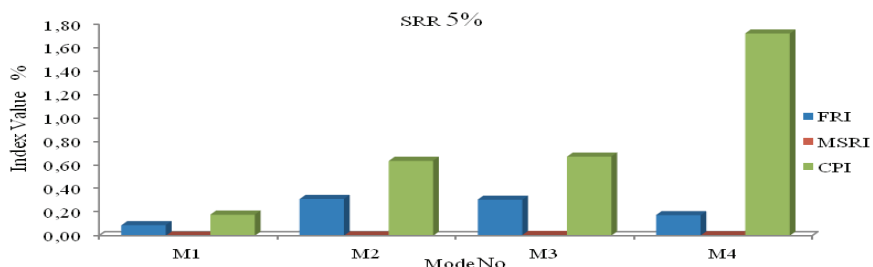


Fig. 13. CPI comparisons with FRI & MSRI for damage at quarter-span

The results prove the higher sensitivity of the CPI compared to the FRI and MSRI. They also show that CPI sensitivity increases when the damage is located elsewhere than mid-span.

Figures 14 and 15 show the index comparisons for the SRR of 12.5% and damage located at mid-span and quarter-span, respectively.

The results prove the higher sensitivity of the CPI compared to the other indices. The results show that the CPI sensitivity increases for the damage cases when it is located elsewhere than mid-span.

The results prove that for the FRI, the first mode was the most sensitive when the damage was located at mid-span and the second mode was the most sensitive when it was located at quarter-span. For the MSRI, the third mode was the most sensitive wherever the damage, while for the CPI, the fourth mode had the highest sensitivity, wherever the damage. The results show that for all the damage levels, all the available modes, and all damage locations, the CPI increased the sensitivity of the FRI and MSRI by at least twice.

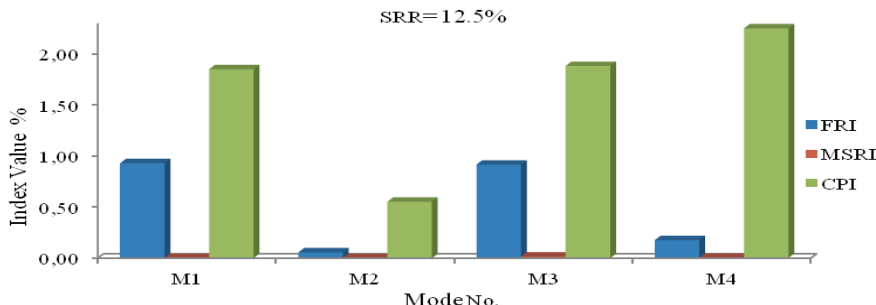


Fig. 14. CPI comparisons with FRI & MSRI for damage at mid-span

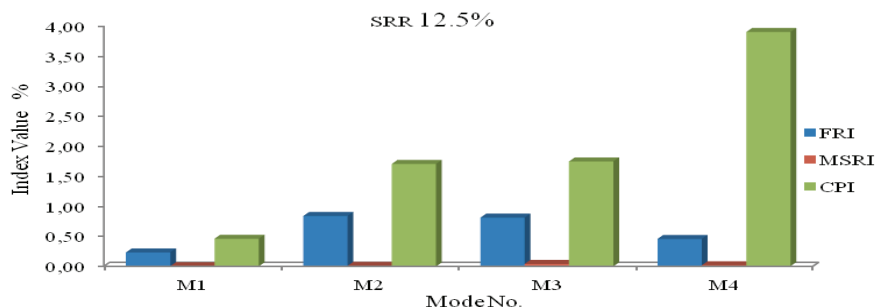


Fig. 15. CPI comparisons with FRI & MSRI for damage at quarter-span

The results prove the higher sensitivity of the CPI compared to the other indices. The results show that the CPI sensitivity increases for the damage cases when it is located elsewhere than mid-span.

The results prove that for the FRI, the first mode was the most sensitive when the damage was located at mid-span and the second mode was the most sensitive when it was located at quarter-span. For the MSRI, the third mode was the most sensitive wherever the damage, while for the CPI, the fourth mode had the highest sensitivity, wherever the damage. The results show that for all the damage levels, all the available modes, and all damage locations, the CPI increased the sensitivity of the FRI and MSRI by at least twice.

The average percentage values for mode 1 to mode 4 of the three indices were calculated based on algebraic averaging of the index values for the four modes. Figures 16 and 17 show the graph versus the percentages of the SRR for damage located at mid-span and quarter-span, respectively.

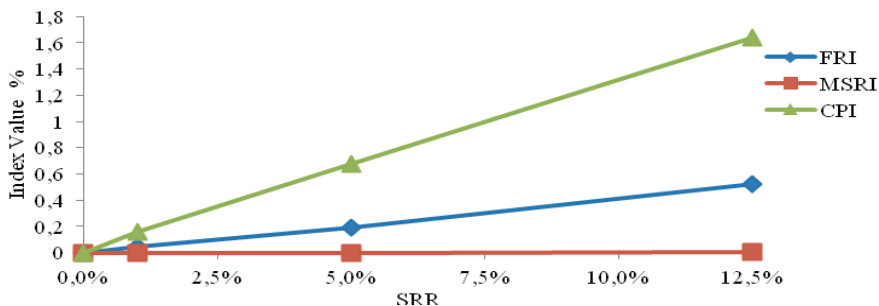


Fig. 16. Indices average values corresponding to damage ratios for damage located at mid-span

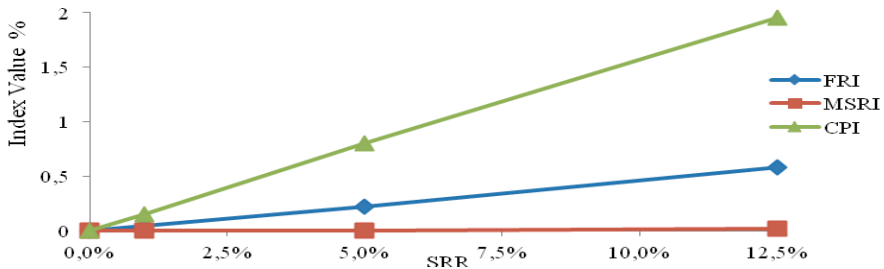


Fig. 17. Indices average values corresponding to damage ratios for damage located at quarter-span

The results showed that the MSRI was the least sensitive at all damage levels, the CPI was the most sensitive to any change in stiffness, and the FRI was between these two indices. For the smallest damage level when SRR was 1%, the CPI increased sensitivity by 3.6 and 3.2 times when the damage was located mid-span and quarter-span, respectively. For the second damage level where SRR was 5%, the CPI increased sensitivity by 3.5 and 3.7 times when the damage was located at mid-span and quarter-span, respectively. For the higher damage level when SRR was 12.5%, the CPI increased sensitivity up to 3.2 and 3.4 times when the damage was located at mid-

span and quarter-span, respectively. The averaging results validate the CPI as the higher sensitivity index compared to FRI and MSRI and prove its capability to detect damage located at mid-span and quarter-span.

4.2. Elastic bearing stiffness reduction damage

This section will present the results from the calculation of the FRI, MSRI, and CPI for the first four modes of the control beam model and two support stiffness deterioration levels. Figures 18–20 show the comparison of FRI, MSRI and CPI, respectively, at different values of elastic-bearing stiffness.

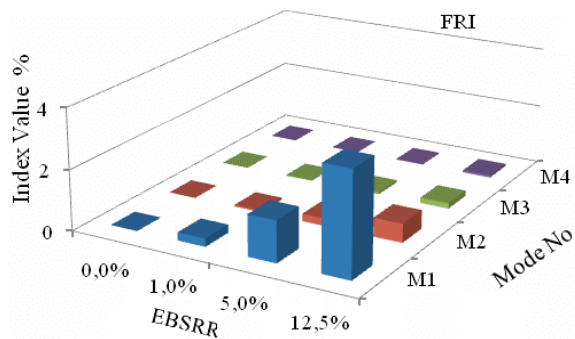


Fig. 18. FRI index values for different elastic bearing damage levels

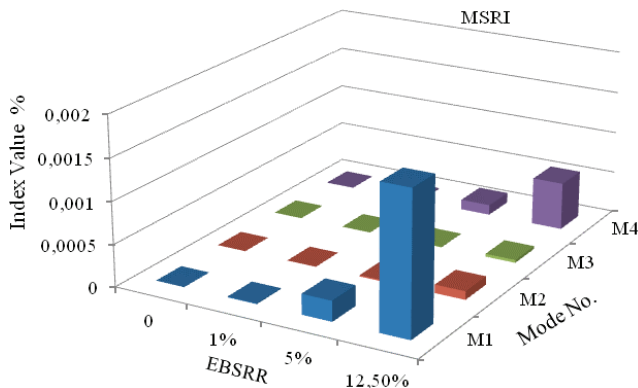


Fig. 19. MSRI index values for different elastic bearing damage levels

The results show that for the FRI, mode one was the most sensitive. For the MSRI, modes one and four had good sensitivity compared to the other modes; however, it still had a very small amount of sensitivity. The CPI had a higher sensitivity for all modes, and mode three was the most sensitive. The sensitivity of all indices increased corresponding to the increase in the support stiffness deterioration level.

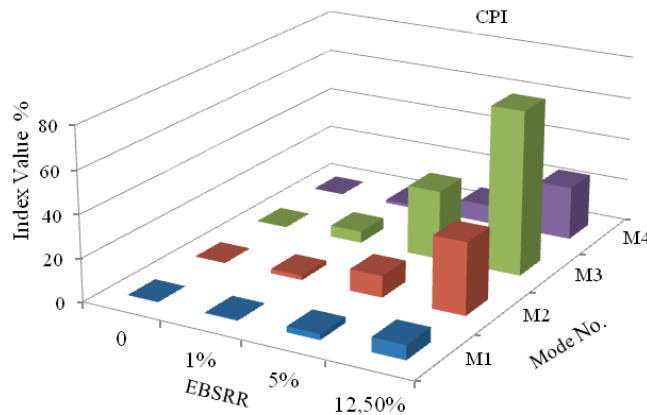


Fig. 20. CPI index values for different elastic bearing damage levels

The results show that for the FRI, mode one was the most sensitive. For the MSRI, modes one and four had good sensitivity compared to the other modes; however, it still had a very small amount of sensitivity. The CPI had a higher sensitivity for all modes, and mode three was the most sensitive. The sensitivity of all indices increased corresponding to the increase in the support stiffness deterioration level.

Figures 21–23 show the indices results at EBSRR of 1%, 5% and 12.5%, respectively. The results showed that the CPI had higher sensitivity than FRI and MSRI. Mode three was the most sensitive mode for the CPI index. CPI increased sensitivity by at least 20 times even for the smallest support stiffness deterioration level.

The average percentage values for mode 1 to mode 4 of the three indices were calculated based on algebraic averaging of the index values for the four modes. Figure 24 shows the average values corresponding to the elastic bearing stiffness reduction ratio.

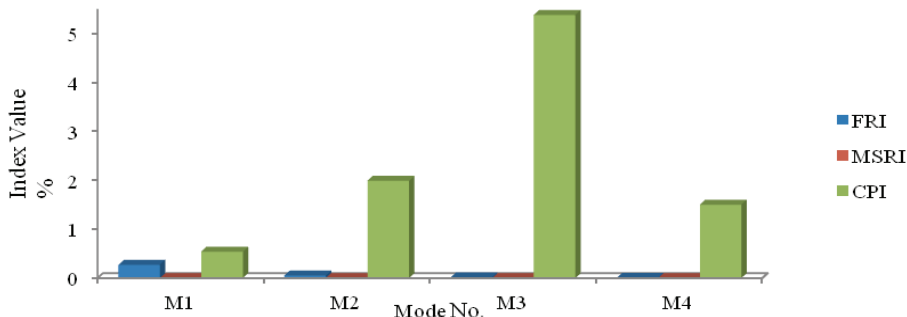


Fig. 21. CPI comparisons with FRI & MSRI for EBSRR of 1%

The results showed that the MSRI was the least sensitive for all elastic-bearing damage levels and CPI the most sensitive to any change in stiffness. The CPI increased sensitivity by 27, 31 and 33 times when the EBSRR was 1%, 5% and 12.5%, respectively. The averaging results for all considered modes validate the CPI as a higher sensitivity index and prove its capability to detect support damage even with small levels.

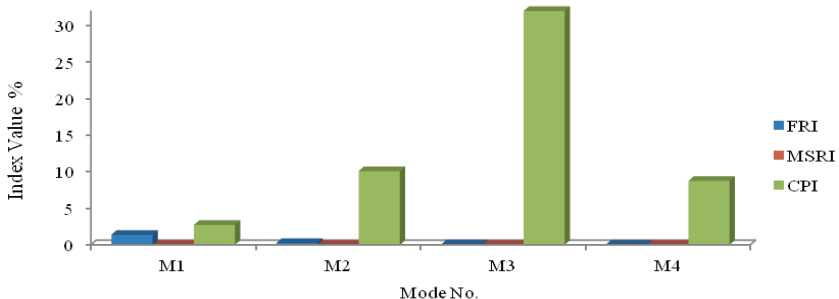


Fig. 22. CPI comparisons with FRI & MSRI for EBSRR of 5%

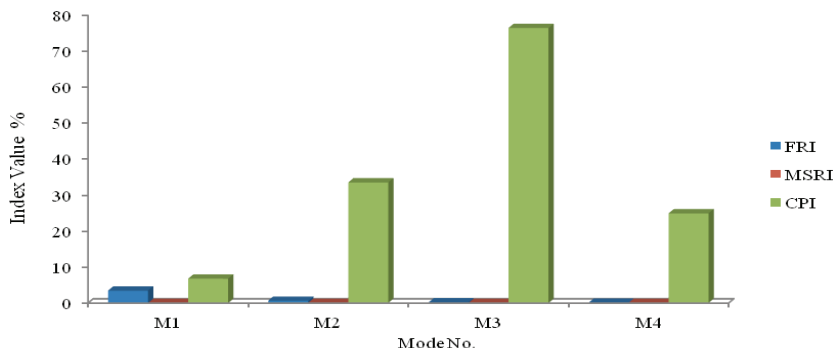


Fig. 23. CPI comparisons with FRI & MSRI for EBSRR of 12.5%

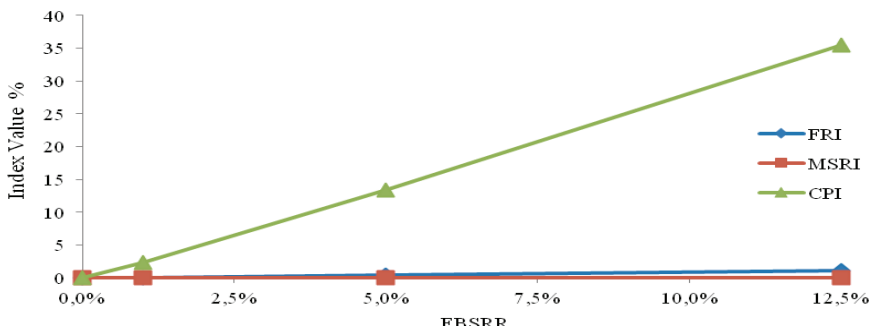


Fig. 24. Indices average values corresponding to the support stiffness reduction ratio

5. Conclusions

The following conclusions can be drawn based on the results from the present study.

- The new damage detection index CPI has higher sensitivity than the existing indices even for a small damage ratio of 1%, which is an increase in the sensitivity by at least 3.2 times.
- The results validate the CPI's capability to detect the damage and to have higher sensitivity for both damage locations, at mid-span and at quarter-span.
- The calculation method of CPI helped to improve the sensitivity of the antisymmetric modes in detecting damage located at the mid-span, in comparison to the FRI and MSRI.
- The CPI's sensitivity will be higher when the damage is located elsewhere than mid-span.
- The CPI increased sensitivity much more than the other indices in the case of deterioration in elastic bearing, with a 27 times increase in sensitivity.
- CPI is more sensitive in the case of elastic-bearing deterioration than for the cases of the structural-element stiffness.

Acknowledgements

The authors would like to acknowledge the financial assistance provided by University of Malaya through a research grant entitled "Development of Algorithms for Structural Health Monitoring using Modal Parameters" (RG090/10AET). The authors would also like to thank all the people who have contributed either directly and indirectly, in making this research possible.

References

- [1] Abdul Razak H., Choi F.C.: *The effect of corrosion on the natural frequency and modal damping of reinforced concrete beams*, Journal of Engineering Structures, Vol. 23, 2001, pp. 1126–1133.
- [2] Catbas F.N., Gul M., Burkett J.L.: *Conceptual damage-sensitive features for structural health monitoring: laboratory and field demonstrations*, Mechanical Systems and Signal Processing, Vol. 22, No. 7, 2008, pp. 1650–1669.
- [3] Chopra A.K.: *Dynamics of structures: theory and applications to earthquake engineering*, New Jersey, Prentice Hall, 1995.
- [4] Craig Jr. R.R.: *Structural dynamics: an introduction to computer methods*, New York, John Wiley & Sons, 1981.
- [5] Deraemaeker A., Reynders E., De Roeck G., Kullaa J.: *Vibration-based structural health monitoring using output-only measurements under changing environment*, Mechanical Systems and Signal Processing, Vol. 22, No. 1, 2008, pp. 34–56.
- [6] Ewins D.J.: *Modal testing: theory, practice and application*, Second Edition, Baldock, Hertfordshire, England, Research Studies Press Ltd, 2000.

- [7] Fayyadh M.M., Abdul Razak H., Khalil R.O.: *The effect of the differential difference in support condition on the dynamic parameters*, Proceeding of the Twelfth East Asia Pacific Conference on Structural Engineering & Construction, Hong Kong, China, 2011.
- [8] Fayyadh M.M., Abdul Razak H.: *Stiffness reduction index for detection of damage location: analytical study*, International Journal of the Physical Sciences, Vol. 6, No. 9, 2011, pp. 2194–2204.
- [9] Fayyadh M.M., Abdul Razak H.: *The effect of support condition on dynamic parameters*, Proceeding of the 17th International Congress on Sound and Vibration, Cairo, Egypt, 2010.
- [10] Heylen W., Lammens S., Sas P.: *Modal analysis theory and testing*, Katholieke Universiteit Leuven, Belgium, 1999.
- [11] Jassim Z., Fayyadh M.M., Mustapha F.: *Health monitoring of cantilever rod using vibration test theoretical and numerical study*, Proceeding of the 17th International Congress on Sound and Vibration, Cairo, Egypt, 2010.
- [12] Katsikeros C.E., Labeas G.N.: *Development and validation of a strain-based structural health monitoring system*, Mechanical Systems and Signal Processing, Vol. 23, No. 2, 2009, pp. 372–383.
- [13] Kim J.T., Park J.H., Hong D.S., Park W.S.: *Hybrid health monitoring of prestressed concrete girder bridges by sequential vibration-impedance approaches*, Engineering Structures, Vol. 32, No. 1, 2010, pp. 115–128.
- [14] Kopsaftopoulos F.P., Fassois S.D.: *Vibration based health monitoring for a lightweight truss structure: experimental assessment of several statistical time series methods*, Mechanical Systems and Signal Processing, Vol. 24, No. 7, 2010, pp. 1977–1997.
- [15] Lautour O.R. De, Omenzetter P.: *Damage classification and estimation in experimental structures using time series analysis and pattern recognition*, Mechanical Systems and Signal Processing, Vol. 24, No. 5, 2010, pp. 1556–1569.
- [16] Lee Y.S., Chung M.J.: *A study on crack detection using eigen frequency test data*, Journal of Computers and Structures, Vol. 77, 2000, pp. 327–342.
- [17] Maia N.M.M., Silva E., Julio M.: *Theoretical and experimental modal analysis*, New York, Research Studies Press Ltd. and John Wiley & Sons Inc, 1997.
- [18] Montalvão D., Ribeiro A.M.R., Duarte-Silva J.: *A method for the localization of damage in a CFRP plate using damping*, Mechanical Systems and Signal Processing, Vol. 23, No. 6, 2009, pp. 1846–1854.
- [19] Overbey L.A., Todd M.D.: *Effects of noise on transfer entropy estimation for damage detection*, Mechanical Systems and Signal Processing, Vol. 23, No. 7, 2009, pp. 2178–2191.
- [20] Ricardo P., Consuelo H., Juan M.O.: *Identification of damage in RC beams using index based on local modal stiffness*, Journal of Construction and Building, Vol. 22, No. 8, 2008, pp. 1656–1667.
- [21] Rizos P.F., Aspragathos N., Dimarogonas A.D.: *Identification of crack location and magnitude in a cantilever from the vibration modes*, Journal of Sound and Vibration, Vol. 138, No. 3, 1990, pp. 381–388.
- [22] Rodríguez R., Escobar J.A., Gómez R.: *Damage detection in instrumented structures without baseline modal parameter*, Engineering Structures, Vol. 32, No. 6, 2010, pp. 1715–1722.
- [23] Rytter A.: *Vibration based inspection of civil engineering structures*, PhD Dissertation, Department of Building Technology and Structural Engineering, Aalborg University, Denmark, 1993.

- [24] Timoshenko S., Young D.H., Weaver Jr. W.: *Vibration problems in engineering*, Fourth Edition, New York, John Wiley & Sons, 1974.
- [25] Todorovska M.I., Trifunac M.D.: *Earthquake damage detection in the Imperial County Services Building III: analysis of wave travel times via impulse response functions*, Soil Dynamics and Earthquake Engineering, Vol. 28, No. 5, 2008, pp. 387–404.
- [26] Wang J., Qiao P.: *On irregularity-based damage detection method for cracked beams*, International Journal of Solids and Structures, Vol. 45, No. 2, 2008, pp. 688–704.
- [27] Yan G., Duan Z., Ou J., De Stefano A.: *Structural damage detection using residual forces based on wavelet transform*, Mechanical Systems and Signal Processing, Vol. 24, No. 1, 2010, pp. 224–239.

Łączny parametr modalny jako indeks identyfikacji zniszczenia konstrukcji belkowych: podstawy teoretyczne i weryfikacja numeryczna

W pracy zaproponowano nowy indeks wykrywania stanu uszkodzenia w elementach konstrukcyjnych, który bazuje na łącznym wykorzystaniu parametrów modalnych. Indeks wykorzystuje efekt zmian częstości własnych i zmian kształtu formy własnej, które towarzyszą zmianie sztywności uszkodzonego elementu. Znaczenie i możliwości proponowanego podejścia porównano z innymi algorytmami wykrywania uszkodzeń wykorzystując w tym celu analizę konstrukcji belkowych metodą elementów skończonych. Nowy indeks (*Combined Parameter Index (CPI)*) porównuje efekt redukcji sztywności ze zmianą częstości i zmianą kształtu formy własnej. Testowano różne poziomy i usytuowania miejsc obniżenia sztywności modelujące stopień degradacji konstrukcji w celu kalibracji wrażliwości proponowanego indeksu zniszczenia. CPI testowano także na konstrukcjach z uszkodzonymi więziami podporowymi. Otrzymane wyniki wskazują, że proponowany indeks CPI wykazuje duże możliwości i wrażliwość – jest skuteczny już od poziomu 1% utraty sztywności – w wykrywaniu stanu uszkodzeń elementów i więzi podporowych konstrukcji.

Pore structure of self-compacting concretes made using different superplasticizers

T. GORZELAŃCZYK, J. HOŁA

Wrocław University of Technology, Wybrzeże Wyspiańskiego 27, 50-370 Wrocław, Poland.

The paper presents the results of investigations into the pore structure of self-compacting concretes made from the same components, except for the added (two most commonly used in building practice) superplasticizers. It is shown that the pore structure depends on the superplasticizer used. Also the results of tests carried out to determine the mechanical properties of the investigated concretes, including their compressive strength and the levels of cracking initiating stress and critical stress (demarcating the particular stages in failure under compression), are presented. It is shown that the properties depend on the pore structure.

Keywords: *pore structure, superplasticizer, self-compacting concrete, acoustic methods, failure*

1. Introduction

The structure of hardened concrete includes various pores of different sizes, which reduce the effective load-bearing cross section. According to a common size-based classification of pores, in hardened concrete one can distinguish gel pores, capillary pores and macropores [8, 18]. The diameters of gel pores range from 0.5 to 10 nm depending on the gel crystal structure. Capillary pores have diameters in a range of 10 nm–10 µm and form a network of ducts. Macropores have diameters in a range of 0.1–1.0 mm and form due to the excess of batched water and air bubbles trapped (e.g. under larger aggregate grains) as concrete mix is being vibrated and laid.

Porosity is a physical property which strongly determines the mechanical characteristics of hardened concrete [16, 18]. Besides the total pore volume, also the pore structure is a major determinant in new generation concretes, such as self-consolidating concretes. One can suppose that the pore structure to a considerable degree depends on the chemical admixtures, especially superplasticizers, added to the concrete mix. Such admixtures may have a similar effect on the rheological properties of concrete mix but they may considerably differ in their contribution to the total pore volume and structure. Knowledge in this regard is limited because of insufficient research. The present research at least partially remedies this deficiency.

Considering the above, the pore structure of four self-compacting concretes made from the same components, except for the added (two most commonly used in build-

ing practice) superplasticizers based on different chemicals was investigated. Selected mechanical properties, i.e. compressive strength, the level of cracking initiating stress and the level of critical stress, of the concretes were determined. It is generally accepted that these properties have a bearing on the durability of concrete [1–4, 8–9, 11–12, 15, 19].

2. Description of tests

Four self-compacting concretes, denoted as A/SA, B/SA, C/SV and D/SV, made from the same components, i.e. Portland cement CEM I 42.5R, gravel aggregate, river sand, fly ash, tap drinking water and two different superplasticizers, were subjected to tests.

The maximum aggregate grading was 16 mm for concretes A/SA and C/SV and 8 mm for concretes B/SA and D/SV.

Concretes A/SA and B/SA were made using a superplasticizer denoted as SA while concretes C/SV and D/SV were made using superplasticizer SV. Superplasticizer SA was based on polycarboxylic ether whereas superplasticizer SV was based on polycarboxylans as well as viscosity, bonding and hardening regulators.

Since they contain polycarboxylan PA polymers, according to [12] the two superplasticizers belong to the group of modified sulphonates. It should be noted that at the time of the tests, the two superplasticizers were the most popular superplasticizers added to self-compacting concrete mixes.

The compositions of the designed concrete mixes were as follows:

- coarse aggregate – 1064 kg/m³ (concrete A/SA and C/SV), 896 kg/m³ (concrete B/SA and D/SV),
 - sand – 581 kg/m³ (concrete A/SA and C/SV), 747 kg/m³ (concrete B/SA and D/SV),
 - cement – 355 kg/m³ (concrete A/SA and C/SV), 325 kg/m³ (concrete B/SA and D/SV),
 - fly ash – 143 kg/m³ (concrete A/SA and C/SV), 109 kg/m³ (concrete B/SA and D/SV),
 - water – 164 kg/m³ (concrete A/SA and C/SV), 195 kg/m³ (concrete B/SA and D/SV),
 - superplasticizer – 3.15 kg/m³ concrete A/SA, 3.25 kg/m³ concrete B/SA, 4.18 kg/m³ concrete C/SV and 4.25 kg/m³ concrete D/SV.

The concrete mixes made from the above components were subjected to Abrams cone, J-Ring and L-box tests to determine their basic rheological properties [6, 21]. The test results showed that as regards their rheological properties, the designed concrete mixes met the requirements which self-compacting mixes should satisfy [13, 17, 21]. It became also apparent that despite the fact that the mixes differed in their superplasticizers and in their maximum aggregate grading (16 and 8 mm), they were characterized by similar rheological properties [6].

Average compressive strength f_{cm} of the concretes made from the mixes, determined by carrying out tests on ten $150 \times 150 \times 150$ mm specimens of each of the concretes, after 90 days of curing in a climatic chamber at an air temperature of $+18^\circ\text{C}$ ($\pm 1^\circ\text{C}$) and a relative air humidity of 95% ($\pm 5\%$) amounted to: 44.52 MPa for concrete A/SA, 32.41 MPa for concrete B/SA, 59.22 MPa for concrete C/SV and 41.82 MPa for concrete D/SV.

The pore structure of the 90-day hardened concretes was investigated by carrying out studies on six specimens of each concrete, using a computer image analyzer for a pore diameter range of 10–4000 μm and a mercury porosimeter for a pore diameter range of 10–15000 nm [6–7]. The following parameters were determined by means of the image analyzer:

- the total air content (A),
- the content of micropores less than 0.3 mm in diameter (A_{300}),
- the pore distribution indicator (\bar{L}),
- the specific air pore surface (α).

The following parameters were determined by means of the mercury porosimeter:

- the total porosity (p),
- the specific pore volume (V),
- the average pore radius (\bar{r}),
- the specific pore surface (α').

3. Results of pore structure studies and their analysis

The results of the studies of the pores in the 90-day self-compacting concretes are compared in table 1 for respectively concretes A/SA and B/SA and C/SV and D/SV.

Table 1. Averaged values of selected parameters characterizing pore structure in compared concretes A/S.A. and C/SV and B/SA and D/SV

Concrete batch symbol	Investigated parameter							
	Total air content in hardened concrete A [%]	Below – 0.3 mm-diameter pore content A_{300} [%]	Air pore distribution Index \bar{L} [mm]	Specific air pore surface area α [mm^{-1}]	Total porosity p [%]	Specific pore volume V [mm^3/g]	Average pore radius \bar{r} [nm]	Specific pore surface area α' [m^2/g]
A/SA	6.70	1.50	0.26	17	12.71	24.08	3.90	7.12
B/SA	8.30	2.96	0.11	36	13.02	32.81	6.20	3.97
C/SV	2.90	0.70	0.33	21	11.90	17.85	6.15	2.66
D/SV	4.45	1.74	0.13	45	12.44	29.35	15.70	2.88

Table 1 shows that total air content A , the content of micropores less than 0.3 mm in diameter (A_{300}), total porosity p , specific pore volume V and specific pore surface α in concrete C/SV modified with superplasticizer SV are considerably lower than in

concrete A/SA modified with superplasticizer SA. Whereas pore distribution indicator \bar{L} , average pore radius \bar{r} and specific air pore surface α are higher for concrete C/SV. It can be concluded from the results that the polycarboxylic ether contained in superplasticizer SA causes considerable aeration of the self-compacting concrete. A similar conclusion also emerges from the research conducted by the authors of [5, 14, 20].

Graphs illustrating the distribution of pores in the investigated concretes are presented in Figures 1–4. Exemplary images of the structure of concretes A/SA and B/SA and C/SV and D/SV, with visible pores of various sizes are shown in respectively Figure 5 and 6.

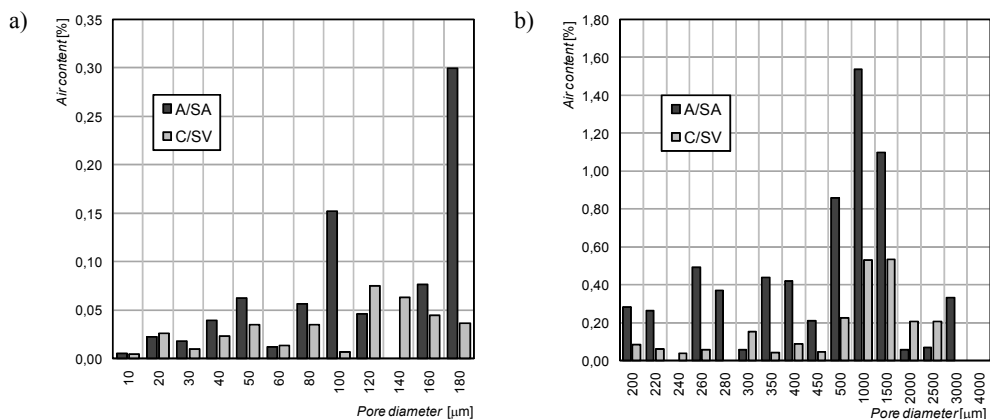


Fig. 1. Averaged distribution of pore content in concretes A/SA and C/SV depending on pore diameter in range of: a) 10–180 μm , b) 200–4000 μm

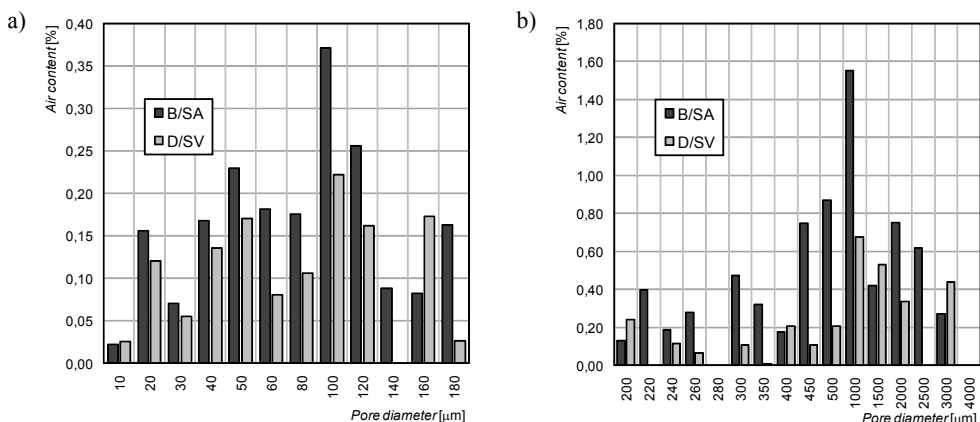


Fig. 2. Averaged distribution of pore content in concretes B/SA and D/SV depending on pore diameter in range of: a) 10–180 μm , b) 200–4000 μm

It appears from Figure 1 that the air content in concrete C/SV is lower in the whole investigated range of macropores. This is particularly visible in the pore diameter range of 180–1500 µm. A similar conclusion emerges from Figure 4, except that in the whole considered range of pore diameters the porosity of concrete C/SV is lower than that of concrete A/SA. Hence one can conclude that the pore structure of concrete C/SV modified with superplasticizer SV is characterized by more advantageous parameters than that of concrete A/SA. Similar conclusions regarding concretes B/SA and D/SV emerge from Table 1 and Figure 2, i.e. concrete D/SV modified with superplasticizer SV has more advantageous pore structure parameters.

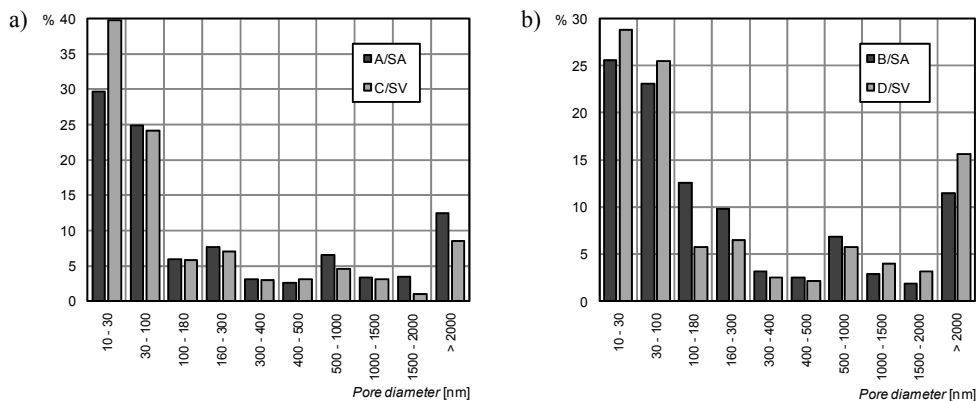


Fig. 3. Averaged pore content percentage within pore diameter range of 10–15000 nm for concretes: a) A/SA and C/SV, b) B/SA and D/SV

It appears from Figure 3 that the percentage of capillary pores with a radius of 10–15000 nm is smaller in concrete C/SV than in concrete A/SA. Practically, only in the pore radius range of 10–30 nm concrete C/SV has a higher percentage of pores. Whereas in the case of concrete D/SV a similar regularity is observed only within a pore radius of 100–1000 nm. It clearly emerges from this analysis that the pore structure differs between the investigated self-compacting concretes, depending on the superplasticizer used to modify the concrete mix. It also appears that the pore structure in concrete C/SV modified with superplasticizer SV and in concrete D/SV modified with superplasticizer SV is characterized by more advantageous parameters than the pore structure of respectively concrete A/SA and concrete B/SA.

If one examines Figure 5 one can conclude that the large pores visible in concrete A/SA were produced by air bubbles trapped in the concrete mix. Such pores also occur in concrete C/SV, but they are smaller than in concrete A/SA. In concrete B/SA, besides the pores produced by air bubbles trapped in the concrete mix there is a large number of air voids at the aggregate/matrix interface. Also in concrete D/SV air voids are visible at the aggregate/matrix interface, but they are much fewer in number than

in concrete B/SA. The results of the above analysis are consistent with the results presented in Table 1, particularly with regard to total air content A .

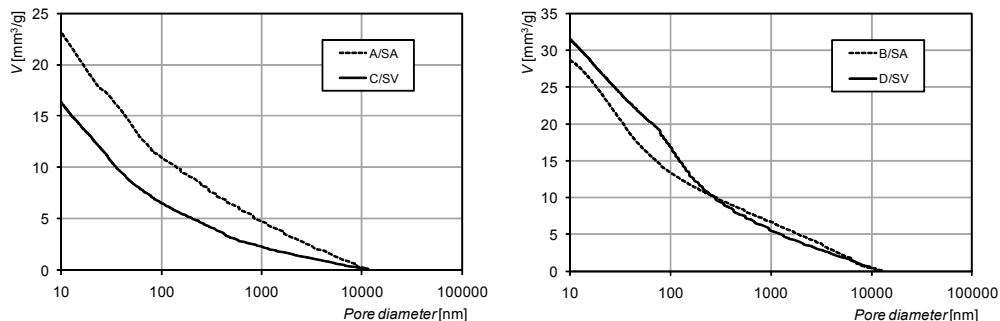


Fig. 4. Porosity (average values) within pore diameter range of 10–15000 nm (pore volume–pore diameter curves) for concretes: a) A/SA and C/SV, b) B/SA and D/SV

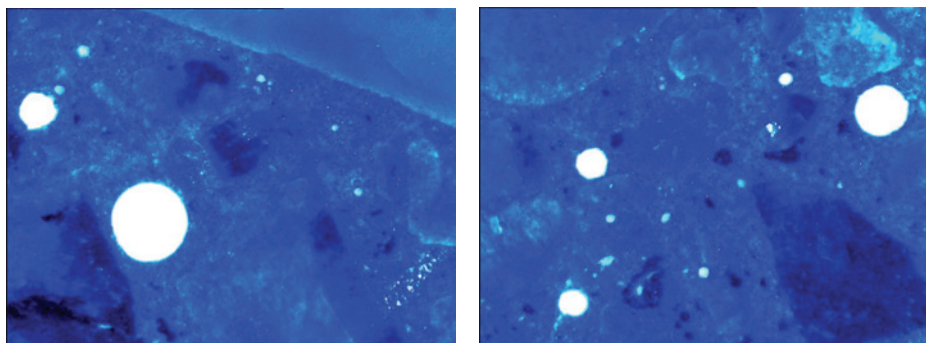


Fig. 5. Exemplary images of structure of concrete A/SA (left) and concrete C/SV (right), magnification about 30×, with clearly visible pores

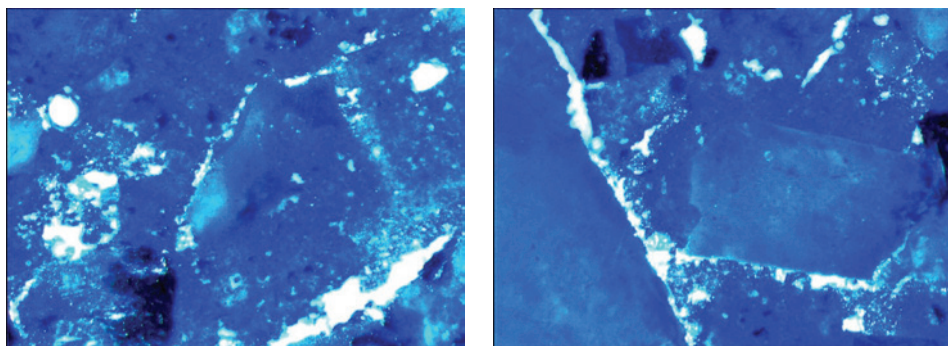


Fig. 6. Exemplary images of structure of concrete B/SA (left) and concrete D/SV (right), magnification about 30×, with clearly visible pores

From the above it clearly emerges that the pore structure is significantly different between the investigated concretes. Undoubtedly it depends on the superplasticizer used to modify the concrete mix. It also becomes apparent that the pore structure in concrete C/SV modified with superplasticizer SV and in concrete D/SV modified with superplasticizer SV is characterized by more advantageous parameters than the pore structure of respectively concrete A/SA and concrete B/SA.

4. Effect of pore structure on selected mechanical properties of investigated concretes

In order to prove that the pore structure affects the selected mechanical properties of the investigated concretes, compressive strength tests were carried out after 90 days of curing and the failure of the concretes under compression was investigated by means of acoustic techniques [6, 10]. Figure 7 shows the averages values of compression strength f_{cm} of the concretes.

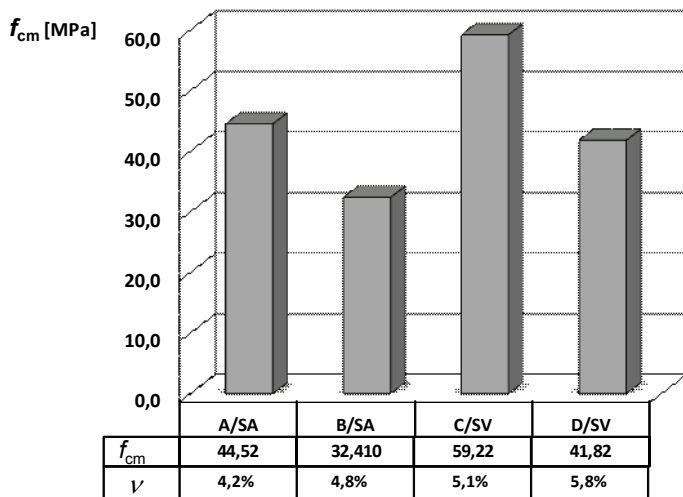


Fig. 7. Average values of compressive strength f_{cm} of investigated self-compacting concretes (ν – coefficient of variation)

The average levels of cracking initiating stress σ_{im} and critical stress σ_{crm} , demarcating the particular stages in the failure of the concrete under compression, determined for all the investigated self-compacting concretes according to the criteria given in [6, 8] are shown in Figures 8 and 9. The levels of the respective stresses were determined by two methods: the ultrasonic method applied to two specimens and the acoustic emission method applied to six specimens. It should be noted that stress σ_i demarcates the stage of stable initiation of cracks and that of the stable propagation of

cracks while stress σ_{cr} demarcates the stages of stable and unstable propagation of cracks [4, 6, 8].

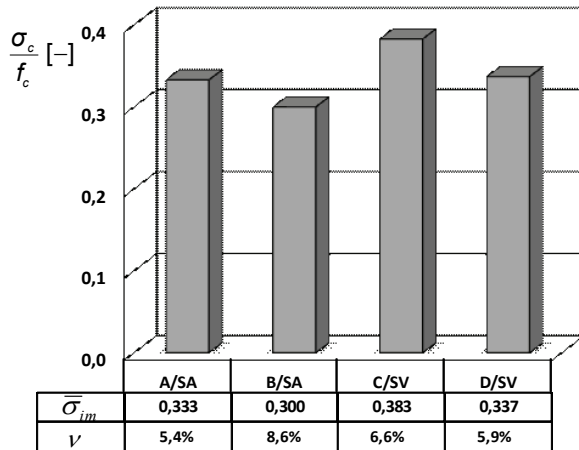


Fig. 8. Average levels of cracking initiating stress σ_{im} , determined for investigated self-compacting concretes (v – coefficient of variation)

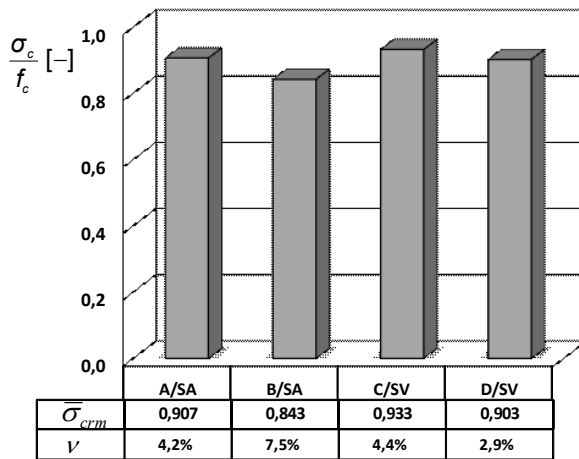


Fig. 9. Average levels of critical stress σ_{crm} determined for investigated self-compacting concretes (v – coefficient of variation)

As it appears from Figures 7–9, concrete C/SV in comparison with the series A/SA concrete is characterized by a higher compressive strength and higher average values of cracking initiating stress σ_{im} and higher levels of critical stress σ_{crm} . The same is

observed for concrete D/SV as compared with concrete B/SA. It should be noted that concretes C/SV and D/SV were made using superplasticizer SV.

From the analysis of Figures 7–9 and Table 1 it emerges that in self-compacting concrete C/SV higher levels of cracking initiating stress σ_{im} and critical stress σ_{crm} correspond to the lower air content (A) and the lower total porosity (p). This may be due to the lower air content in the hardened concrete while the lower total porosity means fewer weak structural points. As a result, the concrete is characterized by higher compressive strength and the stable development of microcracks during failure starts at a higher strain.

It also becomes apparent that the higher values of pore distribution indicator \bar{L} and air pore specific surface α correspond to the higher levels of both stress σ_{im} and stress σ_{crm} . A comparison of concrete C/SV with concrete A/SA shows that the former is characterized by higher values of parameters \bar{L} and α . Hence one can conclude that when air pores are spaced farther apart from one another in the structure of concrete and their specific surface is larger, the structure is more uniform. This is reflected not only in higher compressive strength, but also in the fact that the stable propagation of cracks begins at a higher level of compressive stress and the stage of catastrophic failure becomes slightly shorter. As regards the compared concretes B/SA and D/SV, the obtained results are similar to the ones for concretes A/SA and C/SV and similar conclusions can be drawn from them.

5. Conclusion

The four self-compacting concretes, made from the same concrete mixes differing in the added superplasticizer, have similar rheological properties but differ in their pore structure. The investigations have shown that the pore structure clearly depends on the superplasticizer added to the concrete mix. When superplasticizer SV, based on a combination of polycarboxylans and viscosity, bonding and hardening regulators, is added to concrete mix, the structure of the obtained concrete is characterized by more advantageous parameters than those characterizing the structure of the concrete made from the concrete mix to which superplasticizer SA based on polycarboxylic ether was added.

It has also been found that the self-compacting concretes made using superplasticizer SV, besides being characterized by more advantageous porosity parameters, show much higher compressive strength and markedly higher cracking initiating stress and critical stress levels in comparison with those of the concretes made using superplasticizer SA.

The research findings, indicating that the pore structure has a significant bearing on the mechanical properties of self-compacting concrete and so on its durability, are not only of theoretical value, but also have implications for building practice i.e. when designing the composition of self-compacting concretes and deciding on a superplasticizer, one should consider not only the rheological properties of the concrete mix modified with it, but also the pore structure of the concrete made of this mix.

References

- [1] Bień J.: *Defects and diagnostics of bridge structures* (in Polish), Wydawnictwa Komunikacji i Łączności, Warszawa, 2010.
- [2] Błaszczyński T.: *Durability of cement based composite systems influenced by physico-chemical agents*, Durability of polymer based composite systems for structural applications, ed. by Cardon & Verchery, Elsevier Science Publishers Ltd., 1991, pp. 504–513.
- [3] Błaszczyński T.Z.: *The influence of crude oil products on RC structure destruction*, Journal of Civil Engineering and Management, Vol. 17, No. 1, 2011, pp. 146–156.
- [4] Furtak K.: *Concrete's destruction by stress*, Conference: “Days of Concrete – Tradition and Modernity”, Polski Cement, Szczyrk, 2002, pp. 427–439.
- [5] Gołaszewski J.: *Influence of viscosity enhancing agent on rheology and compressive strength of superplasticized mortars*, Journal of Civil Engineering and Management, Vol. 15, No. 2, 2009, pp. 181–188.
- [6] Gorzelańczyk T.: *Assessment of the failure of self-compacting concretes by means of acoustic methods* (in Polish), PhD dissertation. Reports of the Institute of Building Engineering at Wrocław University of Technology, Ser. PRE, No. 9, Wrocław, 2007.
- [7] Gorzelańczyk T., Hoła J.: *Assessment of the failure of self-compacting concretes differing in their air pore structure by acoustic techniques*, Defektoskopie 2007, 37th International Conference, Proceedings. Prague, Czech Republic, 2007, pp. 75–82.
- [8] Hoła J.: *Relation of initiating and critical stress to stress failure* (in Polish), Scientific Papers of the Institute of Building Engineering of the Wrocław University of Technology. No. 76, Monographs No. 33, Wrocław University of Technology Publishing House, Wrocław, 2000.
- [9] Hoła J.: *Experimentally determined effects of technological and service factors on stress-induced destruction of concrete under compression*. *Engineering Transactions*, Vol. 50, No. 4, 2002, pp. 251–265.
- [10] Hoła J., Kapelko A., Schabowicz K.: *Non-destructive assessment of the strength of self-compacting concrete*, Technologies for sustainable development in regions. TECHSTA 2004, 4th International conference [Electronic document], Prague, CVUT, 2004, pp. 113–118.
- [11] Jamroży Z.: *Concrete and its technologies* (in Polish), Wydawnictwo Naukowe PWN, Warsaw–Cracow, 2005.
- [12] Kurkowski W.: *Cement and concrete chemistry* (in Polish), Association of Cement Producers, Cracow, 2010.
- [13] Li L., Hwang C.: *The mixture proportion and property of SCC*, Proceeding PRO33 – 3rd International RILEM Symposium: Self-Compacting Concrete. RILEM Publications S.A.R.L., 2003, pp. 525–529.
- [14] Łażewska-Piekarczyk B.: *Effect of viscosity stabilizing agents on the properties of self-compacting mortars and concretes*, Cement–Wapno–Beton, No. 1, 2011, pp. 44–51.
- [15] Mačiulaitis R., Vaičienė M., Žurauskienė R.: *The effect of concrete composition and aggregates properties on performance of concrete*, Journal of Civil Engineering and Management, Vol. 15, No. 3, 2009, pp. 317–324.
- [16] Mehta P.K.: *Hardened cement paste-microstructure and its relation to properties*, VIII International Congress Chem., Cement, Rio de Janerio, Vol. 1, 1986, pp. 113–121.
- [17] Nagamoto N., Ozawa K.: *Mixture properties of self-compacting, high-performance concrete*, ACI Materials Journal, Vol. 172, 1999, pp. 623–636.

- [18] Neville A.M.: *Właściwości betonu*, Polski Cement, Kraków, 2000.
- [19] Paczkowski P., Kaszyńska M., Nowak A.S., Lutomirski T.: *Self-consolidating concrete for on-site bridge applications*, Fifth international conference on current and future trends in Bridge design, construction and maintenance: proceedings of the two day international conference ed. Robert Lark London: Thomas Telford Publishing, 2007, pp. 312–320.
- [20] Szwabowski J., Łażewska-Piekarczyk B.: *Air-entrainment problem in self-compacting concrete*, Journal of Civil Engineering and Management, Vol. 15, No. 2, 2009, pp. 137–147.
- [21] The European Guidelines for Self-Compacting Concrete. Specification, Production and Use. EFNARC The European Federation of Specialist Construction Chemicals and Concrete Systems, May 2005. Available from internet: <http://www.efnarc.org/pdf/SCCGuidelinesMay2005.pdf>

Struktura porów w betonach samozagęszczonych wykonanych z użyciem różnych superplastyfikatorów

W pracy przedstawiono wyniki badań struktury porów kilku betonów samozagęszczonych, wykonanych z użyciem takich samych składników i dwóch najczęściej stosowanych w praktyce superplastyfikatorów. Wykazano, że struktura porów zależy od użytego superplastyfikatora. Zaprezentowano także wyniki badań podstawowych cech mechanicznych badanych betonów, w tym wytrzymałości na ściskanie i poziomów naprężzeń inicjujących pękanie i krytycznych rozgraniczających procesy niszczenia pod wpływem obciążen ścis kających. Wykazano, że cechy te zależą od struktury porów.

Modelling of reinforced concrete structures and composite structures with concrete strength degradation taken into consideration

P. KMIECIK, M. KAMIŃSKI

Wrocław University of Technology, Wybrzeże Wyspiańskiego 25, 50-370 Wrocław, Poland.

Because of the properties of the material (concrete), computer simulations in the field of reinforced concrete structures pose a challenge. As opposed to steel, concrete when subjected to compression exhibits nonlinearity right from the start. Moreover, it much quicker undergoes degradation under tension. All this poses difficulties for numerical analyses. Parameters needed to correctly model concrete under compound stress are described in this paper. The parameters are illustrated using the Concrete Damaged Plasticity model included in the ABAQUS software.

Keywords: *numerical modelling, concrete degradation, stress-strain relation, reinforced concrete structures, composite structures, Abaqus, concrete damaged plasticity*

1. Introduction

The two main concrete failure mechanisms are cracking under tension and crushing under compression. However, concrete strength determined in simple states of stress (uniaxial compression or tension) radically differs from the one determined in complex states of stress. For example, the same concrete under biaxial compression reaches strength of between ten and twenty per cent higher than in the uniaxial state while in the hydro-static state (uniform triaxial compression) its strength is theoretically unlimited. In order to describe strength with the equation for triaxial stress, its plane should be presented in a three-dimensional stress space (since concrete is considered to be an isotropic material in a wide range of stress). The states of stress corresponding to material failure are on this surface while the states of safe behaviour are inside. Also the so-called plastic potential surface is located inside this space. After the plasticity surface is crossed, two situations arise [9]:

- an increase in strain with no change in stress (ideal plasticity),
- material weakening (rupture).

2. Strength hypothesis and its parameters

One of the strength hypotheses most often applied to concrete is the Drucker-Prager hypothesis (1952). According to it, failure is determined by non-dilatational strain energy and the boundary surface itself in the stress space assumes the shape of a

energy and the boundary surface itself in the stress space assumes the shape of a cone. The advantage of the use of this criterion is surface smoothness and thereby no complications in numerical applications. The drawback is that it is not fully consistent with the actual behaviour of concrete 0.

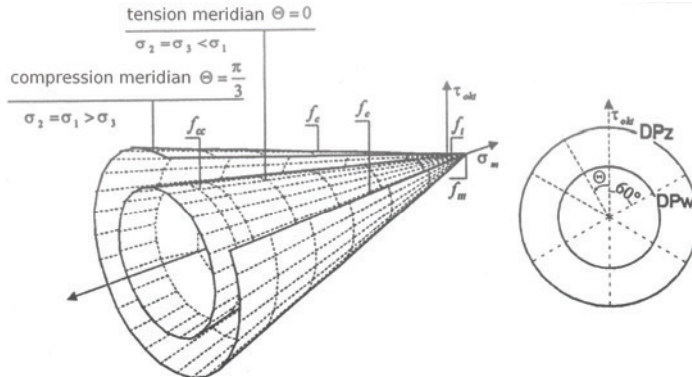


Fig. 1. Drucker-Prager boundary surface 0: a) view, b) deviatoric cross section

The CDP (Concrete Damaged Plasticity) model used in the ABAQUS software is a modification of the Drucker-Prager strength hypothesis. In recent years the latter has been further modified by Lubliner 0, Lee and Fenves 0. According to the modifications, the failure surface in the deviatoric cross section needs not to be a circle and it is governed by parameter K_c .

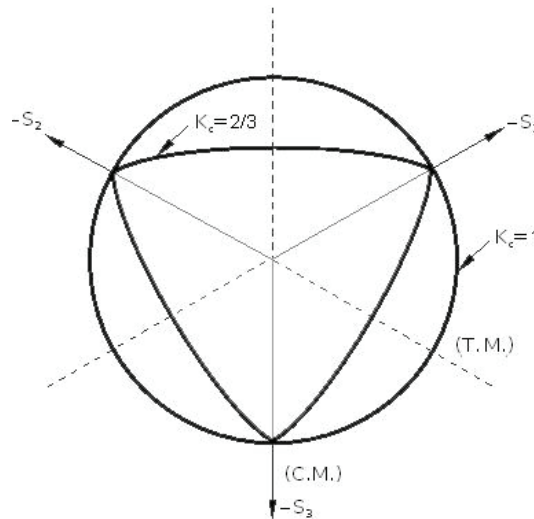


Fig. 2. Deviatoric cross section of failure surface in CDP model 0

Physically, parameter K_c is interpreted as a ratio of the distances between the hydrostatic axis and respectively the compression meridian and the tension meridian in the deviatoric cross section. This ratio is always higher than 0.5 and when it assumes the value of 1, the deviatoric cross section of the failure surface becomes a circle (as in the classic Drucker–Prager strength hypothesis). Majewski reports that according to experimental results this value for mean normal stress equal to zero amounts to 0.6 and slowly increases with decreasing mean stress. The CDP model recommends to assume $K_c = 2/3$. This shape is similar to the strength criterion (a combination of three mutually tangent ellipses) formulated by William and Warnke (1975). It is a theoretical-experimental criterion based on triaxial stress test results.

Similarly, the shape of the plane's meridians in the stress space changes. Experimental results indicate that the meridians are curves. In the CDP model the plastic potential surface in the meridional plane assumes the form of a hyperbola. The shape is adjusted through *eccentricity* (plastic potential eccentricity). It is a small positive value which expresses the rate of approach of the plastic potential hyperbola to its asymptote. In other words, it is the length (measured along the hydrostatic axis) of the segment between the vertex of the hyperbola and the intersection of the asymptotes of this hyperbola (the centre of the hyperbola). Parameter *eccentricity* can be calculated as a ratio of tensile strength to compressive strength [4]. The CDP model recommends to assume $\epsilon = 0.1$. When $\epsilon = 0$, the surface in the meridional plane becomes a straight line (the classic Drucker-Prager hypothesis).

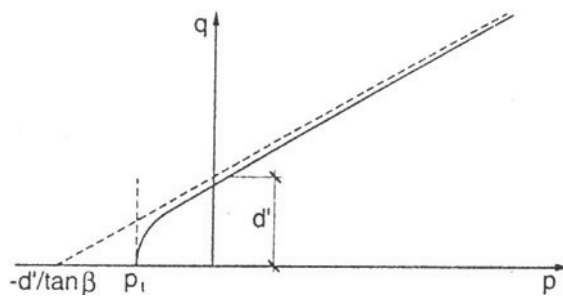


Fig. 3. Hyperbolic surface of plastic potential in meridional plane 0

Another parameter describing the state of the material is the point in which the concrete undergoes failure under biaxial compression. σ_{b0}/σ_{c0} (f_{b0}/f_{c0}) is a ratio of the strength in the biaxial state to the strength in the uniaxial state. The most reliable in this regard are the experimental results reported by Kupler (1969). After their approximation with the elliptic equation, uniform biaxial compression strength f_{cc} is equal to $1.16248 f_c$. The ABAQUS user's manual specifies default $\sigma_{b0}/\sigma_{c0} = 1.16$.

The last parameter characterizing the performance of concrete under compound stress is *dilation angle*, i.e. the angle of inclination of the failure surface towards the

hydrostatic axis, measured in the meridional plane. Physically, dilation angle ψ is interpreted as a concrete internal friction angle. In simulations usually $\psi = 36^\circ$, 0,0 or $\psi = 40^\circ$ 0 is assumed.

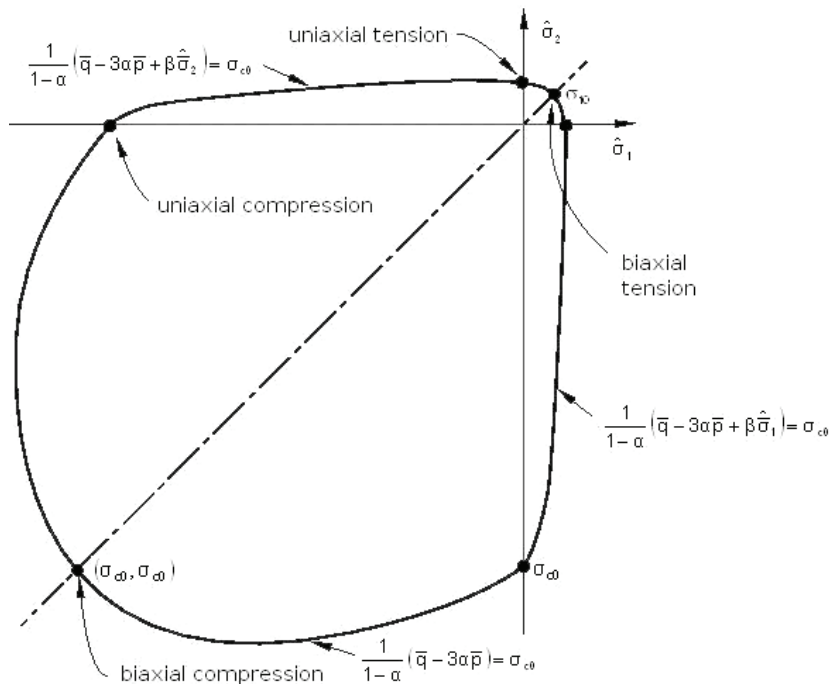


Fig. 4. Strength of concrete under biaxial stress in CDP model 0

Table 1. Default parameters of CDP model under compound stress

Parameter name	Value
Dilatation angle	36
Eccentricity	0.1
f_{bo}/f_{co}	1.16
κ	0.667
Viscosity parameter	0

The unquestionable advantage of the CDP model is the fact that it is based on parameters having an explicit physical interpretation. The exact role of the above parameters and the mathematical methods used to describe the development of the boundary surface in the three-dimensional space of stresses are explained in the ABAQUS user's manual. The other parameters describing the performance of concrete are determined for uniaxial stress. Table 1 shows the model's parameters characterizing its performance under compound stress.

3. Stress-strain curve for uniaxial compression

The stress-strain relation for a given concrete can be most accurately described on the basis of uniaxial compression tests carried out on it. Having obtained a graph from laboratory tests one should transform the variables. Inelastic strains $\tilde{\varepsilon}_c^{in}$ are used in the CDP model. In order to determine them one should deduct the elastic part (corresponding to the undamaged material) from the total strains registered in the uniaxial compression test:

$$\tilde{\varepsilon}_c^{in} = \varepsilon_c - \varepsilon_{0c}^{el}, \quad (1)$$

$$\varepsilon_{0c}^{el} = \frac{\sigma_c}{E_0}. \quad (2)$$

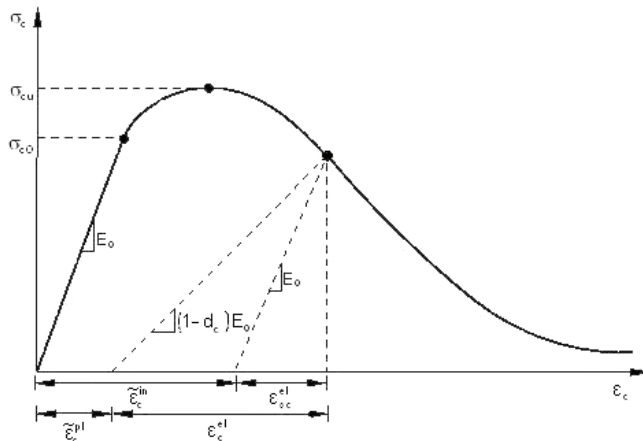


Fig. 5. Definition of inelastic strains 0

When transforming strains, one should consider from what moment the material should be defined as nonlinearly elastic. Although uniaxial tests show that such behaviour occurs almost from the beginning of the compression process, for most numerical analyses it can be neglected in the initial stage. According to Majewski, a linear elasticity limit should increase with concrete strength and it should be rather assumed than experimentally determined. He calculated it as a percentage of stress to concrete strength from this formula:

$$e_{lim} = 1 - \exp\left(\frac{-f_c}{80}\right). \quad (3)$$

This ceiling can be simply arbitrarily assumed as $0.4 f_{cm}$. Eurocode 2 specifies the modulus of elasticity for concrete to be secant in a range of $0\text{--}0.4 f_{cm}$. Since the basic definition of the material already covers the shear modulus and the longitudinal modulus of concrete, at this stage it is good to assume such an inelastic phase threshold that the initial value of Young's modulus and the secant value determined according to the standard will be convergent. In most numerical analyses it is rather not the initial behaviour of the material, but the stage in which it reaches its yield strength which is investigated. Thanks to the level of $0.4 f_{cm}$ there are fewer problems with solution convergence.

Having defined the yield stress-inelastic strain pair of variables, one needs to define now degradation variable d_c . It ranges from zero for an undamaged material to one for the total loss of load-bearing capacity. These values can also be obtained from uniaxial compression tests, by calculating the ratio of the stress for the declining part of the curve to the compressive strength of the concrete. Thanks to the above definition the CDP model allows one to calculate plastic strain from the formula:

$$\tilde{\varepsilon}_c^{pl} = \tilde{\varepsilon}_c^{in} - \frac{d_c}{(1-d_c)} \frac{\sigma_c}{E_0}, \quad (4)$$

where E_0 stands for the initial modulus of elasticity for the undamaged material. Knowing the plastic strain and having determined the flow and failure surface area one can calculate stress σ_c for uniaxial compression and its effective stress $\bar{\sigma}_c$.

$$\sigma_c = (1-d_c) E_0 (\varepsilon_c - \tilde{\varepsilon}_c^{pl}), \quad (5)$$

$$\bar{\sigma}_c = \frac{\sigma_c}{(1-d_c)} = E_0 (\varepsilon_c - \tilde{\varepsilon}_c^{pl}). \quad (6)$$

3.1. Plotting stress-strain curve without detailed laboratory test results

On the basis of uniaxial compression test results one can accurately determine the way in which the material behaved. However, a problem arises when the person running such a numerical simulation has no such test results or when the analysis is performed for a new structure. Then often the only available quantity is the average compressive strength (f_{cm}) of the concrete. Another quantity which must be known in order to begin an analysis of the stress-strain curve is the longitudinal modulus of elasticity (E_{cm}) of the concrete. Its value can be calculated using the relations available in the literature 0:

$$E_{cm} = 22(0.1 f_{cm})^{0.3}, \quad (7)$$

where:

$$f_{cm} \text{ [MPa]},$$

$$E_{cm} \text{ [GPa]}.$$

Other values defining the location of characteristic points on the graph are strain ε_{c1} at average compressive strength and ultimate strain ε_{cu} 0:

$$\varepsilon_{c1} = 0.7(f_{cm})^{0.31}, \quad (8)$$

$$\varepsilon_{cu} = 3.5 \%. \quad (9)$$

The formulas (8–9) are applicable to concretes of grade C50/60 at the most.

On the basis of experimental results Majewski proposed the following (quite accurate) approximating formulas:

$$\varepsilon_{c1} = 0.0014[2 - \exp(-0.024 f_{cm}) - \exp(-0.140 f_{cm})], \quad (10)$$

$$\varepsilon_{cu} = 0.004 - 0.0011[1 - \exp(-0.0215 f_{cm})]. \quad (11)$$

Knowing the values of the above one can determine the points which the graph should intersect.

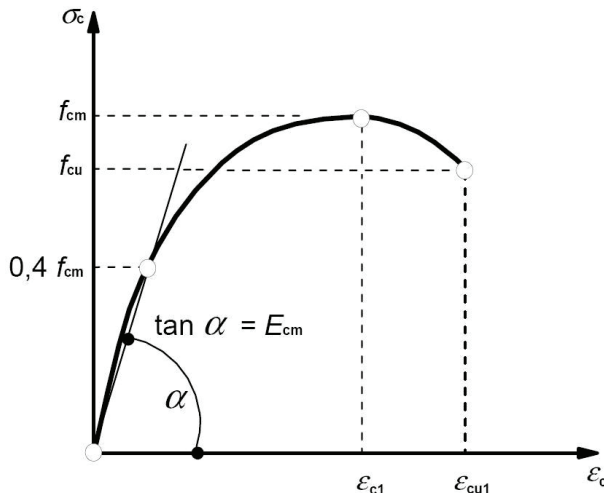


Fig. 6. Stress-strain diagram for analysis of structures, according to Eurocode 2

The curve can be also plotted on the basis of the literature 0, 0, 0,0,0. The most popular formulas are presented in Table 2, but the original symbols have been replaced with the uniform denotations used in Eurocode 2.

Choosing a proper formula form to describe relation $\sigma_c - \varepsilon_c$ one should note whether the longitudinal modulus of elasticity represents initial value E_c (at stress $\sigma_c = 0$) or that of secant modulus E_{cm} . Most of the formulas use initial modulus E_c which is neither experimentally determined nor taken from the standards. Another important factor is the functional dependence itself. Even though the Madrid parabola has been recognized as a good relation by CEB (Comité Euro-International du Béton), this function is not flexible enough to correctly describe the performance of concrete.

Table 2. Stress-strain relation for nonlinear behaviour of structure

Formula name/ source	Formula form	Variables
Madrid parabola	$\sigma_c = E_c \varepsilon_c \left[1 - \frac{1}{2} \left(\frac{\varepsilon_c}{\varepsilon_{cl}} \right)^2 \right]$	$\sigma_c = f(E_c, \varepsilon_{cl})$
Desay & Krishnan formula	$\sigma_c = \frac{E_c \varepsilon_c}{1 + \left(\frac{\varepsilon_c}{\varepsilon_{cl}} \right)^2}$	$\sigma_c = f(E_c, \varepsilon_{cl})$
EN 1992-1-1	$\sigma_c = f_{cm} \frac{k\eta - \eta^2}{1 + (k-2)\eta}$ $k = 1.05 E_{cm} \frac{\varepsilon_{cl}}{f_{cm}}, \quad \eta = \frac{\varepsilon_c}{\varepsilon_{cl}}$	$\sigma_c = f(E_{cm}, f_{cm}, \varepsilon_{cl})$
Majewski formula	$\begin{aligned} \sigma_c &= E_c \varepsilon_c \text{ if } \sigma_c \leq e_{lim} f_{cm} \\ \sigma_c &= f_{cm} \frac{(e_{lim} - 2)^2}{4(e_{lim} - 1)} \left(\frac{\varepsilon_c}{\varepsilon_{cl}} \right)^2 + \\ &\quad - f_{cm} \frac{(e_{lim} - 2)^2}{2(e_{lim} - 1)} \left(\frac{\varepsilon_c}{\varepsilon_{cl}} \right) + f_{cm} \frac{e_{lim}^2}{4(e_{lim} - 1)} \end{aligned} \quad \left. \begin{array}{l} E_c = \frac{f_{cm}}{\varepsilon_c} (2 - e_{lim}), \\ \text{if } \sigma_c > e_{lim} f_{cm} \end{array} \right\} \quad \sigma_c = f(E_c, f_{cm}, \varepsilon_{cl})$ e_{lim} in formula (3)	
Wang & Hsu formula	$\sigma_c = \zeta f_{cm} \left[2 \left(\frac{\varepsilon_c}{\zeta \varepsilon_{cl}} \right) - \left(\frac{\varepsilon_c}{\zeta \varepsilon_{cl}} \right)^2 \right] \text{ if } \frac{\varepsilon_c}{\zeta \varepsilon_{cl}} \leq 1$ $\sigma_c = \zeta f_{cm} \left[1 - \left(\frac{\varepsilon_c / \zeta \varepsilon_{cl} - 1}{2/\zeta - 1} \right)^2 \right] \text{ if } \frac{\varepsilon_c}{\zeta \varepsilon_{cl}} > 1$	$\sigma_c = f(f_{cm}, \varepsilon_{cl})$
Sáenz formula	$\sigma_c = \frac{\varepsilon_c}{A + B\varepsilon_c + C\varepsilon_c^2 + D\varepsilon_c^3}$ symbols in formula (12)	$\sigma_c = f \left(\frac{E_c, f_{cm}, f_{cu},}{\varepsilon_{cl}, \varepsilon_{cul}} \right)$

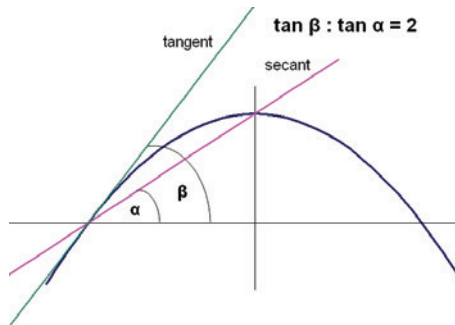
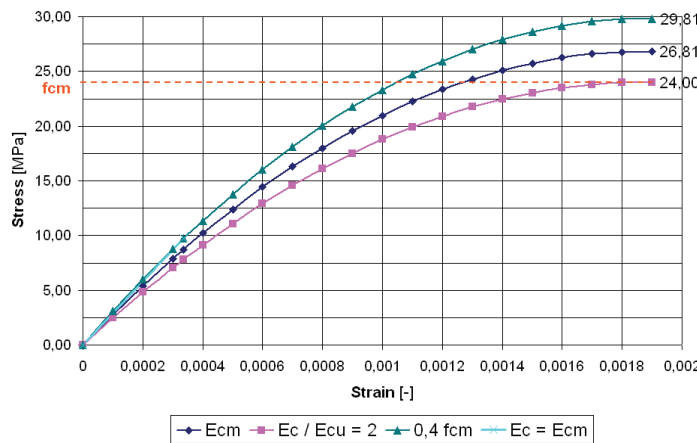


Fig. 7. Property of 2nd order parabola

The 2nd order parabola has this property that the tangent of the angle of a tangent passing through a point on its branch, measured relative to the horizontal axis passing through this point, is always double that of the angle measured as the inclination of the secant passing through the same point and the extremum of the parabola, relative to the same horizontal axis.

Fig. 8. Relation $\sigma_c - \varepsilon_c$ for Madrid parabola depending on longitudinal modulus of elasticity

The consequence of this property of the parabola is either the exceedance of the concrete's strength for a correct initial modulus value or the necessity to lower the value in order to reach a specific stress value in the extreme. Figure 8 shows relation $\sigma_c - \varepsilon_c$ for the Madrid parabola for grade C16/20 concrete. The following batch denotations were assumed:

- $E_{cm} - E_c = E_{cm} = 28608$ MPa was assumed as the initial modulus, calculated extremum $f_{cm} = 26.81$ MPa;
- $E_c/E_{cu} = 2$ – the doubled tangent of the angle of the secant passing through point $(\varepsilon_{c1}, f_{cm})$, amounting to $E_c = 25602$ MPa, calculated extremum $f_{cm} = 24.00$ MPa (correct);

- $0.4f_{cm}$ – the value of initial modulus $E_c = 31808$ MPa matched so that the curve intersects point $(\varepsilon_c, 0.4f_{cm})$, calculated extremum $f_{cm} = 29.81$ MPa;
- $E_c = E_{cm}$ – a straight line describing the elastic behaviour of the concrete up to $(\varepsilon_c, 0.4f_{cm})$.

As one can see, when initial modulus E_c is assumed to amount to E_{cm} , the strength of the concrete is much overrated despite the fact that the initial modulus is still underrated (numerically E_{cm} is not the highest value). In the case of parabolic relations one should artificially lower modulus E_c in order for the graph to intersect the correct value f_{cm} .

A sufficiently detailed description of relation $\sigma_c - \varepsilon_c$ has been proposed by Sáenz. The function with a 3rd order polynomial in the denominator (Table 2) depends on the variables:

$$\left. \begin{aligned} A &= \frac{1}{E_c}, \quad B = \frac{P_3 + P_4 - 2}{P_3 f_{cm}} \\ C &= -\frac{2P_4 - 1}{P_3 f_{cm} \varepsilon_{c1}}, \quad D = \frac{P_4 - 1}{P_3 f_{cm} \varepsilon_{c1}} \\ P_1 &= \frac{\varepsilon_{cu}}{\varepsilon_{c1}}, \quad P_2 = \frac{f_{cm}}{f_{cu}} \\ P_3 &= \frac{E_c \varepsilon_{c1}}{f_{cm}}, \quad P_4 = \frac{P_3(P_2 - 1)}{(P_1 - 1)^2} - \frac{1}{P_1} \end{aligned} \right\} \quad (12)$$

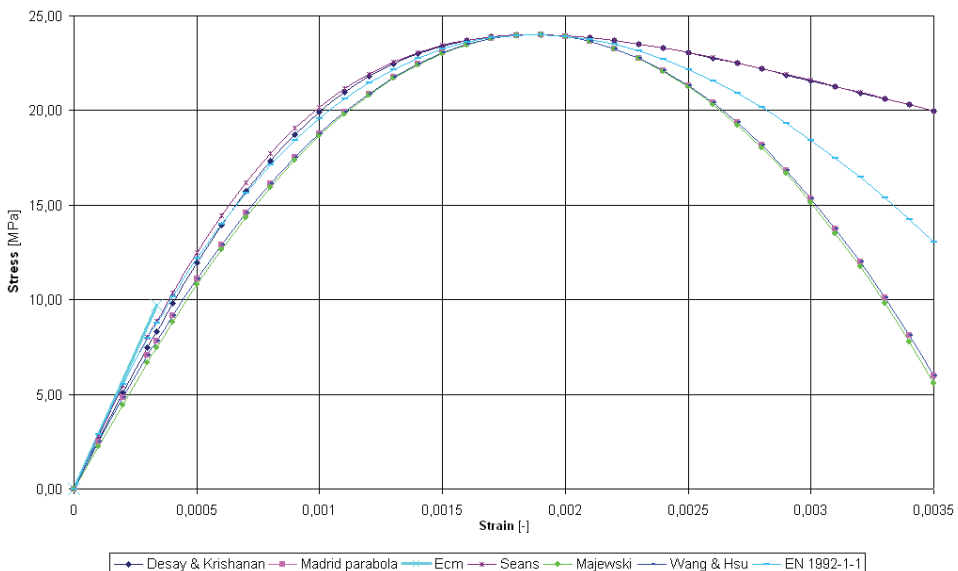


Fig. 9. Comparison of curves $\sigma_c - \varepsilon_c$ based on table 2 relations for grade C16/20 concrete

The above notation allows one to shape the function graph so that it intersects points: $(\varepsilon_{c1}, f_{cm})$ and $(\varepsilon_{cu}, f_{cu})$. The relation proposed by Wang and Hsu is an interesting notation. These are two functions describing the curve's ascending and descending part. They also include coefficient ζ representing the reduction in compressive stress of concrete resulting from locating reinforcing bars in the compressed zone. In figure 9 $\zeta = 1.0$ (no reinforcement taken into account). It is worth noticing that Wang and Hsu relation, the Majewski relation and the Madrid parabola almost coincide. The same applies to the Desay and Krishnan relation and the Sáenz relation, but in the latter case the same point $(\varepsilon_{cu}, f_{cu})$ which followed from the Desay and Krishnan formula was assumed since a lower value of function f_{cu} would result in an improper shape of the curve. The standard relation yields intermediate results.

4. Stress-strain curve for uniaxial tension

The tensile strength of concrete under uniaxial stress is seldom determined through a direct tension test because of the difficulties involved in its execution and the large scatter of the results. Indirect methods, such as sample splitting or beam bending, tend to be used [2]:

$$f_{ctm} = 0.30 f_{ck}^{(2/3)}. \quad (13)$$

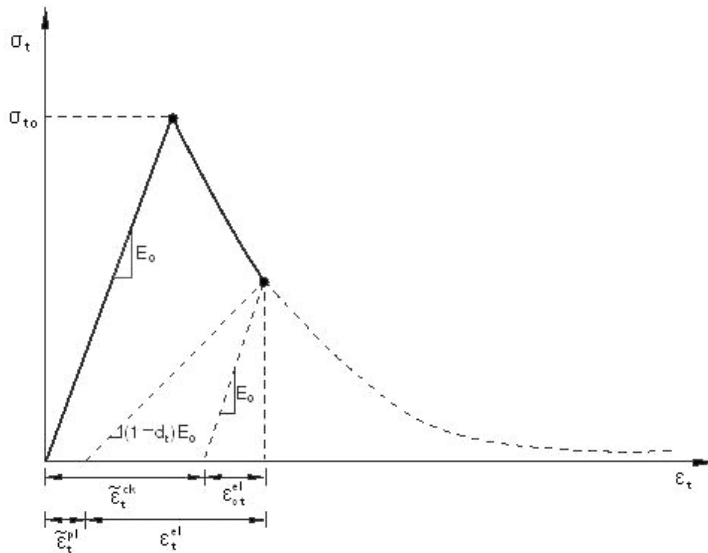


Fig. 10. Definition of strain after cracking – tension stiffening 0

The term *cracking strain* $\tilde{\varepsilon}_t^{ck}$ is used in CDP model numerical analyses. The aim is to take into account the phenomenon called tension stiffening. Concrete under tension is not regarded as a brittle-elastic body and such phenomena as aggregate interlocking

in a crack and concrete-to-steel adhesion between cracks are taken into account. This assumption is valid when the pattern of cracks is fuzzy. Then stress in the tensioned zone does not decrease sharply but gradually. The strain after cracking is defined as the difference between the total strain and the elastic strain for the undamaged material:

$$\tilde{\varepsilon}_t^{ck} = \varepsilon_t - \varepsilon_{0t}^{el}, \quad (14)$$

$$\varepsilon_{0t}^{el} = \frac{\varepsilon_t}{E_c}. \quad (15)$$

Plastic strain $\tilde{\varepsilon}_t^{pl}$ is calculated similarly as in the case of compression after defining degradation parameter d_t .

In order to plot curve $\sigma_t - \varepsilon_t$ one should define the form of the weakening function. According to the ABAQUS user's manual, stress can be linearly reduced to zero, starting from the moment of reaching the tensile strength for the total strain ten times higher than at the moment of reaching f_{ctm} . But to accurately describe this function the model needs to be calibrated with the results predicted for a specific analyzed case.

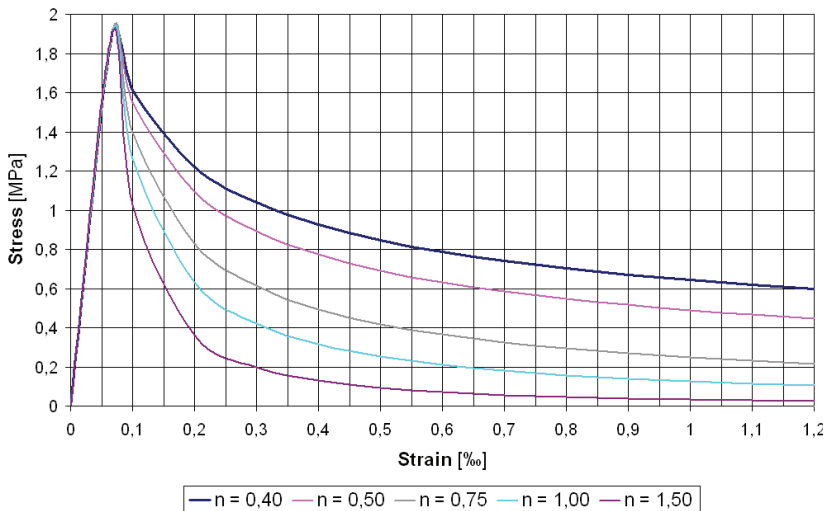


Fig. 11. Modified Wang & Hsu formula for weakening function at tension stiffening for concrete C16/20

The proper relation was proposed by, among others, Wang and Hsu [11]:

$$\left. \begin{aligned} \sigma_t &= E_c \varepsilon_t && \text{if } \varepsilon_t \leq \varepsilon_{cr} \\ \sigma_t &= f_{ctm} \left(\frac{\varepsilon_{cr}}{\varepsilon_t} \right)^{0.4} && \text{if } \varepsilon_t > \varepsilon_{cr} \end{aligned} \right\}, \quad (16)$$

where ε_{cr} stands for strain at concrete cracking. Since tension stiffening may considerably affect the results of the analysis and the relation needs calibrating for a given simulation, it is proposed to use the modified Wang & Hsu formula for the weakening function:

$$\sigma_t = f_{cm} \left(\frac{\varepsilon_{cr}}{\varepsilon_t} \right)^n \quad \text{if } \varepsilon_t > \varepsilon_{cr}, \quad (17)$$

where n represents the rate of weakening.

5. Conclusion

Problems with solution convergence may arise when full nonlinearity of the material (concrete) with its gradual degradation under increasing (mainly tensile) stress is assumed. Simple FE techniques, consisting in reducing the size of stress increment or increasing the maximum number of steps when solving the problem by means of the Newton-Raphson approach, may prove to be insufficient. Therefore the CDP model uses viscosity parameter μ which allows one to slightly exceed the plastic potential surface area in certain sufficiently small problem steps (in order to regularize the constitutive equations). Viscoplastic adjustment consists in choosing such $\mu > 0$ that the ratio of the problem time step to μ approaches infinity. This means that it is necessary to try to match the value of μ a few times in order to find out how big an influence it has on the problem solution result in ABAQUS/Standard and to choose a proper minimum value of this parameter.

The CDP model makes it possible to define concrete for all kinds of structures. It is mainly intended for the analysis of reinforced concrete structures and concrete-concrete and steel-concrete composite structures. However, it is recommended that before an analysis of the structure one should test the behaviour of the material itself, e.g. by carrying out a numerical analysis of cylindrical samples under compression, in order to compare it with the given stress-strain relation. Because of the character of concrete failure, some quantities can be rather assumed than determined in laboratory tests. Therefore the assumptions should be verified by comparing other parameters, e.g. the deflection of the modelled structural component. This means that the model parameters often need to be calibrated several times in the course of the numerical analysis.

Wrocław Centre for Networking and Supercomputing holds a licence for the Abaqus software (<http://www.wcss.wroc.pl>), grant No. 56.

References

- [1] ABAQUS: *Abaqus analysis user's manual*, Version 6.9, 2009, Dassault Systèmes.
- [2] *Eurocode 2: Design of concrete structures. Part 1-1: general rules and rules for buildings*, Brussels, 2004.

- [3] Godycki-Ćwirko T.: *The mechanics of concrete*, Arkady, Warsaw, 1982.
- [4] Jankowiak I., Kąkol W., Madaj A.: *Identification of a continuous composite beam numerical model, based on experimental tests*, 7th Conference on Composite Structures, Zielona Góra, 2005, pp. 163–178.
- [5] Jankowiak I., Madaj A.: *Numerical modelling of the composite concrete-steel beam inter-layer bond*, 8th Conference on Composite Structures, Zielona Góra, 2008, pp. 131–148.
- [6] Kmita A., Kubiak J.: *Investigation of concrete structures. Guide to laboratory classes*, Wrocław University of Technology Publishing House, Wrocław, 1993.
- [7] Lee J., Fenves G.L.: *Plastic-damage model for cyclic loading of concrete structures*, Journal of Engineering Mechanics, Vol. 124, No. 8, 1998, pp. 892–900.
- [8] Lubliner J., Oliver J., Oller S., Oñate E.: *A plastic-damage model for concrete*, International Journal of Solids and Structures, Vol. 25, 1989, pp. 299–329.
- [9] Majewski S.: *The mechanics of structural concrete in terms of elasto-plasticity*, Silesian Polytechnic Publishing House, Gliwice, 2003.
- [10] Szumigala A.: *Composite steel-concrete beam and frame structures under momentary load*, Dissertation No. 408, Poznań Polytechnic Publishing House, Poznań, 2007.
- [11] Wang T., Hsu T.T.C.: *Nonlinear finite element analysis of concrete structures using new constitutive models*, Computers and Structures, Vol. 79, Iss. 32, 2001, pp. 2781–2791.

Modelowanie konstrukcji żelbetowych oraz zespolonych z uwzględnieniem degradacji wytrzymałościowej betonu

Symulacje komputerowe w dziedzinie konstrukcji żelbetowych są wyzwaniem z uwagi na właściwości materiału, jakim jest beton. W przeciwieństwie do stali, jest to materiał, który podczas ściskania wykazuje nielinijowość już od samego początku swojej pracy. Ponadto podczas rozciągania ulega znacznie szybszej degradacji, co skutkuje problemami natury numerycznej. W niniejszej pracy opisano parametry niezbędne do prawidłowego zamodelowania betonu w złożonym stanie naprężenia. Parametry te przedstawiono na przykładzie modelu „Concrete Damaged Plasticity” zawartego w programie ABAQUS.

Behaviour of the steel box-type culvert during backfilling

L. KORUSIEWICZ, B. KUNECKI

Wrocław University of Technology, Wybrzeże Wyspiańskiego 27, 50-370 Wrocław, Poland.

Corrugated steel culverts are increasingly used in road and railway projects as alternative solutions to small bridges and tunnels. This paper describes full-scale tests of the corrugated steel “box” type culvert with a span of 3.55 m and a height of 1.62m. The corrugation pattern was 150 × 50 mm and the steel thickness was 5 mm. Two concrete strip foundations were laid under each end of the arch. The structure was tested during backfilling. Deformations and strains of the steel structure were measured while installing culvert after each layer of 25–30 cm thickness was compacted. In order to specify displacements and stresses in the steel structure, three inductive gauges and twenty two strain gauges were installed on the inside surface of the culvert. The presented tests were carried out at the Road and Bridge Research Institute, Poland, for Via-Con Company, the Norwegian culvert producer. Several full-scale tests have been done in the field to validate the long-term performance and great load bearing capacity of these structures. In contrast to that, only few tests of life-size structures have been performed under fully controlled laboratory conditions like the one in Poland. A nonlinear finite element analysis of the soil–structure system was carried out in order to simulate behaviour of the structure during backfilling. A detailed description of the finite elements used in the analysis is provided. The obtained experimental results were compared with the structure response computed using the FEM. The measured and the computed results are shown in tables and graphs.

Keywords: *corrugated steel culvert, full-scale test, backfilling, deformations, FEM*

1. Introduction

Corrugated steel culverts are increasingly being used in road and railway projects as alternative solutions to bridges and tunnels. Several approaches have been suggested for design of such structures, but no exact theoretical analysis is available. Presently, there exist a multitude of methods for analyzing the stress, strain and deflection characteristics of soil-conduit systems subject to both static (soil weight) and vehicular live loads. Recently, however, due to an increased demand for culverts with large spans, varying barrel shapes and backfill depths, the suitability of earlier developed semi-empirical procedures has been questioned. Consequently, to answer these queries and to advance current perception of soil–structure interaction of buried culverts, research has progressed towards both full-size instrumentation and the development of numerical approaches. Basic information concerning corrugated steel culverts, calculation methods and results of in situ measurements has been presented in books [4, 10]. Several full-scale tests have been carried out in the field to validate the long-term performance and high load bearing capacity of these structures [1–3, 5, 11–12]. In con-

trast to that only few tests of life-size structures have been performed under fully controlled laboratory conditions. Full-size tests of steel and polymer culverts have been done at the Road and Bridge Research Institute, Poland, for a few years now. Results of those tests have been presented in several papers [6–7, 9, 13–14]. The experimental results give an insight into the actual behaviour of such structures under working conditions. The experimental evidence so gathered is a basis for putting forward computation models and their verification.

The behaviour of in-ground conduits has been the subject of extensive study since the beginning of the XX century. Buried structures such as sewers, pipes and tunnels have to be designed to support not only a live loading at the ground surface but also the dead loading of the soil providing cover. Due to the flexibility of that type of shell structures large deflections and internal forces can be obtained during the set-up process and they have to be taken into account in design. The presented paper deals with the effect of the steel structure–soil cover depth on the stress and deformation distribution in the tested culvert during the filling-up process.

2. Description of the structure

A 13.70 m long culvert which cross-sectional dimensions are shown in Figure 1 was subjected to testing. The structure was made from roll-formed corrugated plates of Fe360BFN steel with the minimum yield stress of 245 MPa (in accordance with the European Standard EN10025). The corrugation pattern was 150 × 50 mm and steel thickness was 5.0 mm. The steel plates were joined by 20 mm dia. bolts with the minimum tensile strength of 830 MPa. The top of the culvert was reinforced by additional corrugated steel plates with a width of 1.54m.

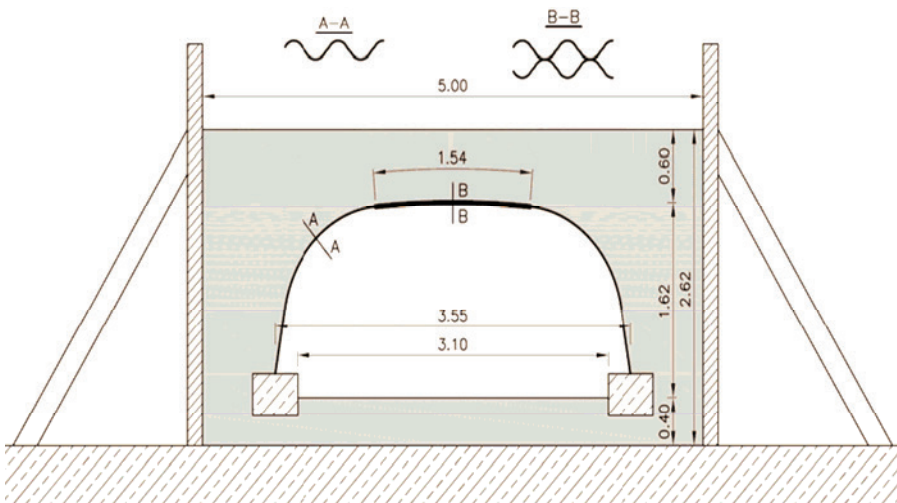


Fig. 1. Cross-sectional dimensions of the tested culvert

The tested structure was located in the test stand at the Road and Bridge Research Institute – Wrocław Division. This test stand has the form of an 80 m long and 12 m wide reinforced concrete foundation with a system of anchors and a steel frame serving as a support structure for hydraulic load-generating equipment – Figure 2.

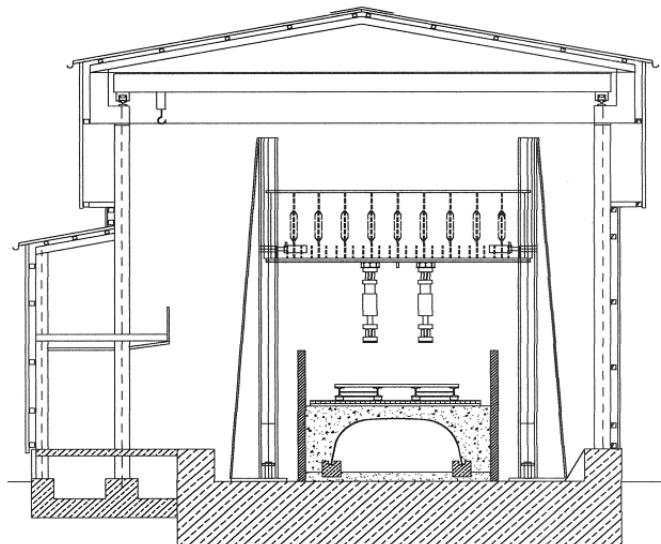


Fig. 2. Complete view of the testing facility

A specially constructed test bin was prepared to perform the experiment. The test bin, made of wooden railway sleepers and steel beams, was 12 m long, 5 m wide and 4 m high. The culvert before getting covered up was placed inside the test bin on two concrete strip foundations. Natural loose sand of different grades extracted from a local deposit was used as the soil fill. The noncohesive filled-up soil was stabilized mechanically in layers with the maximum thickness of 30 cm after compaction. Average degree of compaction was 97% Standard Proctor.

3. Measurement instrumentation

Three induction displacement gauges and eleven pairs of strain gauges were placed in the middle part of the culvert in the arrangement shown in Figure 3.

The displacement gauges (one vertical gauge and two horizontal ones) allowed the relative displacement of the culvert to be measured. The horizontal gauges were installed 37 cm over the top of concrete strip foundation. The strain gauges (two-directional rosettes) were fitted at each location in parallel, one at the top and one at the bottom of the corrugation – Figure 4. Additionally, dummy gauges were installed to provide temperature compensation. For the acquisition of experimental data from

induction and strain gauges a measuring system, consisting of a Hottinger Baldwin Mess-technik UPM100 measuring device and a Macintosh computer with the Beam software package, was used.

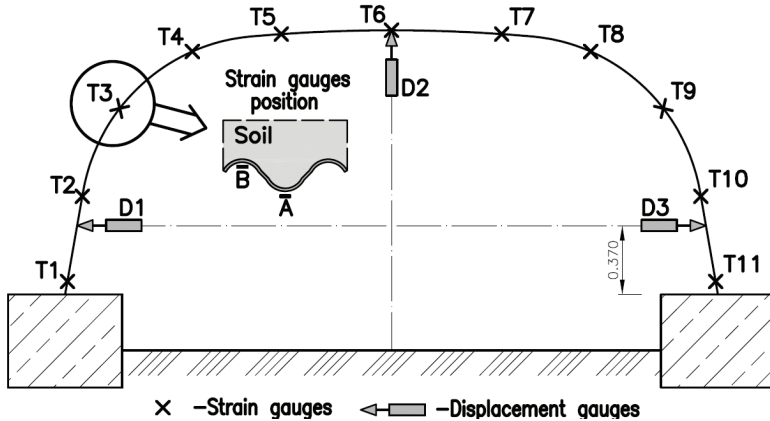


Fig. 3. Arrangement of displacement and strain gauges

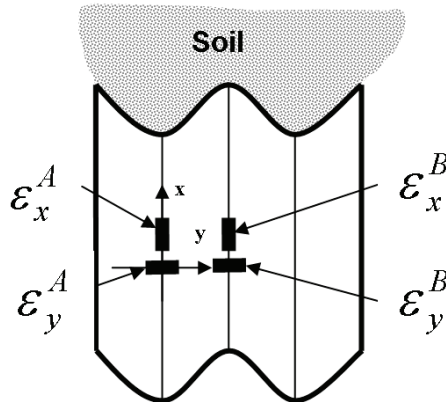


Fig. 4. Arrangement of strain gauges for one measuring point in Figure 3

4. Experimental results

This paper describes only the beginning part of the test concerned with the behaviour of the culvert during the backfilling process (named Stage 1). After the standardized road loadings were performed the backfill material was taken out and the culvert build up process was repeated (Stage 2) to prepare the model for the over-standardized loading phase.

Deformations of the tested culvert following the consecutively laid soil layers are presented in Table 1 and Figure 5 for Stage 1 and in Table 2 and Figure 6 for Stage 2.

Table 1. Deformations of the tested culvert – Stage 1

Layer number	Layer thickness [m]	Total soil thickness [m]	Displacement [mm] Induction gauges		
			D1	D2	D3
1	0.26	0.26	0.00	0.10	-0.10
2	0.26	0.52	-0.05	0.10	0.00
3	0.25	0.77	-0.15	0.25	-0.05
4	0.25	1.02	-0.25	0.40	-0.10
5	0.25	1.27	-0.35	0.90	-0.35
6	0.25	1.52	-0.35	1.10	-0.35
7	0.25	1.77	-0.20	0.45	-0.20
8	0.26	2.03	0.25	-1.35	0.20
Model of pavement	0	2.03	0.35	-1.89	0.29

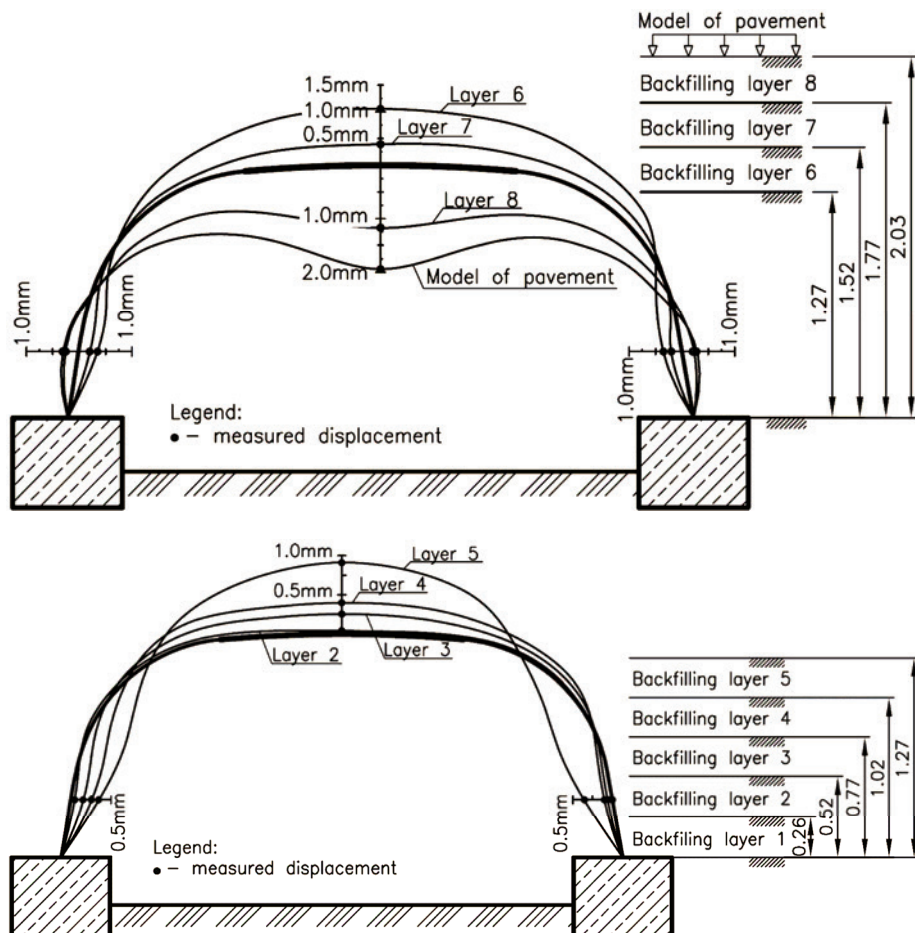


Fig. 5. Culvert deformations – Stage 1

Table 2. Deformations of the tested culvert – Stage 2

Layer number	Layer thickness [m]	Total soil thickness [m]	Displacement [mm] Induction gauges		
			D1	D2	D3
1	0.30	0.30	0.12	-0.09	0.11
2	0.30	0.60	-0.11	0.16	-0.09
3	0.27	0.87	-0.22	0.36	-0.14
4	0.27	1.14	-0.30	0.80	-0.30
5	0.28	1.42	-0.29	1.00	-0.28
6	0.30	1.72	-0.02	0.02	-0.09
7	0.30	2.02	0.25	-1.16	0.16
Model of pavement	0	2.02	0.29	-1.42	0.20

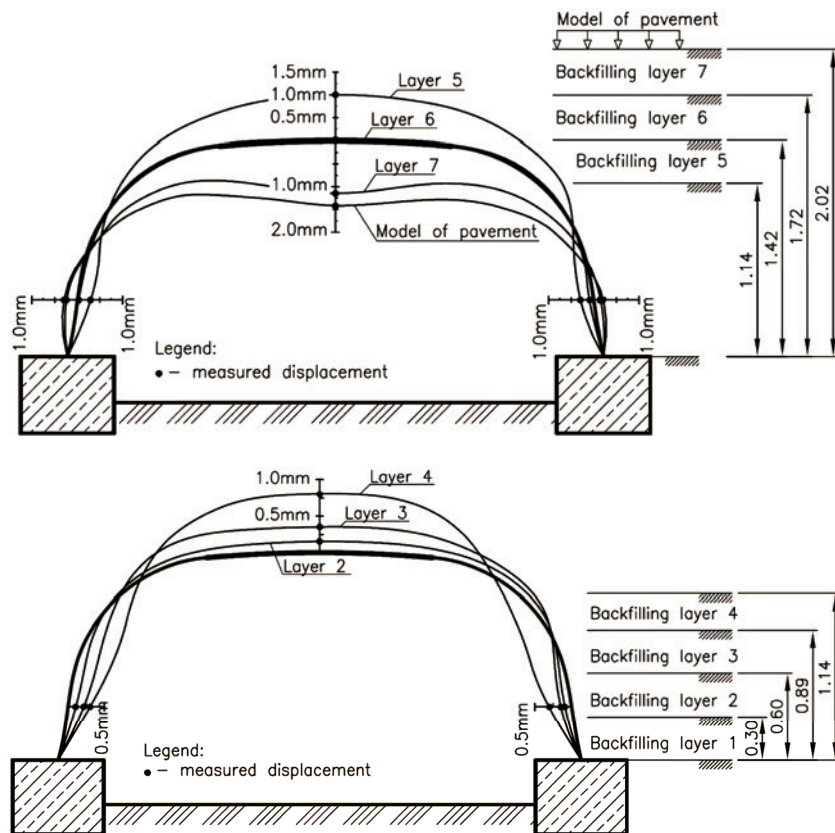


Fig. 6. Culvert deformations – Stage 2

The stresses in the steel structure were calculated based on strains assuming a plane stress state and the elastic modulus of steel $E_S = 2.05 \times 10^5$ MPa and the Poisson's ratio $\nu = 0.3$. The circumferential stresses σ_A and σ_B at each measuring point (see a pair of strain gauges – Figure 4) are expressed by formulae:

$$\begin{aligned}\sigma_A &= \frac{E}{1-\nu^2} (\varepsilon_x^A + \nu \varepsilon_y^A), \\ \sigma_B &= \frac{E}{1-\nu^2} (\varepsilon_x^B + \nu \varepsilon_y^B).\end{aligned}\quad (1)$$

These stresses allow calculating the stress σ_N generated by axial forces and the stress σ_M generated by bending moments according to the following equations:

$$\sigma_N = \frac{\sigma_A + \hat{\sigma}_B}{2}, \quad \sigma_M = \frac{\sigma_A - \hat{\sigma}_B}{2}, \quad (2)$$

where σ_A and $\hat{\sigma}_B$ are the stresses at the crest and at the valley of a corrugation, respectively.

The stress $\hat{\sigma}_B$ is calculated from the formula:

$$\hat{\sigma}_B = \frac{\sigma_B - \sigma_A}{h} (h + g) + \sigma_A, \quad (3)$$

where:

h – height of a corrugation,

g – steel thickness.

This stress is a modification of the stress σ_B which takes into account the fact that strain gauges in the location B were not fitted at the external surface of the culvert.

The above equations can be used in the case of a single corrugation. In the crown zone, where double corrugated sheets were mounted (points T5, T6 and T7 – Figure 3) stresses in external fibres (point C – Figure 7) cannot be predicted, based on the linear extrapolation. Under real circumstances there will be the discontinuity in stress distribution at the contact zone of two plates.

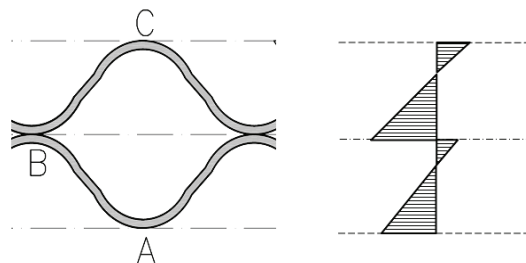


Fig. 7. Stresses in the double-corrugated sheets

Therefore, in this paper only stresses for the main steel structure, not for the over crown region additional steel plates, were taken into consideration.

The σ_N and σ_M stresses for two chosen cases where the extreme values of culvert deformations were detected are shown in Tables 3 and 4. Additionally, diagrams of internal forces for these two cases are presented in Figures 8–11.

Table 3. Stress values – Stage 1

Point	Stage 1			
	Layer 6		Model of pavement	
	σ_N	σ_M	σ_N	σ_M
	[MPa]			
T1	-11.48	-9.43	-10.46	7.79
T2	-8.30	4.00	-10.25	2.87
T3	-6.15	14.76	-14.56	-20.71
T4	-8.30	-4.61	-14.76	-5.13
T5	-11.58	0.51	-1.85	3.69
T6	-6.77	-3.90	1.03	12.92
T7	-8.51	-4.20	-1.33	5.43
T8	-6.05	-7.89	-12.30	-3.28
T9	-3.69	7.59	-12.51	-24.40
T10	-5.23	0.72	-4.92	1.64
T11	-9.84	-10.25	-14.86	8.51

Table 4. Stress values – Stage 2

Point	Stage 2			
	Layer 5		Model of pavement	
	σ_N	σ_M	σ_N	σ_M
	[MPa]			
T1	-0.41	-16.20	-4.31	1.23
T2	-1.44	1.03	-3.49	-0.62
T3	-0.51	13.84	-7.69	-15.89
T4	-2.15	-3.38	-11.17	0.92
T5	-4.51	-3.28	8.71	-1.74
T6	-3.59	-4.82	7.07	9.74
T7	-3.59	-4.20	6.56	4.72
T8	-3.38	-4.82	-6.25	-1.33
T9	-1.13	10.97	-8.61	-17.63
T10	-0.62	0.41	-0.10	0.51
T11	1.85	-12.92	-3.79	1.33

Internal forces (axial forces n and bending moments m) are calculated according to the following equations:

$$n = \frac{E}{(1-\nu^2)} \frac{A}{2ha} [\varepsilon_x^A(h-g) + \varepsilon_x^B(h+g) + \nu(\varepsilon_y^A(h-g) + \varepsilon_y^B(h+g))], \quad (4)$$

$$m = \frac{E}{(1-\nu^2)} \frac{I}{ha} [(\varepsilon_x^A - \varepsilon_x^B) + \nu(\varepsilon_y^A - \varepsilon_y^B)]. \quad (5)$$

where A and I are cross-sectional area and moment of inertia of one wave (corrugation); a – wavelength.

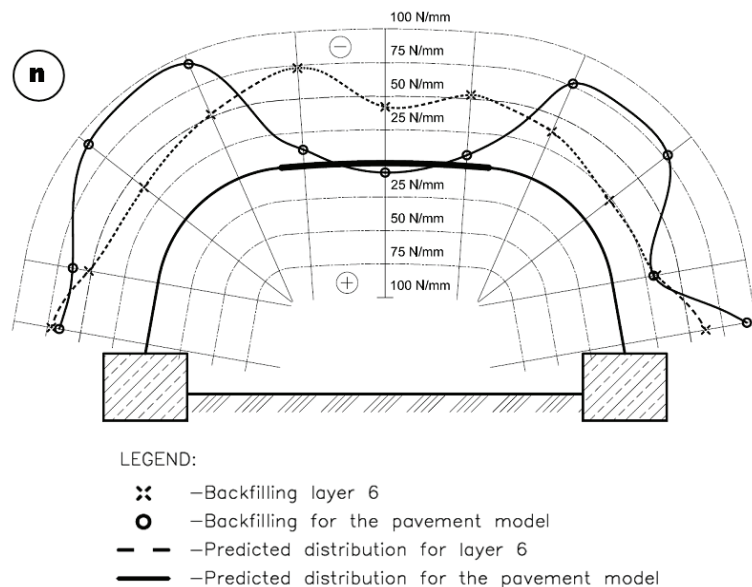


Fig. 8. Axial forces – Stage 1

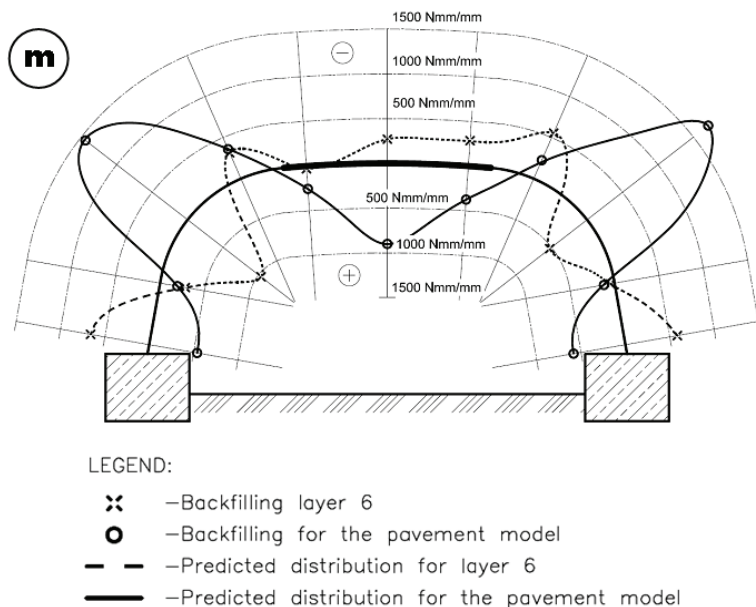
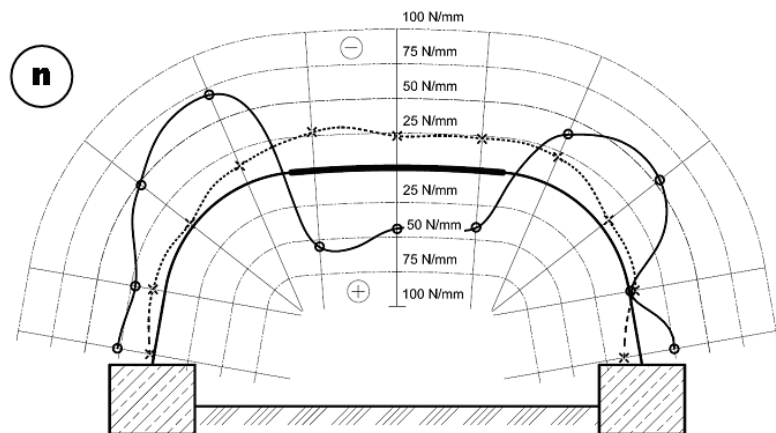


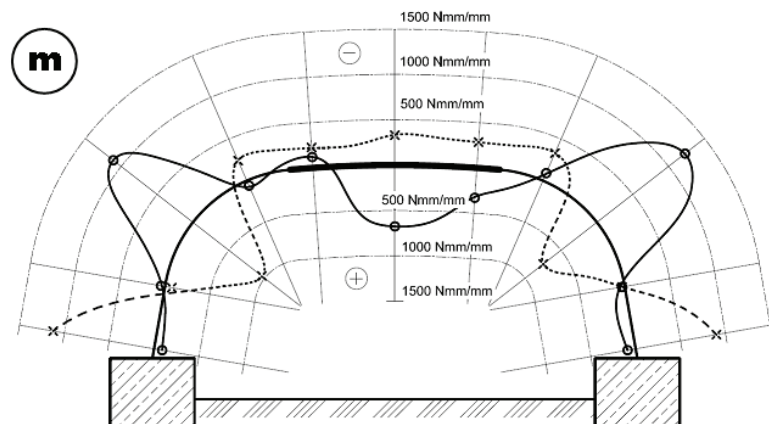
Fig. 9. Bending moments– Stage 1



LEGEND:

- \times — Backfilling layer 5
- \circ — Backfilling for the pavement model
- $-\cdot-$ — Predicted distribution for layer 5
- $-$ — Predicted distribution for the pavement model

Fig. 10. Axial forces – Stage 2



LEGEND:

- \times — Backfilling layer 5
- \circ — Backfilling for the pavement model
- $-\cdot-$ — Predicted distribution for layer 5
- $-$ — Predicted distribution for the pavement model

Fig. 11. Bending moments – Stage 2

5. FEM model of the soil-structure system

Analysis of the soil-structure system was carried out using the Cosmos/M software. The culvert structure and bin walls were modelled by 2-node uniaxial BEAM2D elements. The soil and strip foundations were modelled by 4-node isoparametric two-dimensional PLANE2D elements. The whole FEM model (complete backfilling) included 74 BEAM2D elements for modelling the steel structure, 1984 PLANE2D elements for modelling the soil (1419 for backfilling – layer number 6), 182 PLANE2D elements for modelling the concrete strip foundations and 76 BEAM2D elements for modelling the wooden bin. The static system of soil-structure is shown in Figure 12. Detailed description of elements used in FEM calculations is shown in papers [6, 8].

Calculations were performed taking into consideration the dead weight of soil and structure. To simulate the behaviour of soil material the Drucker–Prager elastic–perfectly plastic model was assumed. Material properties used in calculations for the soil were as follows: modulus of elasticity $E_G = 90$ MPa, Poisson's ratio $\nu = 0.2$, angle of internal friction $\phi = 38.0^\circ$ and cohesive strength $c = 0.1$ Pa. For the steel the modulus of elasticity $E_S = 2.05 \times 10^5$ MPa and Poisson's ratio $\nu = 0.3$ were used.

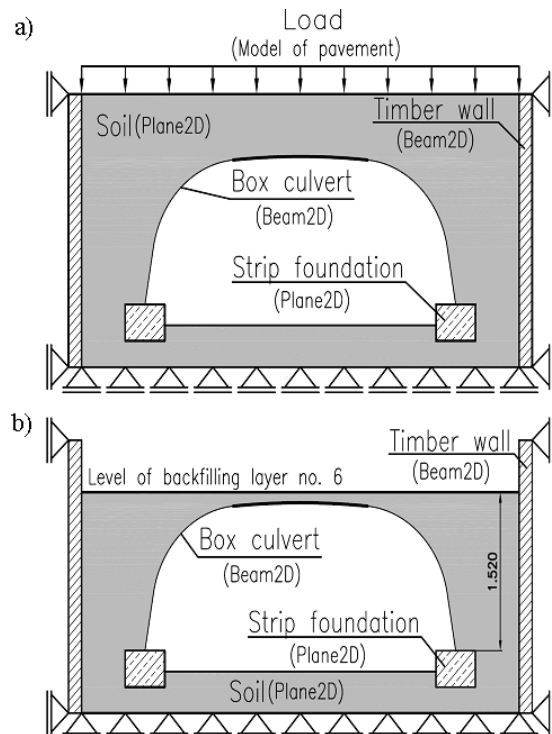


Fig. 12. Static system for: a) complete backfilling with model of pavement,
b) backfilling – layer no. 6

6. FEM results

Displacements and deformation shapes for the FEM model adopted are shown in Figure 13.

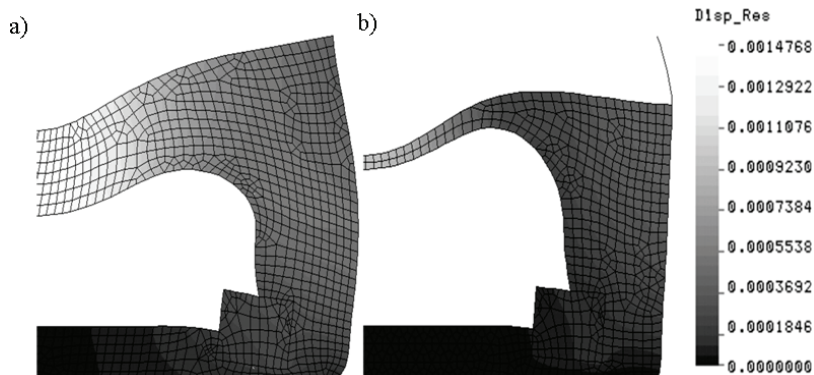


Fig. 13. Displacements and deformation shapes: a) complete backfilling with model of pavement,
b) backfilling – layer no.6

Additionally, calculated displacement values for layer 6, layer 8 and complete backfilling with the model of pavement at points where the induction gauges were placed are presented in Table 5.

Table 5. Displacements obtained from FEM calculations

Layer	FEM displacements [mm]		Points
	D1, D3	D2	
Layer no. 6	0.08	-0.94	
Layer no. 8	0.27	-1.38	
Model of pavement	0.31	-1.47	

Calculated values of the σ_N and σ_M stresses are presented in Table 6.

Table 6. Values of stresses obtained from FEM calculations

Points	Values of stresses			
	Layer no. 6		Model of pavement	
	σ_N	σ_M	σ_N	σ_M
[MPa]				
T1, T11	-20.7	19.5	-44.8	24.4
T2, T10	-16.6	8.2	-44.0	7.2
T3, T9	-10.2	-11.3	-34.5	-38.2
T4, T8	-6.1	-58.3	-14.8	-2.7
T5, T7	-8.2	11.1	-2.1	18.9
T6	-0.3	29.2	0.8	22.7

7. Conclusions

The presented experimental results show that during backfilling the steel culvert shell behaves in a complex manner changing its shape (values and signs of displacements) as the number of soil layers grows. The measured displacements and stresses are approximately equal about the culvert symmetry axis, the degree of that symmetry being higher as the soil depth rises. The effect of loading history where the culvert was covered with soil, then uncovered and covered again is clearly visible. The effect of training manifests itself by lower values of stresses and displacements. Generally speaking, values of stresses due to normal forces and bending moments are small and have no sizable effect on the safety. Maximum experimental values of total stress ($\sigma_N + \sigma_M$) do not exceed 16% of the yield stress of the steel used.

The adopted FEM model proved to be incapable of determining displacements and internal forces in the culvert at the initial stages of backfilling since it took no account of soil compacting forces. It proved to be insensitive to history of loading either. The computational results started to agree with experiment on reaching layer 8 of backfilling and assuming a model of pavement. This can be seen by comparing the results at points D1, D2 and D3. Qualitative changes in σ_N and σ_M stresses at Stage 1 at about full backfilling plus pavement modelling are similar, but their numerical values largely remain higher than experimental ones.

The presented analysis showed that the adopted FEM model has limited applicability in the case under consideration, being still fully acceptable in computing loads due to rolling stock or road vehicles [8].

References

- [1] Bayoglu Flener E.: *Response of long-span box type soil-steel composite structures during ultimate loading tests*, J. Bridge Engng., Vol. 14, No. 6, 2009, pp. 496–506.
- [2] Bayoglu Flener E., Sandquist H.: *Full-scale testing of two corrugated steel box culverts with different crown stiffness*, Archives of Institute of Civil Engineering, No. 1, 2007, pp. 35–44.
- [3] Byrne P.M., Srithar T., Kern C.B.: *Field measurements and analysis of a large-diameter flexible culvert*, Can. Geotech. J., No. 30, 1993, pp. 135–145.
- [4] Janusz L., Madaj A.: *Obiekty inżynierskie z blach falistych. Projektowanie i wykonawstwo*, Wydawnictwo Komunikacji i Łączności, Warszawa, 2007.
- [5] Janusz L., Madaj A., Sturzbecher K.: *Railway grade separation made of corrugated steel plate structure – long term research*, Archives of Institute of Civil Engineering, No. 1, 2007, pp. 99–108.
- [6] Korusiewicz L., Kunecki B.: *On boundary conditions in experimental and numerical models of steel culverts*, 8th International Conference: Shell Structure–Theory and Applications, Jurata, Poland, 2005, pp. 573–576.
- [7] Kunecki, B.: *Full-scale laboratory static tests of steel corrugated pipe-arch culvert*, 8th International Conference: Shell Structure – Theory and Applications, Jurata, Poland, 2005, pp. 589–593.

- [8] Kunecki B.: *Behaviour of orthotropic buried arch shells under static and dynamic live load*, PhD thesis. Report no. 14/2006, Wrocław University of Technology, Institute of Building Engineering, Wrocław, Poland, 2006.
- [9] Kunecki B., Kubica E.: *Full-scale laboratory tests and FEM analysis of corrugated steel culverts under standardized railway load*, Archives of Civil and Mechanical Engineering, Vol. 4, No. 4, 2004, pp. 41–53.
- [10] Machelski Cz.: *Modelowanie mostowych konstrukcji gruntowo-powłokowych*, Dolnośląskie Wydawnictwo Edukacyjne, Wrocław, 2008.
- [11] Pettersson L.: *Full scale tests and structural evaluation of soil steel flexible culverts with low height of cover*, Doctoral Thesis in Civil and Architectural Engineering, KTH, Stockholm, Sweden, 2007.
- [12] Vaslestad J.: *Long-term behaviour of flexible large-span culverts*, Publication No. 74, Norwegian Public Roads Administration, Oslo, 1994, pp. 38–56.
- [13] Vaslestad J., Korusiewicz L., Wysokowski A.: *General description of static and dynamic testing of instrumented steel culvert*, 5th International Conference – Durable and Safe Road Pavements, Kielce, Poland, 1999, pp. 215–221.
- [14] Wysokowski A., Vaslestad J.: *Full scale fatigue testing of large-diameter multi-plate corrugated steel culverts*, Archives of Civil Engineering, Vol. 48, No. 1, 2002, pp. 31–57.

Zachowanie się skrzynkowego przepustu stalowego w procesie zasypywania gruntem

Przepusty stalowe z blachy falistej w coraz większym stopniu są wykorzystywane w projektach kolejowych i drogowych, jako alternatywne rozwiązanie dla małych mostów i tuneli. W artykule przedstawiono badania w skali naturalnej skrzynkowego przepustu stalowego o rozpiętości 3,55 m i wysokości 1,62 m. Grubość blachy o fali 150 × 50 mm wynosiła 5 mm. Przepust, wsparty na dwóch betonowych ławach fundamentowych, badany był podczas zasypywania go gruntem. Deformacje i odkształcenia stalowej konstrukcji mierzone położeniu i zagięciu każdej warstwy gruntu o grubości 25–30 cm. Dla określenia przemieszczeń i naprężeń w powłoce stalowej wykorzystano trzy indukcyjne czujniki drogi i dwadzieścia dwa czujniki tensometryczne, które umieszczone po wewnętrznej stronie przepustu. Przedstawione badania wykonano w Instytucie Badawczym Dróg i Mostów na zlecenie norweskiej firmy Via-Con. Pewna ilość badań polowych tego typu konstrukcji wykonana była w celu wykazania ich długiej żywotności i dużej wytrzymałości (nośności). W przeciwieństwie do badań polowych, w pełni kontrolowane badania laboratoryjne przepustów w skali naturalnej wykonywane były bardzo rzadko.

Dodatkowo przeprowadzono analizę zachowania się układu grunt-przepust stalowy z wykorzystaniem obliczeń metodą elementów skończonych. Opisano szczegółowo rodzaje elementów skończonych wykorzystanych w analizie. Otrzymane wyniki badań doświadczalnych porównano z wynikami obliczeń numerycznych. Wyniki pomiarów i obliczeń przedstawiono w sposób graficzny oraz w tabelach.



Evaluation of fillet weld properties and fatigue behaviour in dependence of welding parameters

M. LEITNER, T. FÖSSL, M. STOSCHKA, W. EICHLSEDER
Montanuniversität Leoben, Franz-Josef-Straße 18, 8700 Leoben, Austria.

Numerous different design codes can be used to describe the durability of welded structures. One wide spread approach is the local notch stress approach, which calculates the fatigue lifetime in dependency of the notch stress factor using different effective radii. To calculate the fatigue behaviour by using the local notch stress approach, the R1MS-concept is commonly used [1]. The evaluation of the influence due to the welding process parameters, especially for high-strength steels, the effect of both the geometrical and metallurgical notch is studied in a parametric way for selected weld joints.

Experimental fatigue tests have been performed to investigate the link between fatigue life and manufacturing process dependent weld toe notch design. To be able to capture the influence of welding parameters, as energy input per unit length, welding velocity, angle of blowpipe, size and shape of the heat input zone in a numerical way, a local coupled thermo-mechanical simulation is build-up. The complexity of this modelling increases very strong by the temperature dependency of the multitudinous phase material properties. The material and manufacturing properties were adjusted by comparison of the temperature profiles. This experimental based procedure defines the simulation base for more complex welding seams.

Keywords: *welding, fatigue, fillet weld properties, welding simulation, welding parameters*

1. Introduction

To increase the fatigue lifetime of complex welded structures not only material properties but also welding parameters are very essential. High alloyed steel, which achieves strength behaviour through thermal conditioning, react very sensible on alternating circumstances related to the heat input during the welding process. Minor modifications in the cooling behaviour lead to a major change of technological characteristics. The possibility to optimize the welding process in a manner to achieve the highest dynamic operational load is not bonded directly to static properties like ultimate strength or ductility behaviour. Figure 1 demonstrates a methodological iterative procedure to determine the specific values from the design stage of a welded specimen to the properties in the heat-affected-zone. Measurement and simulation practices supplementary evaluate the procedure and permit a comparison to the weld process.

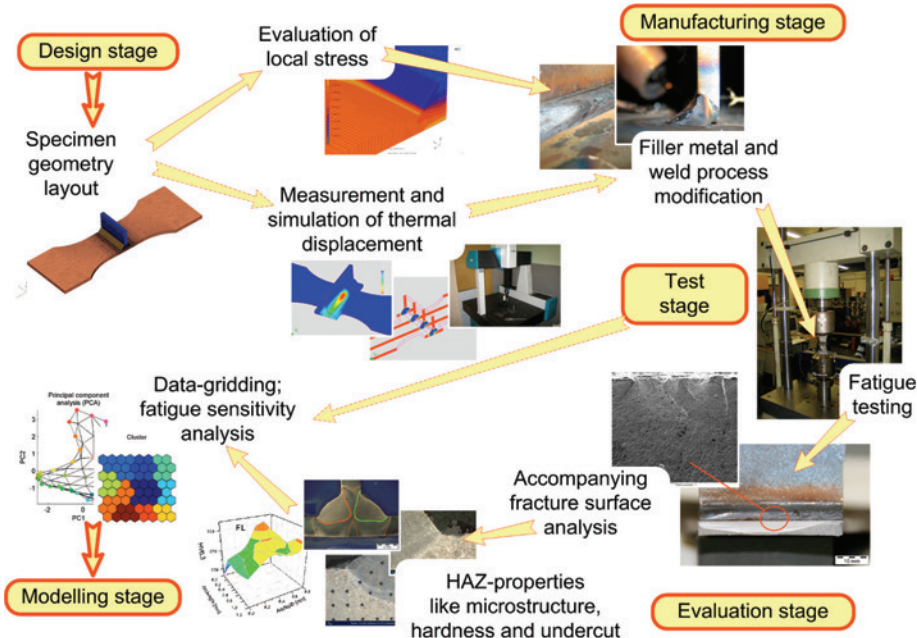


Fig. 1. Methodical approach to determine the influence of welding parameters

To clarify the fatigue strength in relationship to the welding process, a double sided fillet weld was chosen. Conformable to the IIW-Recommendations for Fatigue Design of Welded Joints [2] and numerously applications in mechanical engineering parts, a non load carrying joint was selected for analysis. Incomplete fusion and porosities, which affect the fatigue behaviour in a minor way, were not observed during this investigation. However, primary welding effects like the chosen filler metal and welding gas influences the fatigue lifetime under cyclic loading.

2. Experimental investigations

For the experiments, a total number of about one hundred specimens were tested to gain the influence of the filler metal and the welding gas on the fatigue strength. In every test series the base material is a low-alloyed high-strength steel S960. A G89 solid and a G89 metal-cored wire are used for the filler materials. To guarantee constant welding conditions the double sided fillet weld was welded through a number of 10 specimens. Figure 2 shows the clamping conditions of the multiple weld specimen array and the complementary measurement of the heat input. Additionally compressive residual stresses avoid crack initiation from the machined edges of the specimen during fatigue testing. The final shape of the specimen design as well as the placement of compressive stress treatment is shown in Figure 3.

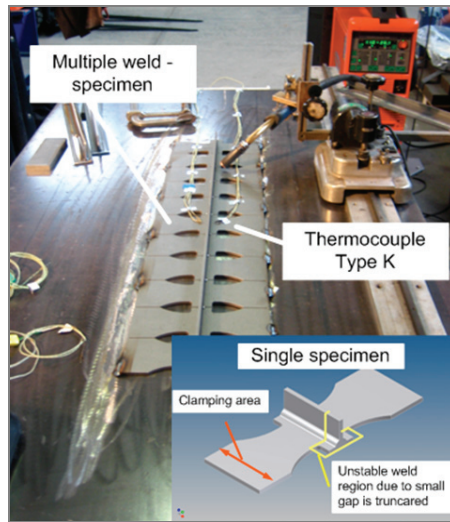


Fig. 2. Manufacturing process

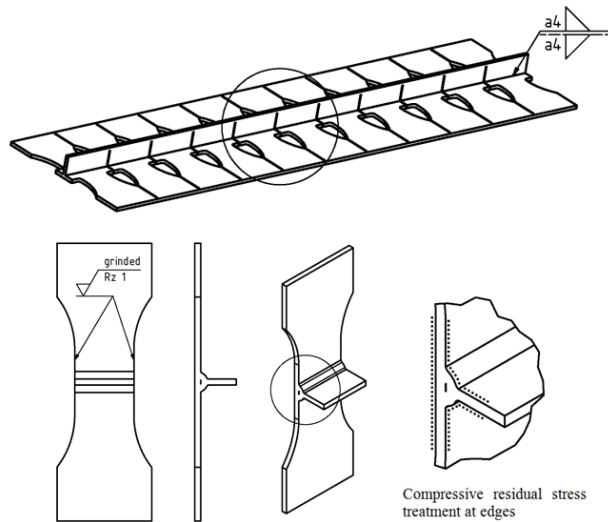


Fig. 3. Fatigue specimen design

During the welding process it was necessary to adjust the heat input to the respective test series to gain an optimal weld seam performance and thereby reproducible results. The three component gas (69% Ar, 30% He, 1% CO₂) needed a less heat-energy-input per unit length E than the standard gas (82% Ar, 18% CO₂) due to the high fraction of 30% He which leads to a higher heat input in the base material and thereby to a comparable expanded fusion penetration.

Table 1. Weld process parameters

Test series	Filler metal	Welding gas	E [kJ/cm]	$t_{8/5}$ [sec]	FAT [MPa]	k [-]
#1	G 89 solid wire	Standard	6.0	10	175	4.1
#2	G 89 solid wire	3 comp. gas	5.5	9	167	4.0
#3	G 89 metal-cored wire	Standard	6.1	10	173	3.9
#4	G 89 metal-cored wire	3 comp. gas	5.8	9	210	4.5

The recommended FAT-nominal stress value is 80 MPa in case of the non-load carrying fillet weld as defined by structural detail 511 of the nominal stress concept [2]. All investigated tests have been carried out at a stress ratio $R = 0.1$. The evaluation in Figure 4 according to the nominal notch stress approach shows that the four main test series indicate a significant higher allowable stress range than the conservative recommendation.

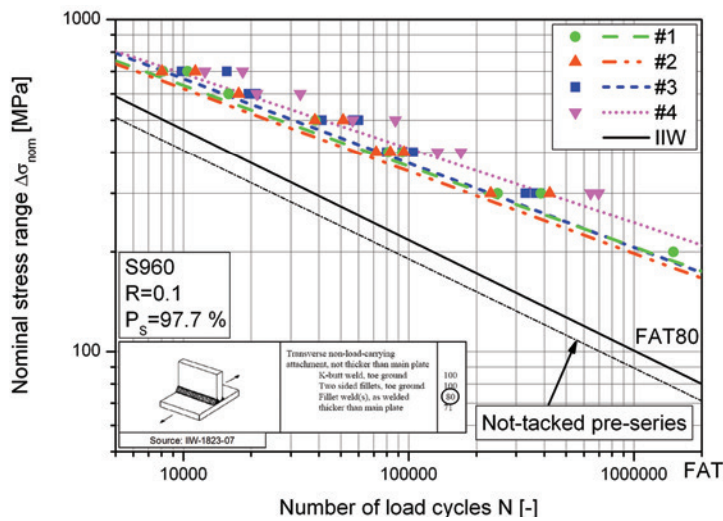


Fig. 4. Capability of filler metal and welding gas on fatigue behaviour

Due to the excessive deformation of the “unclamped” welded specimen (not-tacked pre-series) the resulting very high additional mean stresses lead to fatigue behaviour of FAT 70 below the recommended one. Summarizing, all examined test series are within stress range amplitudes at two million cycles of 167 MPa up to 210 MPa using the nominal stress approach. This exceeds the conservative recommended FAT 80 stress range. The resulting FAT value and the slope k of the S/N curve for each test series are shown in Table 1. To determine the differences concerning the local hardness in the weld interface of the heat-affected-zone and the topological notch formation in the transition region between the filler metal and the ground plate, macro hardness measurements with a Vickers Hardness of HV₁ (Figure 5) and metallographic inspections using light and laser microscopy (Figure 6) were accomplished.

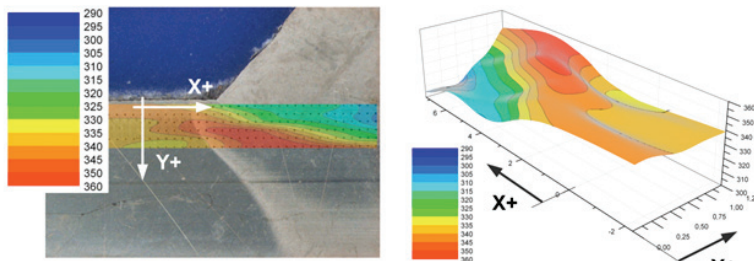


Fig. 5. Hardness measurements

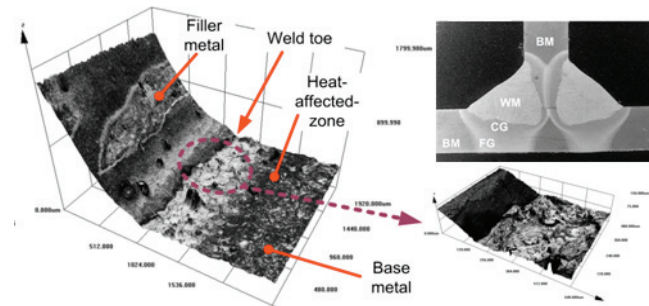


Fig. 6. Metallographic inspections

The hardness measurements demonstrate a maximum value of 360 HV₁ in the fusion line between coarse-grained and fine-grained structure. The topological notch formation changes enormous in dependence on the use of different welding gases. Because of decreasing notch radii in the area of weld interface using the standard gas the fatigue lifetime of the welded structure is reduced. Three component mixed gas encourages the outflow-behaviour and enables a smooth transition region between the filler metal and the ground plate.

3. Numerical investigations

3.1. Modelling guidelines

The numerical investigation of the weld process requires the use of a thermo-mechanical coupled finite element simulation. Due to the time and history-dependent complex material properties, the build up of a weld simulation process based on phase dependent material properties is necessary. The heat-input is generated by using filler elements with an assigned melt-point-temperature or defining the volume welding flux by equations; see [3]. Analytical heat-source models can be divided into thick-walled and “transient” thin-walled ones; the used finite element software applies the double-ellipsoidal heat source model [4] as given in Equation (1).

$$q_f(x,y,z) = \frac{6\sqrt{3}f_f Q}{abc_f \pi \cdot \sqrt{\pi}} \cdot \exp\left(\frac{-3x^2}{a^2}\right) \cdot \exp\left(\frac{-3y^2}{b^2}\right) \cdot \exp\left(\frac{-3z^2}{c^2}\right). \quad (1)$$

To perform a nonlinear weld simulation it is necessary to determine the mechanical and thermal material properties, which depend on temperature and time-history [5–6]. The thermal properties like conductivity, specific heat, emissivity and latent heat depend on the current temperature. In addition, mechanical properties like Young's modulus, mass density, Poisson's ratio and the material plasticity are determined not only by temperature; in addition, the work-hardening behaviour is strongly influenced by the effective strain and the effective strain rate. Finally, the reset of plastic strains when reaching the solidus temperature must be taken in account [7]. To consider the influence of different cooling rates in low carbon steels, a multi-dimensional look-up table representing the behaviour of each phase (ferrite/pearlite, austenite, martensite, bainite and tempered phase) can be used. The importance of the volume change due to α/γ -phase change is shown in Figure 7 by dilatometric measurement.

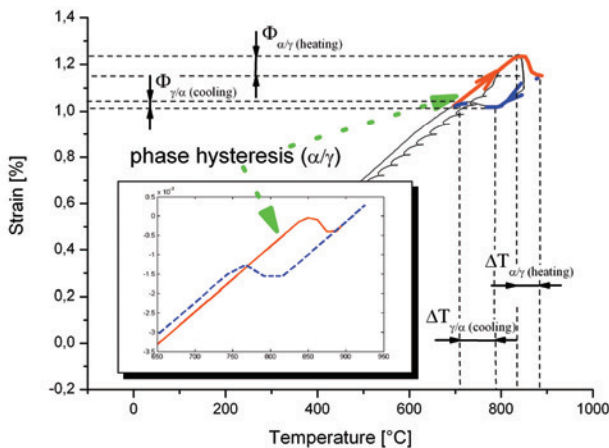


Fig. 7. Volumetric change due to the α/γ -phase change of low carbon steel

3.2. Welding simulation

The finite element model of the T-junction is based on the geometry of the welded seam. This allows a direct comparison of the deformed structure during the heat-treatment process. The thermal conductivity is increased to a high value near the δ -phase region to account for high-conductivity due to the stirring effect in molten metal. The singularity of the specific heat is considered by using a limited peak function. The solid-liquid and solid-solid transitions are taken into account by a phase dependent numerical implemented CCT-diagram which supports an additional adjustment [8].

Simulating the presented T-joint the following parameters are used: The sheet thickness for both plates is 5 mm and the energy input per unit length E is varying from 6.5 kJ/cm to 8.2 kJ/cm. The velocity of the blowpipe varies between 70 and 80 cm/min. The model was build-up according to the recommendations given in [6–7] due to the interactions between thermal and mechanical runs and the different convergence behaviour. The simulated manufacturing parameters are suitable for the arc welding process of thin metal sheets.

The weld filler elements keep deactivated until the blowpipe reaches this area and the heat flow starts. Weld path and reference line are shown in subfigure 8. During the heating-up process beginning with the first joint, the cover plate deforms slightly due to thermal shrinking. With decreasing temperature due to heat flux from the hot filler region to the base metal, the observed displacement is reduced.

Due to the comparable high conductivity of the higher strength carbon steel a major part of the thermal energy flows from the weld filler region into the adjacent base metal areas. Both the material properties and the heat input by the double-ellipsoid shape are adjusted by the thermocouple measurements. The resulting residual von-Mises stress distribution after welding and the thermal behaviour during the welding process is shown in Figure 8.

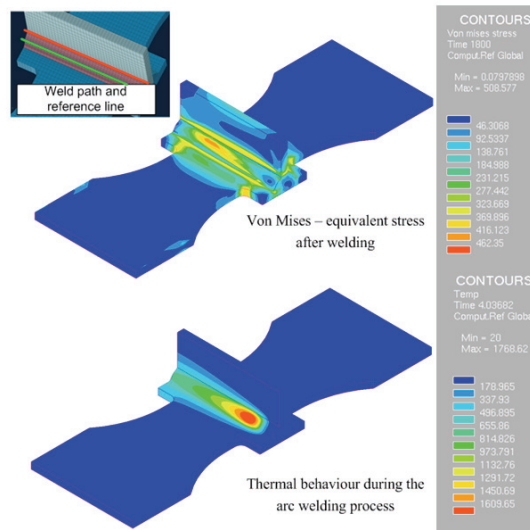


Fig. 8. Thermo-mechanical welding simulation

Further on, the time-temperature curve on four different points near the weld seam was measured in the distance y of 8 up to 20 mm (Figure 9). The numerical achieved temperature distribution shows similar curves. The peak temperature is nearly identical in measurement and simulation. The outer measurement point shows slight differences in temperature. This deviation can be caused by difference in surface film pa-

rameters and uncertainties in positioning of the thermocouples. The temperature decreases exponential from the peak value, which is in accordance to the dependency of the heat transfer coefficient. Comparing the temperature distribution on the opposite side of the base metal, only a minor deviation between measurement and simulation temperature is observed. Finally, it can be stated that the energy input in the heat-affected-zone matches the experiment.

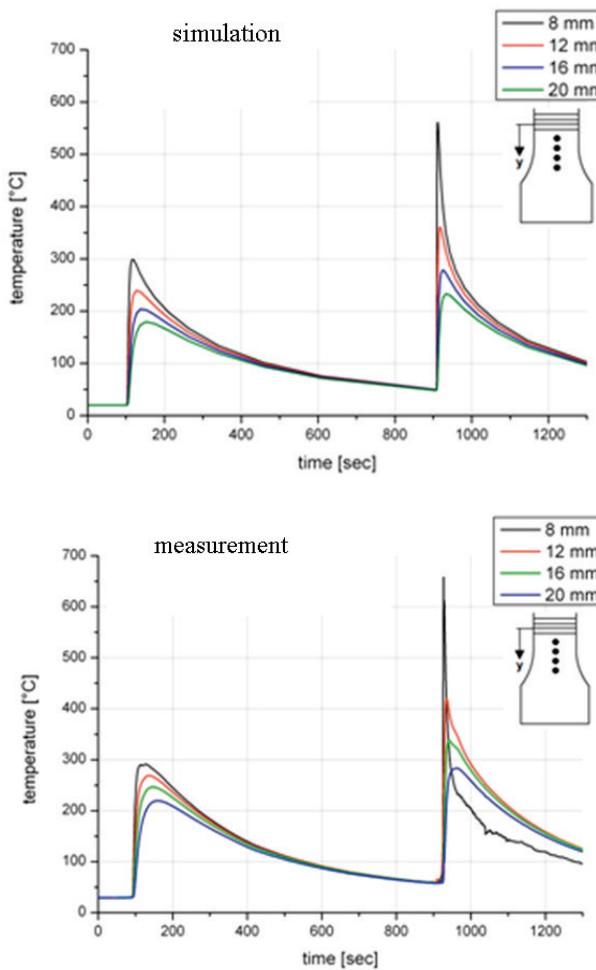


Fig. 9. Thermal behaviour

4. Conclusion

The presented scientific investigation illustrates a closed-loop design technique to evaluate welding parameters under cyclic loading behaviour applicable for high-strength

steels. A great potential to enhance the component lifetime shows the notch factor near weld toe region, whereas formation of microstructure in the heat-affected-zone influences the fatigue life less.

By filler metal adaptation and optimization of the weld gas and heat input, the FAT-class can increase up to the value of 2.6 compared to the conservative IIW-recommendations given in [2].

To calculate the local deformation after the thermo-mechanical welding process, a detailed knowledge of the material properties is fundamental. Using time-temperature-dependent material properties in addition with simplified weld-manufacturing suited definitions of the energy input and the blowpipe orientation, temperature and stress distributions can be achieved numerically. The numerous simulation parameters are adjusted by local measurements of the temperature and the deformed structure during the welding process. Based on this knowledge, more complex models and interfering welds will be considered further on. The overall goal of the work is to determine the main influence factors between thermo-mechanical sub-modelling and structural stress approach regarding fatigue life assessment. The final object is the examination of the applicability regarding the residual stress state obtained from the thermo-mechanical simulation to improve the fatigue lifetime calculation.

Acknowledgement

Financial support by the Austrian Federal Government and the Styrian Provincial Government, represented by Österreichische Forschungsförderungsgesellschaft mbH and Steirische Wirtschaftsförderungsgesellschaft mbH, within the research activities of the K2 Competence Centre on “Integrated Research in Materials, Processing and Product Engineering”, operated by the Materials Center Leoben Forschung GmbH under the frame of the Austrian COMET Competence Centre Programme, is gratefully acknowledged.

References

- [1] Radaj D. and Sonsino C.M.: *Fatigue assessment of welded joints by local approaches*, 2nd edition Cambridge, Woodhead Publishing Ltd., 2006.
- [2] Hobbacher A.: *Recommendations for fatigue design of welded joints and components*, IIW-Dokument XIII-1823-07, International Institute of Welding, updated December 2008.
- [3] Grong Ø.: *Metallurgical modelling of welding*, Norwegian University of Science and Technology, Department of Metallurgy, Second Edition, 1997, pp. 24–44.
- [4] Goldak J., Chakravarti A.: *A new finite element model for welding heat sources*, Metallurgical Transactions B., Vol. 15B, June, 1984, pp. 299–305.
- [5] Davids R.J., Mills M.K., Lampman R.S.: *Properties and selection: irons, steels and high-performance alloys*, ASM Handbook, Vol. 1, 1993.
- [6] Rahman M., Enzinger N.: *Parameter optimization and FE – Simulation of multi-layer welding considering welding residual stresses and post weld treatment*, Graz University of Technology, 2008, pp. 125–127.

- [7] Loose T., Sakkiettibutra J., *Leistungsmerkmale der Schweißstruktursimulation*, Schweißen und Schneiden, Vol. 60, No. 9, 2008, pp. 487–491.
- [8] Cerjak H., Bhadeshia H.K.D.H., Kozeschnik E.: *Mathematical modelling of weld phenomena* 7, Graz University of Technology, First publisher, 2005, pp. 39–62.

Ocena właściwości oraz zachowania zmęczeniowego spoiny pachwinowej w zależności od parametrów spawania

Obecnie stosowane są liczne metody do określenia trwałości struktur spawanych. Jedną z nich jest metoda naprężeń karbu, która pozwala obliczyć trwałość zmęczeniową spoin. W pracy zostały przedstawione eksperymenty zmęczeniowe, na podstawie których określono zależności pomiędzy trwałością spoiny a parametrami procesu jej wytwarzania.

Digital Material Representation as an efficient tool for strain inhomogeneities analysis at the micro scale level

L. MADEJ, L. RAUCH, K. PERZYNSKI, P. CYBULKA

Akademia Górnictwa Hutnicza, Al. Mickiewicza 30, 30-059 Kraków,
Faculty of Metals Engineering and Industrial Computer Science,
Department of Applied Computer Science and Modelling.

The summary of recent research towards development of a tool for detailed microstructure modelling is presented within the paper. The main focus is put on micro scale behaviour, where advantages of digital material representation can be taken into account. Digital Material Representation allows modelling of microstructures along with features such as crystallographic orientation, grain boundaries or phase boundaries represented in an explicit manner. Incorporation of these digital microstructures into the numerical simulation methods provides the possibility to improve the quality of numerical results. The developed method can be used to design specifically dedicated microstructures, which meet very strict requirements. The clear motivation and importance of the work is presented in the first part of the paper followed by a short description of the developed approaches for creation of the digital microstructures. Two approaches are considered that provide an exact and statistical representation of the real microstructure. The main focus is put on the application of image processing and cellular automata techniques. Afterwards, obtained digital microstructures are used as input data for the finite element analysis of the micro scale compression test. Examples of applications during multiscale simulation are also presented in the paper.

Keywords: *Digital Material Representation, cellular automata, image processing*

1. Introduction

The finite element (FE) method is historically the main tool used in industry to simulate large scale forming processes, and it gives satisfactory results [2, 11, 16–17]. This method describes material behaviour as a continuum based on general strain-stress relationships [18]. Plastometric tests at various deformation conditions (temperatures, strain rates, etc.) are usually performed to obtain accurate flow stress necessary for the FE analysis. An inverse method is applied to eliminate the effect of heterogeneities due to such factors as friction in the tests and to obtain strain-stress relationships that are insensitive to material geometry [22]. Since large scale problems containing billions of grains are usually considered, the major assumption of this approach is that behaviour and interaction of particular grains is homogenized in the form of a single flow stress model. Inverse analysis is commonly combined with finite element modelling to solve problems occurring during metal forming. The same approach is used to support development of new technologies for the processes of rolling, forging, stamping, etc.

During the last few years several challenges imposing significant changes to this commonly used approach have been spotted by industry and researchers. One of them is the rapid development of modern steel grades (TRIP, TWIP, DP, Bainitic, etc.). As presented in Figure 1, the number of new steel grades developed from the year 2000 has increased exponentially. These modern steels are characterized by elevated material properties, which are the results of sophisticated microstructures with a combination of features such as large grains, small grains, inclusions, precipitates, nanoparticles, different phases, Luders bands, Portevin-le-Chatelier bands, shear bands etc. Interaction among these features at the micro scale and the surrounding material under loading conditions results in required properties at the macro scale [1, 9, 21, 23].

Omnipresent miniaturization, which requires development of new micro forming technologies, is another important challenge. Since the sample is no longer a large aggregate of billions of grains – it may contain only hundreds of grains – an interaction between each particular grain becomes important. These grains are characterized by different crystallographic orientations or different properties, which during deformation results in heterogeneous material flow [10].

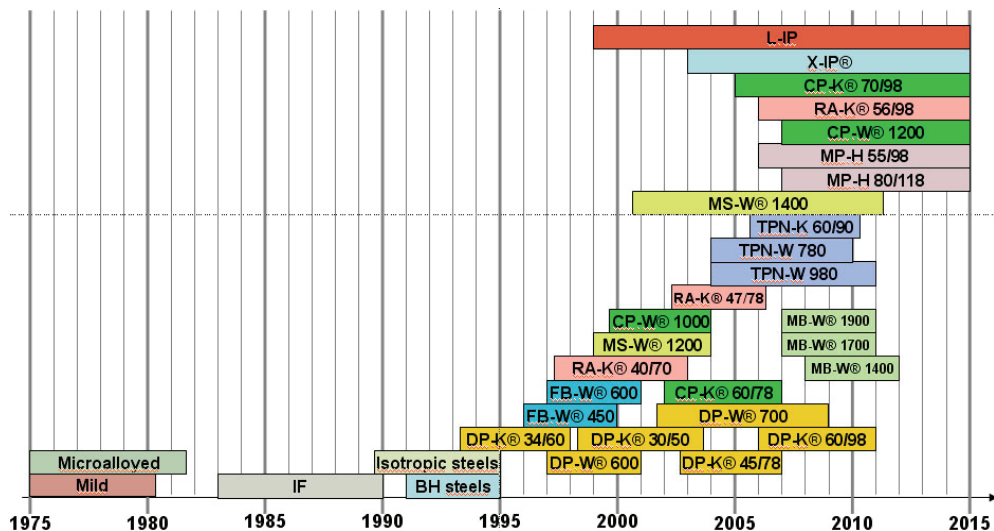


Fig. 1. New steel grade development chart in the ThyssenKrupp Steel company (DP – dual phase, BH – baking hardening, IF – interstitial free, CP – complex phases, MS – martensitic, FB – ferrite-bainite, RA – retained-austenite, TPN – three-phase nano, X-IP – iron-manganese TWIP, L-IP – light induced plasticity) [9]

New numerical methodologies are needed to meet these two challenges. Digital Material Representation (DMR), which is the subject of the present work, is one of the possible solutions. A description of recent developments in the DMR concept in various research laboratories located mainly in United States and Europe is described in another work of one of the Authors [14].

The main objective of the DMR system developed by the Authors of this work is to create the digital microstructure with its features (e.g., grains, sub grains, grain boundaries) presented explicitly. The created digital representation can be used in numerical simulations of forming processes for modern steels, as well as micro forming processes. However, the detailed representation of the initial microstructure subjected to loading is of importance in this approach. The more precise DMR applied, the more realistic results of calculations regarding material behaviour are obtained. Utilization of SEM/EBSD maps provides very accurate results [15], but on the other hand obtaining of an EBSD image is time consuming and expensive. That is why in this work particular attention is put on application of the image processing methods to optical microscopy images and transforming them into the digital representation format. Optical microscopy is accessible without any restrictions which makes it a very good source for the creation of the precise digital material representation. Detailed description of the developed image processing algorithm that is used for transferring microscopy images into the digital form is described in the first part of the paper. It is followed by a description of an alternative solution based on statistically representative microstructures.

2. Creation of the digital material representation

2.1. Pre-processing of microscopic images

Image segmentation algorithms offer the highest reliability in the creation of microstructure representations. On the basis of microscopic images the grains shape, grain borders, inclusions, precipitations etc. are replicated in detail in the DMR. However, the final quality of created structures depends on the quality of input images. Most optical microscopy images contain noise or are corrupted or blurred. These visible picture distortions greatly affect performance of segmentation algorithms and quality of the obtained DMR. Therefore, the stage of pre-processing in the case of microstructure images is proposed on a basis of three algorithms responsible for luminance equalization, denoising and reconstruction. Luminance equalization is a well known procedure based in most cases on the following steps: image duplication, inverse of colours, Gaussian blur with standard deviation within the range of 20–40 pixels, 50% opacity and merge of original image with its duplicate. Denoising and reconstruction are often required, especially in the cases of optical microscopy and scanning electron microscopy with electron back scattered diffraction (SEM/EBSD) pictures.

All of mentioned algorithms were designed to be independent of the images' contents, which release the final user from additional manual operations.

Due to this assumption the Dynamic Particles (DP) algorithm was designed, implemented [19] and applied for both 1P and 2P materials [20]. The main advantage of this solution is its universality, which allows application of the DP method not only for images but also for signals and sophisticated multidimensional data. The basis of

this method is in the definition of the particle, which can be treated as an N -dimensional object, which in the case of images is a 3D vector [X -axis, Y -axis, grey-scale value] related to pixels inside the analysed images. The main idea of the DP algorithm consists in the appropriate movement of each particle according to the following set of differential equations:

$$\begin{cases} m_i \frac{d\vec{v}_i}{dt} = -\nabla V_{ij} - f_c \vec{v}_i, \\ d\vec{r} = \vec{v}_i dt \end{cases}, \quad (1)$$

where:

m_i – mass,

\vec{v}_i – a velocity of the i -th particle,

V_{ij} – a potential between particles i and j , depending on the distance between them,

f_c – a friction coefficient responsible mainly for the convergence of calculations.

The magnitude of the force that causes the movement of the considered particle is reduced by the friction coefficient $f_c < 1$. It was found that according to the Newtonian laws of motion if all of the pre-conditions have been fixed properly, the entire system would remain stable and convergent to the expected results. Additionally, the friction coefficient f_c can be modified during the calculations of the algorithm, which influences the final smoothness of the results, as well as the stop criterion of the DP algorithm. One very important consideration in this method is to normalize data before calculations in order to equalize the impact of each dimension on the finally obtained results. Otherwise, the process of filtering will fail, giving an inappropriate shape of the denoised image. The normalization of the input data does not influence the density of the data on each axis, and the data are re-scaled after calculations to their primary range. However, the problem of the boundary points of the analysed image has not been solved yet. They remain fixed during calculations, which may cause some problems, while the boundary points are superimposed by the noise of a higher ratio than other particles.

An example of the results of denoising, shown in Figure 2, is further analyzed to distinguish separated areas inside images to gather information about boundaries of grains and subgrains, as well as about visible micro shear bands or slip surfaces.

Processing of single phase microstructures after filtering and reconstruction processes resolves the detection of edges based on the modified Canny Detector algorithm. The proposed approach consists of the following steps:

- Edge detection and enhancement by using the undirected Laplace convolution filter – this algorithm enhances the borders between different areas of the image by calculating colour gradients of neighbouring pixels. The main disadvantage of this technique is the effect of twin borders, which is obtained through the convolution of the two matrices, giving the left and right borders. Suppression of the twin-border effect is performed in the subsequent step of the proposed approach.

- Detection of edge directions – this step is based on the previously detected borders. Four main directions are taken into consideration: horizontal, vertical and two diagonals. These directions are marked by four different grey colours. This assumption can be stated due to the regular deployment of pixels inside an image.
- Tracing of edges – detected edges and their directions are used in the process of edge tracing. This is the most important step of calculations, giving efficient detection of edges, which are poorly visible. Two thresholds are used in this process, namely higher (TH) and lower (TL). TH is used to determine initial edges characterized by the brightest pixels. Then TL is applied to detect darker pixels, which are placed nearby already detected borders. Therefore, the reliability of such a solution is higher than in the case of traditional approaches.
- Elimination of small groups of pixels (blobs) – this step of calculations is focused on the thinning of thick borders and deletion of small groups of pixels. The thinned borders detected between grains are in most cases long and narrow, while the remaining distortions are still visible in the form of compact groups of pixels. The sizes of such groups do not usually exceed several pixels.
- Drawing of unclosed edges – the algorithm is based on the Bresenham method dedicated to rastering of a straight line between two separated points. In case of microstructure images these points are detected as the last elements of unclosed grain borders after performance of all the previously described steps.

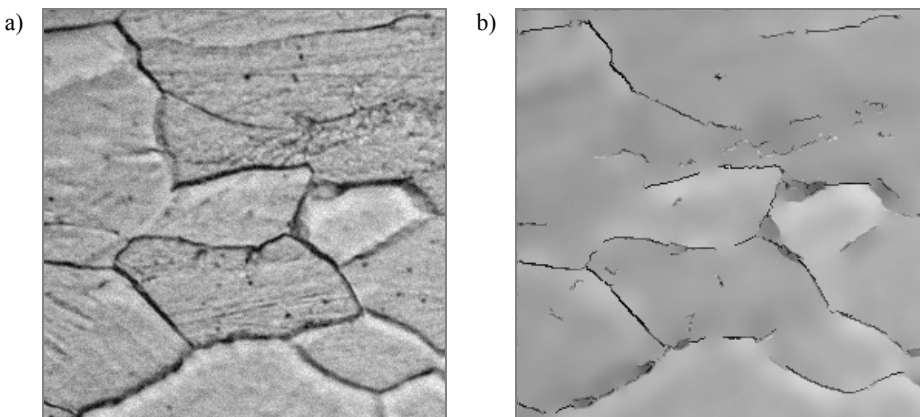


Fig. 2. Original picture of the microstructure taken by the
a) optical microscope and b) filtering result

The resultant structure of the data after edge analysis is in the form of an array composed of 0 values (non-border pixels) and 1 values (border pixels). This structure is used to map an image into a set of different areas related to particular grains and subgrains in the material microstructure presented in Figure 3.

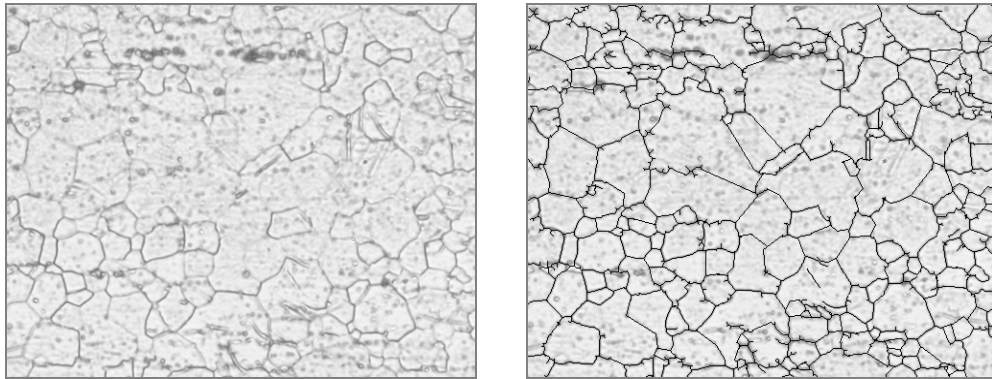


Fig. 3. Original pictures of Mg alloy (a) and its analysed equivalent picture with detected grain borders (b)

The described image processing methods precisely replicate all microstructure features. However, when a large number of calculations of DMR behaviour under loading are required, this method is unfortunately time consuming and expensive. Every numerical simulation has to be preceded by experimental research and metallographic analysis in order to provide an input image. That is why a method providing statistically realistic digital microstructure faster and cheaper is required. Two such methods are investigated within this work. The first is based on the Voronoi Tessellation. The second is based on the cellular automata framework.

2.2. Artificial methods

2.2.1. Voronoi method

Voronoi tessellation is a commonly used method dedicated to generation of initial microstructures as well as to interpretation of some metallographic phenomena [8]. The idea of this method is based on the mapping of the bounded area onto a group of specific polygons $P = \{p_1, \dots, p_n\}$, generated around a set of initial points $S = \{s_1, \dots, s_n\}$. Each polygon p_x is characterized by the two following features:

- It is connected exactly to one point s_x , where $x = 1 \dots n$.
- Each point inside the polygon is closer to s_x than to any other point from S .

For the purposes of this work points from the S set represent grains nuclei, while the polygon areas around these points, called Voronoi cellars, represent final grains in the microstructure.

Several algorithms used to determine the Voronoi diagram can be distinguished. One of them, based on the Brutal Forces approach, points out bisectrices between each pair of points and then eliminates bisectrices that do not satisfy Voronoi assumptions [3]. Nevertheless, this algorithm is very time consuming. Thus, the Fortune algorithm [3], which is much more efficient, has been chosen for the purposes of the DMR system.

Examples of the obtained results with the Fortune algorithm for a different number of grains are presented in Figure 4.

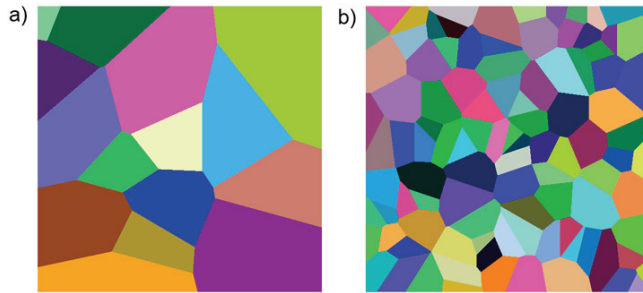


Fig. 4. Results of a) 15 and b) 150 grains

The obtained grain shapes are still far from the shapes of real grains observed under optical microscopes. That is why the Authors have decided to implement a grain growth algorithm based on the cellular automata method.

2.2.2. Cellular automata algorithm

The cellular automata technique was originally developed in the early 1960s by Janos Von Neumann [25] to simulate the behaviour of discrete, complex systems. In the early stages the capabilities of computers were the main obstacle limiting development of this method. However, this technique has become more popular with the increasing computational power of present-day computers. During the last few years the CA method has also been applied to model material behaviour during plastic deformation [5–6, 13]. In this work the CA-based algorithm was applied to generate the initial microstructure used later in some specific thermo-mechanical simulations.

The principle of cellular automata is based on three basic concepts:

- The cellular automaton space (a grid of a finite number of cells described by several internal variables).
- The cell neighbourhood (qualifies its closest neighbours).
- The transition rules that control the changes in the cell states.

In every time step, the internal variable describing the state of each cell in the lattice is determined by the previous states of its neighbours and the cell itself, by a set of precisely defined transition rules f :

$$\gamma_i^{t+1} = f(\gamma_j^t), \quad (2)$$

where:

$j \in N(i)$, $N(i)$ – surrounding of the i -th cell,

γ_i – state of the i -th cell.

On the basis of the CA method, modelling of the grain growth in the microstructure can be easily performed. The first step in the CA method is to establish the discrete space composed of cellular automata. With reference to 2D space it will be a grid consisting of squares. In the next step of the algorithm a set of CA cells is selected randomly, and then an internal variable describing the cells' state is set to "already grown". These cells represent grain nuclei. The second step of the algorithm is focused on grain growth. The transition rule for this stage is defined as follows: when a neighbour of a particular cell in the previous time step was in the state "already grown", then this particular cell can also change its state. Particular grains grow with no restrictions until the impingement with other grains. After that they grow only in the area where no grains are observed. This process is performed until the entire space is filled with grains.

Using this method, microstructure with significantly different grain sizes can be created, as seen in Figure 5. However, mentioned approach is very sensitive to the selection of the cellular automata neighbourhood. This behaviour is studied elsewhere [14].

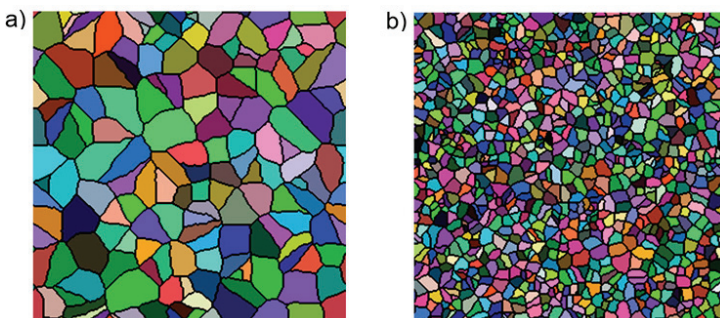


Fig. 5. Examples of 2D digital microstructures containing a) 150 and b) 1000 grains generated by the cellular automata approach

It can be concluded that the CA approach with the appropriate neighbourhood can very closely replicate in a statistical manner the geometry of a real microstructure after annealing or static/metadynamic recrystallization. The digital microstructure is then considered during numerical simulations of loading conditions as a statistical representation of a real microstructure.

3. Finite element modelling based on DMR

3.1. Homogeneous finite element meshes

The obtained digital microstructures can be incorporated into the commercial FE software by application of user defined subroutines. This procedure is designed to be performed automatically and does not require any other actions than running a con-

ventional FE simulation. Thus it can be used by engineers with no experience in the field of numerical methods. The algorithm is as follows:

- Based on the input data from DMR, the generation of the isotropic triangular mesh is performed. Then each element within this mesh is checked with the underlying DMR to which grain it belongs. When particular groups of mesh nodes are located inside separated grains, that means that different grains are distinguished.
- The selected flow curves describing particular materials (e.g., ferrite, austenite, martensite) are assigned to particular grains in the microstructure. These flow curves are reported in literature [4, 24, 26] or can be identified experimentally during simple monotonic deformation of a sample in a particular phase or particular crystallographic orientation. Examples of the flow curves obtained for steels in different phases are presented in Figure 6. Flow curves for different steel phases were identified by using micro scale experimental methods (i.e., nanoindentation tests) [4].
- In the simplified approach the possibility of capturing differences in grain flows due to various crystallographic orientations is due to diversification in the flow curves for each grain. This diversification is introduced here using the random Gauss distribution (Figure 6b).
- Starting the FE simulation is the final step.

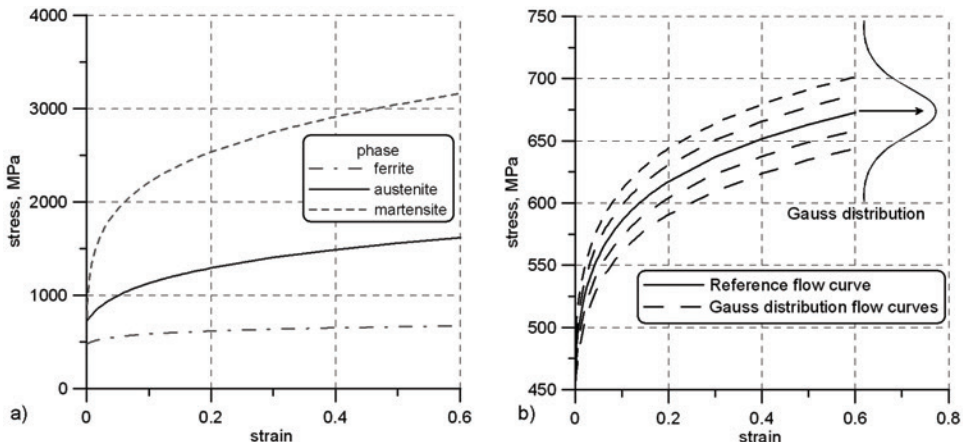


Fig. 6. a) Flow stress models for different steel phases [4], b) Idea of diversification in flow curves for the ferrite phase using the Gauss distribution function

The mentioned methodology was applied to the initial microstructure obtained from a real optical microscopy image. In this case a Fe30Ni sample was deformed. The flow stress model for this steel was diversified using the Gauss distribution function to represent differences in crystallographic orientations, as shown in Figure 6b. The initial optical microstructure and digital one is presented in Figure 7.

These results are then imported into the commercial FE software, and generation of the triangular mesh is performed (Figure 7c). As mentioned, particular groups of mesh

nodes are located inside separated grains, and a specific rheological model is assigned to each grain. The simulations of the behaviour and interactions of particular grains in the polycrystalline aggregate during channel die compression are shown in Figure 8.

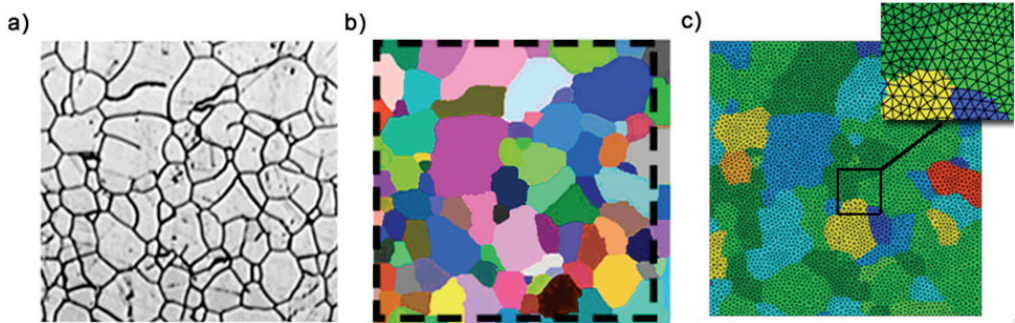


Fig. 7. a) initial optical microstructure, b) digital microstructure obtained after image processing and c) digital microstructure with the finite element mesh generated in Forge code

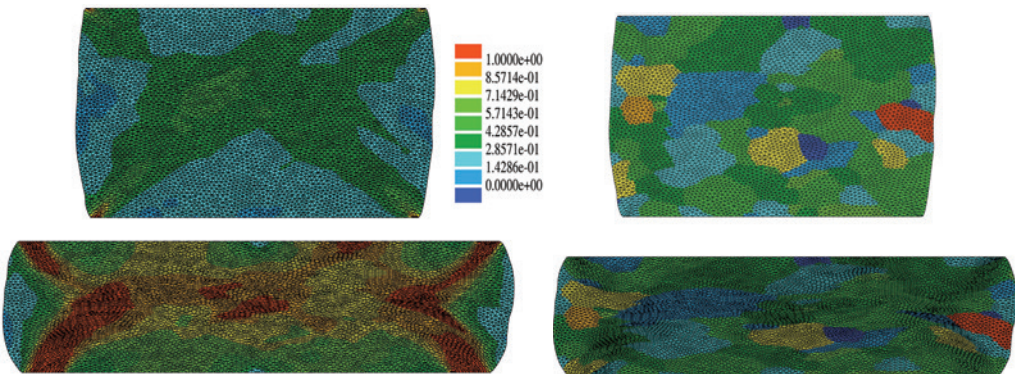


Fig. 8. Results of simulations of the channel die compression of a Fe30Ni sample,
a) strain distribution at the beginning and end of compression, b) evolution
of microstructure deformation. Size of the microstructure is $300 \times 300 \mu\text{m}$

As seen in Figure 8, despite the same material being under consideration the strain distribution is not behaving in a uniform manner. The strain distribution is affected by small differences in the flow stress models assigned to particular grains. When a sample containing billion of grains is considered, then the unification of grains behaviour into only one stress model is justified. However, when the amount of grains is limited to 100 for example, then behaviour of each particular grain due to differences in shape or crystallographic orientation plays an important role.

To highlight differences in strain distribution during deformation that are related to variation in grain properties (e.g. crystallographic orientation), a series of simple triple grain systems was considered. Each grain describes an Al in a different crystallographic

orientation: Cube, Hard, Goss or Shear. In this case the flow stress models for different crystallographic orientations were obtained through a series of monocrystalline sample deformations [24, 26].

The numerical simulation was performed with the assumption that three grains create a triple point junction, and the initial grain arrangement is the same. Examples of results obtained after compression are shown in Figure 9.

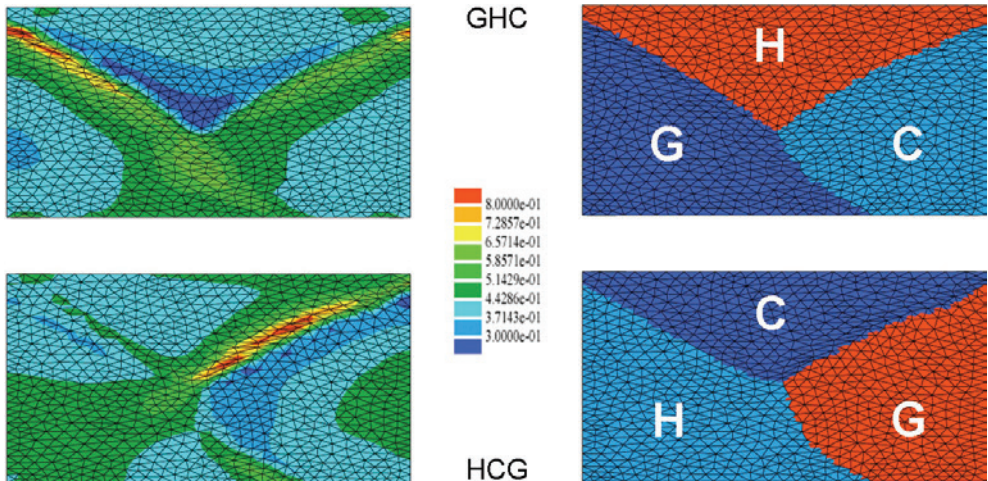


Fig. 9. Strain distribution (left) and corresponding final grain shape obtained for two different arrangements of crystallographic orientations: (Goss, Hard, Cube) and (Hard, Cube, Goss)

It can be pointed out that the assumption of free edges in the case of only three grains is not appropriate. However, this example is only to investigate possibilities and limitations of applying the digital microstructures. As seen in Figure 9, despite having the same initial geometry within this three grain system, the final shape is significantly different. Large differences in strain distribution are also clearly visible with the highest values of accumulated strain in the grain with Cube orientation and the lowest in Hard orientation. Zones with high strain localization are clearly visible, especially along the grain boundaries.

Despite the presented possibilities and advantages provided by the use of digital material representation with the homogenous finite element meshes, some disadvantages were also noticed. The first is that since application of the homogenous meshes cannot exactly capture the geometry of the grain boundaries, there are some small deviations. The second disadvantage is related to the accuracy of results and the computational time. As seen in Figure 9 the strain localization usually occurs along grain boundaries. To properly describe this phenomenon by homogenous meshes, a highly refined mesh has to be created in the entire area, which leads to lengthy computations. To properly capture material behaviour along the grain boundaries and not extend computational time, specific heterogenic FE meshes have to be used. The FE mesh is

highly refined along the grain boundary, while the centre of the grains is discretized by a coarse mesh. Since this kind of functionality is not available in commercial FE mesh generators, the Authors have decided to use a newly created code developed within the present work. To create these meshes, information provided from the digital microstructure regarding position of the grain boundary, as well as grain nuclei, was used. To control the finite element refinement along the grain boundaries, a simple function was introduced that specifies the amount of new nodes located in these areas. An example of the mesh generation with this code is shown in Figure 10.

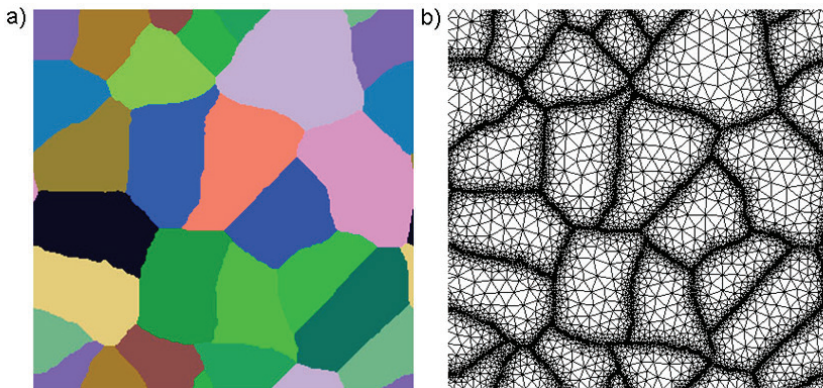


Fig. 10. Digital material representation and subsequent steps of FE mesh refinement along the grain boundaries

As seen in Figure 10, the size of the finite elements decreases along the grain boundary to obtain a refined mesh for accurate modelling of strain gradients and course mesh for modelling grain interior. These refined meshes with differently assigned material properties are again input data for the finite element simulation. Examples of results of simple plain strain compression tests performed at the micro scale level for one-phase materials are shown in the following chapter. Particular attention is placed on analysis of the influence of mesh refinement on accuracy of the obtained results.

3.2. Heterogeneous finite element meshes

To analyze how the level of mesh refinement along the grain boundaries influences the accuracy of numerical simulations, four different cases were investigated as seen in Figure 11. The initial microstructure contained twenty ferrite grains. Additionally four grains were assumed to be in the austenite range. That way a clear property gradient was introduced into the material to provide easier analysis of the differences. As shown, the stress concentration is clearly visible in all four cases along the grain boundaries between the ferrite and austenite phases. However, when the refinement level increases, the stress concentration becomes localized in the narrow region in the

area of the three-point junctions, which can be observed in Figure 11d. This behaviour is important as these regions may be the precursor of material failure. The obtained results point out the advantage in proper material description offered by the refined meshes in comparison with the homogenous meshes. Unfortunately, with increasing accuracy the computational time increases as well, which makes the selection of the appropriate solution a balance between time and accuracy.

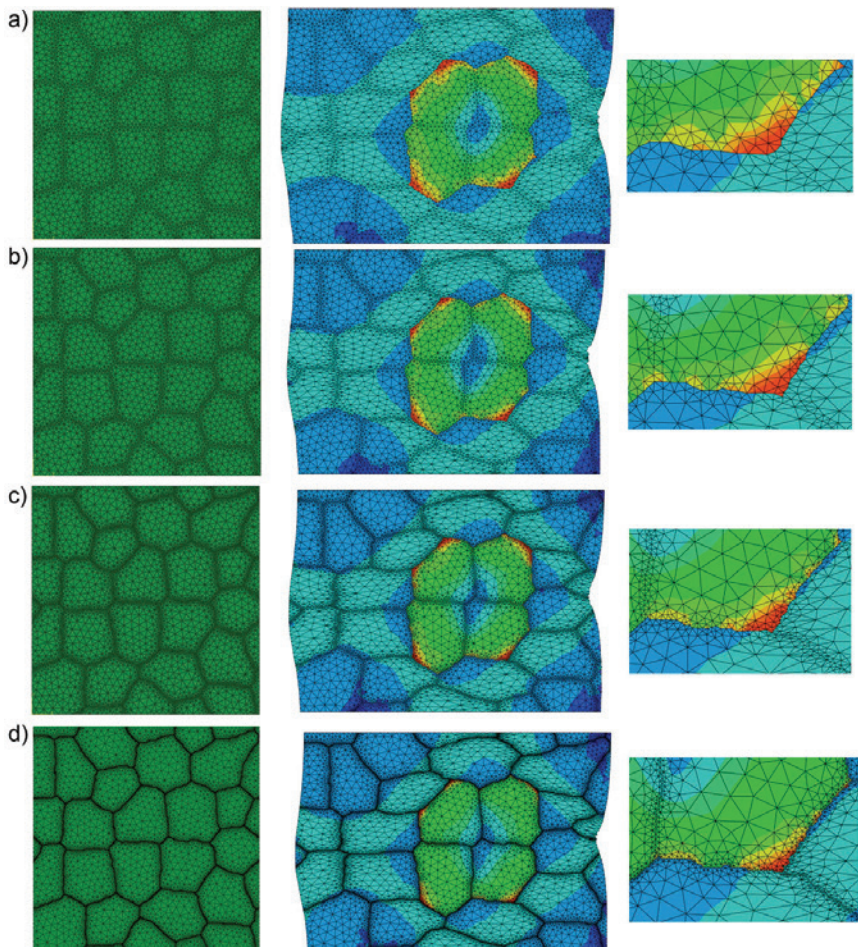


Fig. 11. Digital material representation and subsequent steps of FE mesh refinement along the grain boundaries: initial mesh (left), strain distribution after deformation (centre), enlargement of the strain distribution close to the triple point junction (right). Size of the microstructure is $300 \times 300 \mu\text{m}$

As presented in the earlier chapter, the developed digital material representation system combined with the finite element method can provide valuable data of material behaviour at the micro scale level to simulate micro forming processes. However, to

provide capabilities of material behaviour not only at the micro scale level, the digital material representation has to be combined with the macro scale information. The multi scale concurrent model (e.g., CAFE model) is one of the possibilities [12–13]. The idea of this approach and examples of numerical simulations are shown below.

4. Multi scale model

In the present work a multi scale concurrent finite element based model is proposed. In this approach the macro scale material behaviour is modelled as a global model with a relatively coarse finite element mesh. However, some regions in this mesh are selected, and finite element meshes created on the basis of the digital material representation are attached. In this way the model provides general strain, stress, temperature, etc. information at the macro scale level and at the same time very detailed information about microstructure behaviour at the micro scale level. The idea of this model is shown in Figure 12.

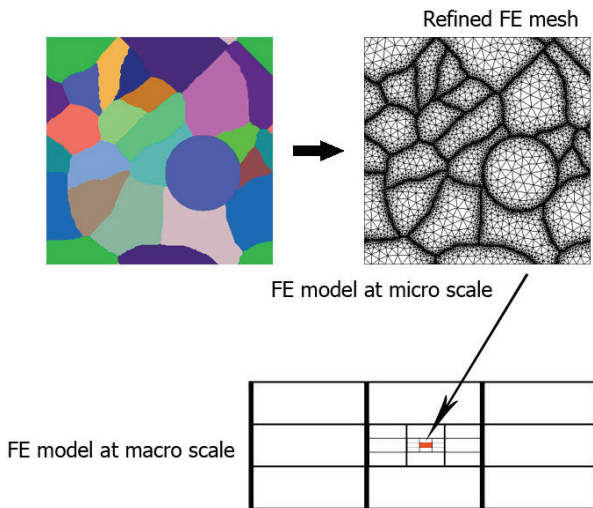


Fig. 12. Illustration of the idea of the multi scale concurrent method based on digital material representation

A sub-model is created using the partition of the global model. The refined sub-model is then resubmitted with displacement boundary conditions taken from the global simulation.

Presented multi scale approach is used in the work to perform simulation of a simple plastometric tension test as well as real industrial rolling process. In the first case a digital representation of dual phase (DP) steel is used. A real image of the microstructure obtained from literature [7] is used as an input to create a digital material representation. The image processing approach presented in section 2.1 is used to

transfer microstructure image into the digital form (Figure 13). Obtained DMR with dimensions $57 \mu\text{m} \times 45 \mu\text{m}$ is attached at the centre of the specimen to exactly reflect experimental procedure described in [7]. Example of obtained numerical simulation results both at the macro and micro scale levels are shown in Figure 13.

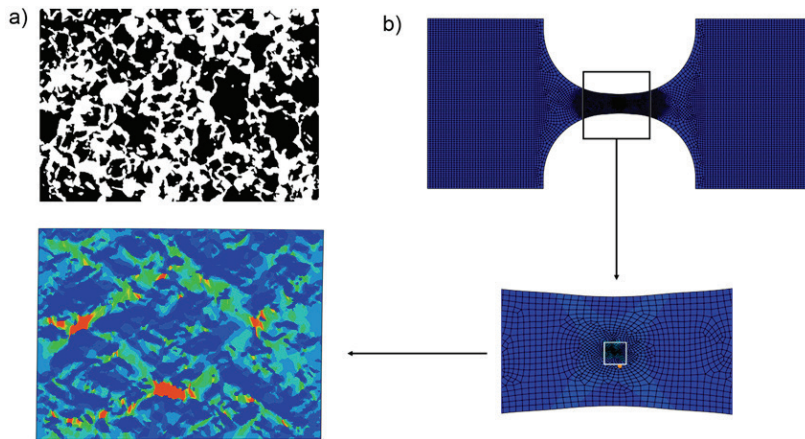


Fig. 13. a) real microstructure image transferred into the digital form, b) equivalent strain distribution obtained from multi scale numerical simulation. Size of the microstructure is $57 \times 45 \mu\text{m}$

It is reported in [7] that the strain localization bands initiate inside the ferrite phase, and then cross martensite islands as they progress. It was also found that the highest strain values are located in the ferrite phase, but very close to the interface with the martensite. The same behaviour is observed numerically as seen in Figure 13. Obtained equivalent strain distribution field is in a qualitative agreement with the experiment. Characteristic strain distribution pattern involving strain localization bands aligned 45° to the deformation direction is visible. Results presented in Figure 13 confirm good predictive capabilities of the developed digital material representation approach.

This approach was then tested during the simulation of the rolling process. Digital microstructures were obtained using cellular automata grain growth algorithm. Examples of simulation at the macro as well as micro scale level are presented in Figure 14.

The highest strain values are observed at the surface of the rolling plate (point 1). In this region a failure due to strain localization is also the most probable. The lowest values of strain are observed in the centre of the plate (point 3). In this research the same microstructure was attached to all three locations to highlight how different strain distributions can be obtained at the micro scale level. Proper description of this behaviour is possible due to highly refined FE meshes in these regions. These inhomogeneities at the micro scale level play a significant role when other phenomena such as dynamic recrystallization or crack initiation are considered. The macro scale model itself cannot provide such detailed information about the actual state of the material.

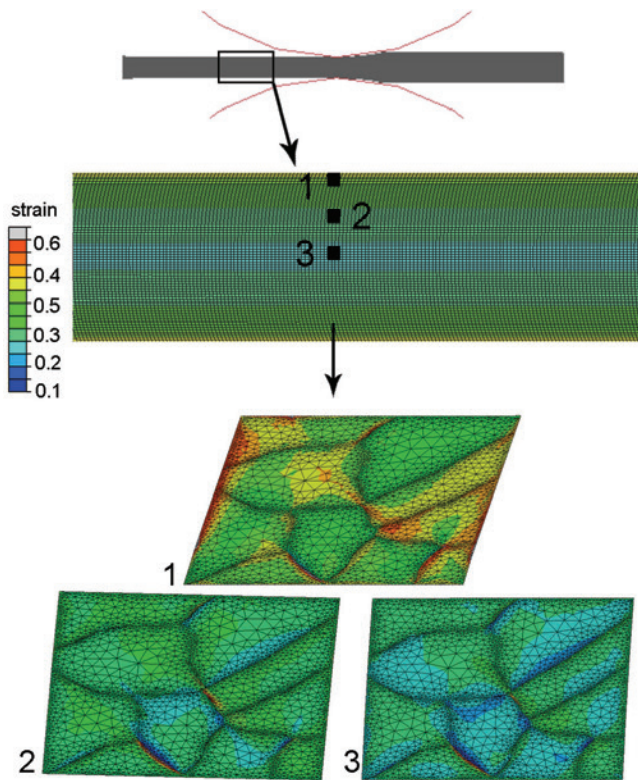


Fig. 14. Strain distribution at the macro and micro scale level during the rolling process with the locations of the sub-models based on digital microstructures. Size of each microstructure is $300 \times 300 \mu\text{m}$

5. Summary

The results of research on the development of a digital representation of microstructures and the advantages provided by this technique were discussed in the paper. Finally it can be concluded that:

- The image processing algorithms give the possibility to obtain a realistic digital microstructure based on the easily accessible optical microscopy images. Unfortunately, there are three major drawbacks of this approach. Firstly, the final quality of created structures depends on the quality of input images. The more distorted the images are, the less accurate digital representations can be obtained. Secondly, this procedure becomes more complex when 3D microstructures are considered because it must be combined with reconstruction algorithms in order to obtain a 3D structure from 2D images. Finally, if a large number of simulations are required on the basis of various microstructures (e.g., with small grains or large grains) a series of experimental research must be performed first, which will increase costs and time required for analysis.

- To solve issues related to image processing, an alternative solution based on CA and Voronoi tessellation can be used. That way statistically representative micro-structures are obtained and can be used during FE analysis.
- The developed approach, which uses refined meshes, predicts better strain localization along the grain boundaries in comparison to homogeneous meshes. This is important because severe strain localization can develop in a narrow region that can be a precursor of material failure. When microstructure features, such as phase boundaries or inclusions, are analyzed, these refined meshes are especially important.
- The simple multi scale model based on digital material representation provides very interesting results on strain distribution at the micro as well as macro scale.

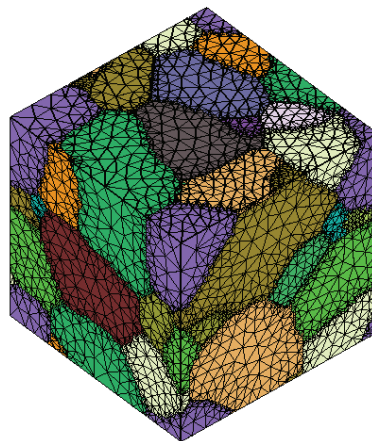


Fig. 15. 3D digital representation with created refined FE mesh

There is also a possibility to combine the presented approach based on DMR with the crystal plasticity model and to extend the capabilities to solve 3D problems. Initial results of the 3D approach that will be further investigated are presented in Figure 15.

Acknowledgements

Project within N N508 583839 is acknowledged. One of the Authors (LM) is grateful for the financial support of the Foundation for Polish Science within the Start program. FEM calculations were realized at the ACK CYFRONET AGH MNiSW/IBM_BC_HS21/AGH/075/2010.

References

- [1] Beladi H., Adachi Y., Timokhina I., Hodgson P.D.: *Crystallographic analysis of nano-bainitic steels*, Scripta Materialia, Vol. 60, 2009, pp. 455–458.

- [2] Chenot J.-L., Chastel Y.: *Mechanical, thermal and physical coupling methods in FE analysis of metal forming processes*, Journal of Materials Processing Technology, Vol. 60, No. 1–4, pp. 11–18.
- [3] De Berg M., Van Krevel M., Overmars M., Schwarzkopf O.: *Computational geometry algorithms and applications*, Springer-Verlag, 2000.
- [4] Delannay L., Doghri I., Pierard O.: *Prediction of tension-compression cycles in multi-phase steel using a modified incremental mean-field model*, International Journal of Solid and Structures, Vol. 44, 2007, pp. 7291–7306.
- [5] Gawad J., Paszynski M., Matuszyk P., Madej L.: *Cellular automata coupled with hp-adaptive Finite Element Method applied to simulation of austenite-ferrite phase transformation with a moving interface*, Steel Research International, Vol. 79, 2008, pp. 579–586.
- [6] Gawad J., Madej L., Szeliga D., Pietrzyk M.: *Cellular automaton technique as a tool for a complex analysis of the microstructure evolution and rheological behaviour*, Acta Metallurgica Slovaca, Vol. 11, 2005, pp. 45–53.
- [7] Ghadbeigi H., Pinna C., Celotto S., Yates J.R.: *Local plastic strain evolution in a high strength dual-phase steel*, Materials Science and Engineering A, Vol. 527, 2010, pp. 5026–5032.
- [8] Grujicic M., Zhang Y.: *Determination of effective elastic properties of functionally graded materials using Voronoi cell finite element method*, Material Science Engineering A, Vol. A251, 1998, pp. 64–76.
- [9] Jaroni U., Imlaau K.P., Osburg B.: *Neue Lösungsansätze für innovative Produkte und Umformtechnologien im Automobilbau*, Proc. ASK25, Aachen, 2010, pp. 3–14.
- [10] Justinger H., Hirt G.: *Estimation of grain size and grain orientation influence in micro-forming processes by Taylor factor considerations*, Journal of Material Processing Technology, Vol. 209, 2009, pp. 2111–2121.
- [11] Kobayashi S., Oh S.I., Altan T.: *Metal forming and the finite element method*, Oxford University Press, New York, Oxford, 1989.
- [12] Madej L., Mrozek A., Kus W., Burczynski T., Pietrzyk M.: *Concurrent and upscaling methods in multi scale modelling – case studies*, Computer Methods in Material Science, Vol. 8, 2008, pp. 1–15.
- [13] Madej L., Hodgson P.D., Pietrzyk M.: *Development of the multi-scale analysis model to simulate strain localization occurring during material processing*, Archives of Computational Methods in Engineering, Vol. 16, 2009, pp. 287–318.
- [14] Madej L.: *Digital material representation of polycrystals in application to numerical simulations of inhomogenous deformation*, Computer Methods in Materials Science, Vol. 10, 2010, pp. 143–155.
- [15] Melchior M.A., Delannay L.: *A texture discretization technique adapted to polycrystalline aggregates with non-uniform grain size*, Computational Material Science, Vol. 37, 2006, pp. 557–564.
- [16] Montmitonnet P., Logé R., Hamery M., Chastel Y., Doudoux J-L., Aubin J-L.: *3D elastic-plastic finite element simulation of cold pilgering of zircaloy tubes*, Journal of Materials Processing Technology, Vol. 125–126, 2002, pp. 814–820.
- [17] Pietrzyk M.: *Through-process modelling of microstructure evolution in hot forming of steels*, Journal of Materials Processing Technology, Vol. 125–126, 2002, pp. 53–62.
- [18] Pietrzyk M., Madej L., Szeliga D., Kuziak R., Pidvysotskyy V., Paul H., Wajda W.: *Rheological models of metallic materials*, in: Research in Polish Metallurgy at the Begin-

- ning of XXI Century, eds. K. Swiatkowski, M. Blicharski, K. Fitzner, W. Kapturkiewicz, M. Pietrzyk, J. Kazior, Akapit, Krakow, 2006, pp. 325–346.
- [19] Rauch L., Kusiak J.: *Image filtering using dynamic particles method*, Modelling dynamics in processes and systems, Vol. 180, 2009, pp. 153–163.
- [20] Rauch L., Madej L.: *Deformation of the dual phase material on the basis of digital representation of microstructure*, Steel Research International, Vol. 79, 2008, pp. 247–254.
- [21] Sabirov I., Estrin Y., Barnett M.R., Timokhina I., Hodgson P.D.: *Tensile deformation of an ultrafine-grained aluminium alloy: Micro shear banding and grain boundary sliding*, Acta Materialia, Vol. 56, 2008, pp. 2223–2230.
- [22] Szeliga D., Pietrzyk M.: *Testing of the inverse software for identification of rheological models of materials subjected to plastic deformation*, Archives of Civil and Mechanical Engineering, Vol. 7, 2007, pp. 35–52.
- [23] Timokhina I.B., Hodgson P.D., Ringer S.P., Zheng R.K., Pereloma E.V.: *Precipitate characterisation of an advanced high-strength low-alloy (HSLA) steel using atom probe tomography*, Scripta Materialia, Vol. 56, 2007, pp. 601–604.
- [24] Trebacz L., Madej L., Wajda W., Paul H.: *Simulation of plastic behaviour of FCC metals accounting for lattice orientation*, Proc. WCCM'08, Venice, CD, 2008, pp. 1–2.
- [25] Von Neumann J.: *Theory of Self Reproducing Automata*, ed., Bamk A W, University of Illinois, Urbana, 1966.
- [26] Wajda W., Paul H.: *Modelling of microstructure and texture evolution of channel-die deformed aluminum bicrystals with $\{100\} <001>/\{110\} <011>$ grains orientation*, Computer Methods in Material Science, Vol. 9, 2009, pp. 277–282.

Analiza niejednorodności odkształcenia w skali mikro z wykorzystaniem Cyfrowej Reprezentacji Materiału

W pracy przedstawiono koncepcję tworzenia Cyfrowej Reprezentacji Materiału oraz jej zastosowanie do analizy niejednorodności odkształcenia na poziomie mikro skali. Omówiono dwie grupy metod odwzorowujących mikrostrukturę z jej cechami charakterystycznymi np. ziarna, granice ziaren. Pierwsza z nich obejmuje metody analizy obrazu rzeczywistych zgładów metalograficznych. Druga natomiast dotyczy metod tworzenia statystycznie reprezentacyjnych mikrostruktur. Otrzymane reprezentacje stanowią dane wejściowe do dalszej analizy niejednorodności odkształcenia na poziomie mikrostruktury. Przykłady zastosowań w symulacjach wieloskalowych również zostały omówione w ramach niniejszej pracy.



Dwelling selection by applying fuzzy game theory

M. MEDINECKIENE, E.K. ZAVADSKAS, Z. TURSKIS

Vilnius Gediminas Technical University, Faculty of Civil Engineering, Department of Construction Technology and Management, Sauletekio ave. 11, LT-10223 Vilnius, Lithuania.

The paper describes model of dwelling selection, using fuzzy games theory. Two types of buildings are under consideration: traditional single flat dwelling house and loft flat dwelling house. Four alternatives of heating system are taking into account: coal based, gas based, biomass based, and combined biomass and gas based systems. Alternatives are described by a criteria set. Values of the criteria are determined by simulation and according to the statistic. Fuzzy games are applied for decision aiding. The problem solution result shows that fuzzy matrix games theory is appropriate for such purposes.

Keywords: *dwelling, alternative, selection, multiple criteria, fuzzy, game theory, MCDM, heating system*

1. Introduction

Decision making in real life is selection process among feasible alternatives, taking into account several criteria. Various decision making approaches have been proposed to tackle the problem. The Multi-Criteria Decision Aid (MCDA) has been one of the very fast growing areas of Operations Research during the last decade. The MCDA often deals with ranking of alternatives from the best to the worst ones based on multiple criteria [3]. Traditional optimization, statistical and econometric analysis approaches used within the engineering context are often based on the assumption that the considered problem is well formulated and decision-makers usually consider the existence of a single objective, evaluation criterion or point of view that underlies the conducted analysis [53]. Since the suitability of a dwelling-house for living depends on a number of attributes, like temperature, noise isolation, annual heat requirements, etc., a multi-attribute decision making (MADM) methods are used for their assessment [18]. Multi-criteria classification problems have gained significant interest among researchers working on MCDA [8]. The criteria are often qualitative and conflicting. A decision should be made by taking relevant opinions from the experts because inherent complexity and uncertainty in a business environment necessitate the participation of many experts in the decision making process [28].

In contemporary management, the performance is evaluated against multiple criteria rather than considering a single factor-cost [11]. In decision-making involving multiple criteria, the basic problem stated by analysts and decision-makers concerns the way by which the final decision should be made [13]. Multi-criteria decision making (MCDM) is not a prescriptive answer but a transparent and informative decision proc-

ess which helps to uncover how peoples' intuitive decision procedures can be informed by a structured rational analytic process [1]. MCDM is concerned with the ranking of decision alternatives based on preference judgements made on decision alternatives over a number of criteria [7].

Fuzzy theory has been regarded as a very important technique for quality management of distributed manufacturing system and attracts the attentions of academic and industry [46].

Model and using of dwelling selection, based on fuzzy game theory, is described in this paper.

The rest of the paper is organized as follows: section 2 shows game theory application in engineering, according on the literature review; section 3 describes a review of fuzzy sets in multi-criteria decision making, short about fuzzy theory authors and detail about investigation methodology of fuzzy set theory and fuzzy games, and review of case study; section 4 is dedicated for results and discussion; section 5 summarize the conclusions.

2. Game theory application in engineering

Game theory is developed to study decision making in situations of conflict and sometimes cooperation. Game theory provides a mathematical process for selecting an optimal strategy [22]. Game theory can be applied to solve decision-making problems in engineering. That approves some works of scientists, which published their researches in this area:

In the field of Civil Engineering one of the first authors was professor Peldschus [29, 31], who used game theory and fuzziness in MCDM. A review of his works is focused in publication of Kapliński and Tamošaitienė [19].

Hennet and Arda [10] evaluated the efficiency of different types of contracts between the industrial partners of a supply chain. The model combines queuing theory for evaluation aspects and game theory for decisional purposes.

Liu et al. [24] proposed a method for multi-objective categorization based on the game theory and Markov process. They adopt Shapley value in coalitional games to measure the player's satisfaction degree in a group.

Sharma and Gopal [39] presented new direction that seeks to synergize broad areas of Reinforcement learning and Game theory, as an interesting and challenging avenue for designing intelligent and reliable controllers.

Long and Yu [25] applied the game theory to analyze the optimal strategy between the government and the enterprises in the process of implementing energy-saving and emission-reduction action, to get a mixed strategy Nash equilibrium solution.

Charilas and Panagopoulos [6] collected applications of game theory in wireless networking and presents them in a layered perspective, emphasizing on which fields game theory could be effectively applied.

Bompard et al. [4] presented a medium run electricity market simulator based on game theory.

Fiestras-Janeiro et al. [9] provides a review of the applications of cooperative game theory in the management of centralized inventory systems.

Madani [27] reviewed applicability of game theory to water resources management and conflict resolution through a series of non-cooperative water resource games. His paper illustrates the dynamic structure of water resource problems and the importance of considering the game's evolution path while studying such problems.

As multi-discipline coupling and components interference often affect the aircraft configuration decision-making and analysis during conceptual design process, Runyan et al. [36] presented an approach of multidimensional game theory based on aircraft components to deal with this problem.

Applying of matrix game theory in civil engineering was investigated only by several authors [30, 32–34, 42, 51]. Matrix game theory software was developed for problems solution in economics, management and civil engineering [49, 50, 52]. The software was successfully applied to solve the problems.

3. Review of Fuzzy sets in multi-criteria decision making

There are some modern works with fuzzy sets in multi-criteria decision making:

In order to address the imprecision of suppliers or decision makers in formulating the preference value of various attributes in MCDM, a fuzzy TOPSIS based methodology along with a mechanism for determination of fuzzy linguistic value of each attribute is proposed in paper of Singh and Benyoucef [40].

Vahidnia et al. [44] developed a Multi-Criteria Decision Analysis process that combines Geographical Information System analysis with the Fuzzy Analytical Hierarchy Process, and use this process to determine the optimum site for a new hospital in the Tehran urban area.

A fuzzy MCDA model was applied by Xi et al. [45] for analyzing the optimal solutions among the three alternatives in waste management.

Kahraman and Kaya [17] suggested a fuzzy multi-criteria decision-making methodology for the selection among energy policies. The methodology is based on the analytic hierarchy process (AHP) under fuzziness. It allows the evaluation scores from experts to be linguistic expressions, crisp or fuzzy numbers. In the application of the proposed methodology, the best energy policy is determined for Turkey.

To reflect the vague side of human thinking and evaluation Kahraman et al. [14] incorporated the fuzzy set theory into multi-attribute model. Fuzzy TOPSIS is the selected fuzzy multi-attribute method because of its effectiveness and applicability.

Liu et al. [23] documented how an integrated Deliberative Multi-Criteria Evaluation and fuzzy set approach can tackle the dual challenges of conflicting goals and uncertainty in the analysis of Invasive Alien Species risk management strategies.

Boroushaki and Malczewski [5] presented the fuzzy majority approach using Induced ordered weighted averaging procedure for GIS-based multi-criteria decision-making and its implementation in the ArcGIS environment.

Torfi [41] proposed a Fuzzy multi-criteria decision-making approach (FMCMD) to evaluate the alternative options in respect to the user's preference orders. Two FMCMD methods are proposed for solving the MCDM problem: Fuzzy Analytic Hierarchy Process is applied to determine the relative weights of the evaluation criteria and the extension of the Fuzzy Technique for Order Preference by Similarity to Ideal Solution (FTOPSIS) is applied to rank the alternatives.

Kaya and Kahraman [20] applied an integrated VIKOR–AHP methodology to make a selection among the alternative forestation areas in Istanbul. In the proposed methodology, the weights of the selection criteria are determined by fuzzy pair-wise comparison matrices of AHP.

Lu and Wang [26] provided an alternative approach, the non-additive fuzzy integral, to deal with the fuzzy MCDM problems especially when there is dependence among considered criteria.

Fuzzy multi-criteria decision-making methodologies have also been used for the selection of renewable energy alternatives, where fuzzy axiomatic design was applied to the selection of the renewable energy alternatives in Turkey [16].

Civil engineering problems are multiple-criteria problems. There should be taken into account different criteria, values of which are imprecise or fuzzy. Plebankiewicz [35] presented a model based on fuzzy sets for contractor prequalification. The model takes into consideration different criteria of contractor evaluation and the objectives the construction owner to achieve in the project.

Hui [12] pointed on that the fuzzy tactical asset allocation with the inclusion of experts judgments, which contain information usually not found in historical data, is able to produce a portfolio just as efficient as traditional asset allocation models while minimizing the potential issues due to imprecision and vagueness of information.

By understanding properly fuzzy problems, real estate developers can adopt appropriate actions and strategies to utilize organization resources more effectively to enhance their competitiveness, thus improve their business performance in the market [55].

On the foundation of the theory of the intuitionistic fuzzy set, Zhang and Liu [54] use the triangular fuzzy number to denote the membership degree and the non-membership degree and propose the triangular intuitionistic fuzzy number. Then the operation rules of triangular intuitionistic fuzzy numbers are defined.

Traditional valuation methods are less viable under uncertainty [43]. Fuzziness is one aspect of uncertainty. It is the vagueness found in the definition of a concept or the meaning of a term. Fuzzy memberships represent similarities of objects to imprecisely denoted properties, while probabilities convey information about relative frequencies [15].

All the proposed works use fuzzy multi-criteria decision making methods in different areas: domestic energy, renewable energy selection, invasive species management, selection of the site, selection of the forestation areas and in the industrial cooperation

program transaction strategies. In this work the fuzzy set theory is used to help the costumer in selection the living apartment.

3.1. Fuzzy set theory

Zadeh [47–48] was the first, who proposed nonlinear dependency functions:

$$\mu_A = \begin{cases} 0, & \text{when } A \leq a_1, \\ 2 \times \left(\frac{A - a_1}{a_3 - a_1} \right)^2, & \text{when } a_1 \leq A \leq a_2, \\ 1 - 2 \times \left(\frac{A - a_3}{a_3 - a_1} \right)^2, & \text{when } a_2 \leq A \leq a_3, \\ 1, & \text{when } A \geq a_3, \end{cases} \quad (1)$$

where a_1, a_2, a_3 are subjectively set values.

Dependency function is a description of dependence of dependency value's (μ) from the options of the values (x), based on the models of the parameters $\mu_{(x, p)}$.

Leberling [21] nonlinear dependency function expressed with hyperbolic function:

$$\mu_{(x)} = \frac{1}{2} \cdot \frac{e^{(x-(a+b)/2)\delta} - e^{-(x-(a+b)/2)\delta}}{e^{(x-(a+b)/2)\delta} + e^{-(x-(a+b)/2)\delta}} + \frac{1}{2}, \quad (2)$$

where a and b – two extreme values.

But Leberling didn't explain how to determine δ value.

The fuzzy set theory is used in decision making methods of utility theory. Here is an analogy between dependency function and utility function. For the description of the utility is usable volatile event and concave form function. This describes Bamberg and Coenenberg [2], Schneeweiss [37].

3.2. Investigation methodology. Fuzzy set theory and fuzzy games

Methodology is composed from the documents, which are cited in this section and according on the methodology of Omran and Peldschus [29], Peldschus and Zavadskas [31].

Schwab [38] proposed nonlinear dependency functions, which can be used in multi-criteria decision making. Schwab tried to present defined requirements for the dependency function. Here are the general of them:

- continuity,
- constant variation,
- monotony.

Those requirements should be done for the defined function, which necessary should go throw the three subjectively defined points. The partition into classes of area of the alternatives run throw the selection of three points (a_0, a_d, a_m), in which the dependency values are $\mu_{(a0)} = 0$, $\mu_{(ad)} = 0.5$, $\mu_{(am)} = 1$. In this way the set of the alternative is divided into four groups:

$$\begin{aligned} x_I = B_1 &\Leftrightarrow x_{ij} \leq a_j, \\ x_I = B_2 &\Leftrightarrow a_m \leq x_{ij}, \\ x_I = B_3 &\Leftrightarrow a_0 < x_{ij} \leq a_d, \\ x_I = B_4 &\Leftrightarrow a_d < x_{ij} \leq a_m. \end{aligned} \tag{3}$$

Mathematical three requirements look as follows ((a) – (f)):

(a) μ_i is constant a_j , for each $\varepsilon > 0$ and $\delta > 0$, a_j^1 and a_j^2 with $|a_j^1 - a_j^2| < \delta$ available, $|\mu_j(a_j^1) - \mu_j(a_j^2)| < \varepsilon$.

This means, that when we have close values of the parameters, it can be only slight difference between dependency values.

(b) $d\mu_j/dx_j$ exists and a_j is constant.

(c) $d\mu_j/dx_j$ exists and $[a_0, a_m]$ or $[a_m, a_0]$ is constant.

(d) Raises one more fourth requirement $[a_m, a_0]$, and minimum curvature of the dependence function, that means that curve, described with dependency function, runs as much strait as it possible and this makes $d\mu_j/dx_j$ as possible small.

According on the requirements ((a) – (d)) and on the three selected points, exists one and only one function, which can fulfil these requirements; just interpolation of S function. From here are formulating third degree polynomials, in $[a_0, a_D]$ and $[a_D, a_m]$ intervals.

$$\mu_j(a) = \begin{cases} 0, & \text{when } a \leq a_0, \\ Aa^3 + Ba^2 + Ca + D, & \text{when } a_0 \leq a \leq a_d, \\ Ea^3 + Fa^2 + Ga + H, & \text{when } a_d \leq a \leq a_m, \\ 1, & \text{when } a_m \leq a. \end{cases} \tag{4}$$

Coefficients (A, \dots, H) are calculating by the help of equation system. According on the requirement (1) about μ_j constancy or on the initial points of the function, we can write four functions, and they look as follows:

$$\begin{aligned} (G1) \quad &Aa_0^3 + Ba_0^2 + Ca_0 + D = 0, \\ (G2) \quad &Aa_d^3 + Ba_d^2 + Ca_d + D = 0.5, \\ (G3) \quad &Ea_d^3 + Fa_d^2 + Ga_d + H = 0.5, \\ (G4) \quad &Ea_m^3 + Fa_m^2 + Ga_m + H = 1. \end{aligned} \tag{5}$$

Requirement (2) about μ_j first derivative or about the limited solutions of the function requires those three equations:

$$\begin{aligned} (G5) \quad & 3Aa_0^2 + 2Ba_0 + C = 0, \\ (G6) \quad & 3Ea_m^2 + 2Fa_m + G = 0, \\ (G7) \quad & 3Aa_d^2 + 2Ba_d + C - 3Ea_d^2 - 2Fa_d - G = 0. \end{aligned} \quad (6)$$

The last equation is obtained from the (3) requirement μ_j or from the properties of the function, which polynomials in the starting points got connection, double continuously:

$$(G8) \quad 6Aa_d + 2B - 6Ea_d - 2F = 0. \quad (7)$$

This linear equation system $\{(G1)-(G8)\}$ is „full” and has unambiguous solution $\{A, \dots, H\}$.

Dependency function must satisfy the next two conditions:

- (e) $\mu_j(a_j) \in [0, 1]$.
- (f) μ_j monotonic a_j .

However, this is valid not in all cases, when μ_j function is described by (a)–(d) requirements and three points (a_0, a_d, a_m) . When a_d is close to a_0 or a_m , μ_j values goes beyond the range $[0, 1]$ and in this way μ_j is not monotonic anymore. In order to prevent this, this inequality has to be fulfilled:

$$-1 + \sqrt{2} \leq \frac{|a_m - a_d|}{|a_d - a_0|} \leq 1 + \sqrt{2}. \quad (8)$$

The next step of the calculations is fuzzy games. Fuzzy games generally can be described by this formula:

$$\Gamma_m = \left\{ (x_i, y_i), (y_i, \mu_{ij}), (a_{ij}, \mu_{ij}^*) \right\}, \quad \text{for } i = 1, \dots, m, j = 1, \dots, n, \quad (9)$$

where:

- Γ_m – Fuzzy zero sum game of two persons,
- x_i – first player's strategy (the set of the alternatives),
- μ_i – dependency function of the first player's strategy,
- y_i – strategy of the second player,
- μ_{ij} – second player's strategy dependency function from the first player's strategy,
- a_{ij} – utility function (determination function) for fuzzy game theory,
- μ_{ij}^* – dependency function for the indefinite game matrix of the utility function.

The transition from the original version can be described in three steps:

1. According to the first player's strategy. Determination of the dependency values of the inner impact factors:

(x_i, μ_i) – Indefinite set of the alternatives with:

$$\mu_i = \frac{1}{L} \sum_{i=1}^L \mu_i, \quad (10)$$

where $i = 1, \dots, m$, and μ_i is dependency function for concerned criterion. Assumed, that arithmetic average (Laplace criterion) is suitable.

Table 1 shows the calculation of the dependency values, where A_i – set of the alternatives, $i = 1, \dots, m$, μ_{il} – dependency value of the x_l criterion.

Table 1. Matrix of the dependency values for the inner impact factors

	x_1	x_2	...	x_l	...	x_k	μ_i
A_1	μ_{11}	μ_{12}	...	μ_{1l}	...	μ_{1k}	$\frac{1}{k} \sum_{l=1}^k \mu_{1l} = \mu_1$
A_2	μ_{21}	μ_{22}	...	μ_{2l}	...	μ_{2k}	$\frac{1}{k} \sum_{l=1}^k \mu_{2l} = \mu_2$
...
A_i	μ_{i1}	μ_{i2}	...	μ_{il}	...	μ_{ik}	$\frac{1}{k} \sum_{l=1}^k \mu_{il} = \mu_i$
...
A_m	μ_{m1}	μ_{m2}	...	μ_{ml}	...	μ_{mk}	$\frac{1}{k} \sum_{l=1}^k \mu_{ml} = \mu_m$

2. According to the second player's strategy. Strategy set of the second player described the same like dependency function. Outer values, possibility and environmental criteria compose the strategy set of the second player. All of them are described by set of the alternatives, recorded like matrix with dependency values (Table 2).

Table 2. Matrix of the dependency values for the outer impact factors

	Y_1	Y_2	...	Y_j	...	Y_n
A_1	μ_{11}	μ_{12}	...	μ_{1j}	...	μ_{1n}
A_2	μ_{21}	μ_{22}	...	μ_{2j}	...	μ_{2n}
...
A_i	μ_{i1}	μ_{i2}	...	μ_{ij}	...	μ_{in}
...
A_m	μ_{m1}	μ_{m2}	...	μ_{mj}	...	μ_{mn}

3. Cut-section through the both sides of the set. Here are summarized the results of the both steps. The result, which satisfies formally both of the strategies can be described as cut-section throw the both sets, and is presented in the general decision making matrix (Table 3).

From the general decision making matrix (Table 3) is shaping the final decision making matrix, which can be named as fuzzy game matrix, where $\mu_{ij}^* = \min(\mu_i, \mu_j)$ is dependency functions of the fuzzy set. Decision is making by the minimax principle, i.e. from the dependency functions of the fuzzy set, which are presented in general decision making matrix, is chosen maximum value. The results are presented in matrix (Table 4). This game solution is determined by minimax principle, which is used in the classic game theory.

Table 3. General decision making matrix

	Y_1	Y_2	...	Y_j	...	Y_n
(x_1, μ_1)	$\min(\mu_1, \mu_{11})$	$\min(\mu_1, \mu_{12})$...	$\min(\mu_1, \mu_{1j})$...	$\min(\mu_1, \mu_{1n})$
(x_2, μ_2)	$\min(\mu_2, \mu_{21})$	$\min(\mu_2, \mu_{22})$...	$\min(\mu_2, \mu_{2j})$...	$\min(\mu_2, \mu_{2n})$
...
(x_i, μ_i)	$\min(\mu_i, \mu_{i1})$	$\min(\mu_i, \mu_{i2})$...	$\min(\mu_i, \mu_{ij})$...	$\min(\mu_i, \mu_{in})$
...
(x_m, μ_m)	$\min(\mu_m, \mu_{m1})$	$\min(\mu_m, \mu_{m2})$...	$\min(\mu_m, \mu_{mj})$...	$\min(\mu_m, \mu_{mn})$

Table 4. Fuzzy game decision making matrix

	Y_1	Y_2	...	Y_j	...	Y_n	Minimax
A_1	μ_{11}^*	μ_{12}^*	...	μ_{1j}^*	...	μ_{1n}^*	$\min(\mu_{1n}^*)$
A_2	μ_{21}^*	μ_{22}^*	...	μ_{2j}^*	...	μ_{2n}^*	$\min(\mu_{2n}^*)$
...
A_i	μ_{i1}^*	μ_{i2}^*	...	μ_{ij}^*	...	μ_{in}^*	$\min(\mu_{in}^*)$
...
A_m	μ_{m1}^*	μ_{m2}^*	...	μ_{mj}^*	...	μ_{mn}^*	$\min(\mu_{mn}^*)$

3.3. Case study

One flat dwelling house and loft type apartment were selected for investigation. All the values are determined by simulation, according to the prices of the market. There are two alternatives with four types of heating system:

- coal based heating system,
- gas based heating system,
- biomass based heating system,
- combined biomass and gas based heating system.

Alternatives are described as follows:

A_1 – one flat dwelling house with coal based heating,

A_2 – one flat dwelling house with gas based heating,

A_3 – one flat dwelling house with biomass based heating,

A_4 – one flat dwelling house with combined biomass and gas based heating,

A_5 – loft flat dwelling house with coal based heating,

A_6 – loft flat dwelling house with gas based heating,

A_7 – loft flat with biomass based heating,

A_8 – loft flat dwelling house with combined biomass and gas based heating.

Ten criteria, of each alternative, which describes apartment's life cycle, were selected for decision making. They are:

x_1 – material, used for construction process (t/m^2),

x_2 – energy, used for construction process (GJ/m^2),

x_3 – water, used for construction process (m^3/m^2),

x_4 – energy use for 50 year operation phase (kWh/m^2),

x_5 – enclosures with heat losses (m^2),

x_6 – CO_2 use for 50 year operation phase (kg/m^2),

x_7 – price of the apartment ($€/m^2$),

x_8 – labor costs (human hour/ m^2),

x_9 – Fuel annual price ($€/100m^2$),

x_{10} – Price of energy use for 50 year operation phase (Lt/m^2).

Initial decision making matrix with 8 alternatives and 10 criteria is presented in Table 5.

Table 5. Initial decision making matrix

	Criteria									
	Material used for construction process (t/m^2)	Energy use (GJ/m^2)	Water, used for construction process (m^3/m^2)	Energy use for 50 year operation phase (kWh/m^2)	Enclosures with heat losses (m^2)	CO_2 use for 50 year operation phase (kg/m^2)	Price of the apartment (EUR/m^2)	Labour costs (human hour/ m^2)	Fuel annual price ($EUR/100 m^2$)	Price of energy use for 50 year operation phase (Lt/m^2)
	x_1	x_2	x_3	x_4	x_5	x_6	x_7	x_8	x_9	x_{10}
Optimization direction										
	min	min	min	min	min	min	min	min	min	min
A_1	1.6	31.5	51.4	7969.0	308.0	2966.0	869.6	1005.0	800.6	3586.1
A_2	2.1	41.3	67.4	7054.0	308.0	1522.0	886.9	1012.0	317.1	3174.3
A_3	1.8	35.4	57.8	8843.0	308.0	314.0	897.4	1010.0	211.4	3979.4
A_4	2.3	45.3	73.8	7317.0	308.0	257.0	932.2	1004.0	268.2	3292.7
A_5	1.5	27.1	41.7	5903.0	362.5	2194.0	724.6	1220.0	800.6	2656.4
A_6	1.9	35.5	54.5	5149.0	362.5	1112.0	739.1	1229.0	317.1	2452.1
A_7	1.7	30.5	46.9	6408.0	362.5	228.0	747.8	1209.0	211.4	2883.6
A_8	2.2	39.1	60.0	5586.0	362.5	196.0	776.8	1202.0	268.2	2513.7

Table 6 shows inner impact factors of the decision making matrix. These criteria are selected as the factors, which impact only the inner factors of the construction process ($x_1 - x_5$ criteria).

Table 7 shows outer impact factors, which impact on the construction process or the construction process impact on the environment ($x_6 - x_{10}$ criteria).

Value of each criterion is described by three values: a_0 – is lowest value of the j criteria, a_m – the highest value of the j criteria, a_d – the average between a_0 and a_m values.

Table 6. Inner impact factors

Description of the alternative		x_1	x_2	x_3	x_4	x_5
		Optimization direction				
		min	min	min	min	min
A_1	One flat dwelling house with coal based heating	1.6	31.5	51.4	7969.0	308.0
A_2	One flat dwelling house with gas based heating	2.1	41.3	67.4	7054.0	308.0
A_3	One flat dwelling house with biomass based heating	1.8	35.4	57.8	8843.0	308.0
A_4	One flat dwelling house with combined biomass and gas based heating	2.3	45.3	73.8	7317.0	308.0
A_5	Loft flat dwelling house with coal based heating	1.5	27.1	41.7	5903.0	362.5
A_6	Loft flat dwelling house with gas based heating	1.9	35.5	54.5	5149.0	362.5
A_7	Loft flat dwelling house with biomass based heating	1.7	30.5	46.9	6408.0	362.5
A_8	Loft flat dwelling house with combined biomass and gas based heating	2.2	39.1	60.0	5586.0	362.5
a_0		1.5	27.1	41.7	5149.0	308.0
a_d		1.9	36.2	57.7	6996.0	335.3
a_m		2.3	45.3	73.8	8843.0	362.5

Table 7. Outer impact factors

Description of the alternative		x_6	x_7	x_8	x_9	x_{10}
		Optimization direction				
		min	min	min	min	min
A_1	One flat dwelling house with coal based heating	2966.0	869.6	1005.0	800.6	3586.1
A_2	One flat dwelling house with gas based heating	1522.0	886.9	1012.0	317.1	3174.3
A_3	One flat dwelling house with biomass based heating	314.0	897.4	1010.0	211.4	3979.4
A_4	One flat dwelling house with combined biomass and gas based heating	257.0	932.2	1004.0	268.2	3292.7
A_5	Loft flat dwelling house with coal based heating	2194.0	724.6	1220.0	800.6	2656.4
A_6	Loft flat dwelling house with gas based heating	1112.0	739.1	1229.0	317.1	2452.1
A_7	Loft flat dwelling house with biomass based heating	228.0	747.8	1209.0	211.4	2883.6
A_8	Loft flat dwelling house with combined biomass and gas based heating	196.0	776.8	1202.0	268.2	2513.7
a_0		196.0	724.6	1004.0	211.4	2452.1
a_d		1581.0	828.4	1116.5	505.9	3215.7
a_m		2966.0	932.2	1229.0	800.6	3979.4

4. Results and discussion

Coefficients A, \dots, H are calculated and presented for inner impact factors in Table 8 and for outer impact factors in Table 9. They are calculated according on the Equation (5–7).

Dependency values of the inner impact factors are presented in the Table 10, according on the methodology, which is presented in Table 1.

Dependency values for the outer impact factors are presented in Table 11, according on the methodology, which is presented in Table 2.

In Table 12 is shown final fuzzy decision making matrix, according on the methodology, which is presented in Table 3 and Table 4.

Table 8. Inner impact factor's A, B, C, D, E, F, G, H values

	x_1	x_2	x_3	x_4	x_5
A	-4.216599152	-0.00033553	-6.0011E-05	-3.99192E-11	-1.23568E-05
B	24.15947678	0.036436025	0.010395047	8.36929E-07	0.012427797
C	-44.21871738	-1.236167373	-0.553586156	-0.005443661	-4.138862525
D	26.20228189	13.41905768	9.360210363	11.28999679	456.8629208
E	-4.216599152	-0.00033553	-6.0011E-05	-3.99192E-11	-1.23568E-05
F	24.1627495	0.036437112	0.010393951	8.38718E-07	0.012428006
G	-44.23121916	-1.236246014	-0.553459588	-0.005468691	-4.139002405
H	26.21422109	13.42048101	9.356556553	11.3775504	456.8863681

Table 9. Outer impact factor's A, B, C, D, E, F, G, H values

	x_6	x_7	x_8	x_9	x_{10}
A	-9.40734E-11	-2.23701E-07	-1.75645E-07	-9.77283E-09	-5.61145E-10
B	4.46264E-07	0.000555957	0.000588309	1.48371E-05	5.41378E-06
C	-0.000164094	-0.453339934	-0.650165576	-0.00496235	-0.016427981
D	0.015727037	121.69385	237.5025178	0.478301473	16.00461744
E	-9.40734E-11	-2.23701E-07	-1.75645E-07	-9.77283E-09	-5.61145E-10
F	4.46116E-07	0.000555932	0.000588337	1.48318E-05	5.41306E-06
G	-0.000163624	-0.453297484	-0.650227906	-0.004956997	-0.01642336
H	0.015355336	121.676267	237.5373136	0.476947174	15.99718644

Table 10. Dependency values of the inner impact factors

x_1	x_2	x_3	x_4	x_5	μ_i
0.029	0.145	0.218	0.857	0.000	0.250
0.836	0.879	0.897	0.523	0.000	0.627
0.294	0.436	0.502	1.000	0.000	0.445
1.000	1.000	1.000	0.629	0.000	0.726
0.000	0.000	0.000	0.108	1.000	0.222
0.652	0.444	0.352	0.000	1.000	0.490
0.149	0.092	0.070	0.270	1.000	0.316
0.946	0.731	0.605	0.039	1.000	0.664

As the calculation goes through a very long determination faze and is transformed with big algorithms, so the results are not so exact. And this case study shows only

one suitable alternative – the best alternative is A_2 (One flat dwelling house with gas based heating system). This can be impacted of the closest values of the criteria to the average results of a_d value. As the fuzzy set theory calculation is according on the triangle diagram framework, with three point, which in this case study are described as (a_0, a_d, a_m) , in which the dependency values are $\mu_{(a0)} = 0$, $\mu_{(ad)} = 0.5$, $\mu_{(am)} = 1$.

Table 11. Dependency values of the outer impact factors

Y_1	Y_2	Y_3	Y_4	Y_5
1.000	0.782	0.000	1.000	0.835
0.468	0.878	0.004	0.085	0.459
0.005	0.925	0.002	0.000	1.000
0.001	1.000	0.000	0.026	0.575
0.810	0.000	0.995	1.000	0.049
0.256	0.014	1.000	0.085	0.000
0.000	0.035	0.977	0.000	0.194
0.000	0.158	0.960	0.026	0.005

Table 12. Fuzzy game decision making matrix

Alternatives		μ_i	Y_1	Y_2	Y_3	Y_4	Y_5	Minimax
A_1	One flat dwelling house with coal based heating	0.250	0.250	0.250	0.000	0.250	0.250	0.000
A_2	One flat dwelling house with gas based heating	0.627	0.468	0.627	0.004	0.085	0.459	0.004
A_3	One flat dwelling house with biomass based heating	0.445	0.005	0.445	0.002	0.000	0.445	0.000
A_4	One flat dwelling house with combined biomass and gas based heating	0.726	0.001	0.726	0.000	0.026	0.575	0.000
A_5	Loft flat dwelling house with coal based heating	0.222	0.222	0.000	0.222	0.222	0.049	0.000
A_6	Loft flat dwelling house with gas based heating	0.490	0.256	0.014	0.490	0.085	0.000	0.000
A_7	Loft flat dwelling house with biomass based heating	0.316	0.000	0.035	0.316	0.000	0.194	0.000
A_8	Loft flat dwelling house with combined biomass and gas based heating	0.664	0.000	0.158	0.664	0.026	0.005	0.000
The best alternative is A_2 – one flat dwelling house with gas based heating system								0.004

5. Conclusions

Choosing apartment for living is multiple criteria problem. This case study shows the possibility to use the fuzzy set theory, combining with fuzzy games in decision making in choosing apartment for living.

Also, paper uses combined technique's methodology to combine fuzzy sets and decision making. According to the fuzzy set theory general matrix is divided into two general decision making matrix of inner impact factors and outer impact factors.

Second part of the calculation is by the help of fuzzy games compose the general decision making matrix and the fuzzy game decision making matrix. Results are ranked according on the minimax principle.

Determination process goes threw a long calculation and values are transformed with a big algorithms, so the results are not so exact. But it doesn't impact on the choosing right solution.

The fuzzy set theory is appropriate to use in different areas, because of its possibility to be adapt in a lot of ways of decision making. But it is still not popular in decision making in civil engineering.

References

- [1] Ananda J., Herath G.: *A critical review of multi-criteria decision making methods with special reference to forest management and planning*, Ecological Economics, Vol. 68, No. 10, 2009, pp. 2535–2548.
- [2] Bamberg G., Coenenberg A.G.: *Betriebswirtschaftliche Entscheidungslehre*, 7. Aufl., München, 1992.
- [3] Behzadian M., Kazemzadeh R.B., Albadvi A., Aghdasi M.: *PROMETHEE: A comprehensive literature review on methodologies and applications*, European Journal of Operational Research, Vol. 200, No. 1, 2010, pp. 198–215.
- [4] Bompard E., Carpaneto E., Ciwei G., Napoli R., Benini M., Gallanti M., Migliavacca G.: *A game theory simulator for assessing the performances of competitive electricity markets*, Electric Power Systems Research, Vol. 78, No. 2, 2008, pp. 217–227.
- [5] Boroushaki S., Malczewski J.: *Using the fuzzy majority approach for GIS-based multi-criteria group decision-making*, Computers & Geosciences, Vol. 36, No. 3, 2010, pp. 302–312.
- [6] Charilas D.E., Panagopoulos A.D.: *A survey on game theory applications in wireless networks*, Computer Networks, Vol. 54, No. 18, 2010, pp. 3421–3430.
- [7] Deng Y., Chan F.T.S., Wu Y., Wang D.: *A new linguistic MCDM method based on multiple-criterion data fusion*, Expert Systems with Applications, Vol. 38, No. 6, 2011, pp. 6985–6993.
- [8] Doumpos M., Marinakis Y., Marinaki M., Zopounidis C.: *An evolutionary approach to construction of outranking models for multicriteria classification: The case of the ELECTRE TRI method*, European Journal of Operational Research, Vol. 199, No. 2, 2009, pp. 496–505.
- [9] Fiestras-Janeiro M.G., García-Jurado I., Meca A., Mosquera M.A.: *Cooperative game theory and inventory management*, European Journal of Operational Research, Vol. 210, No. 3, 2011, pp. 459–466.
- [10] Hennet J.-C., Arda Y.: *Supply chain coordination: A game-theory approach*, Engineering Applications of Artificial Intelligence, Vol. 21, No. 3, 2008, pp. 399–405.
- [11] Ho W., Xu X., Dey P.K.: *Multi-criteria decision making approaches for supplier evaluation and selection: A literature review*, European Journal of Operational Research, Vol. 202, No. 1, 2010, pp. 16–24.
- [12] Hui E.C.M., Lau O.M.F., Lo K.K.: *A fuzzy decision-making approach for portfolio management with direct real estate investment*, International Journal of Strategic Property Management, Vol. 13, No. 2, 2009, pp. 191–204.

- [13] Jacquet-Lagrèze E., Siskos Y.: *Preference disaggregation: 20 years of MCDA experience*, European Journal of Operational Research, Vol. 130, No. 2, 2001, pp. 233–245.
- [14] Kahraman C., Engin O., Kabak Ö., Kaya İ.: *Information systems outsourcing decisions using a group decision-making approach*, Engineering Applications of Artificial Intelligence, Vol. 22, No. 6, 2009, pp. 832–841.
- [15] Kahraman C., Kaya İ.: *Investment analyses using fuzzy probability concept*, Technological and Economic Development of Economy, Vol. 16, No. 1, 2010, pp. 43–57.
- [16] Kahraman C., Kaya I., Cebi S.: *A comparative analysis for multi-attribute selection among renewable energy alternatives using fuzzy axiomatic design and fuzzy analytic hierarchy process*, Energy, Vol. 34, No. 10, 2009, pp. 1603–1616.
- [17] Kahraman C., Kaya İ.: *A fuzzy multicriteria methodology for selection among energy alternatives*, Expert Systems with Applications, Vol. 37, No. 9, 2010, pp. 6270–6281.
- [18] Kalibatas D., Zavadskas E.K., Kalibatiene D.: *The concept of the ideal indoor environment in multi-attribute assessment of dwelling-houses*, Archives of Civil and Mechanical Engineering, Vol. 11, No. 1, 2011, pp. 89–101.
- [19] Kapliński O., Tamošaitienė J.: *Game theory applications in construction engineering and management*, Technological and Economic Development of Economy, Vol. 16, No. 2, 2010, pp. 348–363.
- [20] Kaya T., Kahraman C.: *Fuzzy multiple criteria forestry decision making based on an integrated VIKOR and AHP approach*, Expert Systems with Applications, Vol. 38, No. 6, 2011, pp. 7326–7333.
- [21] Leberling H.: *On finding compromise solutions in multi-criteria problems using fuzzymin-operator*, Fuzzy sets and systems, No. 6, 1981, pp. 105–118.
- [22] Limaei S.M.: *Mixed strategy game theory, application in forest industry*, Forest Policy and Economics, Vol. 12, No. 7, 2010, pp. 527–531.
- [23] Liu S., Proctor W., Cook D.: *Using an integrated fuzzy set and deliberative multi-criteria evaluation approach to facilitate decision-making in invasive species management*, Ecological Economics, Vol. 69, No. 12, 2010, pp. 2374–2382.
- [24] Liu W.-Y., Yue K., Wu T.-Y., Wei M.-J.: *An approach for multi-objective categorization based on the game theory and markov process*, Applied Soft Computing, Vol. 11, No. 6, 2011, pp. 4087–4096.
- [25] Long R., Yu L.: *Study on regulation design about energy-saving and emission-reduction based on game theory*, Procedia Earth and Planetary Science, Vol. 1, No. 1, 2009, pp. 1641–1646.
- [26] Lu W.-M., Wang T.-C.: *Fuzzy multi-criteria model for the industrial cooperation program transaction strategies: A case in Taiwan*, Expert Systems with Applications, Vol. 38, No. 3, 2011, pp. 1490–1500.
- [27] Madani K.: *Game theory and water resources*, Journal of Hydrology, Vol. 381, No. 3–4, 2010, pp. 225–238.
- [28] Noor-E-Alam M., Lipi T.F., Hasin M.A.A., Ullah A.M.M.S.: *Algorithms for fuzzy multi expert multi criteria decision making (ME-MCDM)*, Knowledge-Based Systems, Vol. 24, No. 3, 2011, pp. 367–377.
- [29] Omran J., Peldschus F.: *Entscheidungen mit unscharfen Spielen*, Wissenschaftliche Berichte der Technischen Hochschule Leipzig, No. 6, 1990, pp. 28–38.

- [30] Peldschus F., Zavadskas E.K., Turskis Z., Tomasaitiene J.: *Substainable assessment of construction site by applying game theory*, Inzinerine Ekonomika-Engineering Economics, Vol. 21, No. 3, 2010, pp. 223–237.
- [31] Peldschus F., Zavadskas E.K.: *Fuzzy matrix games multi-criteria model for decision-making in engineering*, Informatica, Vol. 16, No. 1, 2005, pp. 107–120.
- [32] Peldschus F.: *Experience of the game theory application in construction management*, Technological and Economic Development of Economy, Vol. 14, No. 4, 2008, pp. 531–545.
- [33] Peldschus F.: *Game-theory solutions in construction operation*, in: Skibniewski M.J., Vainiuinas P., Zavadskas E.K. (Eds), *Modern building materials, structures and techniques*, The 9th International Conference in May 16–18, 2007, Vilnius, Lithuania, Selected papers, 2007, pp. 348–353.
- [34] Peldschus F.: *The analysis of the quality of the results obtained with methods of multi-criteria decisions*, Technological and Economic Development of Economy, Vol. 15, No. 4, 2009, pp. 580–592.
- [35] Plebankiewicz E.: *Contractor prequalification model using fuzzy sets*, Journal of Civil Engineering and Management, Vol. 15, No. 4, 2009, pp. 377–385.
- [36] Runyan P., Heping W., Zhengping W., Yu L.: *Decision-making of aircraft optimum configuration utilizing multi-dimensional game theory*, Chinese Journal of Aeronautics, Vol. 23, No. 2, 2010, pp. 194–197.
- [37] Schneeweiss C.: *Entscheidungskriterien bei Risiko*, Berlin: Springer Verlag, 1967.
- [38] Schwab K.D.: *Ein auf dem Konzept der unscharfen Mengen basierendes Entscheidungs Modell bei mehrfacher Zielsetzung*, Peter Lang, Frankfurt am Main, Diss. TH Aachen, 1983.
- [39] Sharma R., Gopal M.: *Synergizing reinforcement learning and game theory. – A new direction for control*, Applied Soft Computing, Vol. 10, No. 3, 2010, pp. 675–688.
- [40] Singh R.K., Benyoucef L.: *A fuzzy TOPSIS based approach for e-sourcing*, Engineering Applications of Artificial Intelligence, Vol. 24, No. 3, 2011, pp. 437–448.
- [41] Torfi F., Farahani R.Z., Rezapour S.: *Fuzzy AHP to determine the relative weights of evaluation criteria and Fuzzy TOPSIS to rank the alternatives*, Applied Soft Computing, Vol. 10, No. 2, 2010, pp. 520–528.
- [42] Turskis Z., Zavadskas E.K., Peldschus F.: *Multicriteria optimization system for decision making in construction design and management*, Inzinerine Ekonomika-Engineering Economics, No. 1, 2009, pp. 7–17.
- [43] Uçal İ., Kahraman C.: *Fuzzy real options valuation for oil investments*, Technological and Economic Development of Economy, Vol. 15, No. 4, 2009, pp. 646–669.
- [44] Vahidnia M.H., Alesheikh A.A., Alimohammadi A.: *Hospital site selection using fuzzy AHP and its derivatives*, Journal of Environmental Management, Vol. 90, No. 10, 2009, pp. 3048–3056.
- [45] Xi B.D., Su J., Huang G.H., Qin X.S., Jiang Y.H., Huo S.L., Ji D.F., Yao B.: *An integrated optimization approach and multi-criteria decision analysis for supporting the waste-management system of the city of Beijing, China*, Engineering Applications of Artificial Intelligence, Vol. 23, No. 4, 2010, pp. 620–631.
- [46] Yaqiong L., Man L.K., Zhang W.: *Fuzzy theory applied in quality management of distributed manufacturing system: A literature review and classification*, Engineering Applications of Artificial Intelligence, Vol. 24, No. 2, 2011, pp. 266–277.
- [47] Zadeh L.A.: *Fuzzy Algorithmus*, Information and Control, No. 12, 1968, pp. 94–102.

- [48] Zadeh L.A.: *Fuzzy sets*, Information and Control, No. 8, 1965, pp. 338–353.
- [49] Zavadskas E.K., Turskis Z.: *A new logarithmic normalization method in games theory*, Informatica, Vol. 19, No. 2, 2008, pp. 303–314.
- [50] Zavadskas E.K., Ustinovichius L., Peldschus F.: *Development of software for multiple criteria evaluation*, Informatica, Vol. 14, No. 12, 2003, pp. 259–272.
- [51] Zavadskas E.K., Peldschus F., Turskis Z., Tamosaitiene J.: *The values of the equilibrium point for the sustainable decision making in construction*, [in:] Grasserbauer M., Sakalauskas L., Zavadskas E.K. (Eds), *Knowledge-based technologies and OR methodologies for decisions of Sustainable Development (KORSD-2009)*, The 5th International Vilnius Conference and EURO Mini Conference, September 30–October 3, 2009, Vilnius, Lithuania, Selected papers, Vilnius: Technika, pp. 154–158.
- [52] Zavadskas E.K., Peldschus F., Turskis Z.: *Multi-criteria optimization software LEVI-4.0 – A tool to support design and management in construction*, in: Zavadskas E.K., Kaklauskas A., Skibniewski M.J. (Eds): 25th International Symposium on Automation and Robotics in Construction (ISARC – 2008), June 26–29, 2008, Vilnius, Lithuania, 2009, pp. 731–736.
- [53] Zavadskas E.K., Turskis Z., Vilutiene T.: *Multiple criteria analysis of foundation installment alternatives by applying Additive Ratio Assessment (ARAS) method*, Archives of Civil and Mechanical Engineering, Vol. 10, No. 3, 2010, pp. 123–141.
- [54] Zhang X., Liu P.: *Method for aggregating triangular fuzzy intuitionistic fuzzy information and its application to decision making*, Technological and Economic Development of Economy, Vol. 16, No. 2, 2010, pp. 280–290.
- [55] Zhang X., Tan Y., Shen L., Wu Y.: *An alternative approach of competitiveness evaluation for real estate developers*, International Journal of Strategic Property Management, Vol. 15, No. 1, 2011, pp. 10–25.

Wybór mieszkania przez zastosowanie teorii gier

W artykule przedstawiono model służący do oceny mieszkania. Do badań przyjęto dwa typy budynków: tradycyjny budynek mieszkalny z kawalerkami oraz budynek mieszkalny z „loftami”. Pod uwagę wzięto cztery alternatywne systemy ogrzewania budynków: węglem, gazem, biomasą oraz system mieszanym, tj. biomasą i gazem. Alternatywne systemy są opisane przez zbiór kryteriów. Wartości kryteriów zostały wyznaczone metodą symulacji oraz przy zastosowaniu metod statystycznych. Do wspomagania procesu decyzyjnego zastosowano rozmytą teorię gier. Wynik rozwiązania postawionego w artykule problemu wskazuje, że rozmyta macierz teorii gier jest odpowiednia do takich celów.



Analysis of modern trends of logistics technology development

T. NOWAKOWSKI

Wrocław University of Technology, Faculty of Mechanical Engineering, 5 Łukasiewicza Street,
50-370 Wrocław, Poland.

In the paper the projects proposed to the European Award for Logistics Excellence in 2011 are analysed. The Award is presented to a company or individual who has made an outstanding contribution to the logistics profession. Thus, it is possible to formulate the up to date trends of logistics technologies implemented by companies. Also the general assumptions of the winner project are presented. The project called "Redesign Dual Use Tractor Trailer" involved the design and test of a transportation concept which combines liquid and pallet freight in order to improve the cost-effectiveness and efficiency of transports and can reduce CO₂ emissions and highway congestion.

Keywords: *logistics, technology, development, analysis*

1. Introduction

The definitions of logistics (many of them are proposed during last twenty years) have evolved with the internationalization of companies' operations and consequently globalization. Generally speaking logistics is defined as an optimization process of the location, movement and storage of resources from the point of origin, through various economic activities, to the final consumer. According to the Council of Logistics Management definition [5]: logistics is the management of the flow of goods, information and other resources, including energy and people, between the point of origin and the point of consumption in order to meet the requirements of consumers (frequently, and originally, military organizations). Certainly each organization focuses on a different aspect of logistics, depending on its area of interest. Note that irrespective of source of the definition, it is underlined that logistics involves the integration of flow of materials (i.e. transportation, warehousing, packaging) with flow of related information and capital and acts of planning, organizing and managing activities [6]. Sometimes it is graphically presented as a "logistic house" with three legs: goods flow technology leg, information flow leg and organization/economics one.

Thus, analysing trends of logistics development one should answer the questions:

- are all logistic "legs" developing in the same pace,
- if not, which "leg" is leader of development,
- how it can effect on logistic technologies development at global or European market.

One of the possibilities of searching for such answers gives analysis of projects proposed to the European Award for Logistics Excellence.

2. Analysis of logistics projects

2.1. Sources of information

The European Award for Logistics Excellence is made annually by ELA, the European Logistics Association [10]. ELA is a federation of 30 national organisations, covering almost every country in Central and Western Europe. The goal of ELA is to provide a forum for co-operation for any individual or society concerned with logistics within Europe and to assist industry and commerce in Europe.

The European Award for Logistics Excellence is presented to a company or individual who has made an outstanding contribution to the logistics profession. Entries describe a logistics project that has been implemented by a company. The criteria used to select the winner of the Award are designed to encourage entries from companies of all sizes, as well as from individuals.

The Award is chosen from the proposed projects by national logistics association by the jury composed of representatives of the following sectors: industry, retailing, consulting, service providers, academics and last 3 winners. The evaluation criteria are based on the formal aspects of the project (layout, style, readability), the substantial aspects (problem, solution, result) and the excellence of the solution (grade of difficulty, actuality, originality, use for Logistics Market) [6, 10].

Presentation of the projects must include information on the member Association proposing the project, information on the candidate and information on the project. The presentation is generally focused on economical, technological and environmental aspects of obtained results. List of the candidates put up for the 2011 Award is shown in Table 1.

Table 1. Candidates for the European Award for Logistics Excellence in 2011

	Information on the member Association		Information on the candidate			
	Name	Country	Name organisation	City	Website	Business Activity (sector)
1	2	3	4	5	6	7
1.	APLOG – Associação Portuguesa de Logística	Portugal	Luís Simões Logística Integrada, S.A.	Loures	www.luis-simoes.com	Logistics
2.	ARILOG Romania	Romania	Groep H. Essers – Romania	Oradea	www.essers.ro	Logistics Services, Transport, Distribution
3.	ARILOG	Romania	OTZ LOGISTICS GROUP	Posta Calnau	www.otz.ro	Integrated Logistics Solutions

1	2	3	4	5	6	7
4.	German Logistics Association (BVL)	Germany	1) Geis Industrie-Service GmbH	Nürnberg	www.geis-group.com	Logistics Services
			2) AVAYA GmbH & Co. KG	Frankfurt/Main	www.avaya.com	Telecommunication
5.	German Logistics Association (BVL)	Germany	NORD STREAM AG	Zug	www.nord-stream.com	Energy; Natural gas supply
6.	CEL (Centro Español de Logistica)	Spain	BECTON DICKINSON, S.A	Fraga (Huesca)	www.bd.com	Manufacturing Medical Devices
7.	CEL (Centro Español de Logistica)	Spain	Desigual	Barcelona	www.desigual.com	Textil
8.	CEL (Centro Español de Logistica)	Spain	Grupo Cortefiel	Madrid	www.grupocortefiel.com	Fashion Apparel retailer
9.	The Chartered Inst. of Log. and Transport in UK	United Kingdom	Damco	Felixstowe, Suffolk	www.damco.com	Third Party Logistics
10.	Czech Logistic Association	Czech Republic	ICZ a.s. / SSI Schäfer s.r.o	Praha 4/ Hranice	www.i.cz/ www.ssi-schaefer.cz	ICT/Logistic technologies and systems
11.	GS 1 Switzerland	Switzerland	Badertscher Badi Transport AG	Kleinandelfingen	www.badi-transport.ch	Transport (collecting milk and supplying dairies/milk products)
12.	GS 1 Switzerland	Switzerland	Innoffreight Swiss GmbH	Herzogenbuchsee	www.innoffreight.com	Transport + logistics of bulk goods
13.	GS 1 Switzerland	Switzerland	CSB-SYSTEM AG	Kestenholz	www.csb-system.com	Industry-specific Business Solutions
14.	GS 1 Switzerland	Switzerland	SBB Cargo AG	Basel	http://www.sbbcargo.com/index	Rail transportation
15.	Hungarian Association of Logistics	Hungary	Robert Bosch Power Tool Elektromos Szerszámgártó Kft.	Miskolc	www.bosch.com	Producing power tools
16.	Polish Logistics Association	Poland	Auchan Poland, Makro Cash and Carry Polska	Piaseczno, Warszawa,	www.auchan.pl, www.makro.pl	FMCG Distribution
17.	Polish Logistics Association	Poland	STANMET Sp. z o. o.	Wlynkówo	www.stanmet.pl	Consulting, Design services, Manufacturing

1	2	3	4	5	6	7
18.	VIB – Vereniging voor Inkoop en Bedrijfslogistiek	Belgium	Barco n.v.	Kortrijk	www.barco.com	Electronic equipment
19.	VIB – Vereniging voor Inkoop en Bedrijfslogistiek	Belgium	2XL nv.	Zeebrugge	www.2xl.eu	Transport & Logistics

2.2. Structure of the companies

Mean number of proposed projects is about 12 per year. In 2009 it was 9, in 2010 – 6 projects [6]. In 2011 – 19 projects; the structure of countries is shown in Figure 1 and the structure of business activity sectors – in Figure 2.

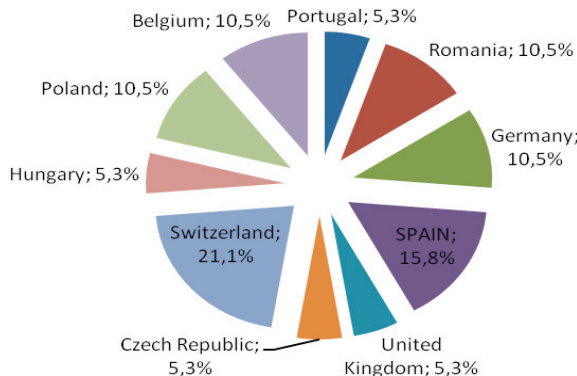


Fig. 1. Countries – candidates for the Award in 2011

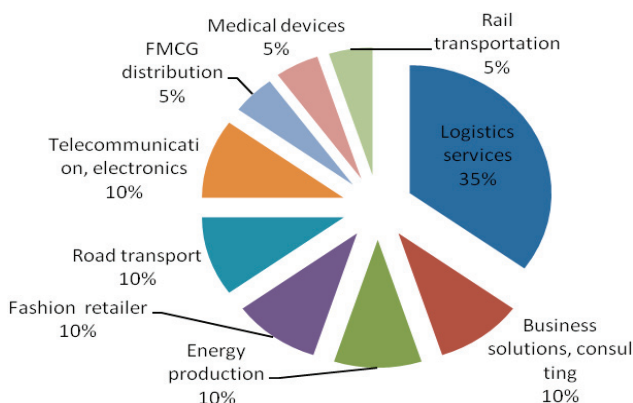


Fig. 2. Business activity sectors of the candidates

To the most active country association belong Switzerland, Spain, Germany and Belgium. This year we have some projects from Hungary, Poland and Romania. A year ago we obtained a proposal also from Ukraine.

Analysing the structure of business activities we can observe as usual the domination of logistics service concepts [7–8]. But in 2009 and 2010 the biggest amount of projects concerned medical devices and health service. And FMCG distribution and automotive industry are also well presented. This year there are no post service and household goods manufacturing representatives.

2.3. Projects objectives

The project objectives belong to all mentioned groups of tasks. They were formulated by candidates as follows:

- multi – costumer automatic warehouse implementation,
- cost reduction (fuel, inventory), paperless, transparency, stock accuracy,
- case study of OTZ's new partnership with British American Tobacco Romania Investment,
- integration European network, complexity reduction by web-based IT-integration,
- integration of a WEB-based tool in service logistics with centralized inventory, complexity reduction, simplification and automation of processes,
- cross-national, environmental friendly and sustainable logistics,
- VSM integration; materials, process information and distribution in order to eliminate variability in our processes,
- automation of current manual processes, and increase the distribution productivity needs as the company's growth does with the new automatic system,
- convert the Supply Chain in a competitive advantage for Grupo Cortefiel,
- create innovative solution in order to help our customers make their inventory management more efficient,
- enlarge the capacity of warehouse in limited space; optimize internal logistic processes by means of up-to date identification and information,
- new transportation concept which greatly improves the cost effectiveness,
- establish new technologies for combined transports on the European transport market with the main focus to strengthen the railway business,
- integral logistics of perishables and automation in a skilled butcher's business,
- to increase attractivity of the European wagonload network with regards to road competition by:
 - implementing the new Xrail production standard among freight railways,
 - implementing a common IT system for enhanced quality, better transparency (Track&Trace) and a faster offer process,

- improving co-operation and supplier performance by consultative assistance and supporting,
- to eliminate the problems related to using EUR pallets in Poland,
- improve the safety conditions in the use of racking equipment in supply chains and implement of the expert inspections of the racking equipment in accordance with EN 15635 and support for the reengineering process in supply chains,
- improving new product industrialization, manufacturing scalability and operational excellence in a technology driven company by focusing on quality management and manufacturing excellence,
- implement ideas of green logistics.

Thus, analyzing the objectives according to kind of technology field, the rate of projects focused on mechanical technology development is about 60%. While, organizational improvements concern about 20% the implemented solutions and information or informatics projects only about 10%. Taking into consideration the winning projects of 2009, 2010 and 2011 Awards this trend is to be confirmed.

Such a structure of the developed technologies is unexpected and in contradiction to the fields of activity discussed in the published in scientific papers and in the observed research tasks carried on polish and foreign logistic institutes [1, 2, 4]. Also the structure of forecasted fields of interest in the industrial enterprises in Germany, Chine and USA [8] is different rate of answers important and very important):

- process approach – 74 %,
- informatics system – 66%,
- logistic technologies – 57%,
- organization structure improvement – 35%.

Certainly such a sharp division of the technologies is for the logistics processes difficult or even impossible because fundamental feature of the logistics is integration of the flows.

3. “Dual Use Tractor Trailer” project

In 2011 project it is possible to notice superiority of mechanical technologies development with comparison to management and informatics solutions. That tendency was expressed also by the results of voting the winner of 2011 Award. The winner is project “Dual Use Tractor Trailer” of Badertscher Badi Transport AG – a typical mechanical design of the trailer, which allows to combine liquid (milk) and pallet transportation.

The starting point of the project is based on consideration that the requirements for transporting milk from the producers (farmers) to the processors (dairies) have been subject to many changes in recent years. Liquid transports (tankers) and pallet transports (tractor trailers) seldom find suitable freight for the return trip to avoid empty runs. In the case of tankers there are empty runs 100 percent of the time; in the case of

pallet transports the percentage of empty runs is as high as 90 percent. Thus, there are large amounts of cargo (like fresh milk) to and (milk products) from the dairies, which could be optimally combined.

The solution is the system that combines liquid and pallet transportation and completely meets the requirements of milk transport (hygiene, cooling, loading and unloading, cleaning, etc.) and of pallet transport (cooling, simple loading with existing equipment and loading ramps, pallet height, etc.). By using a cubic-shaped tank as opposed to a classic cylindrical tank there is more transport volume – see Figure 3. The parameters of the solution are: total permissible weight – 40 tons, total loading capacity – 22 tons, milk tank volume – 24 000 dcm², interior height if tank is hoisted – 1800 mm ([9]).

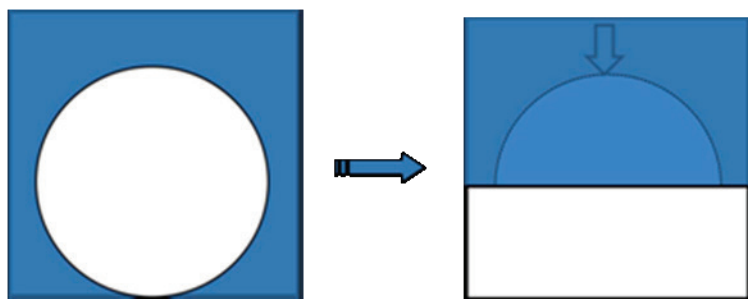


Fig. 3. Schema of “Dual Use Tractor Trailer” conception [9]

4. Conclusions

According to the recent research works [3, 7–8] reliability and safety requirements will lead to modifications of logistics systems. Logistics reliability is understood as the measure of the ability of an item to operate without placing a demand on the logistics support structure for repair or adjustment. Logistics reliability recognizes the effects of occurrences that place a demand on the logistics support structure without regard to the effect on mission or function.

Every link of the logistics system/supply chain has to provide oneself with the raw materials, supplies, and components in order to carry out its basic functions (e.g. production). Every step may generate logistic failures understood as discrepancies between values of planned and real supply process in any 7R formula criterions such as [5]: material quality, price, punctuality of delivery, completeness of delivery, service level, payment conditions, documentation correctness, package quality, and way of controversy solutions.

Thus, it is still a significant trend for innovation ability of logistics system development in every field of technical and organizational activity.

References

- [1] *China 2015: Transportation and logistics strategies*, A.T. Kearney, Inc. 2010, www.atkearney.com, (20.06.11).
- [2] Legutko S.: *Development trends in machine operation maintenance*, Maintenance and Reliability, No. 2, 2009, pp. 8–16.
- [3] Magott J., Nowakowski T., Skrobanek P., Werbińska-Wojciechowska S.: *Analysis of logistic support system using fault trees with time dependencies*, Archives of Transport, Vol. 19, Iss. 4, 2007, pp. 57–75.
- [4] Michłowicz E.: *Nowe wyzwania dla logistyki produkcji*, Gospodarka Materiałowa & Logistyka, grudzień, 2010, pp. 58–61.
- [5] Nowakowski T.: *Analysis of possibilities of logistics system reliability assessment*, Safety and reliability for managing risk, Eds. C.G. Soares, E. Zio, Leiden: Taylor and Francis, Vol. 3, 2006, pp. 2343–2349.
- [6] Nowakowski T.: *Analysis of the selected logistics project realized in 2009/2010 years (in Polish)*, Logistyka, Vol. 2, 2011, pp. 477–484.
- [7] Pfohl H.-C.: *New development of the supply chain & logistics concept*, Carbon footprint, Atlanta Logistics Forum, 2010, www.forumalf.com, (20.06.11).
- [8] Straube F., Cetinkaya B.T.: *Trends und Strategien im Logistikmanagement 2008*, Kongressband, 25. Deutscher Logistik-Kongress, Berlin, 2008, pp. 38–39.
- [9] www.badi-transport.ch
- [10] www.elalog.org

Analiza aktualnych trendów rozwoju technologii logistycznych

Omówiono projekty zgłoszone do Europejskiej Nagrody Logistycznej organizowanej przez Europejskie Towarzystwo Logistyczne ELA. Szukano odpowiedzi na pytania dotyczące rodzaju obszarów logistyki decydujących o jej obecnym rozwoju; czy są to technologie związane z przepływem materiałów (technologie mechaniczne), czy technologie informatyczne wspierające przepływ informacji i podejmowanie decyzji, czy doskonalenie procesów logistycznych dotyczy problemów organizacji i zarządzania. Wskazano na dalszy rozwój technologii mechanicznych w obszarze zarówno magazynowania jak i transportu dalekiego. Omówiono zwycięski projekt w 2011 roku dotyczący naczepy o podwójnym zastosowaniu: cysterny do transportu cieczy (w tym przypadku mleka) w jedną stronę i transportu palet w drodze powrotnej. Takie rozwiązanie w istotny sposób minimalizuje puste przebiegi i przyczynia się do ograniczenia emisji dwutlenku węgla w procesach transportowych. Spełnia zatem jeden z najważniejszych celów sformułowanych w Europejskiej Polityce Logistycznej na lata 2011–2025.



Computer aided interpretation of results of the Jominy test

M. PIETRZYK

Akademia Górnictwo-Hutnicza, Al. Mickiewicza 30, 30-059 Kraków, Poland.

R. KUZIAK

Instytut Metalurgii Żelaza, K. Miarki 12–14, 44-100 Gliwice, Poland.

Jominy end quench test is considered in the paper. Finite element simulations of this test were performed including phase transformations modelling. To demonstrate the capability of the model, the numerical simulations results for two bainitic steels with different chemical composition are presented. Phase transformation model for these steels was developed on the basis of the dilatometric tests. These models were implemented in the FE code and kinetics of transformations during the Jominy test was calculated. Distributions of the structural constituents in the sample after the tests were determined. Comparison of the hardenability of the two investigated steels was made on the basis of the results of simulations.

Keywords: *hardenability, Jominy test, finite element modelling, phase transformations, bainitic steels*

1. Introduction

Hardenability is a measure of the depth to which steel will harden, by the development of martensite/bainite in the microstructure, when quenched from the austenitizing temperature. It is measured quantitatively, usually by measuring the extent or depth of hardening of a standard size and shape of test specimen in a standardized quench conditions. Capability of modelling of the hardenability of steels is very useful in selection of the appropriate combination and quantity of alloying elements in a steel and heat treatment conditions to minimize thermal stresses and distortion in manufacturing components of different sizes and shapes. The most common methods of characterizing the hardenability include the end-quench or Jominy Test and a method of calculating the hardenability of steel from the chemical composition based on the original work by Grossman [6]. The former method is the topic of the present work. Interpretation of results of these tests is now based on experience of researchers. The objective of the present paper is the finite element simulation of this test and prediction of the kinetics of phase transformation in the volume of the Jominy sample subject to water cooling according to standard procedure. Comparison of hardenability of two bainitic steels with different chemical composition is the second objective of the paper.

2. Measurement of the hardenability

2.1. Hardenability of steels

A practical indication of steel hardenability is the critical minimum cooling rate for the formation of a fully martensitic microstructure. Hardenability is measured quantitatively, usually by determining the extent or depth of hardened zone of a standard size and shape of test specimen in a standardized quench conditions. The hardness variation with the depth of the Jominy sample is a result of variation in the type and content of martensite, bainite, ferrite and pearlite which arises since the cooling rate decreases with distance from the water quenched end. Hardenability depends on the chemical composition of the steel and also can be affected by prior processing conditions, such as the austenitizing temperature which affects the austenite grain size and amount of carbide/nitride forming elements in solid solution.

Hardening of steels can be understood by considering that on cooling from high temperature, the austenite phase of the steel can transform to either martensite or a mixture of bainite, ferrite and pearlite. The ferrite/pearlite transformation involves diffusion, which takes time. However, the martensite transformation does not involve diffusion and essentially is instantaneous. On the contrary, the bainitic transformation may be considered as a one combining the features of diffusionless martensitic transformation and diffusion controlled ferritic/pearlitic transformation. In the latter case, carbon is the only diffusing species affecting the type of the bainitic microstructure. These two types of reaction are competitive, and martensite is obtained if the cooling rate is fast enough to avoid the slower, diffusion-controlled formation of ferrite and pearlite. In alloyed steels, the ferrite/pearlite transformation is further slowed down due to the solute drag effect, which allows martensite to be obtained using slower cooling rates. Transformation to another possible phase (bainite) can be understood in a similar way.

Steels having high hardenability are required to make large high-strength components, such as large extruder screws for injection moulding of polymers, pistons for rock breakers, mine-shaft supports, aircraft undercarriages, as well as small, high-precision components, such as die-casting moulds, drills and presses for stamping coins. The slower cooling rates that can be used for high hardenable steels can reduce thermal stresses and distortion. Steels having low hardenability may be used for smaller components, such as chisels and shears, or for surface-hardened components, such as gears, where there is a desire to maintain a ferrite/pearlite microstructure at the core to improve toughness.

2.2. Jominy test

The Jominy end quench test is a standard test used to characterize hardenability of steel. Applications of this test to steels is most frequent [7, 12], but other materials are also tested, see e.g. paper [4] for aluminium. In the case of steels this test describes the

ability of steel to be hardened in depth by quenching. It not only is necessary to understand the basic information provided from the test, but also to understand how the information obtained from the Jominy test can be used to understand the effects of alloying in steels and the steel microstructure. Properly carried out test will illustrate the effect of mass upon a chosen steel when heat treated and indicate if the steel is of a shallow, medium or deep hardening type.

Schematic illustration and dimensions of the Jominy test considered in the present work are shown in Figure 1. A steel cylinder (diameter: 25 mm; length: 100 mm) is heated within the austenitic domain during a preset time and quenched from its lower end with a controlled and standardized jet of water. The temperature of the water must be between 15 and 25 °C. The cooling rate along the Jominy test specimen varies from about 225 °C/s to 2 °C/s, depending on the distance from the quenched end. After cooling the Jominy bar is polished parallel to the cylinder axis on both sides. The surface is ground back to remove any effects of decarburisation and the hardness profile is measured along this grounded surface at intervals from the quenched end. Thus, hardness measurements are carried out along the cylinder axis as a function of the distance from the quenched extremity.

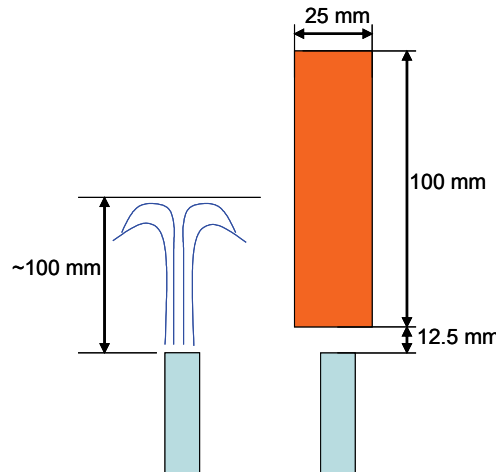


Fig. 1. Schematic illustration and dimensions of the Jominy test considered in this work

3. Model

Modelling the temperature field in the Jominy sample subject to water cooling is usually made by a typical finite element approach. Several examples of such solutions can be found in the scientific literature [4, 7, 12, 14]. Finite volume method is applied in [16]. Authors of [15] applied closed form formulae combined with the Grossman diagram [6]. Phase transformation model is included in works [14, 16]. The FE solution applied in the present work is described briefly below.

3.1. Finite element solution

The model is based on the non-steady state solution of the heat diffusion equation:

$$\nabla \cdot (k \nabla T) + Q = c_p \rho \frac{\partial T}{\partial t}. \quad (1)$$

where:

- k – conductivity,
- T – temperature,
- Q – heat generated due to transformation,
- ρ – density,
- c_p – specific heat,
- t – time.

Solution of Equation (1) has to satisfy the specified boundary conditions. There are three commonly used types of boundary conditions which are applicable to the simulation of forming processes, see for example [13]. The combination of the 2nd (Neumann) and 3rd (Fourier) kinds of boundary conditions is used in the modelling of the Jominy test. The normal derivative of the temperature is prescribed at the boundary surface and it is a function of surface temperature of the workpiece as well as of both time and position:

$$n \cdot (k \nabla T) = q + \alpha(T - T_a) \quad (2)$$

where:

- n – unit vector normal to the surface,
- q – heat flux through the boundary,
- T – surface temperature of the workpiece,
- α – heat transfer coefficient,
- T_a – temperature of the surrounding medium.

Neumann boundary condition is applied at the axis of symmetry and $q = 0$ is introduced. Fourier boundary condition with the heat transfer coefficient α is applied at the water cooling surface and at the air cooled side of the sample.

Determination of the heat transfer coefficient is crucial for the accuracy of simulations of the Jominy tests. As it is shown in [12], two concepts regarding dependence of this coefficient on the temperature are proposed. The first hypothesis involves the presence of vaporization, boiling and forced convection on the surface according to the level of the temperature. In the second hypothesis, a coefficient less dependent from the temperature is assumed. The two hypotheses are based on the global analysis of the lower surface. For the purpose of this study, the first hypothesis with the higher variations of coefficients is chosen. An attempt is made to take into account a heat transfer coefficient varying not only with temperature of lower surface but also with the radius. Following the examination performed in [12] of the water jet on the lower

side, we can consider a point or a surface arrest in the centre ($r = 0$) and, then, a heat transfer coefficient depending on the radius (Figure 1). The following equation describes this relation [12]:

$$\alpha = \alpha_0 (-5 \times 10^{-5} r^5 + 1.7 \times 10^{-3} r^4 - 1.87 \times 10^{-2} r^3 + 5.71 \times 10^{-2} r^2 + 0.1367r + 0.4076) \quad (2)$$

where:

α_0 – basic value of the heat transfer coefficient,

r – radial coordinate.

The basic value of the heat transfer coefficient is introduced as a function of the temperature, accounting for the presence of vaporization, boiling and forced convection. Following the research performed in [7, 12, 14], it is assumed that the maximum value of the heat transfer coefficient is for the surface temperature 300 °C. It is also assumed that this coefficient is constant for the temperature below 200 °C and above 600 °C. The following relations are proposed:

$$\alpha_0 = 5000 \frac{W}{m^2 K} \text{ for } T > 600 \text{ °C},$$

$$\alpha_0 = 2500 \frac{W}{m^2 K} \text{ for } T < 200 \text{ °C},$$

$$\alpha_0 = \alpha_0^{200} + (\alpha_0^{300} - \alpha_0^{200})(T - 200) \text{ for } 200 \text{ °C} < T < 300 \text{ °C}, \quad (4)$$

$$\alpha_0 = \alpha_0^{300} + (\alpha_0^{600} - \alpha_0^{300})(T - 300) \text{ for } 300 \text{ °C} < T < 600 \text{ °C},$$

$$\alpha_0^{300} = 10000 \frac{W}{m^2 K}.$$

Details of the FE code for simulations of the heat transfer can be found in [13]. 12-node quadrilateral elements are applied in this solution.

3.2. Phase transformation model

A number of phase transformation models are available in the literature, from the simplest ones based on the Avrami equation [2] to more advanced models based on phase field [3] or solution of differential equation [17]. Since the objective of the present work is the prediction of transformation temperatures and volume fractions of structural components, a simple model based on Avrami equation is selected:

$$X = 1 - \exp(-kt^n), \quad (5)$$

where:

X – transformed volume fraction,

k, n – coefficients.

Theoretical considerations show that, according to the type of transformation (nucleation and growth process, site saturation process) a constant value of coefficient n in Equation (5) can be used. On contrary, value of the coefficient k must vary with temperature in a way linked to the form of a TTT diagram. The formalism of the function $k = f(T)$ must be carefully chosen to describe properly its temperature dependence of k . Various functions were tested in the present work. A modified Gaussian function proposed by Donnay et al. [5] was selected for the ferritic transformation:

$$k = k_{\max} \exp \left[- \left(\frac{T - T_{\text{nose}}}{a_8} \right)^{a_7} \right]. \quad (6)$$

The four coefficient k_{\max} , T_{nose} , a_7 , a_8 allow description of all shapes of the TTT curves in a quite intuitive way. Thus, k_{\max} is the maximum value of k , T_{nose} is a temperature position of the nose of the Gaussian function, a_7 is proportional to the nose width thickness at mid height and a_8 is related to the sharpness of the curve. The equations, which are used to calculate coefficients k_{\max} and T_{nose} are:

$$k_{\max} = \frac{a_5}{D_\gamma}, \quad (7)$$

$$T_{\text{nose}} = Ae_3 + \frac{400}{D_\gamma} - a_6, \quad (8)$$

where D_γ is austenite grain size at the beginning of transformation.

Slightly simpler function was selected for the pearlitic transformation:

$$k = \frac{a_{14}}{D_\gamma^{a_{16}}} \exp(a_{13} - a_{12}T). \quad (9)$$

In the bainitic transformation relation on the grain size D_γ is neglected:

$$k = a_{23} \exp(a_{22} - a_{21}T). \quad (10)$$

Coefficients in Equations (7–10) are selected that way that the model reflects relations of the driving force of transformations on the temperature. Function (5) with

coefficient k described by Equation (6) does not require the incubation time. Introduction of the modified Gauss function (6) into the Avrami equation results in a very slow progress of transformation just below A_{c3} temperature. It is assumed that ferritic transformation begins when the volume fraction of ferrite achieves 5%. Contrary, incubation times (τ_p , τ_b) are introduced before calculations using Equation (5) for the pearlitic and bainitic transformations begin. These times are calculated as:

$$\tau_p = \frac{a_9}{(Ae_1 - T)^{a_{11}}} \exp\left(\frac{a_{10} \times 10^3}{R\hat{T}}\right), \text{ pearlitic} \quad (11)$$

$$\tau_b = \frac{a_{17}}{(T_b - T)^{a_{19}}} \exp\left(\frac{a_{18} \times 10^3}{R\hat{T}}\right), \text{ bainitic} \quad (12)$$

where \hat{T} is temperature in the absolute scale.

Additional relationships in the model are given in Table 1. Equilibrium concentrations $c_{\gamma\alpha}$ and $c_{\gamma\beta}$ in this table are calculated as functions of temperature. Coefficients in these functions were determined for the considered chemical compositions of steels using ThermoCalc software and they are given in Table 2. Chemical compositions of the investigated bainitic steels are given in Table 3.

Table 1. Additional equations in the model

$c_\gamma = \frac{(c_0 - X_f c_\alpha)}{1 - X_f}, \quad X_{f0} = \frac{c_{\gamma\alpha} - c_0}{c_{\gamma\alpha} - c_\alpha},$
$c_\alpha = -0.069 + 0.000435T - 9.1658 \times 10^{-7} T^2 + 6.487 \times 10^{-10} T^3 \text{ for } T < 637 \text{ }^\circ\text{C},$
$c_\alpha = -0.0487268 + 0.00017839T - 1.50788 \times 10^{-7} T^2 \text{ for } T > 637 \text{ }^\circ\text{C},$
$c_{\gamma\alpha} = c_{\gamma\alpha 0} + c_{\gamma\alpha 1}T, \quad c_{\gamma\beta} = c_{\gamma\beta 0} + c_{\gamma\beta 1}T.$

Notation:

c_γ – average carbon content in austenite,

c_α – carbon content in ferrite,

c_0 – carbon content in steel,

$c_{\gamma\alpha}$ – carbon concentration in austenite at the $\gamma\alpha$ boundary,

$c_{\gamma\beta}$ – carbon concentration in austenite at the $\gamma\beta$ boundary,

Table 2. Parameters in equations describing equilibrium carbon contents in Table 1

steel	$c_{\gamma\alpha 0}$	$c_{\gamma\alpha 1}$	$c_{\gamma\beta 0}$	$c_{\gamma\beta 1}$
A	4.8365	-0.005818	-1.09	0.00259
B	4.7125	-0.0056377	-0.887468	0.00221867

Table 3. Chemical composition (wght %) of the investigated steel

Steel	C	Mn	Si	Cr	Al	Cu	P	S	Nb	Ti	B	N
A	0.074	2.0	0.28	—	0.034	0.10	0.012	0.011	0.038	0.13	0.002	0.0038
B	0.051	1.51	0.30	0.2	0.024	0.36	0.01	0.01	—	0.01	—	0.0035

Simulation of phase transformations starts with Equation (5) when the temperature drops below Ae_3 . The transformed volume fraction X_f is calculated with respect to the maximum volume fraction of ferrite X_{f0} in the current temperature. Thus, this volume fraction of ferrite with respect to the whole volume of the body is $F_f = X_{f0}X_f$. During numerical simulation in the varying temperature the current value of X_f calculated from Equation (5) has to be corrected to account for the change of the equilibrium (maximum) volume of ferrite X_{f0} , which according to equation in Table 1 is a function of temperature. The following correction is made:

$$X_f^{i+1} = X_f^i \frac{X_{f0}(T^i)}{X_{f0}(T^{i+1})}, \quad (13)$$

where i is iteration number.

Simulation continues until the transformed volume fraction reaches 1. However, when carbon content in austenite achieves the limiting value $c_{\gamma\beta}$ (see Table 2), the austenite-pearlite transformation begins in the remaining volume of austenite.

Bainite start temperature (T_b) and martensite start temperature (T_m) are functions of the chemical composition of the austenite:

$$T_b = a_{20} - 425[C] - 42.5[Mn] - 31.5[Ni] - 70[Cr], \quad (14)$$

$$T_m = a_{26} - a_{27}c_\gamma, \quad (15)$$

Fraction of austenite, which transforms into martensite is calculated according to the model of Koistinen and Marburger [8], described also in [9]:

$$X_m = 1 - \exp[-0.011(T_m - T)], \quad (16)$$

Equation (16) represents volume fraction of martensite with respect to the whole volume of austenite, which was remaining at the temperature T_m . The volume fraction of martensite with respect to the whole volume of the material is:

$$F_m = (1 - F_f - F_p - F_b)\{1 - \exp[-0.011(T_m - T)]\}, \quad (17)$$

where F_f , F_p , F_b , F_m are volume fractions of ferrite, pearlite and bainite with respect to the whole volume of the sample.

Additivity rule [11] is applied in the model to account for the temperature changes during transformations.

Identification of the phase transformation model was performed next. As it has been mentioned, coefficients in equations describing equilibrium concentrations of carbon in Table 1 were determined using ThermoCalc software and they are given in Table 2. Coefficients $\mathbf{a} = \{a_1 \dots a_{27}\}$ in the phase transformation model were determined using inverse analysis of the dilatometric tests for the investigated steel. Basic principles of the inverse method are described in a number of publications, see for example [18]. The most frequent applications of the inverse method in metallurgy are connected with determination of coefficients in rheological models of materials subjected to plastic deformation. Authors of publication [1] applied the inverse method to identification of the thermal parameters of the quenching process. Applications to identification of the phase transformation model are scarce. Algorithm proposed to plastometric tests in [18] was adapted in the present paper to the dilatometric test and identification of the phase transformation model. Mathematical model of an arbitrary phase transformation can be described by a set of equations:

$$\mathbf{d} = F(\mathbf{a}, \mathbf{p}), \quad (18)$$

where:

$\mathbf{d} = \{d_1, \dots, d_r\}$ – vector of start and finish temperatures of transformations and volume fractions of structural components in the room temperature, which are measured in the dilatometric tests performed with constant cooling rates,

$\mathbf{a} = \{a_1, \dots, a_l\}$ – vector of coefficients of the model,

$\mathbf{p} = \{p_1, \dots, p_k\}$ – vector of such process parameters as cooling rates, austenite grain size and deformation of austenite. Measurements \mathbf{d}_i^m are obtained from the dilatometric tests carried out with constant cooling rates. Components \mathbf{d}_i^c are calculated using one of the models of the direct problem, which are described above.

Identification of parameters of the phase transformation model is composed of two parts. The first is solution of the direct problem, based on the model. The second part is solution of the inverse problem, in which optimization techniques are used.

Results of dilatometric tests, including measurements of the start and end temperatures for transformation and volume fractions of phases after cooling to room temperature, are used as an input to the inverse analysis. Thus, in the particular case of phase transformations the objective function (17) is defined as.

$$\Phi(\mathbf{a}, \mathbf{p}) = \sqrt{\frac{1}{Nt} \sum_{i=1}^{Nt} \left(\frac{T_{im} - T_{ic}}{T_{im}} \right)^2 + \frac{1}{Nv} \sum_{i=1}^{Nv} \left(\frac{X_{im} - X_{ic}}{X_{im}} \right)^2}, \quad (19)$$

where:

T_{im}, T_{ic} – measured and calculated start and end temperatures of phase transformations,
 Nt – number of temperature measurements,

X_{im}, X_{ic} – measured and calculated volume fractions of phases at room temperature,
 Nv – number of measurements of volume fractions of phases.

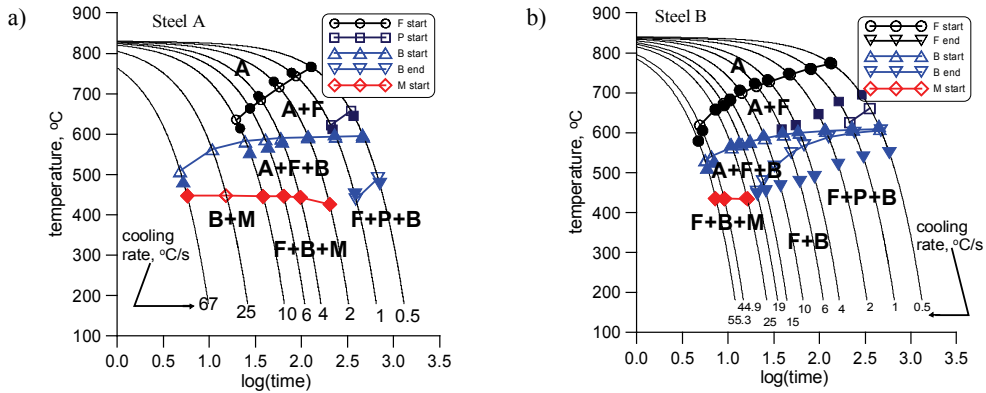


Fig. 2. Comparison of the predictions of the optimized phase transformation model (coefficients in Tables 5 and 6) with measurements for the transformations start and end temperatures, a) steel A and b) steel B

The values of the coefficients a obtained from the inverse analysis are given in Table 4 for the steel A and in Table 5 for the steel B. In general, the whole model for all transformations may contain all together 27 coefficients [19]. However, only 23 of them are active in the transformation model for the considered bainitic steel and are used in the present work. Model with the coefficients in Tables 4 and 5 was validated. It was used to simulate all the dilatometric tests, which were performed. Figure 2 shows comparison of the measured (filled symbols) and predicted (open symbols) start and end temperatures for the phase transformations. Shape of the symbol refers to the temperature in the legend. Analysis of the results shows that the model predicts quite well start and end temperatures for transformations. The accuracy is slightly worse for the end temperature for the bainitic transformation for the steel B.

Table 4. Coefficients in the phase transformation model calculated using inverse analysis for the steel A

a_4	a_5	a_6	a_7	a_8	a_9	a_{10}	a_{11}	a_{12}	a_{13}	a_{14}	a_{15}
1.685	0.016	224.1	45.08	1.174	7.35	0	0	1.87	0.088	6.29	0.2133
a_{16}	a_{17}	a_{18}	a_{19}	a_{20}	a_{21}	a_{22}	a_{23}	a_{24}	a_{26}	a_{27}	
0.48	1.289	0.175	0	714.6	1.713	4.04	0.187	1.453	452	63.94	

Table 5. Coefficients in the phase transformation model calculated using inverse analysis for the steel B

a_4	a_5	a_6	a_7	a_8	a_9	a_{10}	a_{11}	a_{12}	a_{13}	a_{14}	a_{15}
1.126	0.79	235.4	107.7	2.587	0.0393	0.001	0.629	0.0779	3.167	0.00367	0.764
a_{16}	a_{17}	a_{18}	a_{19}	a_{20}	a_{21}	a_{22}	a_{23}	a_{24}	a_{26}	a_{27}	
0.0659	1597	62.06	3.274	696.9	0.323	0.757	0.962	1.087	439.7	90.81	

4. Simulations of the Jominy test

Simulations were performed using the finite element code described in section 3.1 combined with the phase transformation model described and validated in section 3.2.

Changes of the parameters were monitored in 4 points located at the axis of the sample at the distance of 5, 20, 50 and 90 mm from the quenched end, as shown in Figure 3. Simulations were performed for the two bainitic steels with chemical composition given in Table 4 and the coefficients in the phase transformation model given in Tables 5 and 6. Selection of these steels was inspired by promising results of the cold forging tests performed in [9–10].

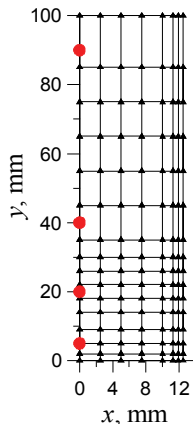


Fig. 3. Finite element mesh and location of sensors, in which results are presented

4.1. Temperatures and transformation kinetics

Results of simulation of temperature changes in the 4 points shown in Figure 3 are presented in Figure 4. Kinetics of transformation in these points is presented in Figure 5 for the steel A and in Figure 6 for the steel B.

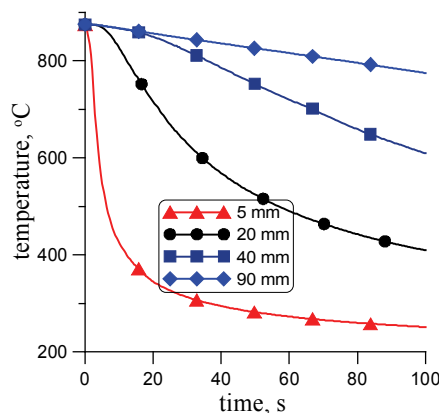


Fig. 4. Time temperature profiles calculated for various distance from the quenched end, initial hundred seconds

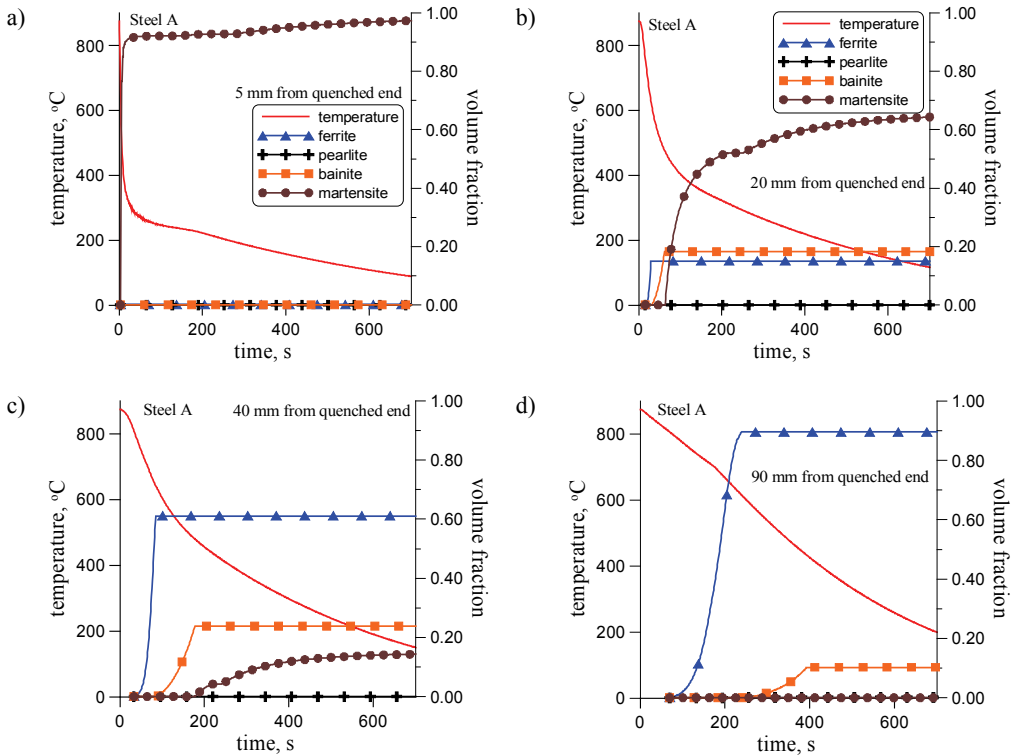


Fig. 5. Kinetics of transformations calculated for steel A in points located from the quenched end:
a) 5 mm, b) 20 mm, c) 40 mm, d) 90 mm

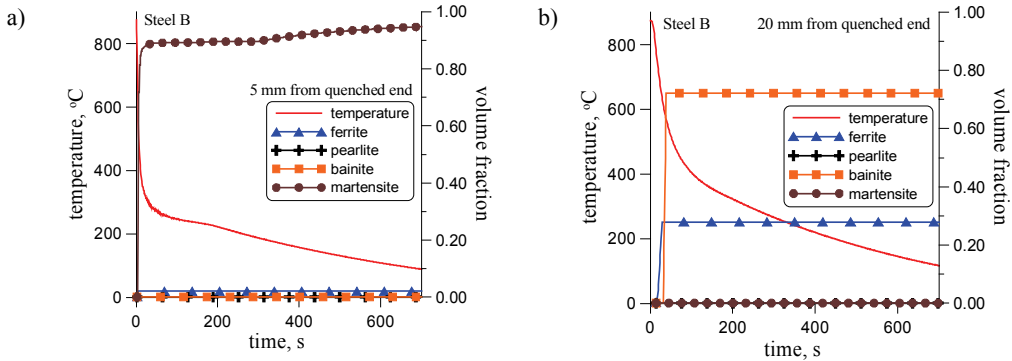


Fig. 6a,b. Kinetics of transformations calculated for steel B in points located from the quenched end:
a) 5 mm, b) 20 mm

Changes of volume fraction of structural components as a function of the distance from the quenched end are shown in Figure 7. Comparison of the distribution of the martensite and bainite along the axis of the sample is shown in Figure 8.

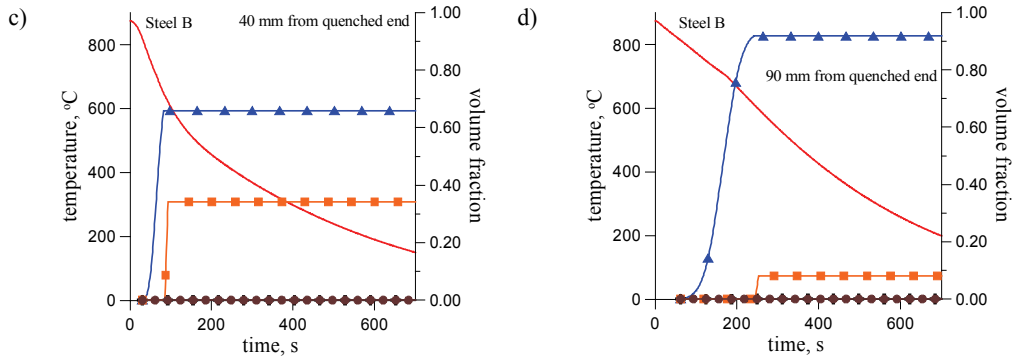


Fig. 6c,d. Kinetics of transformations calculated for steel B in points located from the quenched end:
c) 40 mm, d) 90 mm

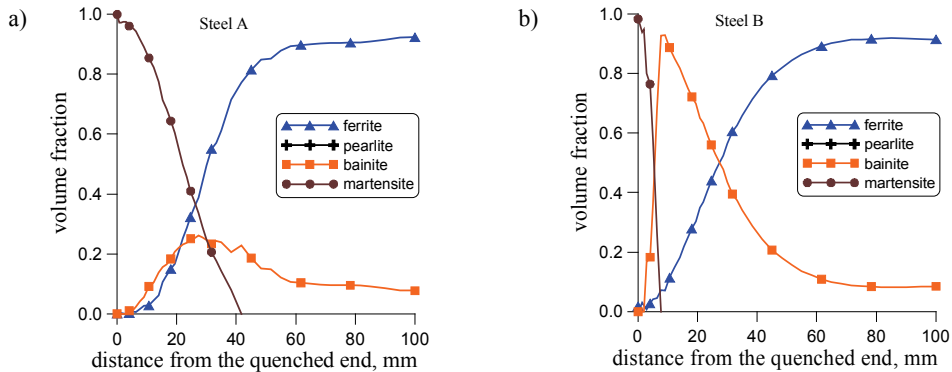


Fig. 7. Changes of volume fraction of structural components as a function of the distance from the quenched end for the steel A (a) and B (b)

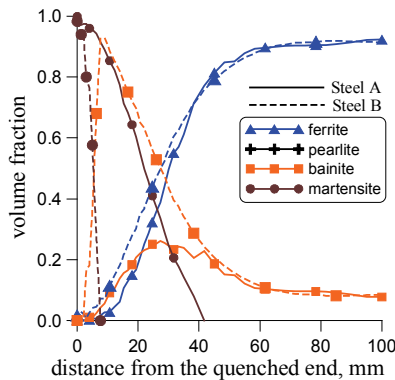


Fig. 8. Comparison of the distribution of the structural components along the axis of the sample in the two considered steels

Figure 8 shows that steel A is more prone to develop the martensite in the structure as compared to steel B. In the latter case, a relatively large content of bainite can be developed applying cooling rate of around 10 °C/s. On the contrary, steel A develops more martensite in the microstructure at the sacrifice of bainite.

Developed model allows to calculate distribution of the volume fractions of structural components as a function of the distance from the quenched end. When hardness of the constituents is known, the distribution of the hardness along the samples can be calculated from the rule of mixture.

5. Discussion and conclusions

The hardenability of steel depends on the nucleation and growth rates of ferrite, pearlite and bainite. Therefore, the main objective of the research activity was to formulate the phase transformation model for the experimental bainitic steels. Next, the identification of coefficients in the model using the results of dilatometric tests and inverse analysis were performed. The model is based on the Avrami type equation, with one of the coefficients described by the Gaussian distribution function. Since during phase transformation several phases appear with their features, a kinetic of phase transformation specific for each appearing phase was adjusted separately. The results of the simulations show that the dependence of the ferrite, pearlite, bainite and martensite microstructure versus cooling rate indicate the capability of steel to develop the martensitic and bainitic microstructure in the depth of the Jominy curve. Steel A has better propensity to develop the martensite in the depth of the sample as opposed to steel B. In the latter case, the steel develops more bainite than martensite. This is due to the fact that steel A has higher content of C and Mn as compared to steel B and also contains boron. This observation is very important and may be used to define qualitatively the bainitic hardenability, which will be the subject of further works.

The following conclusions can be drawn:

- Phase transformation model basing on the Avrami type equation was developed and applied in the paper to predict the phase transformation progress in two steels characterised mainly by different C and Mn content. Besides, steel A contained boron as a very effective element affecting the hardenability.
- Identification of the phase transformation model on the basis of the results of the dilatometric tests improves accuracy of this model. The developed phase transformation model shows good predictive capability.
- Combination of the FE code with the phase transformation model allows simulation of the Jominy test and prediction of the distribution of the volume fractions of the structural components in the sample.
- Thus, the developed model allows evaluation of the hardenability of the steel, assuming that depth of occurrence of the martensite in the sample is a measure of the hardenability.

- The most interesting results of the investigation refer to the dependence of the volume fraction of microstructural constituents on the cooling curve, namely, the content of bainite exhibits the maximum at some specific cooling rate. The maximum is higher when the maximum martensite content is lower in steel. As a result, one may state that martensite and bainite compete in the microstructure at high cooling rates. The result of the competition depends on the amount of carbon and alloying elements.
- The results of the investigation may be very useful in the development of the new class of bainitic steels characterized by high strength and ductility.
- Beyond this, the results of the investigation will be used to formulate the bainitic hardenability criterion.

Acknowledgements

Financial assistance in AGH project 11.11.110.080 is acknowledged.

References

- [1] Archambault P., Denis S., Azim A.: *Inverse resolution of the heat transfer equation with internal heat source: Application to the quenching of steels with phase transformations*, Journal of Materials Engineering and Performance, Vol. 6, 1997, pp. 240–246.
- [2] Avrami M.: *Kinetics of phase change I*, J. Chem. Phys., Vol. 7, 1939, pp. 1103–1112.
- [3] Chen L.-Q.: *Phase-field models for microstructure evolution*, Annual Review of Materials Research, Vol. 32, 2002, pp. 113–140.
- [4] Dolan G.P., Flynn R.J., Tanner D.A., Robinson J.S.: *Quench factor analysis of aluminium alloys using the Jominy end quench technique*, Materials Science and Technology, Vol. 21, 2005, pp. 687–692.
- [5] Donnay B., Herman J.C., Leroy V., Lotter U., Grossterlinden R., Pircher H.: *Microstructure evolution of C-Mn steels in the hot deformation process: the STRIPCAM model*, Proc. 2nd Conf. Modelling of Metal Rolling Processes, (eds), Beynon J.H., Ingham P., Teichert H., Waterson K., London, 1996, pp. 23–35.
- [6] Grossman M.A.: *Hardenability calculated from chemical composition*, AIME Transactions, Vol. 150, 1942, pp. 227–259.
- [7] Hömberg D.: *A numerical simulation of the Jominy end-quench test*, Acta Materialia, Vol. 44, 1996, pp. 4375–4385.
- [8] Koistinen D.P., Marburger R.E.: *A general equation prescribing the extent of the austenite-martensite transformation in pure iron-carbon alloys and plain carbon steels*, Acta Metallurgica, Vol. 7, 1959, pp. 59–60.
- [9] Kuziak R., Pietrzyk M.: *Bainitic steels as alternative for conventional carbon-manganese steels in manufacturing of fasteners – simulation of production chain* (in press), Computer Methods in Materials Science, Vol. 11, 2011.
- [10] Kuziak R., Skóra M., Węglarczyk S., Paćko M., Pietrzyk M.: *Computer aided design of the manufacturing chain for fasteners*, Computer Methods in Materials Science, Vol. 11, 2011, pp. 243–250.

- [11] Scheil E., *Anlaufzeit der Austenitumwandlung*, Archiv. für Eissenhuttenwesen, Vol. 12, 1935, pp. 565–567.
- [12] Le Masson P., Loulou T., Artioukhine E., Rogeon P., Carron D., Quemener J.-J.: *A numerical study for the estimation of a convection heat transfer coefficient during a metallurgical “Jominy end-quench” test*, International Journal of Thermal Sciences, Vol. 41, 2002, pp. 517–527.
- [13] Lenard J.G., Pietrzyk M., Cser L.: *Mathematical and physical simulation of the properties of hot rolled products*, Elsevier, Amsterdam, 1999.
- [14] Li V.M., Niebuhr D.V., Meekisho L.L., Atteridge D.G.: *A Computational model for the prediction of steel hardenability*, Metallurgical And Materials Transactions B, Vol. 29B, 1998, pp. 661–672.
- [15] Olejarczyk I., Adrian A., Adrian H., Mrzygłód B.: *Algorithm for controlling of quench hardening of constructional steel*, Archives of Metallurgy and Materials, Vol. 55, 2010, pp. 171–179.
- [16] Smoljan B.: *Numerical simulation of steel quenching*, Journal of Materials Engineering and Performance, Vol. 11, 2002, pp. 75–79.
- [17] Suehiro M., Senuma T., Yada H., Sato K.: *Application of mathematical model for predicting microstructural evolution to high carbon steels*, ISIJ International, Vol. 32, 1992, pp. 433–439.
- [18] Szeliga D., Pietrzyk M.: *Testing of the inverse software for identification of rheological models of materials subjected to plastic deformation*, Archives of Civil and Mechanical Engineering, Vol. 7, 2007, pp. 35–52.

Wspierana komputerowo interpretacja wyników próby Jominy

Przedmiotem pracy jest próba Jominy, wykonywana w celu wyznaczenia hartowności stali. Wykonano symulacje tej próby metodą elementów skończonych połączoną z modelowaniem przemian fazowych. Zaprezentowano wybrane wyniki symulacji dla dwóch stali bainitycznych o różnym składzie chemicznym. Identyfikację modelu przemian fazowych dla tych stali prowadzono wykorzystując metodę rozwiązania odwrotnego dla prób dylatometrycznych. Wykorzystując połączony model MES i przemian fazowych wyznaczono rozkład produktów rozpadu austenitu w próbce. Na podstawie przeprowadzonych symulacji porównano hartowność dwóch badanych stali.



Reliability analysis of Misses truss

U. RADON

Faculty of Civil and Environmental Engineering, Kielce University of Technology,
Al. 1000-lecia P.P. 7, 25-314 Kielce, Poland.

The present study considers the problems of stability and reliability of truss structure susceptible to stability loss from the condition of node snapping. In the reliability analysis of structure, uncertain parameters, such us load magnitudes, the axial stiffness of bars, coordinate nodes are represented by random variables. Random variables are not correlated. The criterion of structural failure is expressed by the condition of non-exceeding the admissible load multiplier. In the current paper only the time independent component reliability analysis problems are considered. The Hasofer-Lind index in conjunction with transformation method in the FORM was used as a reliability measure.

Keywords: *probability density function, reliability index, design point, stability loss, node snapping*

1. Introduction

In early applications of reliability analysis methods it was accepted that the limit state function is an explicit function of random variables. Such functional dependency can be realized only for very simple examples. In practical realizations this dependence is not explicit and it is determined using numerical procedure, e.g. the finite element methods. The development of numerical methods caused that methods for implicit dependences of the limit state function from basic random variables have become a very desirable instrument in structural reliability theory. One of the methods of this type is the perturbation method proposed in the works of Hisady and Nakagiri [3–4], Liu, Belytschko, Mani [11–12], Shinozuki [18] to solve problems of linear elasticity theory. This method is based on series expansion of stiffness matrix with respect to uncertain parameters by means of Taylor expansion. The perturbation method is not however designed to calculate failure probability, but only to obtain moments of statistical responses of the system. Calculations of probabilities would require introduction of probability distributions of random variables and estimation of higher statistical moments of responses. The application of the perturbation method to calculation by the finite element method is presented in the monograph [6] of Kleiber and Hien. Sniady in the work [21] showed application of the method in stochastic dynamics. Similarly to the perturbation method, using Neumann's extension method (a matrix reverse to stiffness matrix is subject to series expansion), one obtains only information concerning statistical moments of a random variable, being the response of the system. Der Kiureghian and co-authors [9–10] proposed a method which per-

mits estimation of failure probability in the situation when estimation of the structure displacements is executed with the use of the finite element method.

In developing a program that enables reliability analysis with the use of the finite element method, it is most favourable to have access to the source code FEM and the reliability program. In general, however, this is not possible. Therefore, the existing FEM packs are combined with the reliability program applying a different kind of interfaces, however, at the cost of efficiency decrease. This article is to present the communication between the reliability analysis program STAND and external FEM program KRATA. The program STAND was developed in the Institute of Fundamental Technological Research of Polish Academy of Science by J. Knabel, K. Kolanek, V. Nguyen Hoang, R. Stocki, P. Tauzowski [19–20]. The program KRATA was developed by the present author. In the presented example basic random variables are load, axial stiffness of bars and node coordinates; external variables are displacements and load multiplier. Basic random variables are not correlated. In the paper condition of non exceeding admissible load multiplier is considered as the limit state function.

2. Statement of the problem – general solution

The problems of reliability analysis of structures considered in this study are based on the following premises. Firstly, it is assumed that a structure can be in one of two admissible states: safe state or failure state. Failure is understood as non-fulfilment of a certain limitation imposed by the designer on the performance of a structure. It is assumed that parameters describing the state of structure are treated as random variables (as contrasted with random processes). The considered problems of reliability analysis will be related to the so called element reliability. The element is understood here as all the structure or its part, whose state is determined by one limit state function (failure criterion). It is necessary to underline here that this study is not concerned with system reliability in which many limit state functions are taken into account and the possibility of the sequence of particular elements' failures, which leads to the destruction of the whole structure.

In 1974 Hasofer-Lind [2] proposed a modified reliability index that did not exhibit the invariance problem. The “correction” is to evaluate the limit state function at a point known as the “design point” instead of the mean values. The design point is a point on the failure surface. The design point is generally not known a priori, an iteration technique must be used to solve the reliability index.

Consider a limit state function $g(X_1, \dots, X_n)$ where the random variables X_i are all uncorrelated. The limit state function is rewritten in terms of the standard form of the variables (reduced variables) using

$$Z_i = \frac{X_i - \mu_{X_i}}{\sigma_{X_i}} \text{ and } X_i = \mu_{X_i} + Z_i \sigma_{X_i}. \quad (1)$$

Replacing X_1, \dots, X_n by Z_1, \dots, Z_n , we obtain a new limit state function:

$$g'(Z_1, \dots, Z_n). \quad (2)$$

The Hasofer-Lind reliability index is defined as the shortest distance from the origin of the reduced variable space to the limit state function $g'(Z_1, \dots, Z_n) = 0$. It is the most probable point of failure from among all points in this surface. If failure occurs, it is most likely to occur just at this point. Finding a design point is a task for nonlinear programming with limitations. The accuracy of results obtained with the use of the Hasofer-Lind index is often sufficient for practical needs. The index gained a considerable popularity as a reliability measure, particularly in conjunction with transformation methods which use full information about random variable distributions, e.g. in the FORM method.

Atmospheric loads have often a distinctly non-Gaussian character. Such loads as wind, snow, sea currents and waves have effect on the structure with intensity variable in time and they ought to be treated as random processes. However, one can sometimes treat them as random variables with probability distributions that correspond to maximum distributions of these loads in a given (long) time range. Examples of such distributions are Gumbel and Frechet's distributions.

The FORM method is one of most effective approximate methods of the calculation of reliability measures. In a general case, when the probability distribution of vector \mathbf{X} of base variables is not a vector with the Gaussian distribution, transformation is used to reduce this vector to the Gaussian vector whose coordinates are independent standard normal variables. The existence of this type of transformation and the manner of its construction was shown for the first time by Rosenblatt [14] for the case when coordinates of vector \mathbf{X} have uniform distributions. Hohenbichler and Rackwitz [5] adapted this transformation to reliability calculations. The transformation of basic random variables to the Gaussian standard space must assure the equivalence of the formulation of the reliability problem. The probability of failure, defined in space \mathbf{X} , must be equal to the probability defined in space \mathbf{Z} .

Aside from Rosenblatt's transformation, Hermite's transformation and the transformation resulting from the so called Nataf model are also applied. Transformation carries the limit state surface $g(\mathbf{X}) = 0$ to another surface $G(\mathbf{Z}) = 0$. It should be noted that the effective calculation of the integral of the function of the density of the n -dimension of a standard normal distribution along the failure surface is still a complicated problem, except for the case when $G(\mathbf{Z}) = 0$ is a hyperplane in space. However, two essential properties of the density of the standard normal distribution cause the transformation to be effective in the calculation of failure probability. The first of these properties is rotary symmetry around the beginning of the coordinate system. The second property is exponential disappearance of this function together with the square of distance from the beginning of the coordinate system. Therefore, the greatest failure probability originates from the surface in the neighbourhood of the point on the

limit state surface whose distance from the beginning of the coordinate system is the smallest. Therefore, in the FORM method the surface of limit state $G(\mathbf{Z}) = 0$ is approximated by a hyperplane tangential to it at the point nearest to the beginning of the coordinate system. This leads to the following approximate formula of failure probability: $p_F = \Phi(-\beta)$. The minimum distance point is called a design point, while β is a reliability index. As the value of the density of normal distribution is highest at this point in the whole failure surface, then this point is the highest reliability point. Finding the design point is thus reduced to the solution of the optimization problem. A number of algorithms have been developed to this end. The earliest ones, which originated from the works of Hasofer and Lind [2], as well as those of Rackwitz and Fiessler [13], are based on gradient procedures. The subsequent Schittkowski [15–16] and Arora [1] algorithms made use of the method of sequence square programming.

These algorithms are constantly improved for the application in reliability calculation software. It would be difficult to indicate the best algorithm, particularly due to the fact that different criteria can be used, e.g. guaranteed convergence or the least number of operations. It depends in large measure on the size of the problem (number of random variables) and the form of the limit state function. In some ADP systems used for reliability calculations, several algorithms are employed. They are run alternatively depending on the kind of assignment. Coefficients of the sensitivity α_i of reliability index, which are defined as partial derivatives of reliability index in relation to individual parameters of the problem, are sensitivity measures most often applied in the FORM method.

3. Numerical results

The example presents application of the reliability method FORM to the analysis of node snapping of Misses truss (Figure 2). In the study determining the equilibrium path of node 1 of Misses truss is done in two variants. The first variant is a geometrical nonlinear solution. The second variant is a geometrical and physical nonlinear solution. In the analysis, the nonlinear geometrical and physical relations were defined in Lagrangian description. The sources of the nonlinear relations $\underline{\sigma} = f(\underline{\varepsilon})$ are, apart from strictly material features, also geometrical imperfections. In this analysis, the differential constitutive relations were neglected and these were generated for the whole element (i.e. for individual bars). This approach does not enable us to separate the material and geometrical imperfections. The experiments were carried out using bars 163 to 572 mm long. Therefore, it was of the utmost importance to properly interpret the scale effect. The solution was reached by creating a dimensionless load-displacement relation (RLD) for the imperfect compressed bar.

The parameters of the RLD were derived using experimental test results presented by Sendkowski in his Ph.D. thesis [17] and Sendkowski, Kowal, Radoń [7]. The experiments were carried out for the flat rods of St3S steel and for a nominal cross-section 20×10 mm. The experimental data base consisted of 10 sets, each of them

containing 6 to 12 test results for laboratory models of bars. In each of the experiments, 50–90 measuring points for the RLD were determined. Point A indicates linear elasticity limit, B is the maximum load point, C and D points fix the limits of the curve's retreat (Figure 1). Statistical analysis of test results enables the selection of some properties which can be accepted as the following invariants: $P_A/P_B = 0.88065$, $\Delta_A/\Delta_B = 0.808756$, $P_C/P_B = 0.9504942$, $\Delta_C/\Delta_B = 1.10254$.

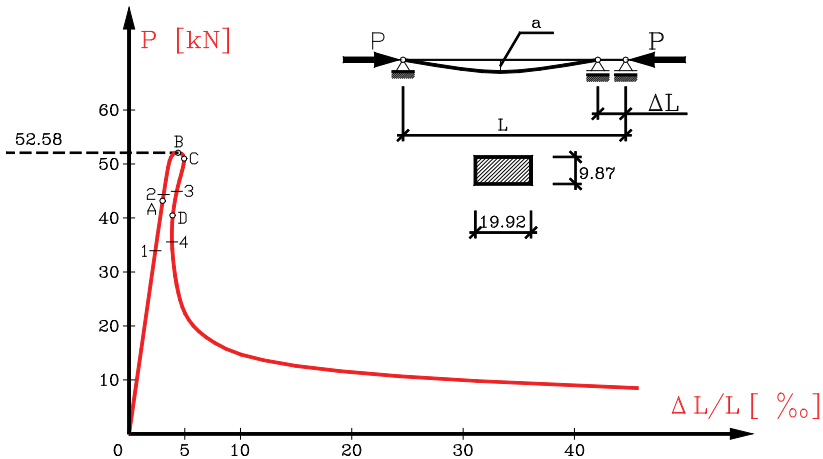


Fig. 1. Example of a RLD for a bar with imperfections

The position of point D was found to have a very high standard deviation, therefore the effect of the curve's retreat was not dealt with. The mathematical form of the RLD was obtained using spline functions of the C^1 class. On the basis of the tests we can find that the first branch between 0 to A points can be approximated by a straight line. The tangent of the inclination angle E' is equal to $0.918E$. The next branch ABC was approximated by a polynomial of the 4th grade with the derivative at B point equal to zero. Finally, the third branch C ∞ was described using the exponential function. The spline conditions at A and C points are of C^1 class. The detailed description of the procedure and the suitable formulas are contained in the papers by Kowal, Radoń [8]. Numerical calculations after the introduction of the constitutive model of compressed model bars gave a decrease in the value of limit load of 9% with a slight change of the vertical displacement corresponding to limit load. This is illustrated in Figure 2.

Limit functions, as a condition of non-exceeding the admissible vertical load of node 1, are formulated on the basis of the coordinates of limit points for:

- a geometrically nonlinear solution $g_1(x) = 1 - \mu(x)/2.262$,
- a geometrically and physically nonlinear solution $g_2(x) = 1 - \mu(x)/2.075$.

In the reliability analysis of the Misses truss the following variables are used: load "P", axial stiffness "EA", coordinate "Z" node 1. Basic random variables are not correlated. In the example, it was considered how introducing subsequent random variables

affects the value of the reliability index. Taking into account mutual correlation of, e.g., random variables describing the axial stiffness **EA** and variable **Z** of node 1 (which is possible) would change the line of investigations adopted for this study.

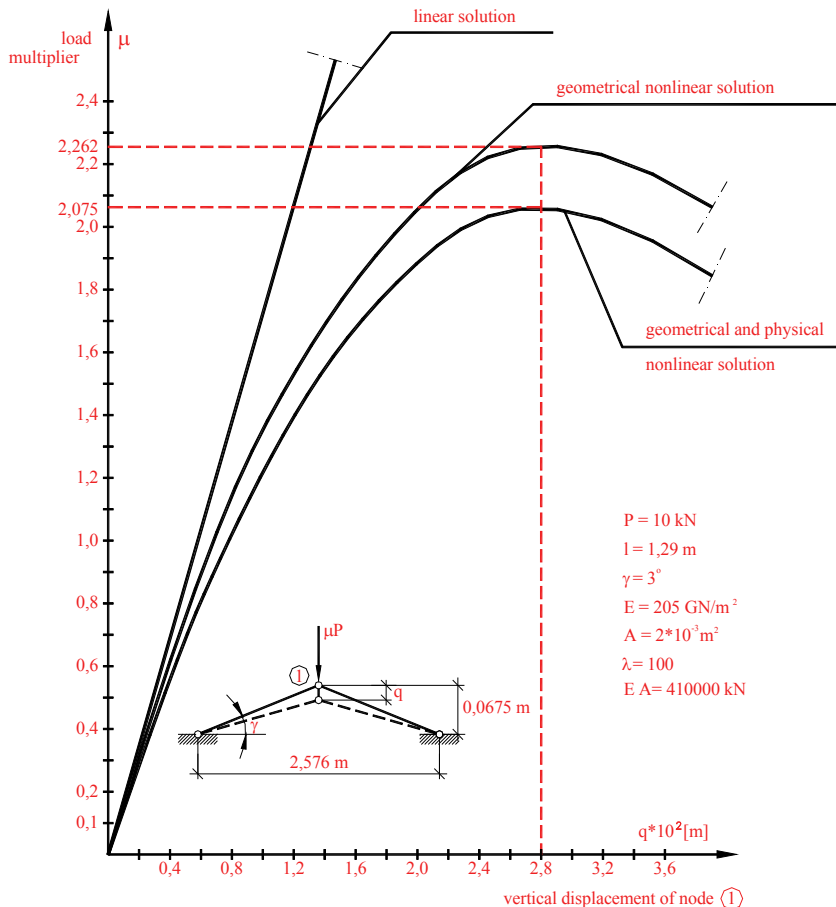


Fig. 2. Equilibrium paths of the Misses truss

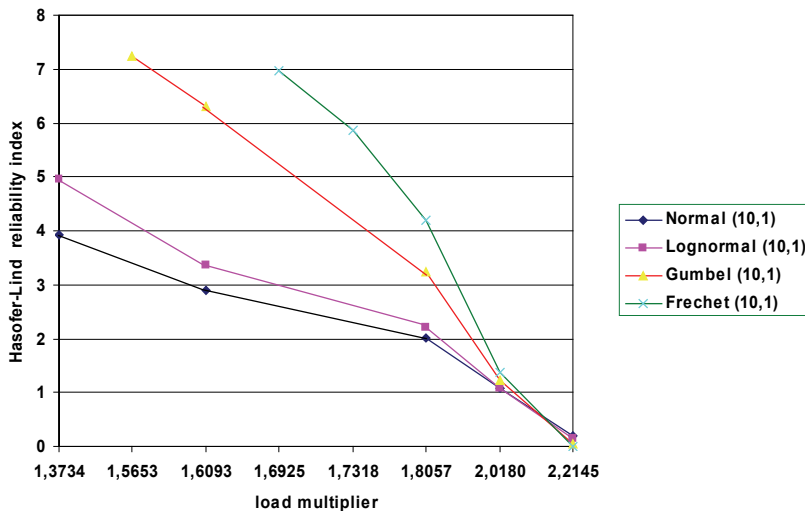
It is employed in 3 cases.

Case 1

- load “P” – random variable (description of changing probability density function shows in Figure 3),
- axial stiffness “EA” – deterministic variable ($EA = 410000 \text{ kN}$),
- coordinate “Z” node 1 – deterministic variable ($Z = 0.0675 \text{ m}$).

Figure 3 shows the effect of the adopted probability distribution which describes load on the value of the Hasofer-Lind reliability index during movement along the

geometrically nonlinear path. With an increasing distance from the limit value of the load multiplier differences in the assessment of structure safety increase markedly.



Notation in Figure 3:

Normal (10,1) – normal probability density function; mean value = 10; standard deviation = 1

Lognormal (10,1) – lognormal probability density function; mean value = 10; standard deviation = 1

Gumbel (10,1) – gumbel probability density function; mean value = 10; standard deviation = 1

Frechet (10,1) – frechet probability density function; mean value = 10; standard deviation = 1

Fig. 3. Effect of the accepted type of probability distribution load on the value of the Hasofer-Lind reliability index

For example: for the load multiplier equal to 1.8057, the values of reliability index for particular distributions are as follows:

- Normal (10 kN, 1 kN) – 2.01378,
- Lognormal (10 kN, 1 kN) – 2.20419,
- Gumbel (10 kN, 1 kN) – 3.24112,
- Frechet (10 kN, 1 kN) – 4.20626,

for the load multiplier equal to 1.6093, the values of reliability index for particular distributions are as follows:

- Normal (10 kN, 1 kN) – 2.88367,
- Lognormal (10 kN, 1 kN) – 3.3591,
- Gumbel (10 kN, 1 kN) – 6.30112.

For Fréchet distribution, no solution was obtained as during the analysis, problems were encountered with computing the gradients of the limit state function, which are necessary to determine the position of the design point.

Case 2

- load “P” – random variable,

- axial stiffness “EA” – random variable,
- description of changing probability density function random variables “P”, “EA” shows below Figure 4 and 5),
- coordinate “Z” node 1 – deterministic variable ($Z = 0.0675$ m).

Moving still along the equilibrium path for a geometrically nonlinear solution, we can observe decrease in the differences of the values of reliability index after the introduction of a random variable which describes the axial stiffness of bars (Figure 4).

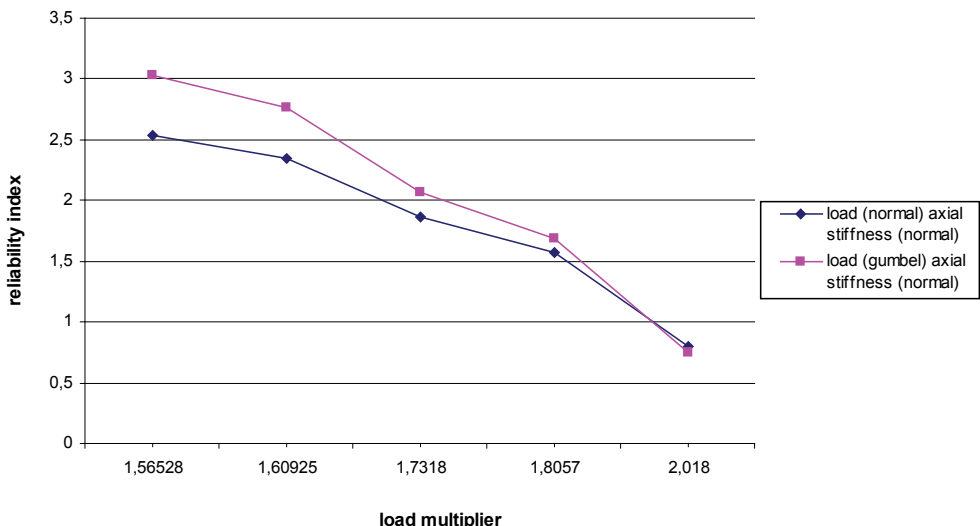


Fig. 4. The influence of the description axial stiffness “EA” on the value of reliability index (nonlinear geometrical solution)

For example: for the load multiplier equal to 1.8057, the values of reliability index for two selected distributions are as follows:

- load (normal (10 kN, 1 kN)), axial stiffness (normal (410000 kN, 41000 kN)) – 1.5763,
- load (gumbel (10 kN, 1 kN)), axial stiffness (normal (410000 kN, 41000 kN)) – 1.6917.

A similar effect can be observed during movement along the equilibrium path for a geometrically and physically nonlinear solution (Figure 5).

For example: for the load multiplier equal to 1.657, the values of reliability index for two selected distributions are as follows:

- load (normal (10 kN, 1 kN)), axial stiffness (normal (376380 kN, 37638 kN)) – 1.5746,
- load (gumbel (10 kN, 1 kN)), axial stiffness (normal (376380 kN, 37638 kN)) – 1.6895.

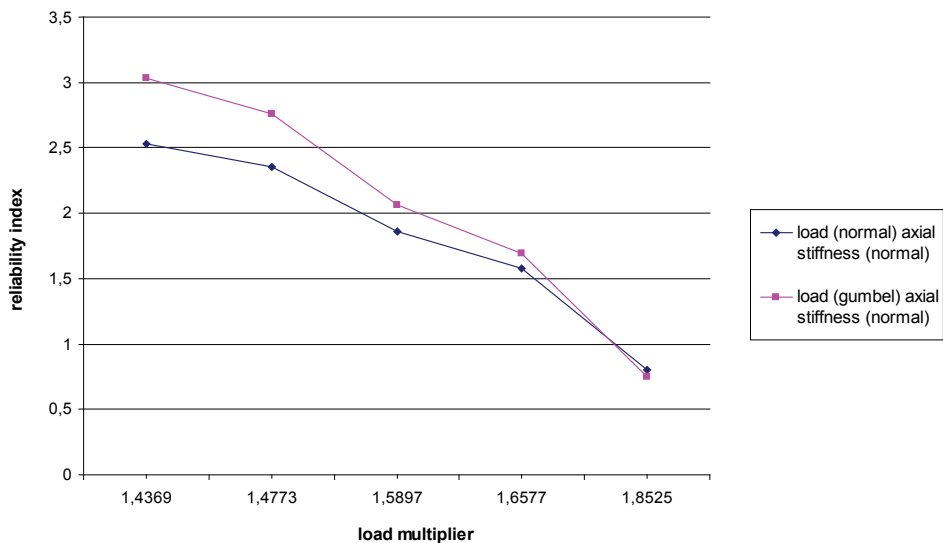


Fig. 5. The influence of the description axial stiffness “EA” on the value of reliability index (nonlinear geometrical and physical solution)

Case 3

- load “P” – random variable,
- axial stiffness “EA” – random variable,
- coordinate “Z” node 1 – random variable.
- Description of the random variables for three variants of standard deviation, i.e. (0.00006 m, 0.0006 m, 0.006 m) variable describes coordinate “Z” node 1 shows on Table 1, 5, 9.

The following step of analysis was the introduction of coordinate “Z” of node 1 as the third random variable. The influence of the standard deviation of the third random variable on the value of reliability index was examined. Tests were carried out for three values of standard deviation, i.e. 0.00006 m, 0.0006 m, 0.006 m, moving along the path for a geometrically non-linear solution. From the point of view of reliability analysis the acceptance of the imperfect bar model is manifested in the adoption of the form of limit function. If we take into account similar positions in percentages on the path in relation to the limit point, then diagrams are almost identical, which can be observed in Figures 4 and 5. Taking into account a physically non-linear bar model has a great significance for the definition of load limit value, which takes place in stability analysis.

Tables 2–3–4, 6–7–8, 10–11–12 present the change of the value of reliability index as well as the sensitivity of the index to subsequent random variables and distribution parameters of each of them. The sensitivity of reliability index is greatest for a random variable that describes the coordinate “Z” of node 1; however it is smallest for a random

variable that describes axial stiffness. This inference also concerns the distribution parameters of random variables. The example is completed with diagrams that describe the considered dependences (Figures 6–7).

In Figure 6 we can notice that for a very small standard deviation of the third random variable ($\sigma = 0.00006$ m, $\sigma = 0.0006$ m), solution tends to achieve the result obtained in Figure 4. Tests have clearly revealed how important is the correct description of the model of structure and load, and it is not only in the sphere of adopted types of probability distributions, but also in distribution parameters.

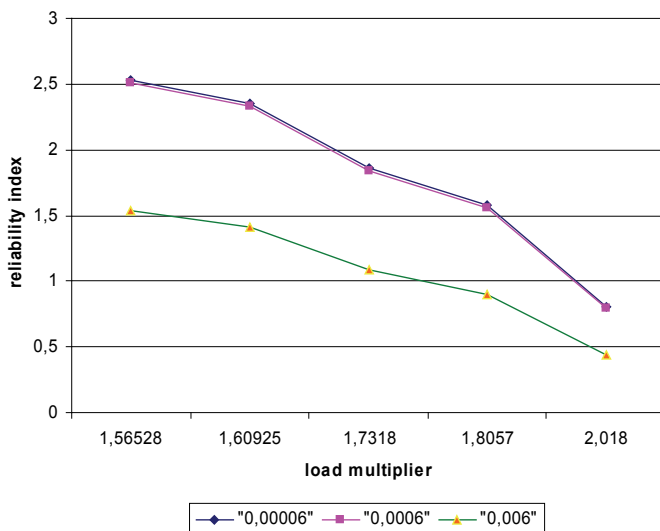


Fig. 6. The dependence of reliability index from the standard deviation of random variable that describes the coordinate “Z” of node “1”

Table 1. Description of the random variables

Random variable	Probability density function	Mean Value	Standard deviation	Coefficient of variation
load “P”	normal	10 kN	1 kN	10 %
axial stiffness “EA”	normal	410000 kN	41000 kN	10 %
coordinate “Z” node 1	normal	0.0675 m	0.006 m	8.9 %

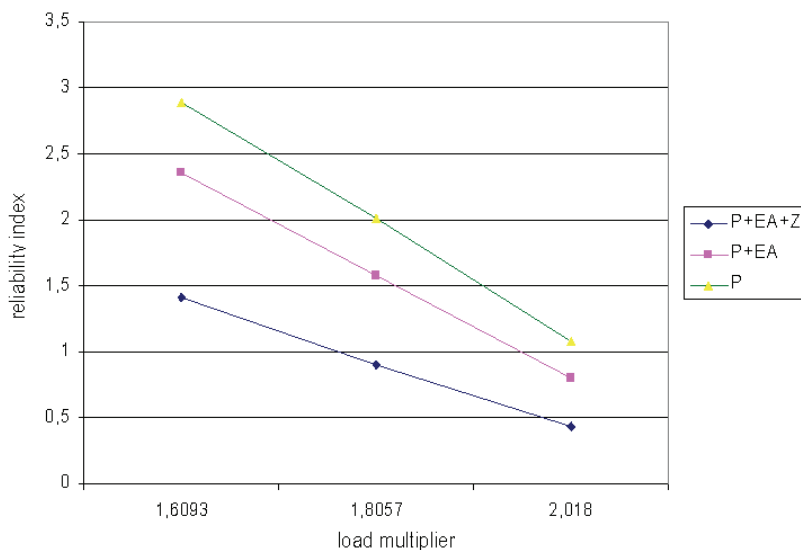
Table 2. Numerical results of the reliability index β and reliability index β sensitivity with respect of random variables

Load multiplier μ	Reliability index β	Reliability index β sensitivity with respect of random variable		
		EA	P	Z
2.01802	0.43624	9.32E-06	-3.95E-01	-1.39E+02
1.80572	0.90351	9.71E-06	-4.30E-01	-1.35E+02
1.73175	1.08639	9.82E-06	-4.43E-01	-1.34E+02
1.60925	1.41217	9.91E-06	-4.59E-01	-1.32E+02
1.56528	1.53751	9.94E-06	-4.66E-01	-1.31E+02

Table 3. Numerical results reliability index β sensitivity with respect of mean values

Load multiplier μ	Reliability index β sensitivity with respect of mean value		
	EA	P	Z
2.01802	-9.32E-06	3.95E-01	1.39E+02
1.80572	-9.71E-06	4.30E-01	1.35E+02
1.73175	-9.82E-06	4.43E-01	1.34E+02
1.60925	-9.91E-06	4.59E-01	1.32E+02
1.56528	-9.94E-06	4.66E-01	1.31E+02

In Figure 7 we can observe influence of the description of the computational model on the reliability index. The greatest values of reliability index are observed when only load **P** is a random variable. The introduction of two subsequent random variables (**EA** and **Z**) significantly decreases the reliability index.



Notation in Figure 7:

curve P: random variable “P” Normal (10.1) – normal probability density function; mean value = 10; standard deviation = 1, axial stiffness “EA” – deterministic variable ($EA = 410000$ kN), coordinate “Z” node 1 – deterministic variable ($Z = 0.0675$ m);

curve P+EA: random variable “P” Normal (10.1) – normal probability density function; mean value = 10; standard deviation = 1, axial stiffness “EA” – random variable Normal(410000 kN, 41000 kN), coordinate “Z” node 1 – deterministic variable ($Z = 0.0675$ m);

curve P+EA+Z: random variable “P” Normal (10.1) – normal probability density function; mean value = 10; standard deviation = 1, axial stiffness “EA” – random variable Normal (410000 kN, 41000 kN), coordinate “Z” node 1 – random variable Normal (0.0675 m, 0.006).

Fig. 7. The influence of the description of the computational model on the reliability index

Table 4. Numerical results reliability index β sensitivity with respect of standard deviations

Load multiplier μ	Reliability index β sensitivity with respect of standard deviation		
	EA	P	Z
2.01802	-1.55E-06	-6.82E-02	-5.07E+01
1.80572	-3.49E-06	-1.67E-01	-9.88E+01
1.73175	-4.29E-06	-2.13E-01	-1.16E+02
1.60925	-5.69E-06	-2.97E-01	-1.47E+02
1.56528	-6.23E-06	-3.34E-01	-1.58E+02

Table 5. Description of the random variables

Random variable	Probability density function	Mean value	Standard deviation	Coefficient of variation
load "P"	normal	10 kN	1 kN	10%
axial stiffness "EA"	normal	410000 kN	41000 kN	10%
coordinate "Z" node 1	normal	0.0675 m	0.00006 m	0.089%

Table 6. Numerical results of the reliability index β and reliability index β sensitivity with respect of random variables

Load multiplier μ	Reliability index β	Reliability index β sensitivity with respect of random variables		
		EA	P	Z
2.01802	0.804773	1.62E-05	-7.48E-01	-2.63E+02
1.80572	1.57616	1.52E-05	-7.83E-01	-2.45E+02
1.73175	1.86099	1.47E-05	-7.96E-01	-2.38E+02
1.60925	2.35099	1.41E-05	-8.17E-01	-2.28E+02
1.56528	2.53237	1.38E-05	-8.25E-01	-2.24E+02

Table 7. Numerical results reliability index β sensitivity with respect of mean values

Load multiplier μ	Reliability index β sensitivity with respect of mean value		
	EA	P	Z
2.01802	-1.62E-05	7.48E-01	2.63E+02
1.80572	-1.52E-05	7.83E-01	2.45E+02
1.73175	-1.47E-05	7.96E-01	2.38E+02
1.60925	-1.41E-05	8.17E-01	2.28E+02
1.56528	-1.38E-05	8.25E-01	2.24E+02

Table 8. Numerical results reliability index β sensitivity with respect of standard deviations

Load multiplier μ	Reliability index β sensitivity with respect of standard deviation		
	EA	P	Z
2.01802	-8.63E-06	-4.51E-01	-3.34E+00
1.80572	-1.48E-05	-9.67E-01	-5.66E+00
1.73175	-1.66E-05	-1.18E+00	-6.35E+00
1.60925	-1.91E-05	-1.57E+00	-7.31E+00
1.56528	-1.98E-05	-1.72E+00	-7.59E+00

Table 9. Description of the random variables

Random variable	Probability density function	Mean value	Standard deviation	Coefficient of variation
load "P"	normal	10 kN	1 kN	10 %
axial stiffness "EA"	normal	410000 kN	41000 kN	10 %
coordinate "Z" node 1	normal	0.0675 m	0.0006 m	0.89 %

Table 10. Numerical results of the reliability index β and reliability index β sensitivity with respect of random variables

Load multiplier μ	Reliability index β	Reliability index β sensitivity with respect of random variables		
		EA	P	Z
2.01802	0.795081	1.60E-05	-7.38E-01	-2.59E+02
1.80572	1.55976	1.50E-05	-7.74E-01	-2.42E+02
1.73175	1.84261	1.46E-05	-7.87E-01	-2.36E+02
1.60925	2.32984	1.40E-05	-8.08E-01	-2.25E+02
1.56528	2.5104	1.37E-05	-8.15E-01	-2.21E+02

Table 11. Numerical results reliability index β sensitivity with respect of mean values

Load multiplier μ	Reliability index β sensitivity with respect of mean value		
	EA	P	Z
2.01802	-1.60E-05	7.38E-01	2.59E+02
1.80572	-1.50E-05	7.74E-01	2.42E+02
1.73175	-1.46E-05	7.87E-01	2.36E+02
1.60925	-1.40E-05	8.08E-01	2.25E+02
1.56528	-1.37E-05	8.15E-01	2.21E+02

Table 12. Numerical results reliability index β sensitivity with respect of standard deviations

Load multiplier μ	Reliability index β sensitivity with respect of standard deviation		
	EA	P	Z
2.01802	-8.35E-06	-4.33E-01	-3.21E+01
1.80572	-1.45E-05	-9.33E-01	-5.47E+01
1.73175	-1.62E-05	-1.14E+00	-6.15E+01
1.60925	-1.87E-05	-1.52E+00	-7.09E+01
1.56528	-1.94E-05	-1.67E+00	-7.38E+01

4. Summary

The present work analyses truss structure subject to stability loss from the condition of node snapping. In the literature we can find many works dealing with this problem in the deterministic approach. It permits to define maximum load that accompanies snapping and the way of achieving this value, i.e. equilibrium path. In the deterministic approach load is described by the standard characteristic value and the safety factor. We are not interested in the possibility of the dispersion of load, which defines standard deviation and the way of the realization of load on the structure. This problem concerns other variables that describe the model of the structure, e.g. axial stiffness of bars or coordinate nodes of the structures. In the probabilistic approach we have a possibility of a more exact or more realistic description of the

influence of variables on the structure by providing the type of distribution and distribution parameters.

In the presented example we can clearly see differences in the values of Hasofer-Lind index depending on the assumed type of a random variable distribution. The value of the reliability index is also influenced by the description of the parameters of a random variable distribution, adoption of a spatial truss bar model as an element with imperfections (utilization of physically non-linear relationships), use of other random variables that characterize bar axial stiffness or coordinate nodes of the structures. The imperfect model of compressed bars strongly influences the shape of equilibrium paths, and what is more important, the value of limit load and the respective displacements of the structure.

It can be seen from the presented considerations that many factors have influence on structural safety evaluation. An essential problem in reliability analysis is therefore adoption of such a stochastic description of both the model of the structure and loads which is closest to the real state. Incomplete statistical data and wrong assumptions can lead to considerable differences in the values of reliability index.

5. Conclusions

On the basis of Tables 2–3–4, 6–7–8, 10–11–12 one can notice a visible difference in the evaluation of the reliability index sensitivity on the random variable that describes the coordinate **Z** node 1 in relation to the remaining random variables. Imperfections of the position of nodes play a very important role in the node snapping of truss structures both in probabilistic and deterministic analyses, which can be observed in many studies dealing with stability. Acquaintance reliability index sensitivity is essential in dealing with the problems of reliability optimization, and also for better understanding of the performance of a structure. If sensitivity of reliability index due to variable *X* is small in comparison with other variables, we can assume that the effect of this random variable on the value of failure probability is small and we can treat it in subsequent calculations as a deterministic parameter. This statement also concerns the parameters of the distribution of the random variable, such as mean value and standard deviation.

Figure 6 shows how big differences in structure safety evaluation can occur when the standard deviation of variable random responsible for imperfection of the node position is incorrectly evaluated. We can notice that for a very small standard deviation of the random variable **Z** ($\sigma = 0.00006$ m, $\sigma = 0.0006$ m), solution tends achieve the result obtained in Figure 4. Random variable that describes the coordinate **Z** node 1 for standard deviation $\sigma = 0.00006$ m, $\sigma = 0.0006$ m we can treat as deterministic parameter.

Figure 7 shows how the values of reliability index for different descriptions of the problem computational model change. The greatest values of reliability index are observed when only load is a random variable. The remaining parameters of the problem are treated as deterministic variables. The introduction of two subsequent random variables (**EA** and

Z) significantly decreases the reliability index. Accounting for a larger number of random variables extends the computation time, yet such a manner of formulating the problem makes it possible to give a more accurate evaluation of a structure safety.

References

- [1] Arora J.S.: *Introduction to optimum design*, McGraw-Hill, 1989.
- [2] Hasofer A.M., Lind N.C.: *Exact and invariant second moment code format*, Journal of the Engineering Mechanics Division, ASCE, Vol. 100, 1974, pp. 111–121.
- [3] Hisada T., Nakagiri S.: *Stochastic finite element developed for structural safety and reliability*, Proc. of the 4th International Conference on Structural Safety and Reliability, 1981, pp. 395–408.
- [4] Hisada T., Nakagiri S.: *Role of the stochastic finite element method in structural safety and reliability*, Proc. of the 5th International Conference on Structural Safety and Reliability, 1985, pp. 385–394.
- [5] Hohenbichler M., Rackwitz R.: *Non-normal dependent vectors in structural safety*, Journal of the Engineering Mechanics Division, ASCE, Vol. 107, 1981, pp. 1227–1238.
- [6] Kleiber M., Hien T.D.: *The stochastic finite element method: Basic perturbation technique and computer implementation*, J. Wiley&Sons, 1992.
- [7] Kowal Z., Sendkowski J., Rabenda-Radoń U.: *Equilibrium paths of the space structures taking into account the real work of their elements*, 10th Polish Conference of Computer Methods in Mechanics Świnoujście, Poland, 1991, pp. 381–388.
- [8] Kowal Z., Radoń U.: *Propozycja modelu konstytutywnego prętów ścisanych do obliczania nośności granicznej rzeczywistych konstrukcji prętowych*, Inżynieria i Budownictwo 12, 1995, pp. 679–683.
- [9] Liu P.L., Der Kiureghian A.: *Multivariate distributions models with prescribed marginals and covariances*, Probabilistics Engineering Mechanics, Vol. 1, No. 2, 1986, pp. 105–112.
- [10] Liu P.L., Der Kiureghian A.: *Finite element reliability methods for geometrically nonlinear stochastic structures*, Report No. UCB/SEMM-89/05, Department of Civil & Environmental Engineering, University of California, Berkeley, CA, 1989.
- [11] Liu W.K., Mani A., Belytschko T.: *Random field elements*, International Journal of Numerical Methods in Engineering, Vol. 23, 1986, pp. 1831–1845.
- [12] Liu W.K., Mani A., Belytschko T.: *Finite elements methods in probabilistic mechanics*, Probabilistics Engineering Mechanics, Vol. 2, No. 4, 1987, pp. 201–213.
- [13] Rackwitz R., Fiessler B.: *Structural reliability under combined random load sequences*, Computers & Structures, Vol. 9, No. 5, 1978, pp. 489–494.
- [14] Rosenblatt M.: *Remarks on a multivariate transformation*, The Annals of Mathematical Statistic, Vol. 23, No. 3, 1952, pp. 470–472.
- [15] Schittkowski K.: *The nonlinear programming method of Wilson, Han and Powell with an augmented Lagrangian type line search function*, Part 1: Convergence analysis, Numerische Mathematik, Vol. 38, No. 1, 1982, pp. 83–114.
- [16] Schittkowski K., Zillober C., Zotmantel R.: *Numerical comparison of nonlinear programming algorithms for structural optimization*, Structural and Multidisciplinary Optimization, Vol. 7, No. 1–2, 1994, pp. 1–19.

- [17] Sendkowski J.: *Trwała nośność graniczna ustrojów kratowych*, praca doktorska, Politechnika Warszawska, Warszawa, 1989.
- [18] Shinozuka M.: *Basic issues in stochastic finite element analysis*, Proc. 5th International Conference on Applications of Statistics and Probability, Vol. 1, 1987, pp. 507–520.
- [19] Stocki R.: *Reliability-based optimization of geometrically nonlinear truss structures – theory and computer program* (in Polish), Ph.D. Thesis, Institute of Fundamental Technological Research, Polish Academy of Sciences, IFTR Reports, 13/99.
- [20] Stocki R., Kolanek K., Knabel J., Tauzowski P.: FE based structural reliability analysis using STAND environment, Computer Assisted Mechanics and Engineering Sciences, Vol. 16, 2009, pp. 35–58.
- [21] Śniady P.: *Podstawy stochastycznej dynamiki konstrukcji*, Oficyna Wydawnicza Politechniki Wrocławskiej, Wrocław, 2000.

Probabilistyczna nieliniowa analiza konstrukcji kratowej

W niniejszej pracy rozważane są zagadnienia stateczności i niezawodności konstrukcji kratowej podatnej na utratę stateczności z warunku przeskoku węzła. Do określenia ścieżki równowagi konstrukcji wykorzystano metodę skalarnego parametru sztywności oraz metodę stałej długości łuku. W pracy jako zmienne losowe przyjęto obciążenie konstrukcji, sztywność osiową prętów, współrzędne węzłów. Rozkłady prawdopodobieństwa zmiennych losowych przyjmowane są spośród kilku, najczęściej stosowanych w praktyce. Rozpatrywany jest warunek nieprzekroczenia dopuszczalnego mnoźnika obciążenia. W analizie niezawodności wykorzystano, jako miarę niezawodności wskaźnik Hasofera–Linda. Dokładność wyników otrzymywanych przy użyciu wskaźnika Hasofera–Linda jest wystarczająca dla potrzeb praktycznych i dlatego też zyskał on dużą popularność jako miara niezawodności, szczególnie w połączeniu z metodami transformacji wykorzystującymi pełną informację o rozkładach zmiennych losowych. Obliczenia probabilistyczne przeprowadzono stosując metodę FORM. Do obliczeń wykorzystano program do analizy niezawodności STAND zbudowany w IPPT PAN. Na podstawie przedstawionych wykresów i tabel możemy zauważać, jak istotnym zagadnieniem w analizie niezawodności jest przyjęcie prawidłowego opisu stochastycznego. Niekompletne dane statystyczne oraz niewłaściwie przyjęte założenia dotyczące rozkładów prawdopodobieństwa oraz parametrów mogą prowadzić do poważnych różnic w ocenie bezpieczeństwa konstrukcji.



Modelling of laser welding process in the phase of keyhole formation

J. RONDA, A. SIWEK

AGH University of Science and Technology, Department of Applied Computer Science and Modelling,
al. Mickiewicza 30, 30-059 Kraków, Poland.

The interaction of keyhole and the welding pool during laser welding is investigated by using a numerical simulation. The shape of keyhole is related to a surface tension and a recoil force. The numerical model is developed on the basis of the program Fluent which is the computational fluid dynamics (CFD) software. Calculations were performed by using parallel processing software and facilities.

Keywords: *CFD, keyhole, laser welding, recoil force, vapour, welding pool*

1. Introduction

Laser welding improved within many years is now generally used in industry. It enables joining of metallic and nonmetallic materials that require either shallow or deep weld penetration. This method, of welding owing to numerous advantages become leading joining technique developed and improved in many research units e.g. [2–7]. Research investigations concerned also modelling of keyhole formation. In many cases, proposed models lead to acceleration of numerical calculations. Simplifications are related mostly to material characteristics, heat exchange processes, laser beam interaction with a substrate, evolution of material composition during welding etc. Laser welding provides high speed of welding with small energy consumption, good accuracy, deep fusion, and small thermal dilatation of a weld joint. High energy concentration can also produce many defects of a weld joint because of high intensity of evaporation and dynamical loss of mass, e.g. porosity, susceptibility to cracking etc. Attempts of phenomenological modelling of the welding pool and evaluation of the weld quality in relation to weld parameters have practical significance. Laser welding models are based on the set of equations: balance of mass, momentum and energy, in welding pool and the heat affected zone (HAZ). System of these equations with appropriate initial and boundary conditions are usually solved by numerical procedures developed especially for parallel processing and multiprocessor computers.

During laser remelting, on a workpiece surface several phenomena proceed. One of them is the beam absorption connected with two mechanisms: Fresnel absorption and inverse Bremsstrahlung. Energy of laser beam is dissipated [8–9] because of multiple

reflections of light, radiation, convection, vaporization, and energy absorption by plasma created in keyhole. A fraction of energy absorbed by a surface is related to radiation intensity, radiation length, shape and porosity of a material surface, and presence of plasma above a surface [12]. The welding pool is created in zone where a laser beam is obliquely incident on the top face of a material. A shape, depth of the welding pool and chemical composition of material inside the pool is related to laser welding parameters. For small power density, energy from the surface of a joint is transferred inside material by conduction and convection generated by the Marangoni force [13]. Oppositely directed fluxes of liquid metal arise on the liquid surface as a result of temperature gradients on a surface and presence of surface active elements that alter the sign of surface tension coefficient [11, 14].

In the case of beams with high power density, the recoil force of vaporized metal is operating on a free surface of liquid and generates a motion of liquid in the welding pool [10, 1]. In early models of laser welding it was assumed that keyhole in the state of equilibrium travels along a weld joint. This approach did not take into account a motion of liquid metal inside keyhole and its hydrodynamic instability. Such simplification decides about limited applicability of the model and obviously decreases accuracy of evaluations. The main objective of our simulation is prediction of welding pool shape during heating and cooling period, this enables validation of welding parameters and also analysis of welding defect reasons. A location of a surface of the welding pool is known only in the initial moment and its relocation can be determined by numerical methods. The correctness of evaluation of the actual position depends on the quality of evaluation of all portions of energy transferred from the laser beam to the pool.

The major objective of this paper is to develop a two-dimensional model of keyhole of laser welding. The model can help in analysis of stages of keyhole formation and their dependence on the following process parameters: welding speed, surface tension, recoil force, chemical composition of welded steel.

Numerical calculations were accelerated significantly by applying procedures for parallel processing and multi-processor computers.

Obtained numerical results show that the convection heat transfer has some impact on shape of the welding pool.

2. Physical description of keyhole formation

Laser beam energy concentrated on a surface is transported inside welding joint by conduction and convection. The surface illuminated by the laser beam becomes heated and then evaporates. The latent heat of evaporation, which is ten times more than the heat of melting, changes the energy balance in the welding region. Therefore, vaporization that has large fraction in energy balance, influences on the mechanism of energy transmission, dynamics of welding region and chemical composition of fusion weld. Modelling of laser welding with deep fusion penetration requires evaluation of the recoil pressure produced by evaporation.

Problem of description of welding pool transformation belongs to the class of problems with free surface. The surface of welding pool is determined by several measures: the buoyant force, the tangent stress produced by a gradient of surface tension, and the recoil force of evaporated metal, among other things. The buoyant force is produced by variation of metal density in the welding pool where large temperature gradient is observed. The Marangoni force (or the Gibbs–Marangoni effect) is produced by variation of surface tension gradient on a surface of the welding pool [13] that facilitates the mass transfer along an interface between two fluids of different temperature.

Energy transport during laser welding can proceed in two various modes: either the conduction mode or the keyhole mode dependently on density of laser beam power and rate of its displacement. In the case of small power density, the energy transport in the region of beam activity proceeds in the mode of conduction. In the case of higher power density, when keyhole is created, the energy transfer mode involves a higher energy density. In the conduction mode, the majority of energy is transferred through conduction via solid material. Vaporization plays the secondary role in this case when the power density is less than $\sim 10^{10}$ W/m². For higher power densities, material evaporate from the region of beam lightening that leads to creation of deep and narrow keyhole.

These two modes of energy transfer during laser welding provide some flexibility to this technique. Working with conductive mode allows the beam to create shallow penetration of a joint. On the contrary, welding with keyhole enables welding with deep penetration. Creation of keyhole improves efficiency of welding process because of intense mixing of melted material and multiple reflection of the beam on channel walls.

3. Mathematical model of laser welding

The mathematical problem of laser welding is considered as three-phase moving boundary problem with two moving interfaces [1] consists of two fundamental problems: solid to liquid transition, and liquid to vapour transition. It is formulated as a system of differential equations expressing the balance of mass, momentum, and internal energy associated with an appropriate set of initial and boundary conditions. The problem can be split into three parts: heat propagation problem from the laser beam to welded joint, and tracing of solid-liquid interface in HAZ, and tracing liquid-vapour interface in the keyhole. One of the first models of laser welding has been proposed in [9]. Recently, more sophisticated model has been proposed by Salonitis et al. [8]. In this paper, the mathematical formulation of heat propagation problem in HAZ is following the paper by Han et al. [3]. Tracing of liquid-vapour free surface follows papers by Jalali et al. [5] and Černy et al. [1].

The Navier–Stokes equations are solved both in liquid and vapour regions of HAZ and the keyhole. As it was mentioned before, the set of body forces are enriched by considering surface tension and thermocapillary force. The recoil pressure is also taken into consideration in evaluation of moving free surfaces.

3.1. Balance equations in solid and liquid part of HAZ

Position of the free solid \Rightarrow liquid interface is evaluated on the basis of enthalpy balance.

The set of governing equations consists of the set of equations controlling conservation of mass, momentum and internal energy. Mass conservation is expressed as follows:

$$\frac{\partial \rho}{\partial t} + \nabla \cdot (\rho \mathbf{V}) = 0, \quad (1)$$

where mass density ρ and velocity $\mathbf{V} = \{v_1, v_2, v_3\}^T$ are taken in Eulerian coordinate system as averaged quantities evaluated by formulas

$$\rho = \varrho_s \rho_s + \varrho_l \rho_l, \quad (2)$$

$$\mathbf{V} = f_s \mathbf{V}_s + f_l \mathbf{V}_l, \quad (3)$$

with $f_s + f_l = (1/\rho)(\varrho_s \rho_s + \varrho_l \rho_l) = 1$ referred to solid and liquid mass fractions and $\varrho_s + \varrho_l = 1$ applied correspondingly to volume fractions.

The momentum conservation is written as follows:

$$\rho \left(\frac{\partial \mathbf{V}}{\partial t} + \mathbf{V} \cdot \nabla \mathbf{V} \right) = -\nabla p + \mu \nabla^2 \mathbf{V} + \rho \mathbf{g} + \mathbf{S}, \quad (4)$$

where:

\mathbf{S} – the contribution related to surface tension, thermo-capillary force,

K – permeability of the two-phase mushy zone

\mathbf{g} – standard gravity.

The law of conservation of energy may be stated as

$$\frac{\partial(\rho h)}{\partial t} + \nabla \cdot (\rho h \mathbf{V}) = \nabla \cdot \left(\frac{k}{c_s} \nabla h \right) - \nabla \cdot \left(\frac{k}{c_s} \nabla (h_s - h) \right) - \nabla \cdot (\rho (h_l - h) (\mathbf{V} - \mathbf{V}_s)), \quad (5)$$

where specific heat, thermal conductivity and enthalpy are written as

$$c = f_s c_s + f_l c_l; \quad k = \varrho_s k_s + \varrho_l k_l; \quad h = f_s h_s + f_l h_l. \quad (6)$$

3.1.1. Solid-liquid interface tracking

The interface solid-liquid is evaluated by enthalpy-porosity technique following papers by Jalali et al. [5] and Černý et al. [1] based on the concept of enthalpy control.

The enthalpy is calculated as the sum of the energy h exchanged by a thermodynamic system that has a change of temperature as its sole effect, called also the sensible heat, and the latent heat ΔH . That is expressed by the formula

$$H = h + \Delta H. \quad (7)$$

The sensible heat is defined by

$$h = h_{\text{ref}} + \int_{T_{\text{ref}}}^T c_p dT, \quad (8)$$

where:

c_p – the specific heat at constant pressure,

h_{ref} – a reference enthalpy,

T_{ref} – the reference temperature. The liquid fraction is evaluated relatively to the temperature of mushy zone T from the following formula

$$f_l = \begin{cases} 0, & T < T_s \\ \frac{T - T_s}{T_l - T_s}, & T_s \leq T \leq T_l, \\ 1, & T > T_l \end{cases} \quad (9)$$

where T_s and T_l stand appropriately for the solidus and liquidus limits. The latent heat can be evaluated by

$$\Delta H = \begin{cases} 0 & \text{for solid,} \\ f_l \lambda & \text{for liquid,} \end{cases} \quad (10)$$

where λ is the latent heat for liquid metal.

The energy conservation equation for the melting/solidification process

$$\frac{\partial}{\partial t} (\rho h + \rho f_l \lambda) + \nabla \cdot (\rho \mathbf{V} h) = \nabla \cdot (K \nabla T), \quad (11)$$

is used to evaluate temperature T by iterating between Equations (11) with a correction of f_l calculated from (9).

3.2. Liquid-vapour interface tracking technique

Majority papers on free surface tracking quote the papers by Nichols et al. [7] and Hirt et al. [4], where the tracking algorithm is based on the concept of a fractional vol-

ume of fluid (VOF) and/or the paper by Unverdi et al. [10], based on the concept of the front-tracking method, and also papers devoted to both concepts published later. The simulation of vaporization in the keyhole during laser welding is carried by applying VOF method implemented in the commercial CFD code FLUENT 12.1. The VOF method is used for tracking the interface between the liquid and vapour phases of metal [6]. The balance equations, governing the process, are solved considering phase volume fractions f_k in each cell. The summation of phase fractions results in unity

$$\sum_{k=1}^n f_k = 1. \quad (12)$$

A particular cell represents the vapour when $f_v = 1.0$ and is filled up by liquid metal for $f_v = 0.0$ but for $0 < f_k < 1$ it represents the intermediate region, where the free surface is searched. The volume fraction is used as a weight for evaluation of each two-phase body material property, e.g. density and viscosity. For example, the density of each two-phase cell is evaluated according to the formula

$$\rho = f_v \rho_v + (1 - f_v) \rho_l, \quad (13)$$

where:

f_v, ρ_v – stand for the volume fraction and density related to the vapour,
 ρ_l – refers to the liquid metal. The phase evolution equation has the following form

$$\frac{\partial f_k}{\partial t} + \mathbf{v} \nabla f_k = \frac{S_{fk}}{\rho_k}, \quad (14)$$

where:

S_{fk} – the mass source,

\mathbf{v} – mass-averaged velocity expressed as follows

$$|\mathbf{v}| = \frac{f_l \rho_l |\mathbf{v}_l| + f_v \rho_v |\mathbf{v}_v|}{\rho_v}. \quad (15)$$

Following this, the momentum equation can be written and solved in the form

$$\rho \left(\frac{\partial \mathbf{v}}{\partial t} + \mathbf{v} \cdot \nabla \mathbf{v} \right) = -\nabla p + \mu \nabla^2 \mathbf{v} + \rho \mathbf{g} + \mathbf{S}, \quad (16)$$

where \mathbf{S} means the volumetric forces produced by the surface tension at the liquid/vapour interface. The convection term ($\mathbf{v} \cdot \nabla \mathbf{v}$) can be expressed without a tensor derivative

$$\mathbf{v} \cdot \nabla \mathbf{v} = \nabla \left(\frac{\|\mathbf{v}\|^2}{2} \right) + (\nabla \times \mathbf{v}) \times \mathbf{v}, \quad (17)$$

The energy equation for two phase fluid has the following form

$$\rho \frac{\partial E}{\partial t} + \nabla \cdot \mathbf{v} \rho E = \nabla \cdot (K \nabla T) + S_{\text{heat}}, \quad (18)$$

where:

E is the mass averaged internal energy per unit mass

$$E = \frac{\sum_{k=1}^n f_k \rho_k E_k}{\sum_{k=1}^n f_k \rho_k}, \quad (19)$$

K – the coefficient of thermal conductivity,

S_{heat} – the volumetric heat source term.

3.3. Boundary conditions

Firstly, we are going to set boundary conditions on the top of the substrate, i.e. on the free surface of melt (or weld) pool. At the end of this subsection, boundary conditions for the bottom and side surfaces of weld pool are proposed.

Energy balance on free surface

$$k \frac{\partial T}{\partial \mathbf{n}} = q_{\text{laser}} - q_{\text{rad}} - q_{\text{conv}} - q_{\text{evap}}, \quad (20)$$

where q_{laser} is the energy supplied by laser beam and defined by

$$q_{\text{laser}}(x_1, x_2) = \eta I(x_1, x_2), \quad (21)$$

where $I(x_1, x_2)$ is the intensity of laser beam at the fluid location (x_1, x_2) . The intensity of laser beam for the laser mode TEM_{10} is expressed by the formula

$$I(x_1, x_2) = \frac{2P}{\pi a^4} [a^2 - 2(x_1^2 + x_2^2)] \exp \left[-\frac{2(x_1^2 + x_2^2)}{a^2} \right], \quad (22)$$

where:

P – laser power,

a – the characteristic radius of laser beam.

Other terms of Equation (20), refer to heat losses due to convection, radiation and evaporation phenomena and can be expressed by formulas:

$$q_{\text{conv}} = h_c (T - T_\infty), \quad (23)$$

$$q_{\text{rad}} = \varepsilon \sigma (T^4 - T_\infty^4), \quad (24)$$

$$q_{\text{evap}} = \rho V_{dv} h_v \quad (25)$$

where:

T – temperature of surface

T_∞ – ambient temperature,

h_c – the convection coefficient,

ε – radiation emissivity of surface,

σ – the Stefan-Boltzmann constant,

V_{dv} – the free surface moving speed induced by evaporation,

the term ρV_{dv} means the speed of vaporisation,

h_v – latent heat of evaporation.

The speed of vaporization, following [11], for steel is given by

$$\log(\rho V_{dv}) = A_v + \log(p_{\text{atm}}) - \frac{1}{2} \log(T), \quad (26)$$

where:

the pressure of steel vapour is evaluated as $\log(p_{\text{atm}}) = 6.121 - \frac{18836}{T}$,

A_v – the vapour constant.

3.3.1. Momentum balance on keyhole free surface

The cell situated on the free surface is subjected to shear and normal stress boundary conditions. Therefore, two balance requirements must be fulfilled in such cell: the shear stress balance

$$\mu \left(\frac{\partial V_s}{\partial n} + \frac{\partial V_n}{\partial s} \right) = \frac{\partial \gamma}{\partial T} \cdot \frac{\partial T}{\partial s}, \quad (27)$$

and the normal stress balance

$$p = p_\sigma + p_v, \quad (28)$$

where γ represents the surface tension coefficient expressed by

$$\gamma = 1.943 - 4.3 \times 10^{-4} (T - 1620) + \\ - 1.3RT \times 10^{-8} \ln \left(1 + 0.00318 f_{sulf} \exp \left(\frac{1.66 \times 10^8}{RT} \right) \right) \quad (29)$$

where:

f_{sulf} = 120 ppm – the sulphur fraction in steel,

V_s, V_n – tangential and normal components of velocity at the free surface,

p_σ – the surface tension,

p_v – the evaporation recoil pressure.

These two balance equations are coupled by

$$\gamma = \frac{p_\sigma}{\kappa}, \quad (30)$$

where κ is the free surface curvature evaluated from the free surface $\Phi(\mathbf{X}, t)$ by the formula

$$\kappa = -\nabla \cdot \frac{\mathbf{n}}{|\mathbf{n}|}, \quad (31)$$

with \mathbf{n} calculated from

$$\mathbf{n} = \frac{\nabla \Phi}{|\nabla \Phi|} \Big|_{\Phi=0}. \quad (32)$$

The normal direction can be alternatively evaluated

$$\mathbf{n} = \nabla f_k, \quad (33)$$

where f_k is evaluated from Equation (14).

The equilibrium pressure of iron vapour calculated following the formula

$$\log(p_{Fe}^0 \times 760) = 11.5549 - \frac{1.9538 \times 10^4}{T} - 6.2549 \times 10^{-1} \log(T) + \\ - 2.7182 \times 10^{-9} T + 1.9086 \times 10^{-13} T^2, \quad (34)$$

is used to evaluate the vaporization rate of alloying component $i = Fe$

$$|\mathbf{J}_{Fe}| = M_{Fe}^{\frac{1}{2}} p_{Fe} (2\pi RT)^{\frac{1}{2}}, \quad (35)$$

where M_{Fe} is the component Fe atomic mass. The vaporization rate and the mass source term from Equation (14) are related by

$$\mathbf{J} = \frac{d\mathbf{S}}{dn}. \quad (36)$$

The volumetric forces from Equation (16) can be expressed in the form

$$\mathbf{S} = \mathbf{S}_\kappa + \mathbf{S}_{rec} + \mathbf{S}_{Mar}, \quad (37)$$

where \mathbf{S}_κ is the force calculated from the formula written following [2] (Section: Theory Guide, 16.3.8)

$$\mathbf{S}_\kappa = \frac{2\gamma}{(\varrho_v + \varrho_l)} \rho \kappa \nabla f_k, \quad (38)$$

the recoil force is given in the vapour cell by

$$\mathbf{S}_{rec} = p_v \nabla \Phi, \quad (39)$$

and the Marangoni's force is defined by

$$\mathbf{S}_{Mar} = \tau |\nabla \Phi| ds \quad (40)$$

where τ is given by

$$\tau = \frac{d\gamma}{ds} \equiv \frac{\partial \gamma}{\partial T} \cdot \frac{\partial T}{\partial s} \quad (41)$$

where $ds = |ds|$.

4. Results

The development of the keyhole during laser welding is shown in Figure 1 for the laser beam moving along the groove from the right to the left. It can be noted, that the keyhole depth gradually advances when temperature of a weld joint increases. The contour lines for gas velocity and vectors of gas stream against a background of the keyhole profile can be seen in Figure 2.

Results are obtained by using the commercial programme FLUENT for material and process parameters shown in Table 1.

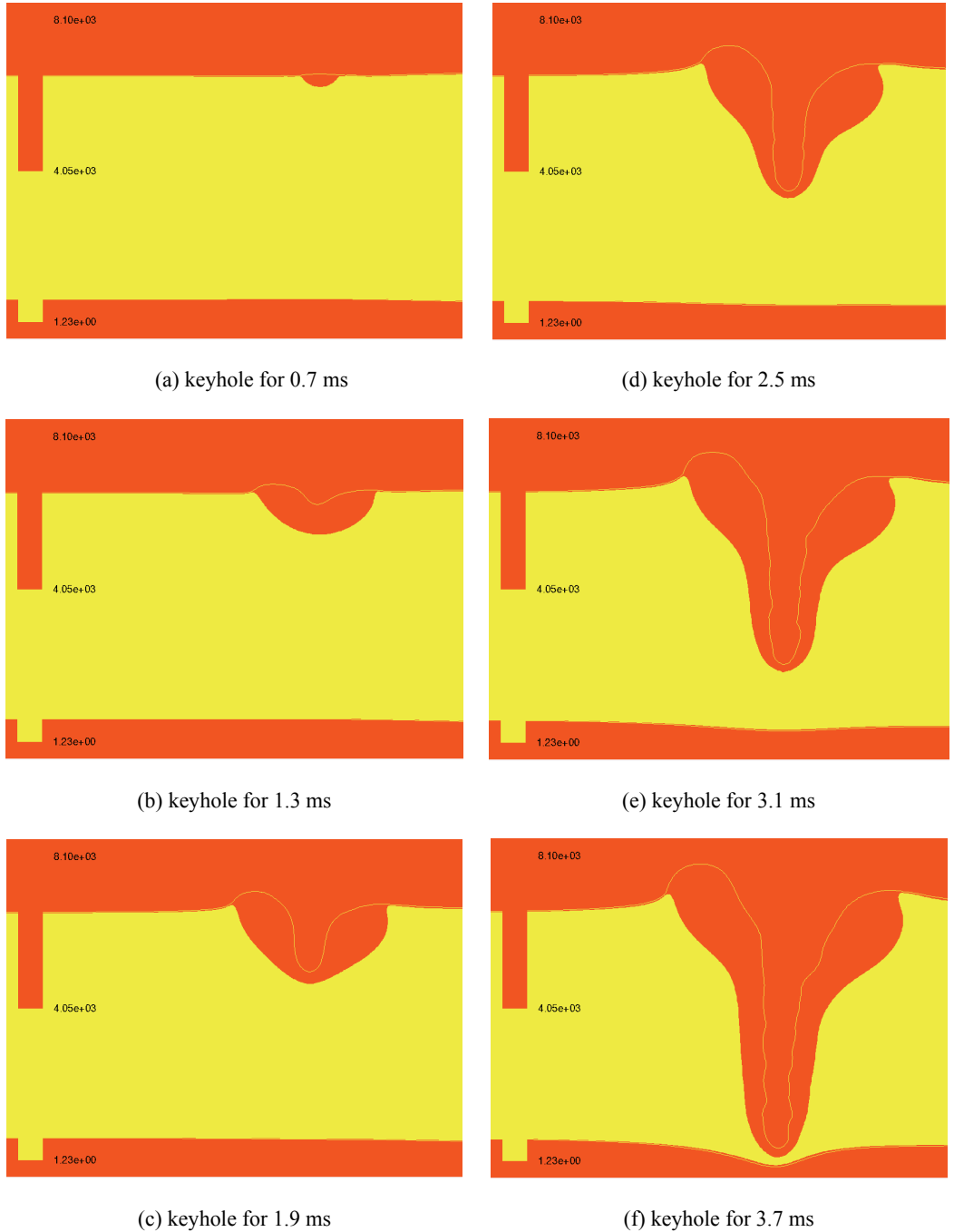


Fig. 1. Development of keyhole during laser welding for time from 0.7 to 3.7 ms

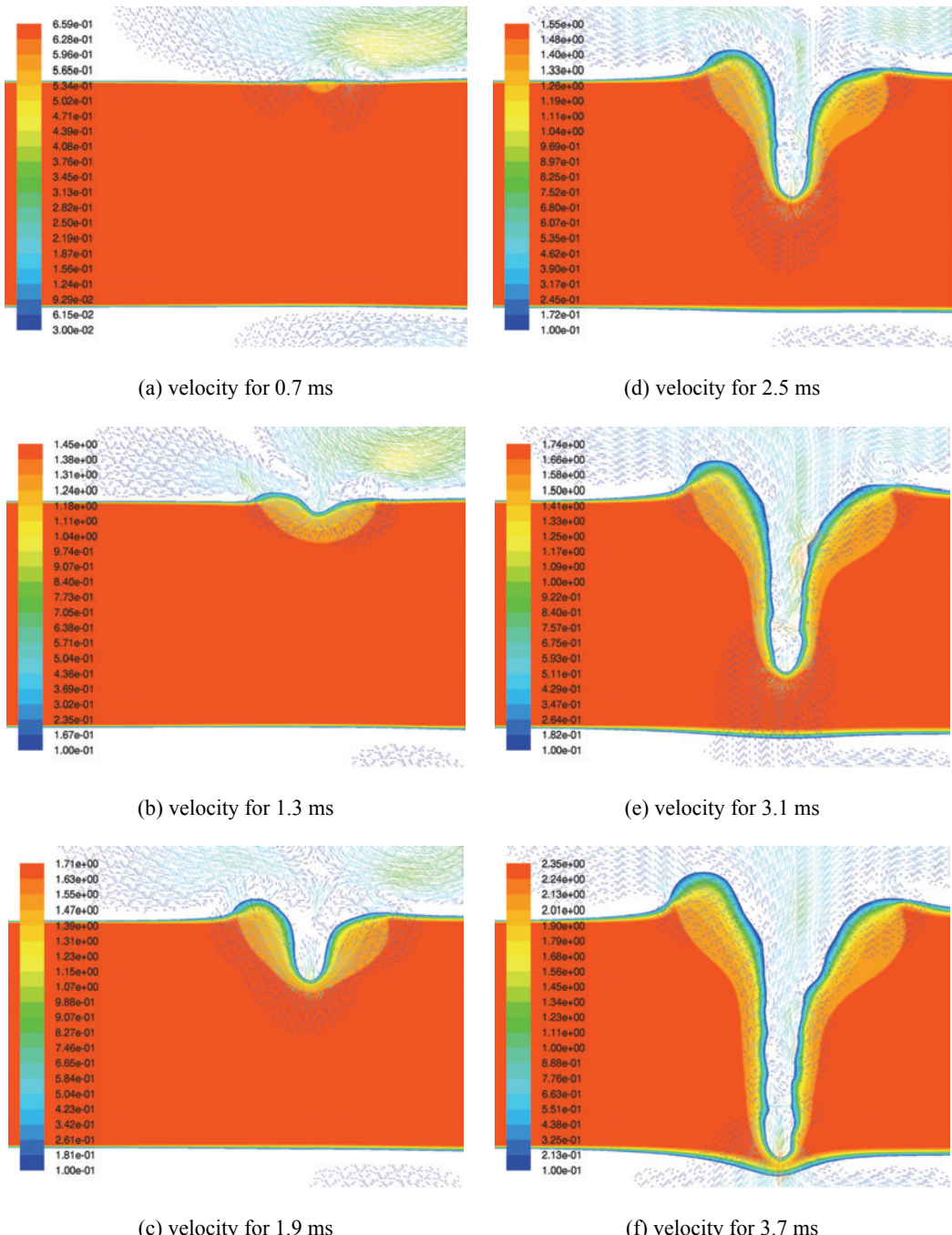


Fig. 2. Vapour velocity in a vicinity of the keyhole during laser welding for time from 0.7 to 3.7 ms

Table 1

Property	Symbol	Value
Absorption coefficient	α	0.13
Emissivity	ε	0.40
Heat of fusion	L_m	2.6×10^5 [J/kg]
Temperature – solidus	T_s	1620 K
Temperature – liquidus	T_l	1740 K
Density of liquid steel	ρ	7300 [kg/m ³]
Heat capacity of solid steel	c_{ps}	411 [J/kg · K]
Heat capacity of liquid steel	c_{pl}	612 [J/kg · K]
Coefficient of heat conductivity for solid steel	λ_s	19 [W/m · K]
Coefficient of heat conductivity for liquid steel	λ_l	70 [W/m · K]
Thermal coefficient of surface tension	A^0	-0.43×10^{-3} [N/m · K]
Coefficient of surface tension	γ_m^0	1.943 [N/m]

5. Conclusions

The model of keyhole formation takes into consideration the temperature dependence of material parameters and characteristics of a laser beam. This model takes into account the influence of the sulphur content on surface tension.

A shape and the depth of melted zone in the laser welding depends on the surface tension, the sulphur content, and a surface temperature of the molten pool when the power and welding velocity ensure the laser conduction welding mode. An influence of the sulphur content on obtained results, when the keyhole is formed, is small. A liquid metal flow on the liquid/gas border is mainly produced by the wall friction in the keyhole.

The quality of numerical results depends mainly on the identification of thermal characteristics of welded material and welding conditions in a work-stand. The applied welding model seems to be applicable to a large group of welded materials and numerous varieties of work-stands.

Acknowledgements

The Authors would like to thank sponsors: The Ministry of Scientific Research and Information Technology for the grant: MNiSW/IBM_BC_HS21/AGH/101/2007 open in the Academic Computer Centre CYFRONET AGH for the IBM cluster: Blade Center HS21.

References

- [1] Chen X., Wang H.X.: *A calculation model for the evaporation recoil pressure in laser material processing*, Journal of Physics D: Applied Physics, Vol. 34, 2001, pp. 2637–2642.

- [2] Černy R., Cháb V., Přikryl P.: *A two-phase moving boundary problem with two moving interfaces in laser processing of materials*, Computational Materials Science, Vol. 8, 1997, pp. 228–242.
- [3] FLUENT 12.1 documentation.
- [4] Han L., Liou F.W.: *Numerical investigation of the influence of laser beam mode on melt pool*, International Journal of Heat and Mass Transfer, Vol. 47, 2004, pp. 4385–4402.
- [5] Hirt C.W., Nichols B.D.: *Volume of fluid (VOF) method for the dynamics of free boundaries*, J. Comp. Phys., Vol. 39, 1982, pp. 201–225.
- [6] Jalali A., Najafi A.F.: *Numerical modeling of the solidification phase change in a pipe and evaluation of the effect of boundary conditions*, Journal of Thermal Science, Vol. 19, No. 5, 2010, pp. 419–424.
- [7] Jeong S-S., Kim S-J., Park G-Ch.: *CFD simulation of codensing vapour bubble using VOF model*, World Academy of Science, Engineering and Technology, Vol. 60, 2009, pp. 209–215.
- [8] Nichols B.D., Hirt C.W., Hotchkiss R.S.: *SOLA-VOS: A solution algorithm for transient fluid flow with multiple free boundaries*, Los Alamos Scientific laboratory, Report LA-8355, August 1980.
- [9] Salonitis K., Drougas D., Chryssolouris G.: *Finite element modeling of penetration laser welding of sandwich materials*, Physics Procedia, Vol. 5, 2010, pp. 327–335.
- [10] Semak V., Matsunawa A.: *The role of recoil pressure in energy balance during laser materials processing*, Journal of Physics D: Applied Physics, Vol. 30, 1997, pp. 2541–2552.
- [11] Siwek A., Didenko T.: *Influence of laser processing on shape of melted zone and character of thermal cycles in steel*, Hutnik, Vol. 71, No. 12, 2004, pp. 583–589.
- [12] Swift-Hook D.T., Gick A.E.F.: *Penetration welding with lasers*, Welding Journal, Vol. 52, No. 11, 1973, pp. 492–499.
- [13] Unverdi S.O., Tryggvason G.: *A front-tracking method for viscous incompressible multifluid flows*, J. Comp. Phys., Vol. 100, No. 25, 1992, pp. 25–37.
- [14] Zacharia T., David S.A., Vitek J.M.: *Effect of evaporation and temperature-dependent material properties on weld pool development*, Metall. Trans., Vol. 22B, 1991, pp. 233–241.

Modelowanie procesu spawania laserowego stali w fazie tworzenia kanału parowego

W pracy przedstawiono wynik symulacji komputerowej dla modelu oddziaływania kanału parowego i jeziorka w procesie spawania laserowego. Kształt i wielkość kanału parowego jest wynikiem oddziaływania napięcia powierzchniowego i siły odrzutu. Model opracowano za pomocą programu do obliczeń dynamiki płynów Fluent oraz własnych procedur. Efektywność modelu potwierdzono na wieloprocesorowym komputerze przez zastosowanie obliczeń równoległych.



Application of generative technologies in the design of reduced stiffness stems of hip joint endoprosthesis

K. ŚCIGAŁA, R. BĘDZIŃSKI, J. FILIPIAK

Wrocław University of Technology, The Division of Biomedical Engineering and Experimental Mechanics, Institute of Machine Design and Operation, ul. Łukasiewicza 7/9, 50-371 Wrocław, Poland.

E. CHLEBUS, B. DYBALA

Wrocław University of Technology, The Division of Mechatronics, Automation, and Production Scheduling, Institute of Machine Technology and Automation, ul. Łukasiewicza 5, 50-371 Wrocław, Poland.

This paper presents proposed new design solutions for hip endoprosthesis stems characterised by reduced stiffness as a result of application of internal lattice structures obtained using generative production techniques. The conducted analysis showed the possibility of achieving lattice structures inside implants as well as the possibility of controlling mechanical characteristics of the end forms of implants. It was demonstrated that the use of inner lattice structures resulted not only in reduced implant stiffness, but also in reduced formation of adverse cancellous tissue trabecular structures. The obtained results indicate that it is possible to obtain implant structures that are much less vulnerable to the stress shielding effect than traditional designs.

Keywords: *hip endoprosthesis, stiffness, generative technologies*

1. Introduction

Long-term clinical trials of the outcomes of treatment of hip joint diseases with the use of endoprostheses having classic stem sizes indicate that in a significant number of cases complications occurring in the long-term postoperative period lead to a loosening of the stem and the need to implant a revision endoprosthesis [2, 15, 20]. Biomechanical analyses, in particular analyses of distribution of stresses and strains in bone tissue around the stem demonstrate that one of the primary causes of loosening are disruptions of the processes of bone tissue remodelling caused by load change due to introduction of the stem. The high stem rigidity means that most of the load is transferred from the endoprosthetic head to the distal femur by the stem itself, resulting in a significantly lower than physiological load on the bones tissue in the area of the proximal femoral epiphysis [4–6]. This effect, called stress shielding, was analysed in the works [8, 11, 24], where a clearly visible relationship was observed between the stem rigidity and a decrease in the density and mechanical properties of the bone tissue. The low level of deformations on the stem surface also reduces stimulation to bone tissue remodelling in the area, which consequently leads to disruptions of the

processes of integration of bone tissue with the stem [21, 35]. In order to eliminate these adverse effects, analyses are being conducted to optimise the stem shape [19, 23, 27]. Additionally, work is underway to develop techniques of selecting the stem of a particular shape, meeting anatomical and biomechanical conditions of compatibility with bone tissue of a specific patient [1, 12, 32]. These works lead not only to specialized techniques of selecting stems but also to development of a customised stem design, for a particular medical case. Work is also underway on the use of new materials thanks to which it will be possible to reduce stem stiffness (compared to the currently used stems). Analyses of this type are aimed at synthesis of new metal alloys [13, 18, 30, 34], polymer materials [7, 14] or carbon fibbers and carbon-carbon alloys [10, 30]. Some works are also focused on development of new surface layers [26].

Thanks to advances made in the recent years in the technology of production by generative methods, it has become possible to design and produce objects that had been very difficult or impossible to manufacture [22, 28, 31]. The main advantages of generative technologies over conventional methods of production are the almost complete lack of relationship between, on the one hand, production costs and times, and, on the other hand, the shapes of the produced objects, and the lack of need to prepare production tools (moulds, matrices, and dies). Generative technologies enable free-shaping (also organic-shaping) of objects, which makes them increasingly popular in the manufacture of medical devices, including stems of hip joint endoprostheses. The technology of layered manufacturing means that new designs, while maintaining the anatomical fit of the stem, can demonstrate reduced rigidity and distribution of deformities on the stem surface, adapted to the deformability of the bone tissue.

The purpose of this work is to develop a new stem design using generative technology capabilities. A comparative analysis was also carried out of the stiffness characteristics of classic stems and new designs as well as a numerical analysis of the impact of stem introduction on the processes of rebuilding of bone tissue in the proximal femoral epiphysis.

2. Material and method

The basic concept that guided the development of the new design was the idea of production of a stem of classic external shape, but with the internal spatial structure of rods having fixed cross-section and appropriate degree of spatial ordering (Figure 1).

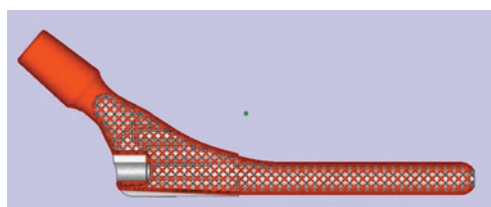


Fig. 1. The concept of a new-generation stem produced with generative technology

Compared to classic stems of hip joint endoprostheses, the proposed design is characterised by much smaller surface areas of the active cross-section, which leads to reduced global stiffness and changes stiffness characteristics along its length. It should be emphasised that, compared to the previously proposed hollow stems [19], use of a rod structure inside the stem provides a much greater scope of control over stem stiffness.

Additionally, stems with significantly thinner outer walls can be used without compromising local stability of the external coating.

During the initial designing stage, several proposed rod-structure designs were developed that could be used as the internal structure of the stem of the hip joint endoprosthesis. All compositions were developed as rectangular structures with the external dimensions of $10 \times 10 \times 17.4$ mm. Figure 2 shows the developed structures.

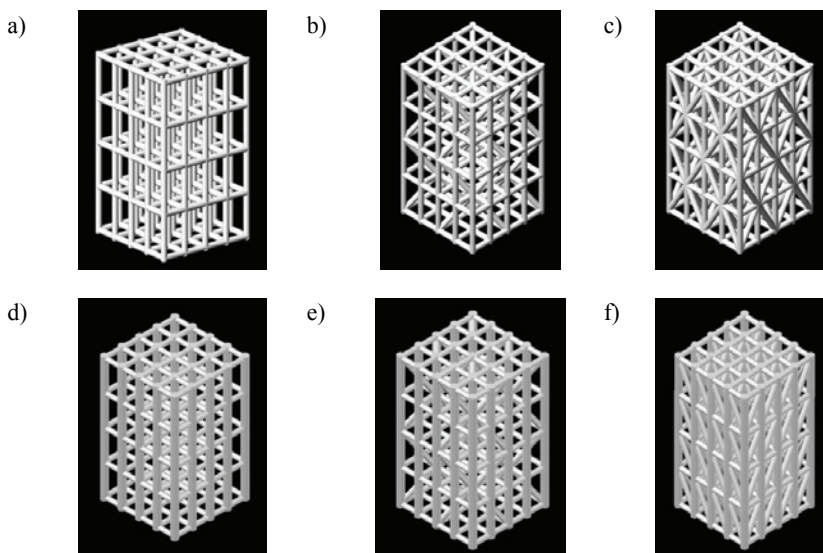


Fig. 2. Analyzed beams structures a) A-06, b) A-06-PC, c) A-06-PB, d) A-09-06, e) A-09-06-PC, f) A-09-06-PB

The new designs can be divided into two groups. The first group, consisting of solutions marked as: A-06, A-06-PC, A-06-2PC and A-06-PB, is characterised by the fact that elements making the structure have the form of trabeculae with circular cross-section, with a diameter of 0.6 mm, the distance between the vertical trabeculae of $b = 2.4$ mm (measured between the axes), and the distance between the horizontal trabeculae of $h = 4.2$ mm. In the second group, consisting of solutions marked as: A-09-06, A-09-06-PC, A-09-06-PB, the trabeculae forming vertical columns have a diameter of 0.9 mm, while the other trabeculae (vertical and oblique) have a diameter of 0.6 mm, and the distances between trabeculae are the same as in the first group.

The actual designs were made out of Ti6Al7Nb titanium alloy on a Realizer II device using the technology of Selective Laser Melting (SLM). The process of selective

melting of metal powders involves application of successive identical layers of powder with the granularity of 20–100 micrometers and laser melting at selected places so that it forms solid material after cooling and solidification. The melted places correspond to consecutive cross-sections through the computer model of the built object.

The actual designs were made out of Ti6Al7Nb titanium alloy on a Realizer II device using the technology of Selective Laser Melting (SLM). The process of selective melting of metal powders involves application of successive identical layers of powder with the granularity of 20–100 micrometers and laser melting at selected places so that it forms solid material after cooling and solidification. The melted places correspond to consecutive cross-sections through the computer model of the built object.

The developed structures were subjected to tests to determine their stiffness. The measurements were performed on a MTS MiniBionix 858 testing machine. Each course of test measurements and acquisition of measurement data were controlled by means of a TestStar II controller made by MTS. The samples were fixed in position in the station with the use of special instrumentation for compressed samples. The samples were loaded using an MTS 242.02 hydraulic actuator with the travel range of 100 mm. The force of reaction of the tested samples was measured with the use of an MTS 661.19F-03 extensometer force transducer with the nominal range of ± 15 kN.

The next stage of the study involved determination of changes in the stiffness of stems filled with the previously-developed rod structures (compared to the solid stem). Two stem versions were developed, shown on Figure 3.

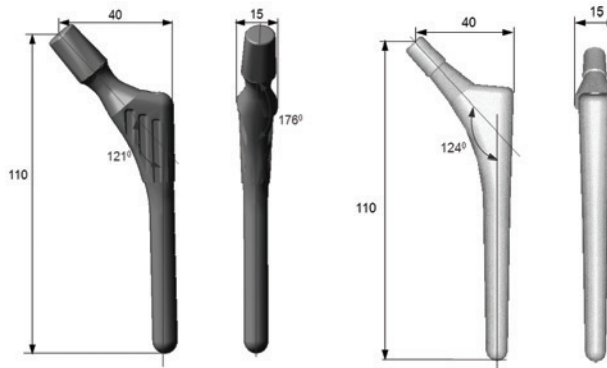


Fig. 3. Geometric models of stems of hip joint endoprostheses used in the analysis

Numerical models of stem were developed that were either solid or filled with selected structures shown on Figure 2. The models were developed using v.12 of the Ansys program. The division into a mesh of finite elements was achieved with TETRA solid elements, with 10 nodes and three degrees of freedom at each node and trabecular elements of 3 nodes and three degrees of freedom at each node. The models were subject to loading as in Figure 4 thanks to which a comparative analysis was possible of the distribution of displacements along the stem length (Będzinski, 1999).

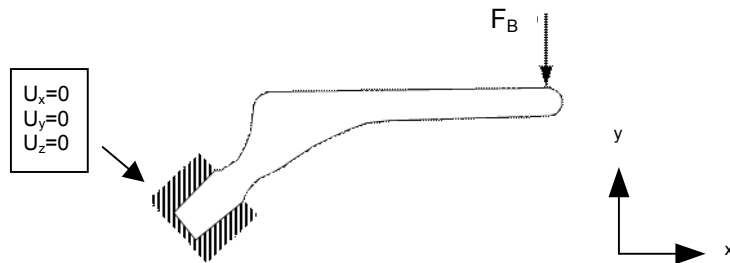


Fig. 4. Load model of the stem of the hip joint endoprosthesis used in the analysis of the stiffness characteristics

The distribution of forces occurring in the hip joint shows that femoral bone with endoprosthetic stem is subjected to a complex load condition. However, as can be observed, one of the main components of this type of load is bending in the frontal plane. Therefore, analysis of displacements (bending) of the stem in the proposed simple load model enables assessment of the impact of changes in its design (introduction of lattice structures) on its stiffness characteristics.

The next stage of the study involves analysis of remodelling of trabecular structures of the cancellous tissues of bones in the proximal femoral epiphysis. Trabeculae structures were examined by checking morphological and physical factors describing properly formed tissue [16, 17].

The analysis of remodelling of trabecular structures of the cancellous tissue in the proximal femoral epiphysis was carried out with the use of the model proposed by [36]. In this case, the remodelling stimulus is defined as proportional to heterogeneity of distribution of stresses on the surface of bone trabeculae:

$$\Gamma = \ln \left(\frac{\sigma_C}{\sigma_D} \right), \quad (1)$$

where:

σ_C – value of stress at the currently analysed point C,

σ_D – value determined on the basis of stress values at the strictly defined surroundings of point C (in accordance with Figure 5).

The value σ_D is determined in accordance with the formula:

$$\sigma_D = \frac{\int_S w(L) \sigma_R dS}{\int_S w(L) dS}, \quad (2)$$

$$w(L) = 1 - \frac{L}{L_L} \quad (0 < L < L_L), \quad (3)$$

$$w(L) = 0 \quad (L_L \leq L). \quad (4)$$

where:

S – active surface,

L – length between points C and R,

σ_R – value of stress at point R,

L_L – radius of the analysed circular area.

Also in this case two-dimensional models were used.

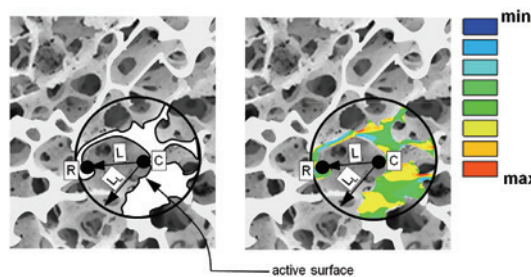


Fig. 5. Determination of the local heterogeneity of stress distribution Γ

The analysis used flat quadrilateral elements of 8 nodes and two degrees of freedom at each node. The initial structure of the model and the load model were shown in Figures 6 and 7.

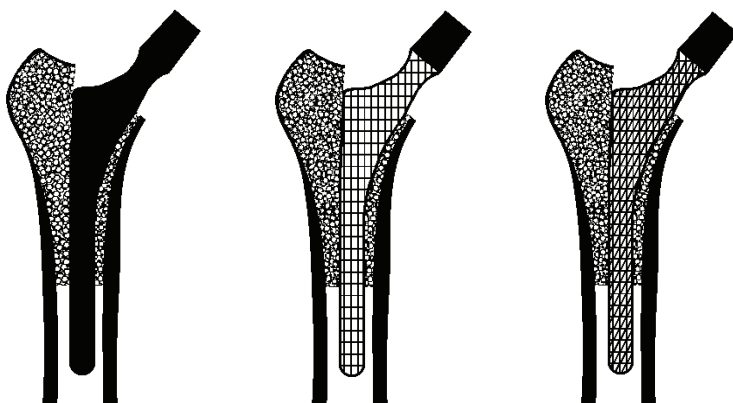


Fig. 6. FEM models used in the analysis of remodelling of trabecular structures of cancellous tissue around the stem

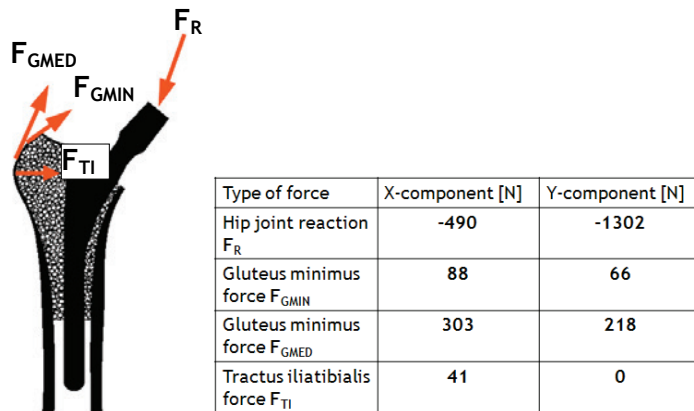


Fig. 7. Load models used in the analysis of remodelling of trabecular structures of cancellous tissue around the stem

3. Results

In the tests of stiffness of rod structures some of the developed structures were subjected to the compression test along the sample axis and some were subjected to the force oriented along the parallel axis. The recorded values of the F force and the d displacement enabled determination of the force-displacement characteristics. Based on those characteristics, the values of the stiffness coefficient were determined for the tested structures, understood as ratio of the F force to the d displacement. Because the obtained F-d characteristics demonstrate some nonlinearity in the initial loading stage, two values of the stiffness coefficient were determined: one corresponds to the part of the characteristics covering the force range from 0 to 4 kN and the other – the force range from 4 to 15 kN. The adopted division of the force ranges also has practical justification. The biomechanics of the hip joint shows that the maximum value of the force of reaction acting on the femoral head while walking reaches approx. 3.6 kN (this value is applicable to the gait of a person weighing 75 kg). Therefore, for the purposes of this project that force range was the most interesting. Figure 8 presents the values of stiffness in the longitudinal and transverse orientations for the analysed force ranges.

The obtained results were used at a later stage of the project, during which selected implant designs were developed. Based on the stiffness values, for both loading ranges the most promising rod structures were selected and in the models used in the later part of the analysis only the structures marked as A-06 and A-06-PB were used. Figure 9 shows distributions of displacements along the stem length for the loading shown on Figure 4. Here, distributions were compared between the solid stem type 1 (Figure 3) and the stems with pre-selected fillings.

In all cases of designs with internal rod structures, a significant reduction in the stem stiffness was obtained at bending in the frontal plane, as demonstrated by the ob-

tained distributions and the values of displacements. For the stem with type A-06 structure, the displacement values obtained in the region of its distal end are twice bigger than in the case of a solid stem. However, it should be stressed that type A-06 structure is characterised by the smallest spatial density of rods, and thus the smallest active cross-section. For the stem with type A-06-PB structure, the maximum values of displacements increased by only approx. 50% compared to the solid stem due to distribution of additional oblique bars stiffening the structure.

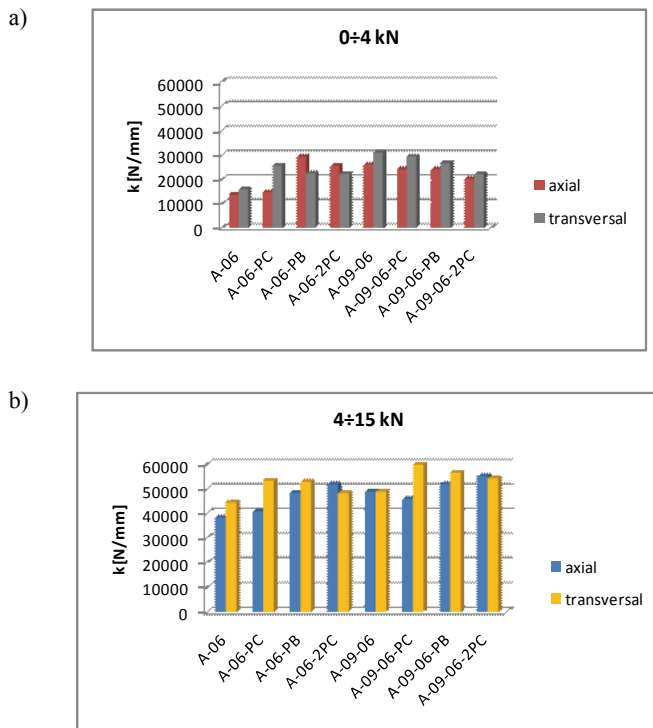


Fig. 8. Comparison of the values of stiffness determined in the longitudinal and transverse orientations for the part of the F-d characteristics corresponding to the force range from 0 to 4 kN (a) and from 4 kN to 15 kN (b)

The obtained results point to the possibility of full control over the stem stiffness by appropriate selection of the filling with the rod structure. Given the large variety of possible spatial combinations of rods, the range of stiffness changes can be very extensive. Analysis of remodelling of trabecular structures of cancellous tissues in the proximal femoral epiphysis with solid stem of the first type confirmed good bonding of the stem with bone tissue on the medial side (Figure 10). The trabecular structures are well developed, consisting of short trabeculae of large diameter, with clear orientation, running perpendicularly to the stem surface in the proximal part (A) and run-

ning randomly in the distal part (B). The trabecular structures on the lateral side consist of trabeculae with significantly greater length and smaller diameter. Those trabeculae also have different orientation. In the proximal part the dominant orientations are upwards and sideways (C), and in the distal part the majority of trabeculae are oriented upwards and inwards (D). Trabeculae perpendicular to the stem surface are only present in the highest lateral part of the stem surface (E).

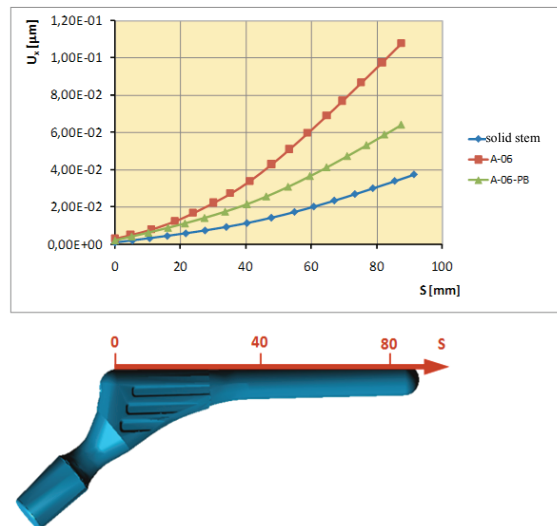


Fig. 9. Comparison of the distribution of displacements (bending) of stems subjected to bending the frontal plane

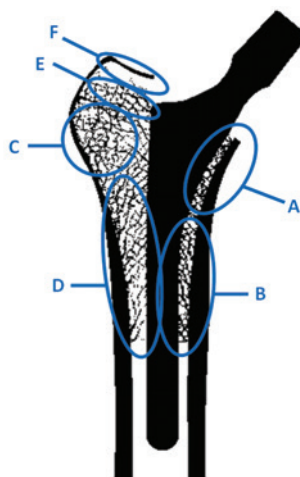


Fig. 10. Distribution of trabecular structures in the proximal femoral epiphysis with solid stem of the first type

However, it should be stressed that the summit of the greater trochanter is a significantly diluted structure, i.e. it has much larger intertrabecular spaces than in the remaining part of the proximal epiphysis (F) and also larger than observed in typical cancellous tissue [24].

In the case of the type A-06 lattice structure stems in the distal part on the lateral side the obtained trabecular structures had distinctly different structures than in the case of the solid stem (Figure 11). The trabeculae are visibly longer, have a smaller diameter, and are morphologically very similar to the structures observed in pathological conditions. Their orientation also changed – compared to structures around the solid stem, they are oriented more upwards. There is also a noticeable loss of bone trabeculae structures in the layer located next to the stem wall (A). This effect should be regarded as unfavourable due to its potential impact on the process of loosening of the stem.

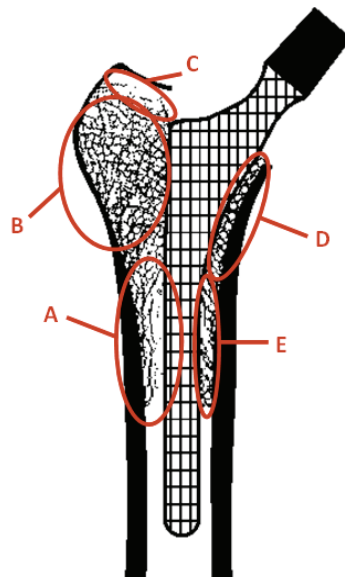


Fig. 11. Distribution of trabecular structures in the proximal femoral epiphysis with solid stem of the first type – type A-06 filling

On the other hand, in the proximal part on the lateral side (B) there is a clearly visible strengthening of bone structures. Compared to the results of simulation in the case of the solid stem, bone trabeculae are characterised by clearly larger diameters, they are shorter, and their spatial density also increased. It should be emphasised that in this area bone structures are also characterised by high density, also in direct proximity of the stem. Bone structures are oriented upwards and sideways, but most trabeculae are short. The area located in the region of the summit of the greater trochanter also decreased, which disappearance of bone structures (C). On the medial

side bone structures located in the proximal part are of a similar type as in the case of the solid stem (D), whereas in the distal part they underwent visible dilution (E).

Structures similar to those described above were obtained in the case of a stem with the type A-06-PB filling (Figure 12). On the lateral side in the distal part bone structures are also diluted, but to a much lesser extent than previously.

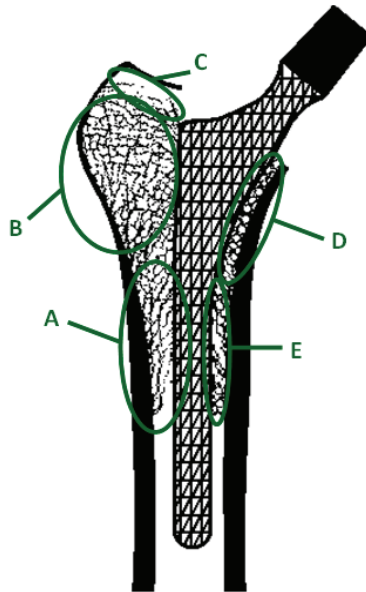


Fig. 12. Distribution of trabecular structures in the proximal femoral epiphysis with stem of the first type – type A-06-PB filling

The structures in the proximal part (B) are still fully-developed load-bearing structures, but the trabeculae have smaller diameters than in the case of a stem with the type A-06 filling. Orientation of the trabeculae in the parts C, D, and E is almost identical as is in the previous case.

It can be concluded that the results obtained for the stem with type A-06-PB filling are intermediate structures between those obtained for the solid stem and the stem with the type A-06 filling.

4. Discussion

As demonstrated by the conducted analysis, the proposed new design of the stem of the hip joint endoprosthesis is characterised by biomechanical characteristics and features that distinguish it from the previously used structures. The use of new production techniques enabled geometric shaping to a much larger extent than was possible in the case of endoprostheses manufactured with conventional techniques.

The obtained results allow us to conclude that application of lattice structure enables shaping of stiffness characteristics of the endoprosthesis over a wide range while maintaining the external shape of the stem adjusted to the anatomy of the tissue environment in which it will be used. However, it should be emphasised that the conducted analyses were pilot studies. Stiffness was only analysed at bending in the frontal plane. The trajectory of movement of the femur during walking shows that a similar analysis will also be necessary for bending in the sagittal plane. Most contemporary endoprostheses of the hip joint are shaped in such way as to reproduce the physiological angle of anteversion, which also points to the need to analyse stiffness at stem twisting.

However, it should be stressed that, in the case of the proposed internal lattice structures, even if the size of the primary cell of the filling and the diameter of the individual rods remain constant, the number of possible combinations of arrangements of the individual rods in the primary cell area is so large that it is possible to control at the same several parameters connected with stem stiffness in different planes.

The performed simulations of the processes of adaptation of bone structures to a new load condition connected with the introduction of the implant demonstrated a positive effect of the use of internal lattice structures on formation and rebuilding of bone load-bearing structures and development of bone tissue in the layers adjoining the implant.

However, not all expected positive effects were achieved in all cases. The performed analysis showed that application of some of the proposed fillings results in stems of such high susceptibility that significant changes are possible in the distribution of loads in the proximal femoral epiphysis, and this leads to negative effects in the adaptive processes. In particular, in the case of a stem with the A-06 filling, there is a disturbing phenomenon of production of fully-developed bone structures in a significant part of the proximal femoral epiphysis, connected, however, with the formation of structures that can be considered pathological in the distal part of the stem. The results of this type show that the design of the internal lattice structure must be optimized, in particular by its differentiation in various parts of the stem. Such differentiation can be achieved by reconfiguration of the primary cell in the stem volume but also by changing its dimensions or dimensions of its constituent rods.

However, it should be noted that generative technologies enable such type of shaping and a stem can be obtained for which negative effects of the remodelling processes will be minimised.

References

- [1] Bargar W.L.: *Shape the implant to the patient: a rationale for the use of custom-fit cementless total hip implants*, Clinical Orthopaedics & Related Research, Vol. 249, 1989, pp. 73–78.
- [2] Barrack R.L., Mulroy R.D. Jr, Harris W.H.: *Improved cementing techniques and femoral component loosening in young patients with hip arthroplasty. A 12-year radiographic review*, Journal of Bone and Joint Surgery – British, Vol. 74-B, 1992, pp. 385–389.

- [3] Beaupre G.S., Orr T.E., Carter D.R.: *An approach for time-dependent bone remodelling and remodelling applications: a preliminary simulation*, Journal of Orthop. Res., Vol. 8, 1990, pp. 662–670.
- [4] Będziński R., Bernakiewicz M., Ścigała K.: *Biomechanical aspects of artificial joint implantation in a lower limb*, Journal of Theoretical and Applied Mechanics, Vol. 37, 1999, pp. 455–481.
- [5] Będziński R., Ścigała K.: *Biomechanical basis of tissue-implant interactions*, Computer methods in mechanics: CMM, Berlin – Heidelberg, Springer, 2010, pp. 379–390.
- [6] Będziński R., Ścigała K.: *Numerical and experimental methods in biomechanics*, Biomechanics, Warszawa, Instytut Podstawowych Problemów Techniki PAN, 2011, pp. 77–178.
- [7] Bougheara H., Bureau M., Campbell M., Vadean A., Yahia L.: *Design of a biomimetic polymer-composite hip prosthesis*, Journal of Biomedical Materials Research, Part A, Vol. 82A, 2007, pp. 27–40.
- [8] Bugbee W.D., Culpepper W.J., Engh C.A. Jr, Engh C.A. Sr: *Long-Term clinical consequences of stress-shielding after total hip arthroplasty without cement*, Journal of Bone and Joint Surgery – American, Vol. 79, 1997, pp. 1007–1012.
- [9] Carter D.R., Beaupre G.S.: *Skeletal function and form*, Cambridge University Press, 2001.
- [10] Christel P., Meunier A., Leclercq S., Bouquet P., Buttazzoni B.: *Development of a carbon-carbon hip prosthesis*, Journal of Biomedical Materials Research, A2 Suppl, 1987, pp. 191–218.
- [11] Cristofolini L.: *A critical analysis of stress shielding evaluation of hip prostheses*, Crit Rev Biomed Eng., Vol. 25, 1997, pp. 409–483.
- [12] Crowninshield R.D., Brand R.A., Johnston R.C., Milroy J.C.: *An analysis of femoral component stem design in total hip arthroplasty*, The Journal of Bone and Joint Surgery, Vol. 62, 1980, pp. 68–78.
- [13] Davidson J.A., Mishra A.K., Kovacs P., Poggie R.A.: *New surface-hardened, low-modulus, corrosion-resistant Ti-13Nb-13Zr alloy for total hip arthroplasty*, Biomed Mater Eng., Vol. 4, 1994, pp. 231–243.
- [14] Degas G.: *New polymer materials in total hip arthroplasty. Evaluation with radiostereometry, bone densitometry, radiography and clinical parameters*, Acta Orthopaedica, Vol. 76, 2005, pp. 4–82.
- [15] Engh C., Bobyn J.D., Glassman A.H.: *Porous-coated hip replacement. The factors governing bone ingrowth, stress shielding, and clinical results*, Journal of Bone and Joint Surgery – British, Vol. 69-B, 1987, pp. 45–55.
- [16] Filipiak J., Kuropka P., Krawczyk A., Morasiewicz L.: *Mechanical stimulation as a determine factor of bone regenerate biomechanical properties*, 26th Danubia-Adria Symposium on Advances in Experimental Mechanics, Montanuniversität Leoben, Austria, 2009, pp. 53–54.
- [17] Filipiak J., Ścigała K.: *Application of FEM in modelling of bone regenerate*, Systems. Journal of Transdisciplinary Systems Sciences, Vol. 9, 2004, pp. 378–384.
- [18] Gronostajski Z., Bandola P., Skubiszewski T.: *Argon-shielded hot pressing of titanium alloy Ti6Al4V powders*, Acta Biomed Bioeng, Vol. 12, 2010, pp. 41–46.
- [19] Gross S., Abel E.W: *A finite element analysis of hollow stemmed hip prostheses as a means of reducing stress shielding of the femur*, Journal of Biomechanics, Vol. 34, 2001, pp. 995–1003.

- [20] Gruen T.A., McNeice G., Amstutz H.: “*Modes of failure*” of cemented stem-type femoral Components: a radiographic analysis of loosening, Clinical Orthopaedics & Related Research, Vol. 141, 1979, pp. 17–27.
- [21] Gustilo R., Pasternak H.: Revision total hip arthroplasty with titanium ingrowth prosthesis and bone grafting for failed cemented femoral component loosening, Clinical Orthopaedics & Related Research, Vol. 235, 1988, pp. 111–119.
- [22] Hopkinson N., Hague R., Dickens P.: *Rapid manufacturing: an industrial revolution for the digital age*, John Wiley & Sons, 2006.
- [23] Huiskes R., Boeklagen R.: Mathematical shape optimization of hip prosthesis design, Journal of Biomechanics, Vol. 22, 1989, pp. 793–804.
- [24] Huiskes R., Weinans H., van Rietbergen B.: The relationship between stress shielding and bone resorption around total hip stems and the effects of flexible materials, Clinical Orthopaedics & Related Research, Vol. 274, 1992, pp. 124–134.
- [25] Huiskes R., Mullender M.G.: Osteocytes and bone lining cells: which are the best candidates for mechano-sensors in cancellous bone?, Bone, Vol. 20, 1997, pp. 527–532.
- [26] Krzak-Roś J., Filipiak J., Pezowicz C., Baszczuk A., Miller M., Kowalski M., Będziński R.: The effect of substrate roughness on the surface structure of TiO_2 , SiO_2 , and doped thin films prepared by the sol-gel method, Acta Biomed Bioeng, Vol. 11, 2009, pp. 21–29.
- [27] Kuiper J.H., Huiskes R.: Mathematical optimization of elastic properties: application to cementless hip stem design, Journal of Biomechanical Engineering, Vol. 119, 1997, pp. 166–174.
- [28] Lipowicz A., Dybała B., Chlebus E.: Scaffolds manufactured via conventional and advanced (LBMM) methods, in: Biocybernetyka i inżynieria biomedyczna. XV Krajowa konferencja naukowa, 12–15 September, 2007, Wrocław, Ośrodek Doskonalenia Kadr SIMP, 2007.
- [29] Nikodem A., Będziński R., Ścigała K., Dragan Sz.: Mechanical and structural anisotropy of human cancellous femur bone, Journal of Vibroengineering, Vol. 11, 2009, pp. 571–576.
- [30] Okazaki Y.: A New Ti–15Zr–4Nb–4Ta alloy for medical applications, Current Opinion in Solid State and Materials Science, Vol. 5, 2001, pp. 45–53.
- [31] Pandremenos J., Paralikas J., Chryssolouris G., Dybala B., Gunnink J.W.: RM product development: design principles, simulation and tools, in: *Additive layered manufacturing: from evolution to revolution*, eds. Igor Drstvensek, Slavko Dolinsek. Maribor: University of Maribor, Faculty for Mechanical Engineering, 2008.
- [32] Robertson D.D., Walker P.S., Granholm J.W., Nelson P.C., Weiss P.J., Fishman E.K., Magid D.: Design of custom hip stem prostheses using three-dimensional CT modelling, Journal of Computer Assisted Tomography, Vol. 11, 1987, pp. 804–809.
- [33] Shirandami R., Esata I.I.: New design of hip prosthesis using carbon fibre reinforced composite, Journal of Biomedical Engineering, Vol. 12, 1990, pp. 19–22.
- [34] Song Y., Xua D.S., Yanga R., Lia D., Wub W.T., Guoc Z.X.: Theoretical study of the effects of alloying elements on the strength and modulus of β -type bio-titanium alloys, Materials Science and Engineering: A, Vol. 260, 1999, pp. 269–274.
- [35] Sumner D., Turnera T.M., Igloiaa R., Urbana R.M., Galantea J.O.: Functional adaptation and ingrowth of bone vary as a function of hip implant stiffness, Journal of Biomechanics, Vol. 31, 1998, pp. 909–917.
- [36] Tsubota K., Adachi T.: Spatial and temporal regulation of cancellous bone structure, Medical Engineering & Physics, Vol. 27, 2005, pp. 305–311.

Zastosowanie technologii generatywnych w konstrukcji trzpieni endoprotezy stawu biodrowego o obniżonej sztywności

W pracy przedstawiono nowe rozwiązania konstrukcyjne trzpieni endoprotezy stawu biodrowego charakteryzujące się obniżoną sztywnością uzyskana przez zastosowanie ażurowych konstrukcji wewnętrznych. Konstrukcje tego typu są otrzymywane przez zastosowanie generatywnych technik wytwarzania. Przeprowadzona analiza wykazała zarówno możliwość uzyskania konstrukcji ażurowych w bardzo szerokim zakresie jak również możliwość sterowania charakterystykami mechanicznymi końcowych postaci implantów. Wykazano, iż zastosowanie wewnętrznych konstrukcji ażurowych prowadzi nie tylko do zmniejszenia sztywności implantu, lecz również prowadzi do zmniejszenia efektu kształtuowania się wokół implantu niekorzystnych struktur beleczek tkanki gąbczastej. Uzyskane wyniki wskazują na potencjalną możliwość uzyskania konstrukcji implantów w znacznie mniejszym stopniu narażonych na efekty „stress shieldingu” niż konstrukcje tradycyjne.



A hydraulic cylinder subjected to Euler's load in aspect of the stability and free vibrations taking into account discrete elastic elements

L. TOMSKI, S. UZNY

Częstochowa University of Technology, ul. Dąbrowskiego 73, 42-201 Częstochowa, Poland.

Theoretical and numerical research into the stability and free vibrations of a slender system in the form of a hydraulic cylinder subjected to Euler's load was carried out in this paper. The rigidities in the constructional nodes realising the load of the considered system were taken into account in the system. Both rotational and translational springs were applied to the loading nodes. Regions of the flexural rigidity asymmetry factor for the piston rod and cylinder, where the system is subject to damage as a result of stability loss, were determined in the frame of numerical research into the hydraulic cylinder. In this paper critical load and characteristic curves were also determined in the plane: load–natural frequency. These two quantities were determined for different parameters of the system: the flexural rigidity asymmetry factor for the piston rod and cylinder, the degree of coverage of cylinder, the rigidities of the rotational and translational springs, and the total rigidity factor of the system.

Keywords: *hydraulic cylinder, free vibrations, stability, slender system, Euler load*

1. Introduction

Hydraulic cylinders were considered in works [3]–[15]. Lech Tomski has devised two basic computational models applied to hydraulic cylinders. The first model presented in [11] is related to a hydraulic cylinder as a slender system. This model is used in research into transverse free vibrations and static stability. The discussed model was applied in [12], [8], [9], [3], [15] to the domain of transverse free vibrations and static stability, while in [4], [5], [15] it was applied in research into parametrical free vibrations and dynamic stability. The second computational model, presented in [10], is related to a hydraulic cylinder as a stocky system. This model is used in research into the free and forced vibrations taking place in a longitudinal direction (comp. [13], [14], [6], [7]). In the mentioned literature, the hydraulic cylinder is subjected to a compressive Euler's load. The piston rod of the cylinder is most often built of only one element. However, a hydraulic cylinder with a piston rod which is built of two elements of different flexural rigidity was considered in [8], [3]. In this case, non-linear theory of moderately large deflections was applied to formulate the boundary problem. The pressure of the liquid in the piston rod of cylinder is also important in research into hydraulic cylinders as it has a direct effect on its strength. L. Tomski in publications [11], [12] presented changes in stress in the piston rod

along all its length on the basis of Lame's solution (the piston rod of the cylinder was treated as a double extra strong pipe). The computational model, proposed by L. Tomski and applied in research into transverse vibrations and stability (hydraulic cylinder as a slender system), was experimentally verified in works [9], [2]. The experimental research relied on frequency analysis (the natural frequency was measured for different values of the external load). The conducted experimental research verified the accuracy of the assumed computational model.

2. Formulation of the boundary problem

In this paper, the hydraulic cylinder is considered as a slender system. A mathematical model is assumed according to work [11]. The considered hydraulic system presented in Figure 1a consists of two basic elements: the cylinder and the piston rod. Both the cylinder and the piston rod were divided into two parts to build the mathematical model (Figure 1b). The cylinder is modelled by elements denoted as 11 and 12 in Figure 1b while the piston rod is modelled by elements denoted as 21 and 22. In the considered model of the hydraulic cylinder, the rigidity of the loading nodes was taken into account. The rotational rigidity of the loading nodes at both ends of the hydraulic cylinder (springs with rigidities C_0 and C_1) and the translational rigidity at one end of the hydraulic cylinder (at the end of the piston fixing) (spring with rigidity C) were also considered.

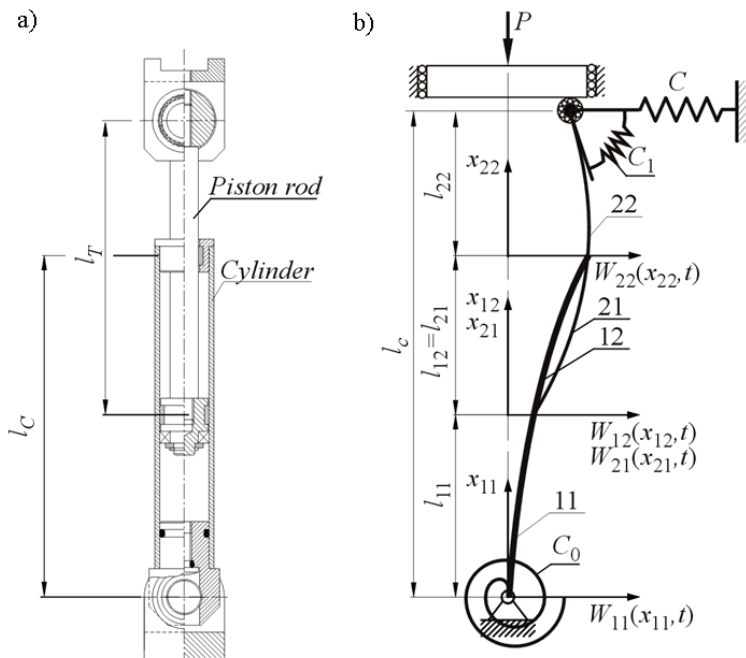


Fig. 1. Diagram of the considered hydraulic cylinder: a) constructional solution, b) mathematical model

The boundary problem of the hydraulic cylinder was formulated in a classic way – on the basis of Hamilton's principle:

$$\delta \int_{t_1}^{t_2} (T - V) dt = 0, \quad (1)$$

where:

T and V – kinetic and potential energy, respectively,

t – time.

The buckling of a thick-wall cylinder ending with a piston, affected by the axial force which generated liquid pressure, is equivalent to the buckling of a rod subjected to a compressive external load. However in the same work conditions for the cylinder and rod (identical rigidities, the same method of fixing and identical axial forces), the cylinder can undergo damage as a result of the material effort and not due to stability loss. There is a different state of stress in the cylinder produced by the liquid pressure. Only a hydraulic cylinder which undergoes damage due to a stability loss is tested in this work

Potential energy V is written in the form:

$$V = \frac{1}{2} \sum_{i=1}^2 \sum_{j=1}^2 (EJ)_{ij} \int_0^{l_{ij}} \left(\frac{\partial^2 W_{ij}(x_{ij}, t)}{\partial x_{ij}^2} \right)^2 dx_{ij} - \\ - \frac{1}{2} P \left(\sum_{j=1}^2 \int_0^{l_{2j}} \left(\frac{\partial W_{2j}(x_{2j}, t)}{\partial x_{2j}} \right)^2 + \int_0^{l_{11}} \left(\frac{\partial W_{11}(x_{11}, t)}{\partial x_{11}} \right)^2 \right) + \\ + \frac{1}{2} C_0 \left(\frac{\partial W_{11}(x_{11}, t)}{\partial x_{11}} \Big|_{x_{11}=0} \right)^2 + \frac{1}{2} C_1 \left(\frac{\partial W_{22}(x_{22}, t)}{\partial x_{22}} \Big|_{x_{22}=l_{22}} \right)^2 + \frac{1}{2} C(W_{22}(l_{22}, t))^2. \quad (2)$$

Kinetic energy T is defined by the following equation:

$$T = \frac{1}{2} \sum_{i=1}^2 \sum_{j=1}^2 (\rho A)_{ij} \int_0^{l_{ij}} \left(\frac{\partial W_{ij}(x_{ij}, t)}{\partial t} \right)^2 dx_{ij} + \frac{1}{2} (\rho A)_C \int_0^{l_{11}} \left(\frac{\partial W_{11}(x_{11}, t)}{\partial t} \right)^2 dx_{11} + \\ + \frac{1}{2} m \left(\frac{\partial W_{11}(x_{11}, t)}{\partial t} \Big|_{x_{22}=l_{22}} \right)^2, \quad (3)$$

where:

$W_{ij}(x_{ij}, t)$ – transversal displacement of the individual elements of the hydraulic cylinder defined by coordinate x_{ij} ,

$(EJ)_{ij}$ – the flexural rigidity of the individual elements of the hydraulic cylinder,

$(\rho A)_{ij}$ – mass per unit length of the individual elements of the hydraulic cylinder,

$(\rho A)_C$ – mass of liquid per unit length of the cylinder.

In the general case of the hydraulic cylinder (the hydraulic cylinder shown in Figure 1) only one geometrical boundary condition is present at $x_{11} = 0$:

$$W_{11}(0, t) = 0. \quad (4)$$

Geometrical continuity conditions which occur between adequate elements of the system (between elements (Figure 1): 11–12, 11–12–21, 21–22, 12–21–22) are as follows:

$$\frac{\partial W_{11}(x_{11}, t)}{\partial x_{11}} \Big|_{x_{11}=l_{11}} = \frac{\partial W_{12}(x_{12}, t)}{\partial x_{12}} \Big|_{x_{12}=0}, \quad (5a)$$

$$W_{11}(l_{11}, t) = W_{12}(0, t) = W_{21}(0, t), \quad (5b)$$

$$\frac{\partial W_{21}(x_{21}, t)}{\partial x_{21}} \Big|_{x_{21}=l_{21}} = \frac{\partial W_{22}(x_{22}, t)}{\partial x_{22}} \Big|_{x_{22}=0}, \quad (5c)$$

$$W_{12}(l_{12}, t) = W_{21}(l_{21}, t) = W_{22}(0, t). \quad (5d)$$

Taking into account the potential energy (2) and kinetic energy (3) and geometrical boundary condition (4) as well as the geometrical continuity conditions (5) in Hamilton's principle (1) the following were obtained:

– the differential equations of motion of the individual elements of the hydraulic cylinder:

$$\frac{\partial^4 W_{ij}(x_{ij}, t)}{\partial x_{ij}^4} + k_{ij}^2 \frac{\partial^2 W_{ij}(x_{ij}, t)}{\partial x_{ij}^2} + \Psi_{ij} \frac{\partial^2 W_{ij}(x_{ij}, t)}{\partial t^2} = 0, \\ i, j = 1, 2, \quad (6)$$

where:

$$k_{11}^2 = \frac{P}{(EJ)_{11}},$$

$$k_{12}^2 = 0,$$

$$k_{21}^2 = \frac{P}{(EJ)_{21}},$$

$$k_{22}^2 = \frac{P}{(EJ)_{22}},$$

$$\Psi_{11} = \frac{(\rho A)_{11} + (\rho A)_C}{(EJ)_{11}},$$

$$\Psi_{12} = \frac{(\rho A)_{12}}{(EJ)_{11}},$$

$$\Psi_{21} = \frac{(\rho A)_{21}}{(EJ)_{21}},$$

$$\Psi_{22} = \frac{(\rho A)_{22}}{(EJ)_{22}}.$$

– natural boundary conditions at $x_{11} = 0$ and at $x_{22} = l_{22}$

$$(EJ)_{11} \left. \frac{\partial^2 W_{11}(x_{11}, t)}{\partial x_{11}^2} \right|_{x_{11}=0} - C_0 \left. \frac{\partial W_{11}(x_{11}, t)}{\partial x_{11}} \right|_{x_{11}=0} = 0, \quad (7)$$

$$(EJ)_{22} \left. \frac{\partial^2 W_{22}(x_{22}, t)}{\partial x_{22}^2} \right|^{x_{22}=l_{22}} + C_1 \left. \frac{\partial W_{22}(x_{22}, t)}{\partial x_{22}} \right|^{x_{22}=l_{22}} = 0, \quad (8)$$

$$(EJ)_{22} \left. \frac{\partial^3 W_{22}(x_{22}, t)}{\partial x_{22}^3} \right|^{x_{22}=l_{22}} + P \left. \frac{\partial W_{22}(x_{22}, t)}{\partial x_{22}} \right|^{x_{22}=l_{22}} - CW_{22}(l_{22}, t) - m \left. \frac{\partial^2 W_{22}(x_{22}, t)}{\partial t^2} \right|^{x_{22}=l_{22}} = 0, \quad (9)$$

– natural continuity conditions between adequate elements of the system (between elements (Figure 1): 11–12, 11–12–21, 21–22, 12–21–22):

$$-(EJ)_{11} \left. \frac{\partial^2 W_{11}(x_{11}, t)}{\partial x_{11}^2} \right|^{x_{11}=l_{11}} + (EJ)_{12} \left. \frac{\partial^2 W_{12}(x_{12}, t)}{\partial x_{12}^2} \right|_{x_{12}=0} = 0, \quad (10a)$$

$$-(EJ)_{21} \frac{\partial^2 W_{21}(x_{21}, t)}{\partial x_{21}^2} \Big|_{x_{21}=l_{21}} + (EJ)_{22} \frac{\partial^2 W_{22}(x_{22}, t)}{\partial x_{22}^2} \Big|_{x_{22}=0} = 0, \quad (10b)$$

$$(EJ)_{11} \frac{\partial^3 W_{11}(x_{11}, t)}{\partial x_{11}^3} \Big|_{x_{11}=l_{11}} - (EJ)_{12} \frac{\partial^3 W_{12}(x_{12}, t)}{\partial x_{12}^3} \Big|_{x_{12}=0} - (EJ)_{21} \frac{\partial^3 W_{21}(x_{21}, t)}{\partial x_{21}^3} \Big|_{x_{21}=0} + \\ + P \frac{\partial W_{11}(x_{11}, t)}{\partial x_{11}} \Big|_{x_{11}=l_{11}} - P \frac{\partial W_{21}(x_{21}, t)}{\partial x_{21}} \Big|_{x_{21}=0} = 0, \quad (10c)$$

$$(EJ)_{12} \frac{\partial^3 W_{12}(x_{12}, t)}{\partial x_{12}^3} \Big|_{x_{12}=l_{12}} + (EJ)_{21} \frac{\partial^3 W_{21}(x_{21}, t)}{\partial x_{21}^3} \Big|_{x_{21}=l_{21}} - \\ - (EJ)_{22} \frac{\partial^3 W_{22}(x_{22}, t)}{\partial x_{22}^3} \Big|_{x_{22}=0} = 0. \quad (10d)$$

The harmonic solutions to differential Equations (6) are assumed in the form:

$$W_{ij}(x_{ij}, t) = Y_{ij}(x_{ij}) \cos(\omega t), \quad (11)$$

where ω is the natural frequency.

Taking into account formula (11) in Equations (6) one can obtain differential equations which must be fulfilled for the length range of the individual elements of the hydraulic cylinder $x_{ij} \in (0, l_{ij})$ at every moment of time t . These new differential equations (after separation of variables) together with the boundary conditions after taking into account (11) form the boundary problem concerning free vibrations.

3. The solution of the boundary problem

Natural frequencies ω in dependence on the parameters of the system (including dependences on the external load) can be determined on the basis of the formulated boundary problem. In this paper the kinetic criterion of stability is used to determine the critical load of the system (stability problem). On the basis of the kinetic criterion of stability, the critical force of the system corresponds to the first zero natural frequency (the considered system is a divergence system).

The solutions to the differential equations obtained after separation of the variables can be written in the form:

$$Y_{ij}(x_{ij}) = A_{ij} \cosh(\alpha_{ij} x_{ij}) + B_{ij} \sinh(\alpha_{ij} x_{ij}) + C_{ij} \cos(\beta_{ij} x_{ij}) + D_{ij} \sin(\beta_{ij} x_{ij}), \quad (12)$$

where:

$$\alpha_{ij} = \sqrt{-\frac{k_{ij}^2}{2} + \sqrt{\frac{k_{ij}^4}{4} + \omega^2 \Psi_{ij}}},$$

$$\beta_{ij} = \sqrt{\frac{k_{ij}^2}{2} + \sqrt{\frac{k_{ij}^4}{4} + \omega^2 \Psi_{ij}}}.$$

By substituting solution (12) into the boundary conditions after separation of the variables, a system of homogeneous equations is obtained:

$$[a_{mn}] \{ A_{ij}, B_{ij}, C_{ij}, D_{ij} \} = 0, \quad i, j = 1, 2; \quad m, n = 1, 2, \dots, 16. \quad (13)$$

The matrix determinant of coefficients, equated to zero, is the transcendental equation, from which the consecutive natural frequencies of the system are determined:

$$|a_{mn}| = 0. \quad (14)$$

4. Stability

The results of numerical simulations concerning the stability problem are presented in this part of the paper. Numerical research was carried out for different parameters of the considered hydraulic cylinders, such as the flexural rigidity asymmetry factor for the piston rod and cylinder μ_a , the degree of coverage ζ_A , and the total rigidity factor of the system γ . It was also assumed that the piston rod and the cylinder are made of the same material. Parameters μ_a , ζ_A , γ are defined by the following equations:

$$\mu_a = \frac{(EJ)_{21}}{(EJ)_{11}}, \quad (15a)$$

$$\zeta_A = \frac{l_{12}}{l_{11} + l_{12}}, \quad (15b)$$

$$\gamma = \frac{(EJ)_S}{(EJ)_{odn}}, \quad (15c)$$

where:

$(EJ)_S$ is the rigidity of the hydraulic cylinder, $(EJ)_S = (EJ)_{11} + (EJ)_{21}$,

$(EJ)_{odn}$ is the reference rigidity.

Rigidity $(EJ)_{odn}$ has only a comparative character. In this work, rigidity $(EJ)_{odn}$ is equal to the rigidity of the system built from a pipe (cross-section of the pipe – A_r , geometrical axial moment of inertia of the pipe – J_r) and a middle rod (cross-section of the rod – A_p , geometrical axial moment of inertia of the rod – J_p), $(EJ)_{odn} = E(J_r + J_p)$. Diameters: d_{zr} – exterior of the pipe, d_{wr} – interior of the pipe, d_p – the rod is evaluated on the basis of a modified equation for slenderness:

$$i_{\min} = \sqrt{\frac{J_r + J_p}{A_r + A_p}} = \frac{\mu_w(l_{11} + l_{12})}{s_{gr}}, \quad (16)$$

where:

i_{\min} – minimal radius of the gyration of the intersection,

s_{gr} – limiting slenderness ratio of material of the hydraulic cylinder,

μ_w – buckling coefficient. The value of the buckling coefficient was assumed as $\mu_w = 1$ (which corresponds to the hinged fixed system). For computations of diameters: d_{zr} , d_{wr} , d_p it was additionally assumed that $J_p/J_r = 0.15$ and $d_p/d_{wr} = 0.8$.

In this paper, only hydraulic cylinders which undergo damage as a result of a loss of stability and not due to material effort were considered. The part of cylinder filled with liquid is especially at risk of damage due to material effort. A dangerous excess of stress in this part of cylinder is caused by liquid pressure. The boundary value of the flexural rigidity asymmetry factor μ_{gr} , where the way in which the damage to the hydraulic cylinder is changing, should be determined assuming the constant flexural rigidity of the hydraulic cylinder $(EJ)_S$. The damage to the hydraulic cylinder is a result of a stability loss at the coefficient $\mu_a \in (0, \mu_{gr})$ (this region of coefficient μ_a is considered in this paper). The damage to the hydraulic cylinder is a result of material effort at the value of coefficient $\mu_a > \mu_{gr}$. The theory of a double extra strong pipe (Lamé theory (compare 0,0, 0,0)) was applied to the computations of stresses in the part of cylinder which is at risk of liquid pressure action.

In Figures 2–6, the dependence of the boundary value of the flexural rigidity asymmetry factor μ_{gr} on the system parameters is presented, while in Figures 2–5, the dependence of the boundary value of factor μ_{gr} on the degree of coverage of the hydraulic cylinder ζ_A is shown.

Numerical computations were carried out for different values of total rigidity of the system $(EJ)_S$, determined on the basis of coefficient γ and reference rigidity $(EJ)_{odn}$. Due to the construction it was assumed that the value of the degree of coverage of the hydraulic cylinder ζ_A was changing in the range $\zeta_A \in \langle 0.1, 0.9 \rangle$ (thick fragments of the curves). Identical lengths of the cylinder and the piston ($l_{11} + l_{12} = l_{21} + l_{22}$) were taken into account in the numerical computations. The diagrams in Figure 2 were made for the rigidity values $c_1 = c_0 = 0.5$, while the diagrams in Figure 3 were made for the rigidity values $c_1 = c_0 = 2.5$.

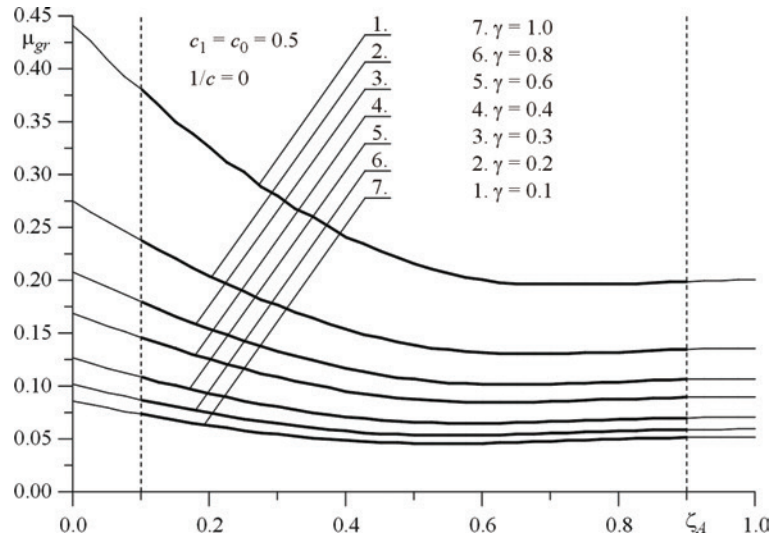


Fig. 2. The boundary value of the flexural rigidity asymmetry factor μ_{gr} in dependence on the degree of coverage of the hydraulic cylinder ζ_A for different values of coefficient γ ($\gamma = 0.1, 0.2, 0.3, 0.4, 0.6, 0.8, 1.0$) and for $c_1 = c_0 = 0.5$ and $1/c = 0$

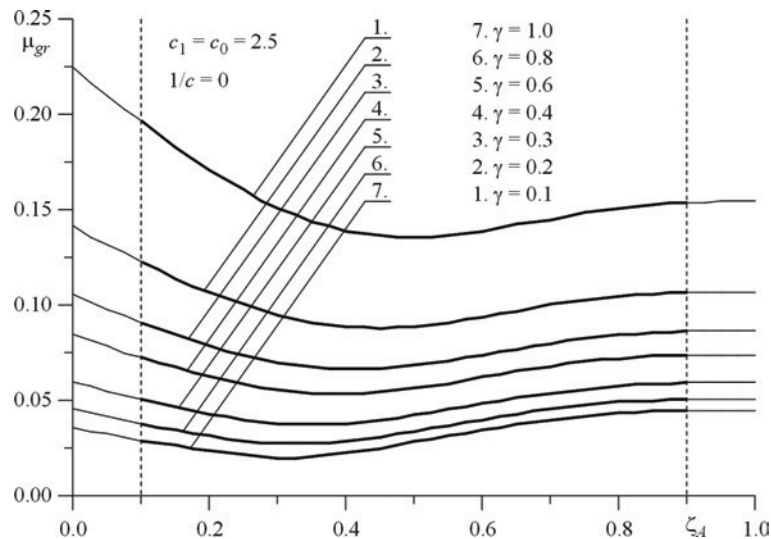


Fig. 3. The boundary value of the flexural rigidity asymmetry factor μ_{gr} in dependence on the degree of coverage of the hydraulic cylinder ζ_A for different values of coefficient γ ($\gamma = 0.1, 0.2, 0.3, 0.4, 0.6, 0.8, 1.0$) and for $c_1 = c_0 = 2.5$ and $1/c = 0$

The dimensionless parameters of the rigidity of the springs were defined as follows:

$$c_0 = \frac{C_0(l_{11} + l_{12})}{(EJ)_S}, \quad c_1 = \frac{C_1(l_{11} + l_{12})}{(EJ)_S}, \quad c = \frac{C(l_{11} + l_{12})^3}{(EJ)_S}. \quad (17)$$

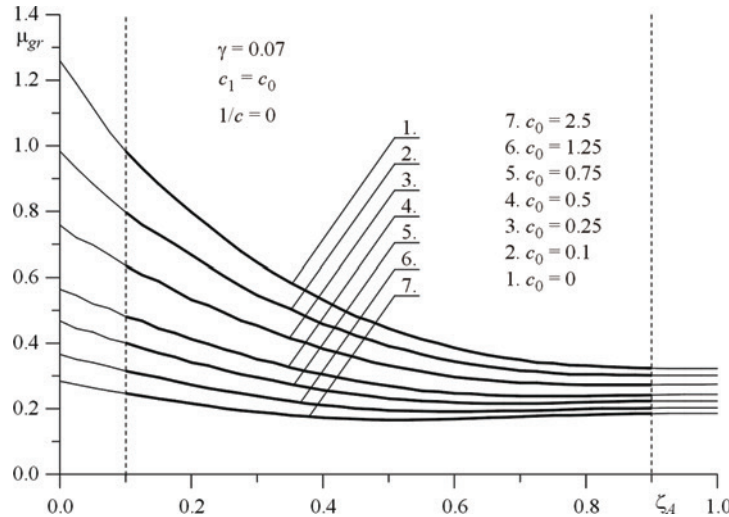


Fig. 4. The boundary value of the flexural rigidity asymmetry factor μ_{gr} in dependence on the degree of coverage of the hydraulic cylinder ζ_A for different values of rigidities of the rotational springs c_0 and c_1 ($c_1 = c_0 = 0, 0.1, 0.25, 0.5, 0.75, 1.25, 2.5$) and for $\gamma = 0.07$ and $1/c = 0$

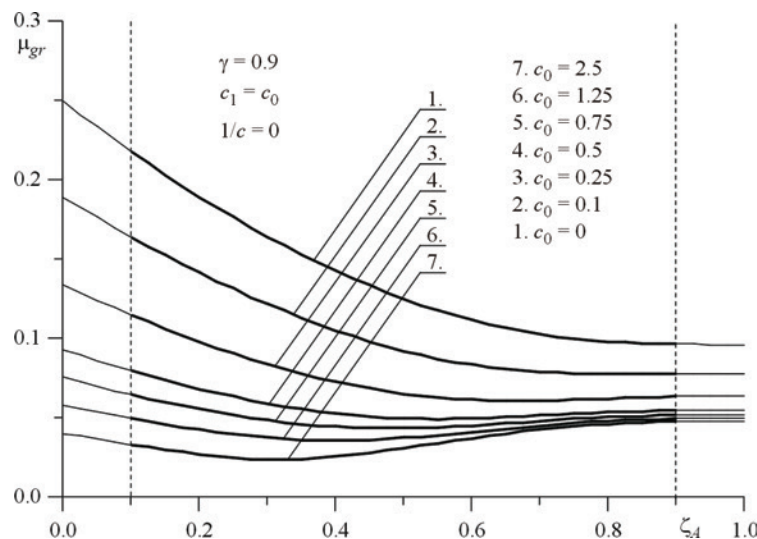


Fig. 5. The boundary value of the flexural rigidity asymmetry factor μ_{gr} in dependence on the degree of coverage of the hydraulic cylinder ζ_A for different values of rigidities of rotational springs c_0 and c_1 ($c_1 = c_0 = 0, 0.1, 0.25, 0.5, 0.75, 1.25, 2.5$) and for $\gamma = 0.9$ and $1/c = 0$

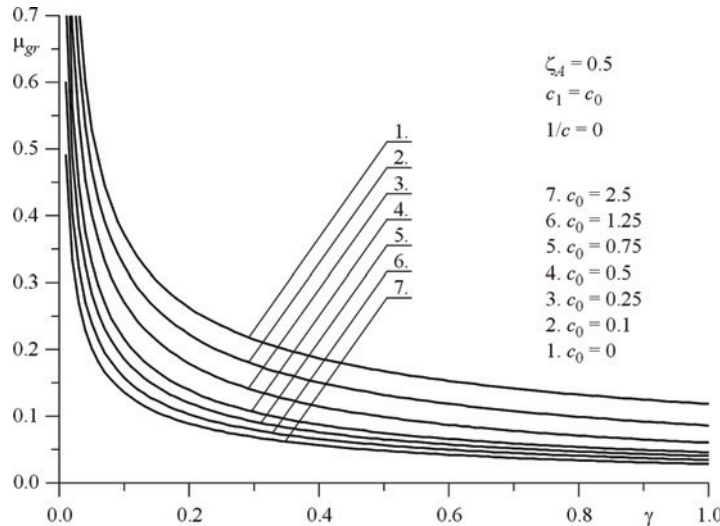


Fig. 6. The boundary value of the flexural rigidity asymmetry factor μ_{gr} in dependence on the degree of coverage of the hydraulic cylinder ζ_A for different values of rigidities of rotational springs c_0 and c_1 ($c_1 = c_0 = 0, 0.1, 0.25, 0.5, 0.75, 1.25, 2.5$) and for $\zeta_A = 0.5$ and $1/c = 0$

In Figures 4 and 5 the change in factor μ_{gr} in dependence on the degree of coverage of the hydraulic cylinder ζ_A is shown. In this case, the numerical computations were carried out for different values of the rigidities of the rotational springs (and equality of rigidity $c_0 = c_1$ was assumed). The following values of the parameter γ ($\gamma = 0.07$ – Figure 4 and $\gamma = 0.9$ – Figure 5) were also assumed. In Figure 6, factor μ_{gr} in dependence on parameter γ , describing rigidity of hydraulic cylinder ($\gamma \in (0, 1)$) is presented. It was also assumed that the degree of coverage is equal to $\zeta_A = 0.5$. The numerical computations were carried out for different values of the rigidities of the rotational springs c_0 and c_1 . All the numerical computations carried out in this work were made at equality of rigidities of springs $c_0 = c_1$ and at an infinite rigidity of the translational spring supporting the system $x_{22} = l_{22}$ ($1/c = 0$). At a given value of coefficient γ , the rigidity of hydraulic cylinder does not undergo changes independently of the values of the remaining parameters including the flexural rigidity asymmetry factor of the piston rod and cylinder μ_a . On the basis of the conducted numerical simulations it was stated that the rotational rigidity of the loading nods influences the change in the method of damage to the system (damage as a result of cylinder material effort or as a result of stability loss). A decrease in the rigidity of the rotational springs leads to an increase in the value of factor μ_{gr} , and so the range of factor μ_a ($\mu_a \in (0, \mu_{gr})$) where the system undergoes damage due to stability loss. The coefficient of system rigidity γ and the degree of coverage of the hydraulic cylinder ζ_A also has an influence on the value μ_{gr} . Together with an increase in the system rigidity (an increase in the value of coefficient γ) the value of factor μ_{gr} decreases.

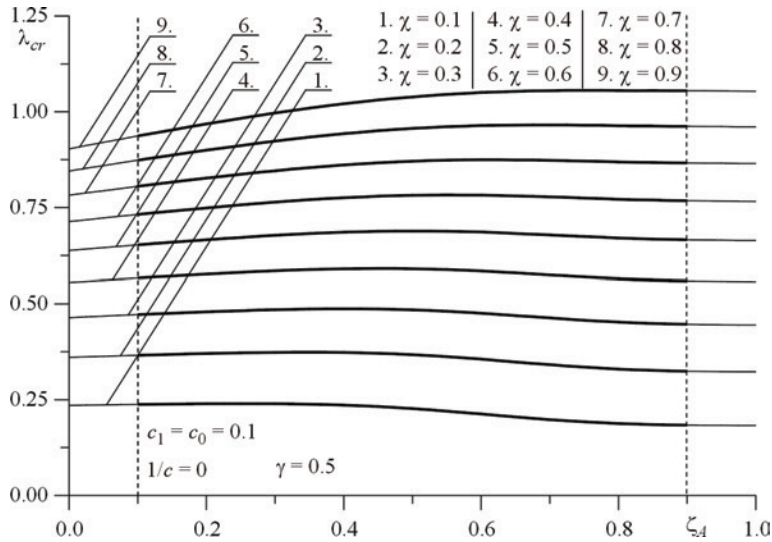


Fig. 7. The value of the dimensionless parameter of a critical force λ_{cr} in dependence on the degree of coverage of the hydraulic cylinder ζ_A for the chosen values of parameter χ and for $c_1 = c_0 = 0.1$, $1/c = 0$ as well as $\gamma = 0.5$

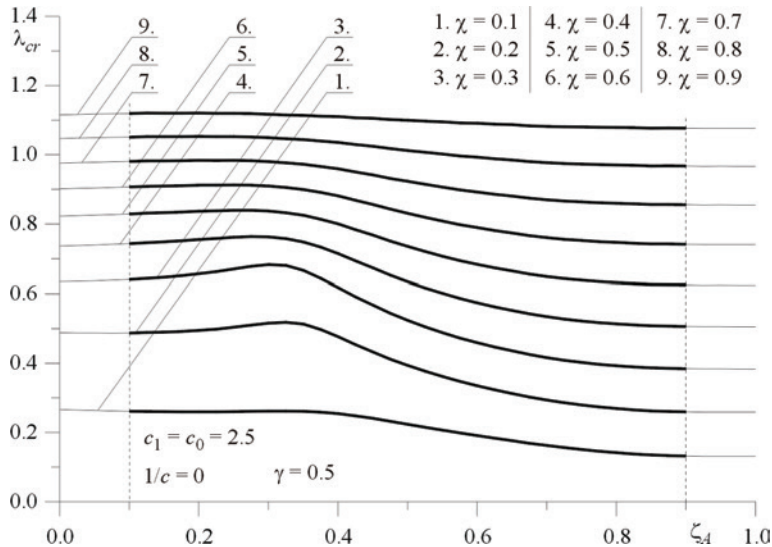


Fig. 8. The value of the dimensionless parameter of a critical force λ_{cr} in dependence on the degree of coverage of the hydraulic cylinder ζ_A for the chosen values of parameter χ and for $c_1 = c_0 = 2.5$, $1/c = 0$ as well as $\gamma = 0.5$

In Figures 7 and 8, the dimensionless parameter of a critical load λ_{cr} in dependence on the degree of coverage ζ_A for chosen values of parameter χ ($\chi = 0.1, 0.2, 0.3, 0.4$,

0.5, 0.6, 0.7, 0.8, 0.9) and $\gamma = 0.5$, $1/c = 0$ are presented. Computations were carried out for $c_0 = c_1 = 0.1$ (Figure 7) and for $c_0 = c_1 = 2.5$ (Figure 8). Parameters λ_{cr} and χ were defined in the following way:

$$\lambda_{cr} = \frac{P_{cr}(l_{11} + l_{12})^2}{(EJ)_S}, \quad (18a)$$

$$\chi = \frac{\mu_a}{\mu_{gr}}. \quad (18b)$$

Parameter χ was introduced to determine the range of factor μ_a , where the system undergoes damage due to stability loss.

5. Free vibrations

In respect of the problem of vibrations, the characteristic curves in the plane: the dimensionless parameter of the load λ – the dimensionless parameter of the first frequency of free vibrations Ω , were presented. Parameters λ i Ω were defined as follows:

$$\lambda = \frac{P(l_{11} + l_{12})^2}{(EJ)_S}, \quad (19a)$$

$$\Omega = \frac{\omega^2((\rho A)_{11} + (\rho A)_{12})(l_{11} + l_{12})^4}{(EJ)_S}. \quad (19b)$$

Numerical computations concerning free vibrations were carried out for hydraulic cylinders which undergo damage due to stability loss (the value of parameter χ is in the range $\chi \in \langle 0.1, 0.9 \rangle$).

In Figures 9 and 10, the characteristic curves of the first frequency of the free vibrations of the considered hydraulic cylinders are presented for different values of parameter ζ_A and for $\chi = 0.5$, $\gamma = 0.5$. The following rigidities of the rotational springs were assumed $c_0 = c_1 = 0.25$ (Figure 9) and $c_0 = c_1 = 2.5$ (Figure 10).

In Figures 11 and 12, the characteristic curves were plotted for different values of parameter χ and for $c_0 = c_1 = 0.25$, $\gamma = 0.5$, $\zeta_A = 0.2$ (Figure 11), $\zeta_A = 0.8$ (Figure 12). All the curves presented in the plane: load – natural frequency are characterised by a negative slope over the whole tested range of external load.

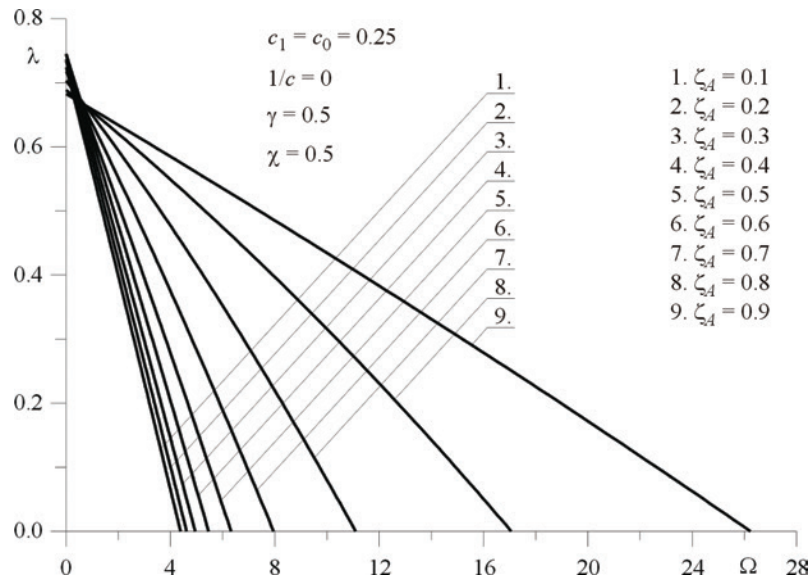


Fig. 9. The characteristic curves in the plane: parameter of the load λ – parameter of the first frequency of free vibrations Ω for different values of the degree of coverage ζ_A ($\zeta_A = 0.1 - 0.9$) and for $\chi = 0.5$, $\gamma = 0.5$, $c_1 = c_0 = 0.25$ and $1/c = 0$

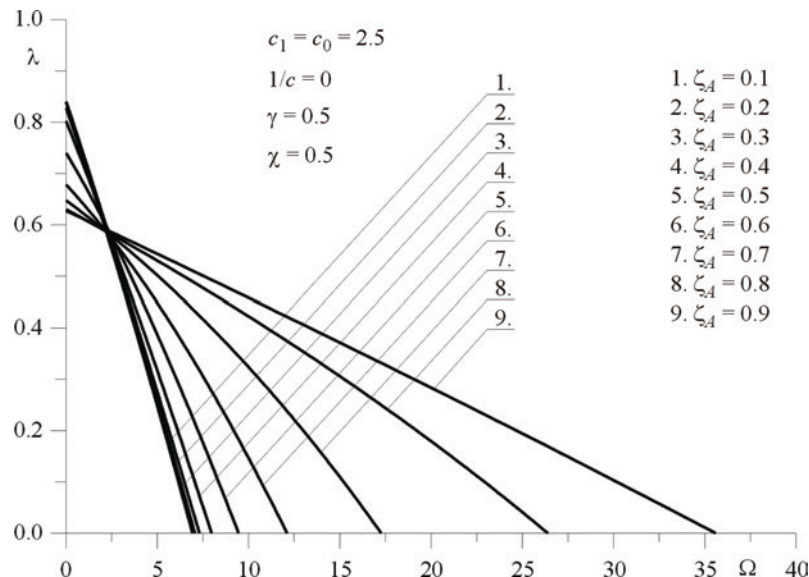


Fig. 10. The characteristic curves in the plane: parameter of the load λ – parameter of the first frequency of free vibrations Ω for different values of the degree of coverage ζ_A ($\zeta_A = 0.1 - 0.9$) and for $\chi = 0.5$, $\gamma = 0.5$, $c_1 = c_0 = 2.5$ and $1/c = 0$

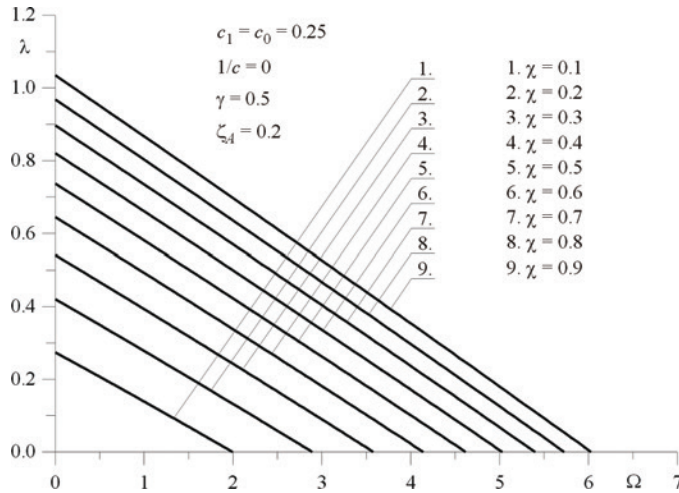


Fig. 11. The characteristic curves in the plane: parameter of the load λ – parameter of the first frequency of free vibrations Ω for different values of the parameter χ ($\chi = 0.1 - 0.9$)
and for $\zeta_A = 0.2$, $\gamma = 0.5$, $c_1 = c_0 = 0.25$ and $1/c = 0$

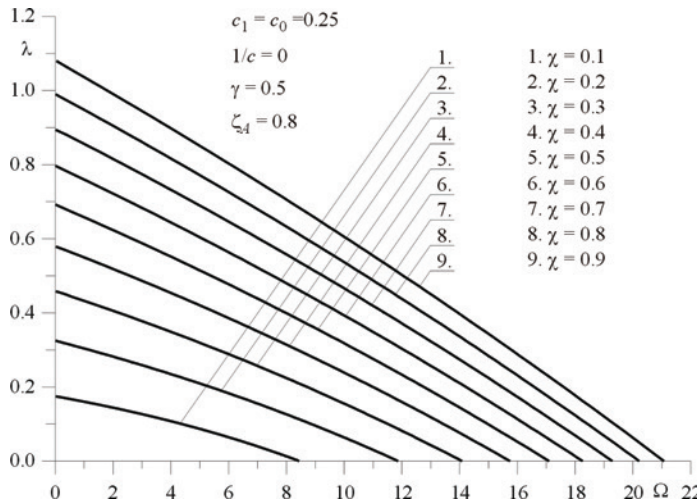


Fig. 12. The characteristic curves in the plane: parameter of the load λ – parameter of the first frequency of free vibrations Ω for different values of the parameter χ ($\chi = 0.1 - 0.9$)
and for $\zeta_A = 0.8$, $\gamma = 0.5$, $c_1 = c_0 = 0.25$ and $1/c = 0$

6. Summary

The boundary problem applied to the free vibrations of a hydraulic cylinder, taking into account discrete elements in the form of rotational springs and a translational spring, is formulated in the paper. Rotational springs are present at both ends of the

hydraulic cylinder. The translational spring is present at only one end of the hydraulic cylinder – at the piston rod. The hydraulic cylinder was subjected to a compressive Euler's load. On the basis of the kinetic criterion of stability, the critical load and the boundary value of the flexural rigidity asymmetry factor were determined. The boundary value of the flexural rigidity asymmetry factor μ_{gr} separates two regions. In the first region $\mu_a \in (0, \mu_{gr})$ the system undergoes damage due to a loss of stability, while in the second region $\mu_a \in (\mu_{gr}, \dots)$ the system undergoes damage due to material effort. The theory of a double extra strong pipe (Lamé theory) was applied to determine stresses in the part of cylinder filled with liquid. The characteristic curves in the plane: load – natural frequency, were plotted in the case of free vibrations. Numerical computations were carried out for different parameters of the system, namely: the flexural rigidity asymmetry factor of the piston rod and the cylinder, the total rigidity factor of the system and the degree of coverage of hydraulic cylinder.

Acknowledgement

The study has been carried out within Research Project No. N N501 117236 and with statutory funds BS-1-101-302-99/P awarded by the Ministry of Science and Higher Education.

References

- [1] Boiarshinov S. Ia.: *Osnovy stroitelnoi mekhaniki mashin*, Mashinostrenie, Moscow, 1973 (in Russian).
- [2] Green A.E., Zerna W.: *Theoretical elasticity*, Oxford, 1954.
- [3] Przybylski J.: *Drgania i stateczność dwuczłonowych układów prętowych wstępnie sprężonych przy obciążeniach niezachowawczych*, Seria Monografie, Wydawnictwo Politechniki Częstochowskiej, Częstochowa, No. 92, 2002.
- [4] Sochacki W., Tomski L.: *Drgania swobodne i stateczność dynamiczna układu zmiany wysięgu żurawia samochodowego*, rozdział 3, *Modelowanie i badania zjawisk dynamicznych wysięgników teleskopowych i żurawi samojezdnych*, Praca zbiorowa wykonana pod red. B. Posiadały, Wydawnictwa Naukowo Techniczne, Warszawa, 2000, pp. 57–80.
- [5] Sochacki W., Tomski L.: *Free vibration and dynamic stability of a hydraulic cylinder set. machine dynamics problems*, Vol. 23, No. 4, 1999, pp. 91–104.
- [6] Tomski L., Chwalba W., Kukla S., Mrowiec A., Posiadała B.: *Dynamical response of hydraulic cylinder connected with external shock absorber subjected to axial mass impact*, Archives of Mining Sciences, Vol. 32, No. 3, 1987, pp. 439–454.
- [7] Tomski L., Kukla S.: *Dynamical response of bar–fluid–shell system simulating hydraulic cylinder subjected to arbitrary axial excitation*, Journal of Sound and Vibration, Vol. 92, No. 2, 1984, pp. 273–284.
- [8] Tomski L., Przybylski J., Posiadała B.: *Static instability of eccentrically loaded hydraulic cylinder with piston rod in the form of two coaxial tubes*, Akademiai Kiado, Publishing House of Hungarian Academy of Science, Budapest, 1988, pp. 1055–1062.

- [9] Tomski L., Uzny S.: *Stateczność i drgania swobodne siłownika hydraulicznego sprężystego zamocowanego*, Zeszyty Naukowe Politechniki Rzeszowskiej, seria: Mechanika, Vol. 258, No. 74, 2008, pp. 369–380.
- [10] Tomski L.: *Dynamika stojaków hydraulicznych obudów górniczych*, praca habilitacyjna, Częstochowa, No. 17, 1979.
- [11] Tomski L.: *Elastic carrying capacity of a hydraulic prop*, Engineering Transactions, Vol. 25, No. 2, 1977, pp. 247–263.
- [12] Tomski L.: *Elastic stability of hydraulic props of longwall supports*, Archives of Mining Science, Vol. 23, No. 3, 1978, pp. 217–231.
- [13] Tomski L.: *Forced vibrations of hydraulic props of longwall supports*, Archives of Mining Science, Vol. 24, No. 1, 1979, pp. 19–33.
- [14] Tomski L.: *Longitudinal mass impact of hydraulic servo*, ZAMM, Vol. 61, 1981, pp. 191–193.
- [15] Uzny S.: *Free vibrations and stability of hydraulic cylinder fixed elastically on both ends*, Proc. Appl. Math. Mech., Vol. 9, No. 1, 2009, pp. 303–304.

Siłownik hydrauliczny poddany obciążeniu Eulera w aspekcie stateczności i drgań własnych z uwzględnieniem dyskretnych elementów sprężystych

W niniejszej pracy przeprowadzono badania teoretyczne i numeryczne dotyczące stateczności i drgań własnych smukiego układu w postaci siłownika hydraulicznego, który poddano obciążeniu Eulera. W układzie uwzględniono sztywności w węzłach konstrukcyjnych realizujących obciążenie rozważanego układu. W węzłach obciążających zastosowano sprężyny rotacyjne jak i translacyjne. W ramach badań numerycznych siłownika hydraulicznego określono obszary współczynnika asymetrii sztywności na zginanie tłocyska i cylindra, przy których układ ulega zniszczeniu w wyniku utraty stateczności. W pracy wyznaczono również obciążenie krytyczne oraz krzywe charakterystyczne na płaszczyźnie obciążenie–częstość drgań własnych. Te dwie wielkości wyznaczono przy różnych wartościach parametrów układu, do których zalicza się współczynnik asymetrii sztywności na zginanie tłocyska i cylindra, stopień przekrycia siłownika, sztywności sprężyn rotacyjnych i translacyjnej oraz współczynnik całkowitej sztywności układu.



Improved implementation of the extended finite element method for stress analysis around cracks

T.T. YU, P. LIU

Dept. of Engineering Mechanics, Hohai University, Nanjing 210098, China.

Although the extended finite element method (XFEM) allows for modelling arbitrary discontinuities, its low order elements often means that frequent improvements on accuracy are required. The generalized finite element method (GFEM), the extension of the conventional FEM, improves the approximation accuracy of the FEM by introducing generalized degrees of freedom and re-interpolating nodal degrees of freedom. This paper enhances the implementation of the XFEM for stress analysis around cracks by coupling the GFEM and XFEM. The generalized node shape functions are used in a cluster of nodes around the cracks, and the conventional finite element shape functions are adopted at nodes outside the cracks, thereby reducing costs and improving the accuracy of stresses in the vicinity of the cracks. Several numerical examples show that the proposed approach generates higher accuracy for stress intensity factor computations at affordable costs.

Keywords: *XFEM, GFEM, crack, stress intensity factor*

1. Introduction

Finite element methods (FEM) have been widely used in research and engineering. However, because of the fact that standard FEMs are based on piecewise polynomial approximations, they are not well suited to solving discontinuity problems. To overcome this deficiency, the extended finite element method (XFEM) was introduced in 1999 [3].

The XFEM is a numerical method used to simulate the discontinuity within the standard finite element framework [29]. In this method, the standard displacement-based approximation is enriched by incorporating discontinuous fields through the partition of unity method [24]. This enables the geometry of discontinuity to be independent of the finite element computation mesh; thus, it is very convenient for discontinuous problem analysis, especially for moving discontinuous problems. In the past decade, numerous efforts have been made to improve or apply the original XFEM for simulations of fractures and other discontinuous phenomena. Studies where the XFEM is used in fracture problems are [3, 29] and [14, 30, 38] for the two-dimensional and three-dimensional elastic crack growths, respectively; [17–18] for cohesive crack propagation; [22, 37] for bi-material interface crack; [25, 27–28] for dynamic crack propagation; [42] for fatigue crack propagation; and [10] for elastic-plastic crack

growth. The surveys of the XFEM for computational fracture mechanics were provided by several scholars in [20, 32, 44]. The XFEM is also successfully used in other areas of computational mechanics such as fluid–structure interactions [13], phase transformations [15], shear band propagation [1], evolution of dislocations [31], and biofilm growth [8]. The XFEM/GFEM was reviewed with an emphasis on applications in materials science problems by Belytschko et al. [4] and highlighting methodological issues by Fries et al. [12].

One difficulty with the XFEM is that it sometimes fails to exhibit the desired accuracy. Numerous studies have been directed toward improving the accuracy of the fields near the crack. Larve [16] replaced the Heaviside step function with a higher-order polynomial B-spline shape function approximation. Stazi et al. [35] used higher-order background elements for linear elastic fracture mechanics that is able to obtain higher accuracy for curved cracks. Liu et al. [22] enriched the crack tip node with the leading, as well as higher-order terms of the asymptotic crack tip fields, in an attempt to significantly improve the accuracy of the directly determined stress intensity factors (SIFs). Recently, elastic fracture work was extended to thermoelastic fractures [45], in which the benefit of including higher-order terms is greater for thermoelastic problems than for either purely elastic or steady state heat transfer problems. Béchet et al. [2] expanded the range of the crack tip enrichment area by a “geometrical” instead of a “topological” enrichment. Numerical accuracy was consequently improved.

The standard formulation of the XFEM approximations leads to problems in blending elements [5], and the existence of blending elements reduces accuracy. Fries proposed “the corrected XFEM” employing a new definition of enrichment [11]. The corrected XFEM showed the effective improvement of accuracy reduction caused by the blending elements. Later, the theoretical validation of “the corrected XFEM” was determined based on the concept of the PUFEM approximation [34].

For dynamic crack propagation in the context of the XFEM, recent work on time-dependent tip enrichment [28] and release of the crack tip element [26] showed some improvement in XFEM accuracy in SIF computation. The enrichment of the XFEM approximations by mesh-free approximations was reported in Reference [25]; this approach leads to higher accuracy in SIF computation, and to the capability to capture the branching point of a propagating crack from the stresses.

An alternative method of enhancing the quality of the stress field near the crack tip is adaptively driven by error estimation developed in [9, 33, 41].

The generalized finite element method (GFEM) was adopted by the Texas school [23] and the Institute of Mathematics of the Chinese Academy of Sciences [21] in 1995–1996. Based on the partition of unity method, the GFEM improves the approximation accuracy of the FEM or achieves the special approximation in particular problems by introducing generalized degrees of freedom (DOF) and re-interpolating nodal DOF. The first GFEM studies involved global enrichments of the approximation space; later, local enrichments for singularities at sharp corners were also developed [7]. Strouboulis et al. [36] systematically studied the GFEM by the combination of

conventional FEM and the partition of unity method. The XFEM and GFEM are basically identical methods; thus, some reviews of the XFEM also include GFEM [4, 12].

The GFEM involving global enrichments of the approximation space can improve accuracy; however, this will considerably increase computational time. A favourable choice is to adopt the GFEM in the domain that requires higher accuracy.

In this paper, we study whether the enrichment of an XFEM approximation by a GFEM approximation can improve the accuracy of stresses in the vicinity of the crack and SIF computations. The main advantage of the GFEM is that it can improve accuracy and seamlessly combine with the FEM. We enrich XFEM with the GFEM around the crack to enhance stress state and capture a better description to drive the crack.

The rest of the paper is organized as follows. Section 2 presents the variational equations. Section 3 introduces and develops the space discretization, i.e., the coupling of the XFEM and the GFEM. Section 4 presents the numerical integration. Section 5 explains the linear dependency and presents the solution of the system. Section 6 describes the numerical examples, and Section 7 presents the conclusion.

2. Variational formulation

Consider the elastic body Ω shown in Figure 1. The boundary Γ is composed of Γ_D , Γ_N and Γ_C . Displacements $\bar{\mathbf{u}}$ are prescribed along Γ_D and tractions \mathbf{t} are prescribed along Γ_N . The crack surface Γ_C is assumed to be traction-free. The virtual work equation without body forces is given by

$$\int_{\Omega} \boldsymbol{\varepsilon}(\mathbf{v}) : \boldsymbol{\sigma}(\mathbf{u}) d\Omega = \int_{\Gamma_N} \mathbf{v} \cdot \mathbf{t} d\Gamma, \quad (1)$$

where:

$\boldsymbol{\sigma}$ – the Cauchy stress,

$\boldsymbol{\varepsilon}$ – the strains,

\mathbf{u} – the space of admissible displacement fields defined by

$$\mathbf{u} = \left\{ \mathbf{u} \in H^1(\Omega) : \mathbf{u}|_{\Gamma_D} = \bar{\mathbf{u}} \right\}, \quad (2)$$

where:

the space $H^1(\Omega)$ is related to the regularity of the solution;

\mathbf{v} – the test function space defined by

$$\mathbf{v} = \left\{ \mathbf{v} \in H^1(\Omega) : \mathbf{v}|_{\Gamma_D} = 0 \right\}. \quad (3)$$

Note that \mathbf{u} and \mathbf{v} are allowed to be discontinuous along the crack.

Assuming small displacements \mathbf{v} , the strains $\boldsymbol{\varepsilon}$ and the displacements of the structure can be related by

$$\boldsymbol{\varepsilon} = \frac{1}{2} [\nabla \mathbf{u} + (\nabla \mathbf{u})^T]. \quad (4)$$

The abovementioned equations are equivalent to the governing equations for the cracked body Ω .

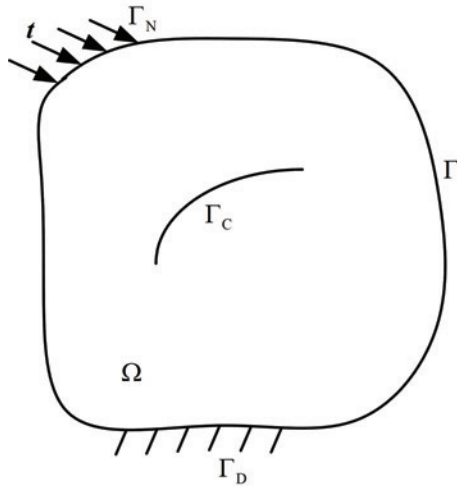


Fig. 1. A cracked body subjected to prescribed boundary tractions and displacements

3. Space discretization: GFEM-enriched XFEM

3.1. GFEM

S_h is the conventional finite element space; Lagrangian type interpolation base functions of conventional FEM are used as $\{\varphi_1, \varphi_2, \dots, \varphi_n\}$, and the nodal DOF vector is $\{\mathbf{u}_1, \mathbf{u}_2, \dots, \mathbf{u}_n\}$. Thus, the displacement field can be expressed in the following form:

$$\mathbf{u}^h = \sum_{i=1}^n \mathbf{u}_i \varphi_i. \quad (5)$$

In the GFEM, the nodal displacements in the conventional FEM are generalized, and an arbitrary series expansion with any number of generalized displacements is assumed on each node [21], i.e.,

$$\mathbf{u}_i = \begin{Bmatrix} u_i \\ v_i \end{Bmatrix} = \sum_{j=1}^{m_i} \begin{bmatrix} f_{ij}(x) & 0 \\ 0 & f_{ij}(x) \end{bmatrix} \begin{Bmatrix} d_{i,2j-1} \\ d_{i,2j} \end{Bmatrix}. \quad (6)$$

By substituting Equation (6) into Equation (5), the new approximation space is obtained thus:

$$\mathbf{u}^h = \sum_{i=1}^n \sum_{j=1}^{m_i} \begin{bmatrix} f_{ij}(x) & 0 \\ 0 & f_{ij}(x) \end{bmatrix} \begin{Bmatrix} d_{i,2j-1} \\ d_{i,2j} \end{Bmatrix} \varphi_i = \sum_{i=1}^n \mathbf{F}_i \varphi_i \mathbf{D}_i = \sum_{i=1}^n \mathbf{N}_i \mathbf{D}_i, \quad (7)$$

where:

\mathbf{D}_i – nodal generalized displacement array, $\mathbf{D}_i = [d_{i,1}, d_{i,2}, \dots, d_{i,m}]^T$;
 \mathbf{N}_i – the new interpolation function matrix. Because the new interpolation function \mathbf{N}_i includes the interpolation function φ_i of the conventional FEM, the compatibility of the GFEM will be naturally satisfied. When $m_i = 1$ and $f_{ij}(x) = 1$, Equation (6) will degenerate as

$$\mathbf{u}_i = \begin{Bmatrix} u_i \\ v_i \end{Bmatrix} = \begin{bmatrix} 1 & 0 \\ 0 & 1 \end{bmatrix} \begin{Bmatrix} d_{i,1} \\ d_{i,2} \end{Bmatrix}. \quad (8)$$

Thus, the GFEM will be reduces to the conventional FEM.

The number of nodal generalized displacements has one-to-one correspondence with the order of nodal interpolation function.

For plane problems, the zero-order nodal displacement interpolation function is

$$\mathbf{F}_i = \begin{bmatrix} 1 & 0 \\ 0 & 1 \end{bmatrix}, \quad \mathbf{D}_i = \begin{Bmatrix} d_{i,1} \\ d_{i,2} \end{Bmatrix}. \quad (9)$$

Thus, each node has two DOFs, and this case is the conventional FEM.

For plane problems, the first-order nodal displacement interpolation function is

$$\mathbf{F}_i = \begin{bmatrix} 1 & 0 & x & 0 & y & 0 \\ 0 & 1 & 0 & x & 0 & y \end{bmatrix}, \quad \mathbf{D}_i = [d_{i,1} \ d_{i,2} \ d_{i,3} \ d_{i,4} \ d_{i,5} \ d_{i,6}]^T. \quad (10)$$

The corresponding DOF of each node is six.

For plane problems, the second-order nodal displacement interpolation function is

$$\mathbf{F}_i = \begin{bmatrix} 1 & 0 & x & 0 & y & 0 & xy & 0 & x^2 & 0 & y^2 & 0 \\ 0 & 1 & 0 & x & 0 & y & 0 & xy & 0 & x^2 & 0 & y^2 \end{bmatrix}, \quad \mathbf{D}_i = [d_{i,1} \ d_{i,2} \ \dots \ d_{i,12}]^T. \quad (11)$$

Thus, each node has twelve DOFs.

With the improvement in the order of nodal displacement interpolation functions, the order of generalized shape functions will accordingly be enhanced.

In general, standard finite element shape functions have the Kronecker – δ property, i.e., $\varphi_i(x_j) = \delta_{ij}$. In a standard finite element approximation, $\mathbf{u}^h(x) = \sum_{i=1}^n u_i \varphi_i(x)$,

which leads to the following desirable features:

- the computed unknowns u_i are directly the sought function values of $\mathbf{u}^h(x)$ at node i , i.e., $\mathbf{u}^h(x) = u_i$.
- the imposition of Dirichlet boundary conditions $\hat{\mathbf{u}}(x)$ is simple: $\mathbf{u}_i = \hat{\mathbf{u}}(x)$.

In standard GFEM approximations, refer to Equation (7); these properties can be achieved by shifting the nodal displacement interpolation functions F_i as

$$F_i^{\text{shift}}(x) = F_i(x - x_i) \quad (12)$$

and using $F_i^{\text{shift}}(x)$ instead of $F_i(x)$ in Equation (7).

Considering the cost and accuracy, the first-order nodal displacement interpolation function is used in the paper, and the generalized shape function of node i is as follows:

$$\mathbf{N}_i = \varphi_i \begin{bmatrix} 1 & 0 & x - x_i & 0 & y - y_i & 0 \\ 0 & 1 & 0 & x - x_i & 0 & y - y_i \end{bmatrix}. \quad (13)$$

3.2. GFEM-enriched XFEM discretization

In the XFEM, the standard finite element approximation is enriched by additional functions to model the flaw(s) and other geometric entities. The enriched displacement approximation can be written as follows:

$$\begin{aligned} \mathbf{u}^h(x) = & \sum_{i \in I} \varphi_i(x) \cdot \mathbf{u}_i + \sum_{j \in L} \bar{\varphi}_j(x) \cdot (H(x) - H(x_j)) \cdot \mathbf{a}_j + \\ & + \sum_{\alpha=1}^4 \sum_{k \in K} \bar{\varphi}_k(x) \cdot (\phi_\alpha(x) - \phi_\alpha(x_k)) \cdot R^\alpha(x) \cdot \mathbf{b}_{k\alpha}, \end{aligned} \quad (14)$$

where:

$\varphi_i(x)$ and $\bar{\varphi}_j(x)$ – finite element shape functions,

\mathbf{u}_i , \mathbf{a}_j and $\mathbf{b}_{k\alpha}$ – the displacement and enrichment nodal variables, respectively. The shape functions $\bar{\varphi}_j(x)$, which localize the enrichment, can differ from the shape functions $\varphi_i(x)$ in the displacement approximation [35]. In this paper, both sets of shape functions are identical and are the shape functions of the underlying finite element approximation. I is the set of all nodes in the discretization; L is the set of nodes whose basis function support

is entirely split by the crack and are enriched with a modified Heaviside step function $\mathbf{H}(\mathbf{x})$, which takes on the value +1 above the crack and -1 below the crack; \mathbf{K}^* is the set of nodes located within a circle centred on the crack tip (2D) or a circular cylinder around the front (3D) with a radius r_a fixed in advance, but usually problem dependent; \mathbf{K} is the set of nodes enriched with the crack-tip fields, and is the set of nodes in \mathbf{K}^* plus their neighbouring nodes (the nodes that share elements with nodes in \mathbf{K}^*); $R^\alpha(\mathbf{x})$ are the ramp functions, $R^\alpha(\mathbf{x}) = \sum_{i \in \mathbf{K}^*} \bar{\varphi}_i(\mathbf{x})$, thereby avoiding problems in blending elements [11].

For isotropic elasticity, the crack tip (front) branch enrichment functions $\phi_l(\mathbf{x}) = (\mathbf{l} = 1, \dots, 4)$ are defined as

$$[\phi_l(\mathbf{x})] = \left[\sqrt{r} \sin \frac{\theta}{2}, \sqrt{r} \cos \frac{\theta}{2}, \sqrt{r} \sin \theta \cdot \sin \frac{\theta}{2}, \sqrt{r} \sin \theta \cdot \cos \frac{\theta}{2} \right], \quad (15)$$

where r and θ are local crack tip (front) polar coordinates.

To improve the accuracy of stresses around the crack and SIF computations, $\varphi_i(\mathbf{x})$ and $\bar{\varphi}_j(\mathbf{x})$ around the crack are adopted as the generalized shape functions shown in Equation (13). They are used as conventional finite element shape functions outside the crack. The nodal generalized shape functions are used only around the crack; hence, the number of the overall DOF slightly increases compared with an XFEM computation. The choice of the nodal subsets for the enrichments and the domain for nodal generalized shape functions are illustrated for the GFEM-enriched XFEM in Figure 2. The node with the generalized shape functions is called generalized DOF node.

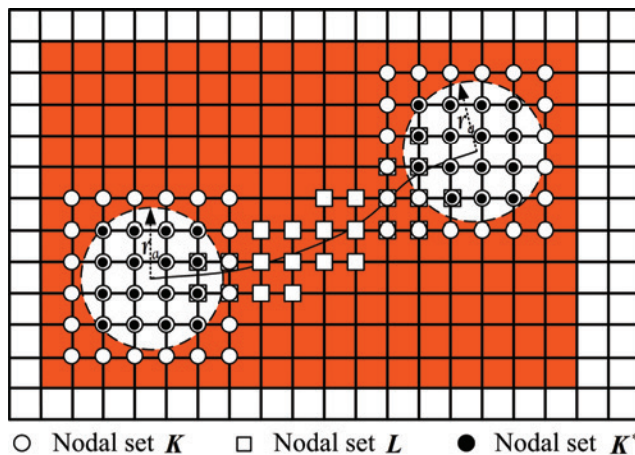


Fig. 2. Nodal subsets for the enrichment in the GFEM-enriched XFEM

(Red areas show where the nodal generalized shape functions are used).

4. Numerical integration

To ensure that the strain field is adequately integrated, the Gauss quadrature for the GFEM-enriched XFEM with four-nodded quadrilateral elements is as follows:

- the standard second order Gauss-Legendre quadrature is used in an element not containing any enriched nodes and generalized DOF nodes;
- the standard three order Gauss quadrature is used in an element that includes a generalized DOF node but not any enriched nodes;
- the standard three order Gauss quadrature is used in an element that includes step-enriched nodes but is not cut by the crack;
- the standard five order Gauss quadrature is used in an element that includes tip-enriched nodes but is not cut by the crack;
- when an element is cut by the crack but does not contain the crack tip, it is divided into a set of triangular sub-domains whose boundaries align with the crack geometry. Within each triangle, the four order Gauss quadrature is applied;
- for an element containing the crack tip, the element is also divided into a set of triangles whose boundaries align with the crack geometry. However, within each triangular sub-domain, the eight order Gauss quadrature is applied.

5. Linear dependency

In the XFEM, using the branch enrichment at all nodes in the domain leads to a rank-deficient system matrix. For the standard/corrected XFEM, the matrix contains only two zero eigenvalues and one can circumvent problems by eliminating two equations resulting for the branch-enriched DOF in the final system matrix [11].

Conversely, the GFEM may lead to a singular stiffness matrix because of the linear dependence of the local approximation functions [40]. In the GFEM, however, the eigenfunctions associated with the zero eigenvalues are, in general, unknown. Generally, we can use the following two methods to solve the system of semipositive definite sparse symmetric linear equations: the perturbation method [36], and multi-frontal sparse Gaussian elimination method [6].

According to the analysis above, we can determine that the system in the GFEM-enriched XFEM is generally rank deficient, and the number of rank deficiency is unknown. In the following numerical examples, we use the perturbation method to resolve the system of equations.

6. Numerical examples and discussion

To confirm the usefulness of the GFEM-enriched XFEM, we present the evaluations of numerical results in the linear fracture mechanics, including comparisons with that using the standard XFEM. The numerical results for the first example are reported

to demonstrate the convergence and efficiency of the proposed method, whereas the last two examples are investigated for the evaluation of the accuracy of linear fracture mechanics parameters.

In all of the following examples, the materials are defined by a Young's modulus (E) of 1000 and Poisson ratio (ν) of 0.3, and the conventional bilinear isoparametric elements are used as background elements. The calculation of the SIF is performed with the domain form of the interaction integral as detailed in [19].

6.1. Mode I crack model in the infinite plate

An infinite plate including a straight crack with a unit fracture Mode I is considered and depicted in Figure 3a. Let us define a local finite square domain Ω including the crack tip in the centre. The domain Ω is smaller than the crack length $2a$ in infinite plate. Along Γ_D , the closed form near-tip displacement field in terms of polar coordinates in a reference frame (r, θ) centred at the crack tip is

$$u_x = \frac{K_I}{2\mu} \sqrt{r/(2\pi)} \cos \frac{\theta}{2} \left(\kappa - 1 + 2 \sin^2 \frac{\theta}{2} \right), \quad (16)$$

$$u_y = \frac{K_I}{2\mu} \sqrt{r/(2\pi)} \sin \frac{\theta}{2} \left(\kappa + 1 - 2 \cos^2 \frac{\theta}{2} \right), \quad (17)$$

where:

$$\mu = \frac{E}{2(1+\nu)} \text{ -- the shear module,}$$

$$\kappa = 3 - 4\nu \text{ -- for plane strain,}$$

$$\kappa = \frac{3-\nu}{1+\nu} \text{ -- for plane stress.}$$

For the numerical computation, the size of the analytical domain Ω is 2×2 and the crack length is 1 as shown in Figure 3b. This is realized by describing the boundary conditions according to $K_I = 1$, $K_{II} = 0$ for a pure crack Mode I computation. Plane stress conditions are assumed. For the XFEM simulations, the nodes around the crack tip within a radius of $r_a = 0.2$ are enriched with the branch functions as described. The GFEM is used in the local domain around the crack as shown in Figure 4.

The normalized energy error norm is computed by

$$\text{energy error} = \sqrt{\frac{\int_{\Omega} (\boldsymbol{\varepsilon} - \boldsymbol{\varepsilon}^h) : \mathbf{C} : (\boldsymbol{\varepsilon} - \boldsymbol{\varepsilon}^h) d\Omega}{\int_{\Omega} \boldsymbol{\varepsilon} : \mathbf{C} : \boldsymbol{\varepsilon} d\Omega}}, \quad (18)$$

where:

ε – the exact strain field,

ε^h – the approximate strain field obtained by the numerical solution.

The numerical results in the convergence study of the energy norm are shown in Figure 5. It is interesting that while the accuracy of the GFEM-enriched XFEM is better, the rate of convergence is actually lower. The same conclusion was drawn by Stazi et al. [35], in which they found that the rate of convergence of the quadratic element is actually lower than that of the linear element, although the accuracy of the quadratic element is better. They believed this behaviour is probably a result of singularity.

The SIF K_I has been evaluated numerically in a radial integration domain of radius $r = 0.6$ around the crack tip. For element size $h = 0.1538$, the relative error of K_I for the standard XFEM and GFEM-enriched XFEM is 1.2267% and 0.0059%, respectively; the DOF for the standard XFEM and GFEM-enriched XFEM is 448 and 1088, respectively. The GFEM-enriched XFEM is much better than the standard XFEM. The GFEM-enriched XFEM enriches more unknowns than does the standard XFEM. Therefore, we compute the case where the element size $h = 0.0952$ with the standard XFEM, the corresponding DOF is 1104, and the relative error of K_I is 0.3574%. For the smaller DOF, the accuracy of the GFEM-enriched XFEM is still better than that of the standard XFEM.

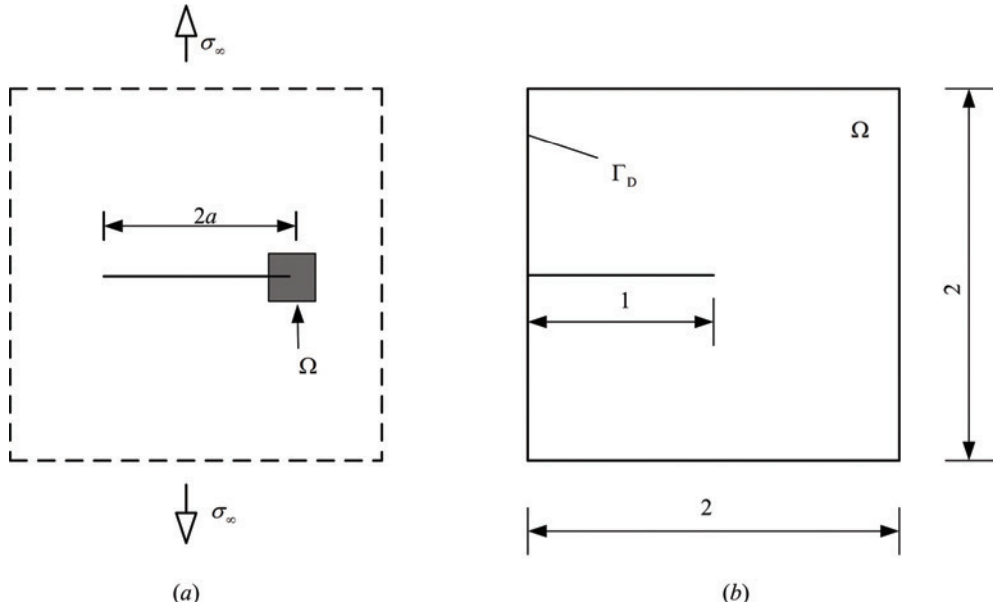


Fig. 3. A Mode I crack model in an infinite plate: (a) infinite crack body with fracture Mode I and (b) numerical model for the domain Ω

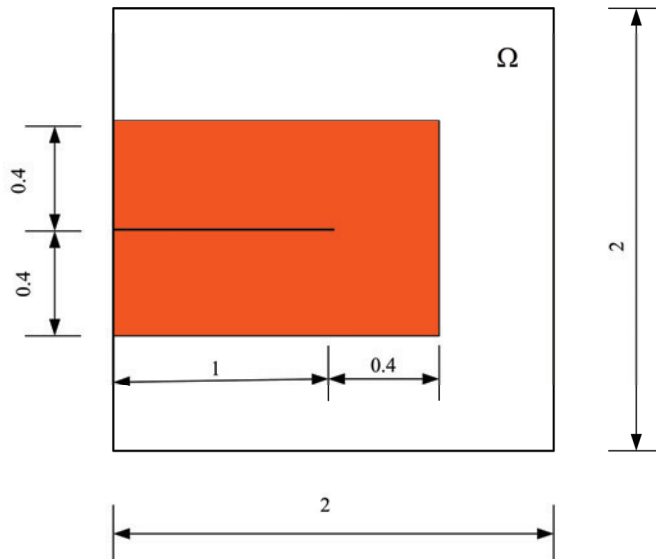


Fig. 4. Domain where the nodal generalized shape functions are used (the red areas)

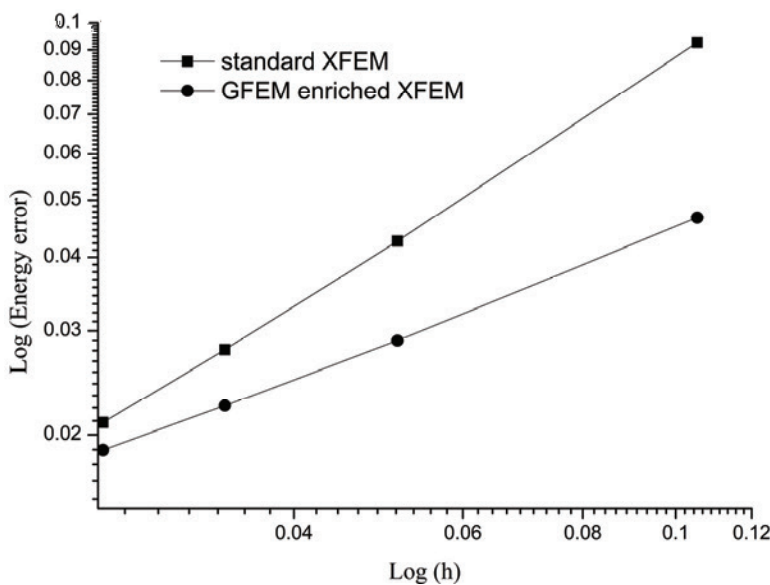


Fig. 5. Convergence results in the energy norm

6.2. Edge-cracked plate under tension

A single edge-cracked plate is loaded by tension $\sigma = 1.0$ unit over the top and bottom edges as shown in Figure 6. The displacement along the vertical direction is fixed

at the bottom right corner, and the plate is clamped at the bottom left corner. The plate has a length $2h = 16$ units, width $b = 7$ units, and the crack length is $a = 3.5$ units. Plane strain conditions are assumed.

The reference mixed-mode SIFs as given in [39] are

$$K_I^{\text{ref}} = \sigma \sqrt{\pi a} F\left(\frac{a}{b}\right), \quad (19)$$

where $F\left(\frac{a}{b}\right)$ is an empirical function. For $\frac{a}{b} \leq 0.6$, the function F is

$$F\left(\frac{a}{b}\right) = 1.120 - 0.231\left(\frac{a}{b}\right) + 10.550\left(\frac{a}{b}\right)^2 - 21.720\left(\frac{a}{b}\right)^3 + 30.390\left(\frac{a}{b}\right)^4. \quad (20)$$

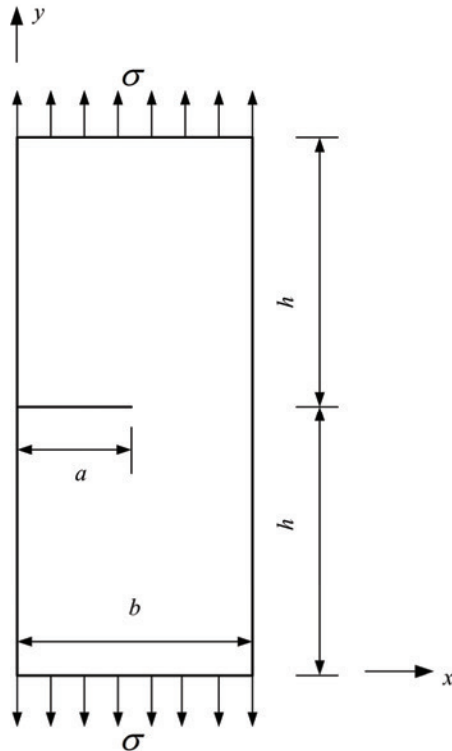


Fig. 6. Edge-cracked plate in tension

The SIFs are obtained using two methods. For the first (GFEM-enriched XFEM), the meshes consist of uniform meshes and evenly spaced 20×40 nodes. All of the

nodes in one element are enriched, which we call enriched element. Nodal generalized shape functions are used on the nodes of enriched elements and m-layer elements around enriched elements (Figure 7). In Figure 7a, $m = 1$; in Figure 7b, $m = 2$; in Figure 7c, $m = 3$; and in Figure 7d, $m = 4$. For the second method (standard XFEM), three different discretizations scenarios are considered. The first consists of uniform meshes and evenly spaced 20×40 nodes, the second consists of 30×60 nodes, and the third 40×80 nodes. The nodes around the crack tip within a radius of $r_a = 0.2$ are enriched with the branch functions.

The SIFs obtained using different methods are shown in Tables 1–2 below.

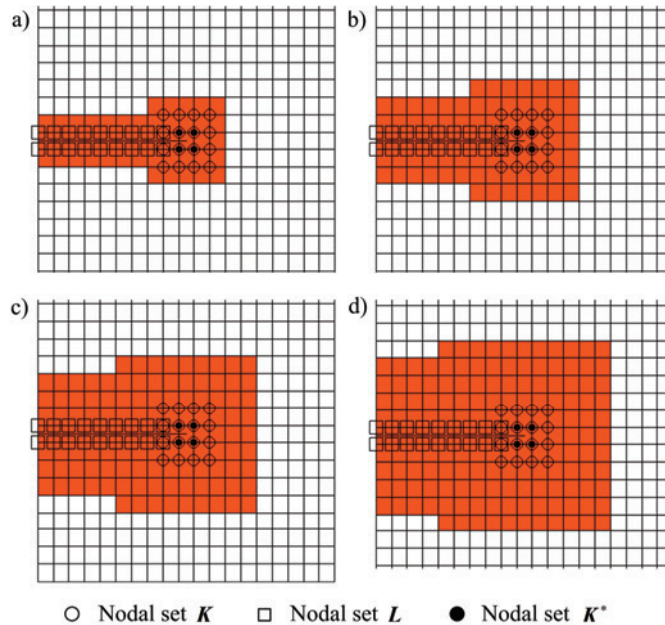


Fig. 7. Local mesh and zoom on the crack area (nodal generalized shape functions are used in red domain). (a) $m = 1$; (b) $m = 2$; (c) $m = 3$; (d) $m = 4$

Table 1. Results for K_I of an edge crack plate under tension (GFEM-enriched XFEM)

Number of layers	DOF	K_I	$\left \frac{K_I - K_I^{\text{ref}}}{K_I^{\text{ref}}} \right (\%)$
$m = 1$	2348	9.3394	0.3671
$m = 2$	2492	9.3466	0.2905
$m = 3$	2652	9.3527	0.2250
$m = 4$	2828	9.3574	0.1750

When the GFEM is used in the enriched elements and one-layer elements around the enriched elements, the accuracy is good, and the results improve with the increase in number of layers used with the GFEM.

Although the number of DOFs in the GFEM-enriched XFEM is smaller, the error level of the GFEM-enriched XFEM is still significantly better than that of the standard XFEM. The main reasons may be: the standard XFEM leads to problems in blending elements, reducing accuracy; and the second order shape functions are used in the GFEM, improving the accuracy of stresses in the vicinity of the crack.

Table 2. Results for K_I of an edge crack plate under tension (standard XFEM)

mesh	DOF	K_I	$\left \frac{K_I - K_I^{\text{ref}}}{K_I^{\text{ref}}} \right (\%)$
20×40	1668	9.0607	3.3400
30×60	3688	9.1799	2.0681
40×80	6508	9.2318	1.5151

6.3. Edge-cracked plate under shear

Consider an edge-cracked plate, as shown in Figure 8, fixed at the bottom and subjected to a uniform shear stress $\tau = 1.0$ unit applied at the top. The plate has a length $L = 16$ units, width $W = 7$ units, and the crack length is $a = 3.5$ units. Plane strain conditions are assumed.

The reference mixed-mode SIFs as given in [39] and [43] are

$$\begin{aligned} K_I^{\text{ref}} &= 34.0, \\ K_{II}^{\text{ref}} &= 4.55. \end{aligned} \quad (21)$$

Tables 3–4 show that the GFEM-enriched XFEM is more accurate. K_I and K_{II} exhibit the same behaviour. The same conclusions can be drawn as the previous example.

Table 3. Results for K_I and K_{II} of an edge crack plate under shear (GFEM-enriched XFEM)

Number of layers	DOF	K_I	$\left \frac{K_I - K_I^{\text{ref}}}{K_I^{\text{ref}}} \right (\%)$	K_{II}	$\left \frac{K_{II} - K_{II}^{\text{ref}}}{K_{II}^{\text{ref}}} \right (\%)$
$m = 1$	2348	33.9135	0.2545	4.5349	0.3328
$m = 2$	2492	33.9364	0.1870	4.5391	0.2392
$m = 3$	2652	33.9601	0.1173	4.5413	0.1914
$m = 4$	2828	33.9791	0.0613	4.5429	0.1553

The accuracy of stresses in the vicinity of the crack and SIF computations can be improved when the GFEM is used around the crack. In general, nodes in one or two layers of elements around the crack are adopted generalized shape functions, and this appears to obtain desirable accuracy. This does not incur expensive costs; however, the accuracy can still be improved.

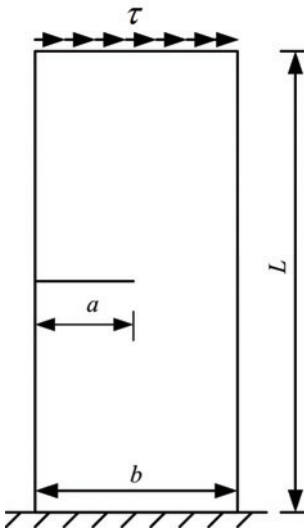


Fig. 8. Edge-cracked plate in shear

Table 4. Results for K_I and K_{II} of an edge crack plate under shear (standard XFEM)

mesh	DOF	K_I	$\left \frac{K_I - K_I^{ref}}{K_I^{ref}} \right (\%)$	K_{II}	$\left \frac{K_{II} - K_{II}^{ref}}{K_{II}^{ref}} \right (\%)$
20×40	1668	32.8512	3.3788	4.4883	1.3556
30×60	3688	33.3400	1.9413	4.5037	1.0170
40×80	6508	33.5467	1.3331	4.5115	0.8460

7. Conclusion

In this paper, a method to enrich the XFEM by GFEM approximations has been described. The GFEM is the extension of the conventional FEM; it improves the approximation accuracy of the FEM by introducing generalized DOFs and re-interpolating nodal DOFs. The advantage is that the GFEM approximation can effectively improve accuracy and seamlessly combine with the conventional FEM. However, the cost is expensive in the GFEM. In this study, the generalized node shape functions are used in a cluster of nodes around cracks, and the conventional finite element shape functions are adopted at nodes outside the cracks, thereby reducing costs and improving accuracy.

The second order shape functions are used in the GFEM, and the error level of the GFEM-enriched XFEM is still significantly better even if the number of DOFs in the GFEM-enriched XFEM is smaller. In general, nodes in one or two layers of elements around the crack are adopted generalized nodal shape functions, and this leads to desirable accuracy.

The proposed method is quite promising for problems where higher accuracy near the crack tip is often beneficial during propagation, and for decreasing the unphysical oscillations in the stress due to the propagation of the crack.

Acknowledgements

This work was funded by the National Basic Research Program of China (“973” Program) (Grant No. 2007CB714104), the Fundamental Research Funds for the Central Universities (Grant No. 2011B03014) and the National Natural Science Foundation of China (Grant No. 50609004).

References

- [1] Areias P.M.A., Belytschko T.: *Two-scale shear band evolution by local partition of unity*, International Journal for Numerical Methods in Engineering, Vol. 66, No. 5, 2006, pp. 878–910.
- [2] Béchet E., Minnebo H., Moës N., Burgardt B.: *Improved implementation and robustness study of the X-FEM for stress analysis around cracks*, International Journal for Numerical Methods in Engineering, Vol. 64, No. 8, 2005, pp. 1033–1056.
- [3] Belytschko T., Black T.: *Elastic crack growth in finite elements with minimal remeshing*, International Journal for Numerical Methods in Engineering, Vol. 45, No. 5, 1999, pp. 601–620.
- [4] Belytschko T., Gracie R., Ventura G.: *A review of extended/generalized finite element methods for material modelling*, Modelling and Simulation in Materials Science and Engineering, Vol. 17, No. 4, 2009, pp. 043001.
- [5] Chessa J., Wang H., Belytschko T.: *On the construction of blending elements for local partition of unity enriched finite elements*, International Journal for Numerical Methods in Engineering, Vol. 57, No. 7, 2003, pp. 1015–1038.
- [6] Du I.S., Reid J.K.: *The multifrontal solution of indefinite sparse symmetric linear systems*, ACM Transactions on Mathematical Software, Vol. 9, No. 3, 1983, pp. 302–325.
- [7] Duarte C.A., Babuška I., Oden J.T.: *Generalized finite element methods for three-dimensional structural mechanics problems*, Computers and Structures, Vol. 77, No. 2, 2000, pp. 215–232.
- [8] Duddu R., Bordas S., Chopp D., Moran B.: *A combined extended finite element and level set method for biofilm growth*, International Journal for Numerical Methods in Engineering, Vol. 74, No. 5, 2008, pp. 848–870.
- [9] Duflot M., Bordas S.: *A posteriori error estimation for extended finite elements by an extended global recovery*, International Journal for Numerical Methods in Engineering, Vol. 76, No. 8, 2008, pp. 1123–1138.
- [10] Elguedj T., Gravouil A., Combescure A.: *Appropriate extended functions for X-FEM simulation of plastic fracture mechanics*, Computer Methods in Applied Mechanics and Engineering, Vol. 195, No. 7–8, 2006, pp. 501–515.
- [11] Fries T.P.: *A corrected XFEM approximation without problems in blending elements*, International Journal for Numerical Methods in Engineering, Vol. 75, No. 5, 2008, pp. 503–532.

- [12] Fries T.P., Belytschko T.: *The extended/generalized finite element method: An overview of the method and its applications*, International Journal for Numerical Methods in Engineering, Vol. 84, No. 3, 2010, pp. 253–304.
- [13] Gerstenberger A., Wall W.A.: *An eXtended finite element method/Lagrange multiplier based approach for fluid-structure interaction*, Computer Methods in Applied Mechanics and Engineering, Vol. 197, No. 19–20, 2008, pp. 1699–1714.
- [14] Gravouil A., Moës N., Belytschko T.: *Non-planar 3d crack growth by the extended finite element and level sets—part ii: level set update*, International Journal for Numerical Methods in Engineering, Vol. 53, No. 11, 2002, pp. 2569–2586.
- [15] Groß S., Reusken A.: *An extended pressure finite element space for two-phase incompressible flows with surface tension*, Journal of Computational Physics, Vol. 224, No. 1, 2007, pp. 40–58.
- [16] Iarve E.V.: *Mesh independent modelling of cracks by using higher order shape functions*, International Journal for Numerical Methods in Engineering, Vol. 56, No. 6, 2003, pp. 869–882.
- [17] James V.C.: *An extended finite element method with analytical enrichment for cohesive crack modelling*, International Journal for Numerical Methods in Engineering, Vol. 78, No. 1, 2009, pp. 48–83.
- [18] Jörg F.U., Stefan E., Carsten K.: *Modelling of cohesive crack growth in concrete structures with the extended finite element method*, Computer Methods in Applied Mechanics and Engineering, Vol. 196, No. 41–44, 2007, pp. 4087–4100.
- [19] Jovicic G., Zivkovic M., Jovicic N., Milovanovic D.: *Improvement of algorithm for numerical crack modelling*, Archives of civil and mechanical engineering, Vol. X, No. 3, 2010, pp. 19–35.
- [20] Karihaloo B.L., Xiao Q.Z.: *Modelling of stationary and growing cracks in FE framework without remeshing: a state-of-the-art review*, Computers and Structures, Vol. 81, No. 3, 2003, pp. 119–129.
- [21] Liang G.P., He J.H.: *Generalized finite element method – a new finite element space* (in Chinese), advances in mechanics, Vol. 25, No. 4, 1995, pp. 562–565.
- [22] Liu X.Y., Xiao Q.Z., Karihaloo B.L.: *XFEM for direct evaluation of mixed mode SIFs in homogeneous and bi-materials*, International Journal for Numerical Methods in Engineering, Vol. 59, No. 8, 2004, pp. 1103–1118.
- [23] Melenk J.M.: *On generalized finite element methods*, PhD Thesis, University of Maryland, 1995.
- [24] Melenk J.M., Babuska I.: *The partition of unity finite element method: basic theory and applications*, Computer Methods in Applied Mechanics and Engineering, Vol. 139, No. 1–4, 1996, pp. 289–314.
- [25] Menouillard T., Belytschko T.: *Dynamic fracture with meshfree enriched XFEM*, Acta Mechanica, Vol. 213, No. 1–2, 2010, pp. 53–69.
- [26] Menouillard T., Belytschko T.: *Correction Force for releasing crack tip element with XFEM and only discontinuous enrichment*, European Journal of Computational Mechanics, Vol. 18, No. 5–6, 2009, pp. 465–483.
- [27] Menouillard T., Réthoré J., Moës N., Combescure A., Bung H.: *Mass lumping strategies for X-FEM explicit dynamics: Application to crack propagation*, International Journal for Numerical Methods in Engineering, Vol. 74, No. 3, 2008, pp. 447–474.

- [28] Menouillard T., Song J.H., Duan Q.L., Belytschko T.: *Time dependent crack tip enrichment for dynamic crack Propagation*, International Journal of Fracture, Vol. 162, No. 1–2, 2010, pp. 33–49.
- [29] Moës N., Dolbow J., Belytschko T.: *A finite element method for crack growth without remeshing*, International Journal for Numerical Methods in Engineering, Vol. 46, No. 1, 1999, pp. 131–150.
- [30] Moës N., Gravouil A., Belytschko T.: *Non-planar 3d crack growth by the extended finite element and level sets-part i: mechanical model*, International Journal for Numerical Methods in Engineering, Vol. 53, No. 11, 2002, pp. 2549–2568.
- [31] Oswald J., Gracie R., Khare R., Belytschko T.: *An extended finite element method for dislocations in complex geometries: Thin films and nanotubes*, Computer Methods in Applied Mechanics and Engineering, Vol. 198, No. 21–26, 2009, pp. 1872–1886.
- [32] Rabczuk T., Bordas S., Zi G.: *On three-dimensional modelling of crack growth using partition of unity methods*, Computers and Structures, Vol. 88, No. 23–24, 2010, pp. 1391–1411.
- [33] Ródenas J.J., González-Estrada O.A., Tarancón J.E., Fuenmayor F.J., Valenciana G.: *A recovery type error estimator for the extended finite element method based on singular + smooth stress field splitting*, International Journal for Numerical Methods in Engineering, Vol. 76, No. 4, 2008, pp. 545–571.
- [34] Shibanuma K., Utsunomiya T.: *Reformulation of XFEM based on PUFEM for solving problem caused by blending elements*, Finite Elements in Analysis and Design, Vol. 45, No. 11, 2009, pp. 806–816.
- [35] Stazi F.L., Budyn E., Chessa J., Belytschko T.: *An extended finite element method with higher-order elements for curved cracks*, Computational Mechanics, Vol. 31, No. 1–2, 2003, pp. 38–48.
- [36] Strouboulis T., Babuska I., Copps K.: *The design and analysis of the generalized finite element method*, Computer Methods in Applied Mechanics and Engineering, Vol. 181, No. 1, 2000, pp. 43–69.
- [37] Sukumar N., Huang Z.Y., Prévost J.-H., Suo Z.: *Partition of unity enrichment for bimaterial interface cracks*, International Journal for Numerical Methods in Engineering, Vol. 59, No. 8, 2004, pp. 1075–1102.
- [38] Sukumar N., Moës N., Moran B., Belytschko T.: *Extended finite element method for three-dimensional crack modelling*, International Journal for Numerical Methods in Engineering, Vol. 48, No. 11, 2000, pp. 1549–1570.
- [39] Tada H., Paris P.C., Irwin R.: *The stress analysis of cracks (Handbook)*, Del Research Corporation, Hellertown, Pennsylvania, 1973.
- [40] Tian R., Yagawa G., Terasaka H.: *Linear dependence problems of partition of unity-based generalized FEMs*, Computer Methods in Applied Mechanics and Engineering, Vol. 195, No. 37–40, 2006, pp. 4768–4782.
- [41] Xiao Q.Z., Karhaloo B.L.: *Improving the accuracy of XFEM crack tip fields using higher order quadrature and statically admissible stress recovery*, International Journal for Numerical Methods in Engineering, Vol. 66, No. 9, 2006, pp. 1378–1410.
- [42] Xu Y.J., Yuang H.: *Computational modelling of mixed-mode fatigue crack growth using extended finite element methods*, International Journal of Fracture, Vol. 159, No. 2, 2009, pp. 151–165.

- [43] Yau J.F., Wang S.S., Corten H.T.: *A mixed-mode crack analysis of isotropic solids using conversation laws of elasticity*, Journal of Applied Mechanics, Vol. 47, No. 2, 1980, pp. 335–341.
- [44] Yazid A., Abdelkader N., Abdelmajjid H.: *A state-of-the-art review of the X-FEM for computational fracture mechanics*, Applied Mathematical Modelling, Vol. 33, No. 12, 2009, pp. 4269–4282.
- [45] Zamani A., Gracie R., Eslami M.R.: *Higher order tip enrichment of extended finite element method in thermoelasticity*, Computational Mechanics, Vol. 46, No. 6, 2010, pp. 851–866.

Udoskonalone zastosowania rozszerzonej metody elementów skończonych do analizy naprężeń wokół pęknięcia

Pomimo że rozszerzona metoda elementów skończonych (XFEM) pozwala modelować przypadkowe nieciągłości, metoda ta wymaga poprawy dokładności. Można to uzyskać poprzez zastosowanie dodatkowych metod modelowania. W pracy przedstawiono zastosowanie połączonych metod GFEM i XFEM do analizy naprężzeń wokół pęknięcia. Kilka numerycznych przykładów wykazało, że proponowane podejście pozwala uzyskać lepszą dokładność od metod dotychczas stosowanych.